Reaction dynamics of metal oxides in solution by NMR

By:

Rupali Sharma

A thesis submitted to the Faculty of Science, Monash University, in fulfilment of the requirements for the degree of *Doctor of Philosophy*

School of Chemistry

Monash University

Australia

May 2017

Abstract

The main objective of my research is to build a better understanding of solution dynamics of metal oxides at solid-solvent interface which is relevant to heterogeneous catalysis and minerals. To accomplish this, I have investigated aqueous behaviour of model complexes such as polyoxometalates (POMs). Central to my research is the use of NMR which is an effective and powerful tool to resolve the reaction dynamics of polyoxometalates in solution. Simultaneously, I have also investigated theoretical predictions of NMR chemical shifts in polyoxometalates to complement experimental measurements.

To begin with, I probed the reaction dynamics of ligands bound to paramagnetic complexes in solution. In these cases, both the exchanging moeities are water molecules. I investigated the pH-dependent solution dynamics of a manganese(II)-substituted Wells-Dawson sandwich complex ($[Mn_4(H_2O)_2(P_2W_{15}O_{56})_2]^{16-}$) and compared it with the corresponding hexa-aqua ion, $[Mn(H_2O)_6]^{2+}$. Swift and Connick formalism was used to estimate the rates of exchange of bound aqua ligands using the paramagnetic line-broadening of the ^{17}O NMR signal of the bulk solvent. It was seen that the rates of exchange were unaffected by pH in the hexa-aqua ion but for the polyoxometalate, the rates increased by seven-fold at low pH. Thus, protonation in the polyoxometalate framework had substantial effect on the rates of exchange of bound waters.

I also examined the oxygen exchange dynamics in polyoxometalates to gain atomic level view of dissolution reactions. I investigated the rates of oxygen isotope-exchange in two nanometer-sized soluble clusters, $[PV_2Nb_{12}O_{42}]^{9-}$ and $[V_3Nb_{12}O_{42}]^{9-}$, as a function of pH using ^{17}O NMR spectroscopy. The two complexes are isostructural and isovalent differing only by a single central atom. The rates of oxygen exchange were investigated by monitoring the decrease in the ^{17}O NMR signal of each structural oxygen as it equilibriates with water. It was seen that all the oxygen atoms respond to changes in the pH enviornment unanimously even though their rates differ by a factor of 10^2-10^4. The substitution of a single atom affects the reaction dynamics of the molecules dramatically. Protonation of the complex also has a

large effect on the rates of oxygen-exchange reactions.

Computational studies in polyoxometalates allowed me to probe the dynamics of polyoxometalates theoretically. NMR is useful to provide site-specific information only if the signal assignments are correct. With this view in mind, Density Functional Theory (DFT) was used as a computational tool to predict NMR chemical shifts of various nuclei in polyoxometalates. I present a detailed study on computation of ^{17}O chemical shifts optimising different variables that control the accuracy in prediction, namely, exchange-correlation functionals and basis sets. I also analysed the influence of incorporating a certain amount of Hartree-Fock exchange, and computed ^{17}O NMR shifts in a wide range of polyoxometalates. I achieved an excellent correlation between the theoretical predictions and the experimental observations. Taking a step forward, I examined the prediction of NMR shifts of other nuclei (^{51}V, ^{183}W, ^{95}Mo and ^{31}P) which play an important role in structural characterisation of POMs. The study involves a search and scrutiny for best functional for each nuclei. The solvation and relativistic effects were included for computing tungsten and molybdenum NMR shifts. In general, NMR chemical shift prediction benefit from the use of hybrid functionals, large basis sets, solvation effects and relativistic effects, even though they are computationally time-consuming.

Declaration

I hereby declare that this thesis contains no material which has been accepted for the award of any other degree or diploma at any university or equivalent institution and that, to the best of my knowledge and belief, this thesis contains no material previously published or written by another person, except where due reference is made in the text of the thesis.

This thesis includes two original papers published in peer reviewed journals. The core theme of the thesis is reaction dynamics of metal oxides in solution by NMR. The ideas, development and writing up of all the papers in the thesis were the principal responsibility of myself, the student, working within the department of chemistry under the supervision of Dr C. André Ohlin.

| Thesis chapter	Publication title	Publication Status	Nature and extent of student's contribution	Co-author name(s), Nature and contribution	Co-author(s), Monash student Y/N
2	pH-dependent solution dynamics of a manganese(II) polyoxometalate, $[Mn_4(H_2O)_2(P_2W_{15}O_{56})_2]^{16-}$, and $[Mn(H_2O)_6]^{2+}$	Published	Initiation, key ideas, experimental work, writing up	J. Zhang and C. A. Ohlin; Supervision, proof-reading and editing (15%)	No
3	Effect of substitution on oxygen isotope-exhange rates in isovalent and isostructural complexes, $[PV_2Nb_{12}O_{42}]^{9-}$ and $[V_3Nb_{12}O_{42}]^{9-}$	Unpublished	Initiation, key ideas, experimental work, writing up	J. Zhang and C. A. Ohlin; Supervision, proof-reading and editing (15%)	No
4	Predicting ^{17}O NMR chemical shifts of polyoxometalates using density functional theory	Published	Initiation, key ideas, experimental work, writing up	J. Zhang and C. A. Ohlin; Supervision, proof-reading and editing (15%)	No
5	A DFT approach for calculation of ^{51}V, ^{183}W, ^{95}Mo and ^{31}P NMR shifts in polyoxometalates	Unpublished	Initiation, key ideas, experimental work, writing up	J. Zhang and C. A. Ohlin; Supervision, proof-reading and editing (15%)	No

Student signature:

Date: 03.05.2017

The undersigned hereby certify that the above declaration correctly reflects the nature and extent of the student's and co-author's contributions to this work.

Main supervisor signature:
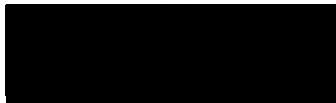
Date: 03.05.2017

Acknowledgements

First and foremost, I would like to express my sincere gratitude to my supervisor Dr C. A. Ohlin for the continuous support of my PhD study, for his guidance and immense knowledge. Apart from guiding through my thesis, I have learnt some IT and writing skills from him which will help me in my future endeavours. I am extremely thankful to him for giving his time and effort in discussing the experimental issues and also providing best possible assistance in writing reports and publications.

I would also like to thank Dr Jie Zhang for his support, encouragement and appreciation during the whole tenure. I could not have imagined having a better co-supervisor for my PhD study.

I am grateful to Peter Nicholas, NMR head at Monash University, who has always given me access to the NMR research facility. Without his precious support it would not have been possible to conduct this research.

I thank my fellow mate Shravan Acharya for his discussions, help, encouragement and for listening to me when I felt low.

Finally, I am indebted to my parents for infusing the right moralities and ethics in me which have helped me be sane during the tough times. I also would not be where I am without my husband who has been thoroughly understanding and a constant support system. Last but not the least, I am blessed to have a lovely son who keeps me going.

Contents

Abbreviations

ADF   Amsterdam density functional

AAE   Average absolue error

ECP   Electron core potential

COSMO   Conductor-like screening model

DOSY   Diffusion ordered spectroscopy

DFT   Density functional theory

FID   Free Induction decay

GGA   Generalised gradient approximations

GIAO   Gauge including atomic orbitals

Hz   Hertz

HF   Hartree-Fock

LSD   Local spin density approximation

MAE   Maximum absolute error

MO   Molecular orbital

NMR   Nuclear magnetic resonance

POM   Polyoxometalates

PCM   Polarizable continuum model

ppm   Parts per million

RF   Radiofrequency

S/N   Signal-to-noise

STO   Slater-type orbitals

XC   Exchange-correlation

ZORA   Zeroth order relativistic approximations

δ Chemical shift

Chapter 1

Introduction

Geological and geochemical processes often occur under conditions and on time scales that are inaccessible to direct experimental investigation. To circumvent this, models are used. However, because the models need to be faithful to the processes modelled, the data used to generate them need to be sufficiently complex as to capture the essential chemistry.

A central question to geochemistry and biogeochemistry is that of metal-oxide mineral dissolution and precipitation, and the types of interactions that occur at the solvent-mineral interface. While bulk data can be obtained for macroscopic heterogeneous systems using various spectroscopic techniques, this often misses the key chemistry involved as most reactions don't occur on an idealised homogeneous surface, but at kink sites and imperfections on the surface. In addition to frustrating geochemists for many decades, these same issues are increasingly facing those involved in the fields of materials science and heterogeneous catalysis, and it's becoming increasingly clear that they may hold the key to the biological evolution of metal enzymes such as the photo system II complex, which contains

a Mn_4O_4Ca unit.

One approach has been to work on the microscopic scale by looking at the reactivity of simple monomers or oligomers, which has allowed for the use of solution phase spectroscopic techniques that yield site specific information with a resolution unobtainable for macroscopic systems. However, generally specific sites or ligands don't react in isolation, and often such cooperative effects can be both surprising and crucial. The holy grail here is the mesoscopic scale, where the systems are large enough that they faithfully capture the behaviour of an extended solid, yet are small enough that the behaviour of each individual site – and their interplay – can be understood.

A path to this end is the use of nanometre-sized soluble metal oxide clusters such as polyoxometalates (POMs), which are approaching the size of the kink sites and imperfections on metal oxide surfaces. They are used for two purposes – to look at how the structural oxygens in the cluster exchange with the environment, most often the solvent, and as ligands to stabilise metal oxide fragments of other target systems, such as birnessite and heterogenite.

Briefly, POMs are polyanionic metal oxide clusters of the group V and VI elements in their highest oxidation states (see figure 1.1).[1] While V, Mo and W polyoxometalates have been studied extensively for many decades, Nb and Ta have only recently been receiving the same kind of attention. The reasons for this discrepancy have been entirely practical, as there previously was a lack of suitable starting materials coupled with an unfortunate choice in counter ions which yielded insoluble amorphous products and a lack of suitable means of analyses, but the outcome has been quite unfortunate. Not only do Nb and Ta POMs exhibit stability in the important weakly-acidic to alkaline region, but the lability of the

structural oxygens means that they react on a time scale uniquely suited to spectroscopic investigation in the laboratory, with the fastest oxygen sites exchanging completely in a matter of hours, and the slowest ones only completely exchanging after six to nine months.
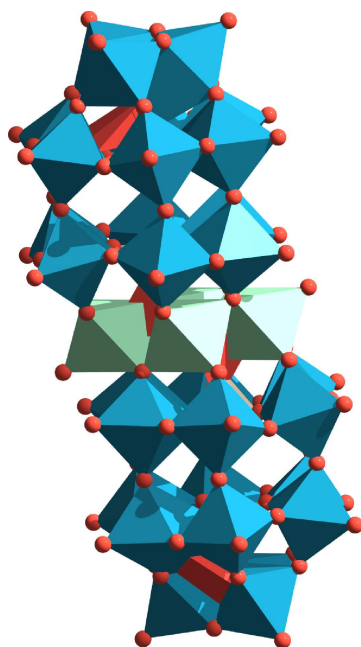

Figure 1.1: Structure of a Wells-Dawsons sandwich complex, $[Mn_4(H_2O)_2(P_2W_{15}O_{56})_2]^{16-}$. Mn(II) atoms, tungsten-centered polyhedra, phosphorous tetrahedra and oxygen atoms are shown in green, blue, orange, and red, respectively.[2]

Although the structural oxygen atoms in the classical W and Mo polyoxometalates generally react too slowly to be conveniently monitored, they can be used as ligands to stabilise fragments of minerals that are of interest, such as the sandwiched CoO sheet in $\alpha\beta\beta\alpha$-$[Co_4(H_2O)_2(P_2W_{15}O_{56})_2]^{16-}$ (see figure 1.1) which resembles heterogenite. In these cases it is generally the lability of bound ligands that are of interest and these are often relevant to catalytic reactions such as water

oxidation.[3]

1.1 Polyoxometalates

Polyoxometalates (POMs) are anionic metal-oxo clusters of group V and group VI transition metals of general formula, $[X_x M_m O_y]^{q-}$, where M is a transition metal and X is a heteroatom.[4, 1] There is a vast library of polyoxometalates with transition metals V^V, W^{VI} and Mo^{VI}, however Nb^V and Ta^V compounds are much less known. Compounds that have octahedra of one transition metal are isopolyanions while complexes which contain an extra element X are heteropolyanions. Polyoxometalates have tunable physical and chemical properties which render them extremely useful in various applications.[5, 6] One of the most important and well-studied application of POMs is catalysis, such as in water-oxidation.[7, 8] They are promising in catalysis of peroxide based oxidations or as oxidation catalysts.[9, 10] Also, they have been effective in catalysing reduction of nitrite when impregnated on carbon electrodes as multi-layer film.[11] Moreover, some latest advancements have shown their effect on biomedicine including anti-viral, anti-tumor, anti-bacterial and anti-HIV activities.[12]

Polyoxometalates are used as models to detail the behaviour of metal-oxides such as minerals. These are nanometer-sized complexes which are largely soluble in water display sufficiently complex acid-base chemistry useful for studying the reaction dynamics of extended metal oxides at solid-solvent interface such as a mineral surface.[13, 14]

1.2 NMR as a dynamic tool

Nuclear magnetic resonance is a powerful analytical chemistry tool used in research for many purposes like structural characterisation of compounds, determining the purity of a sample and reaction dynamics of complexes. Only those nuclei which possess spin can produce an NMR signal. The principle behind the technique is that a sample is placed in a magnetic field and is subjected to radiofrequency (RF) radiation at the appropriate frequency. The nuclei in the sample can absorb the energy, and the frequency at which the absorption occurs depends on the type and chemical enviornment of the nucleus. It is important that the magnetic field is homogeneous over the sample except for some diffusion experiments where the magnetic field is varied to achieve a gradient along the tube.

1.2.1 Nuclear spin resonance

Spin is a fundamental property of elemental isotopes which can be integral (I = 1, 2, 3...) or fractional (I = 1/2, 3/2, 5/2..). NMR is performed on nuclei with isotopes which have unpaired nuclear spins. Each spinning nucleus behaves like a magnet with a magnetic moment (μ) proportional to the spin. When an external field is applied, this nucleus will align itself with the external magnetic field. The low energy state is where the nuclear spin is aligned parallel to the external field, and that is the most favorable position while the opposite is the high energy state (antiparallel to the external magnetic field). The difference in the energy between these two states is very small, and depends on the strength of the magnetic field applied. NMR spectrometers have strong pwerful magnets with magnetic fields ranging from 1 to 20 Tesla (T). The earth's magnetic field is approximately 10^{-4}

T at ground level. A particle absorbs a radiation in the low energy state and transitions to the upper high energy state. The energy of this radiation must be equal to the difference in the energy between the two states. The energy is related to its frequency by:

$$\Delta E \;\; = h\nu \tag{1.1}$$

where h is the Planck's constant. The frequency ν depends on the gyromagnetic ratio of the nucleus (γ). The SI unit of γ is radian per sec per Tesla (rad·s^{-1}T^{-1}. The value of $\gamma/2\pi$ is generally quoted which has units HzT^{-1}. So

$$\nu \;\; = \gamma B \tag{1.2}$$

Therefore the energy of the electromagnetic radiation required to cause a transition between the two different states is

$$\Delta E \;\; = \;\; \frac{\gamma h B_0}{2\pi} \tag{1.3}$$

where B_0 is the external magnetic field and the SI unit is Tesla (T).

In the NMR experiment, the frequency of the radiation is in the radiofrequency (RF) range. The signal results from the difference in the energy absorbed by the spins to move from low energy state to high energy state and the energy emitted by the spins which simultaneously make a transition from high energy state to low energy state. This is called the resonance process. The frequency of the radiation which causes resonance is called Larmor frequency. After the RF pulse, the nucleus relaxes and returns to the original state which is collected as free induction decay

(FID).

1.2.2   Magnetisation

The nuclear spins are either aligned parallel (positive z-axis) or antiparallel (negative z-axis) to the direction of the magnetic field. At any instant time, the magnetic field due to all the spins can be represented as the magnetisation vector. The total magnetisation (M_0) is simply the sum of all nuclear spins experiencing the same magnetic field. At equilibrium, the external magnetic field and the net magnetisation are both along the z-axis (see figure 1.2). Since there will slightly more nuclei oriented along the positive z-axis, the magnetization will also be towards positive z-axis. When a nucleus is exposed to an energy of a frequency equal to the
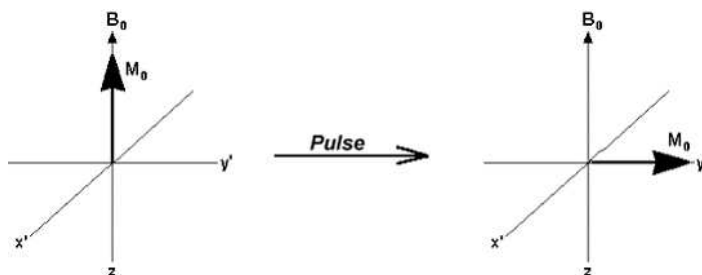

Figure 1.2: The bulk magnetisation (M_0 parallel to the external magnetic field (B_0 on the positive z-axis at equilibrium (left). On applying $\pi/2$ pulse, the magnetisation shifts on to the Y axis.[15]

difference between the energy of the two spin states, the net magnetisation shifts from the z-axis on to the xy plane. The time required by M_z to return back to its equilibrium position is the spin-lattice relaxation time (T_1). The components in the lattice can interact with the nuclei in high energy state and cause them to loose energy (returning to low energy state). It governs the recovery of the

longitudinal relaxation. The rotation of the net magentisation in the XY plane about the z-axis at the Larmor frequency is called precession.

In addition to rotation, each nuclear spin experience a slightly different magnetic field and start to rotate at its own Larmor frequency. T_2 is the time required to return to equilibrium the transverse magnetisation. Spin-spin interactions are interactions between neighbouring nuclei of same precessional frequency but different spin states. Both the processes occur simultaneously except that T_2 is always less than or equal to T_1.

In pulsed NMR spectroscopy, a radio frequency pulse is applied which rotates the net magnetisation onto the XY plane. Once the magnetisation vector is in the transverse plane, it rotates along the z-axis in the direction of the applied field. This rotation induces a current in the coil of wire which is located near the X axis. The current is plotted as a function of time which gives a sine wave. This wave decays with time constant T_2 due to dephasing of the spins. After a pulse, each nucleus relaxes slowly to the equilibrium magnetization along the z-axis. This is acquired as a free induction decay (FID). The application of RF pulse sufficient to rotate the magnetisation perpendicular to the z-axis is called a 90° or $\pi/2$ pulse (ref. 1.2). Applying a pulse twice as long will result in inversion of magnetisation towards negative z-axis and that is π or 180° pulse.

The line-width of an NMR signal at half height is inversely related to T_2.

According to Heisenberg uncertainity principle:

$$\Delta E \cdot \Delta t \;=\; \frac{h}{2\pi} \tag{1.4}$$

$$h \cdot \delta \nu \cdot \delta t \;=\; \frac{h}{2\pi} \tag{1.5}$$

$$\Delta \nu \;=\; \frac{1}{2\pi T_2} \tag{1.6}$$

$$\Delta \nu_{1/2} \;=\; \frac{1}{\pi T_2} \tag{1.7}$$

$\nu_{1/2}$ is the half-width at half height. Short T_2 means broader signals. This means that the nuclei which relax fast like ^{17}O and ^{51}V will have broad signals. T_2 is also called transverse relaxation time because it measures how fast the nuclear spins exchange energy in the transverse plane. T_1 is also called longitudinal relaxation time as it is a measure of how fast the magnetization returns back to the z-axis. Short T_1 means magnetisation recovers more rapidly and the spectrum can be acquired in less time.

The spin-lattice (T_1) relaxation time can be determined by using an inversion recovery delay experiment (180° - τ - 90°). A 180° pulse is applied first which inverts the magnetization. After time τ, 90° pulse is applied to be able to detect any magnetization. As τ gets longer, full T_1 relaxation occurs between the two pulses and a strong signal is detected with full positive intensity. If τ is too short, full recovery is not achieved and the detected signal has negative intensity.

1.2.3 Chemical Shift

Different elements have different gyromagnetic ratios, and therefore experience resonance at different frequencies in a particular magnetic field. However, same

type of nuclei are also subjected to resonate at different frequencies beacuse of the non-identical enviornment of each nucleus. Each nucleus experience magnetic field which is slightly different to the applied magnetic field, and this is because of the presence of electrons around the nucleus that shield them from the applied field. Consequently, the magnetic field perceived by the nucleus is slightly smaller than the applied field. The difference between the applied magnetic field and the magnetic field observed by the nucleus is nuclear shielding. A chemical shift can be given as frequency difference (hertz), however the chemical shift in Hz would depend on the magnetic field. So, the common way to express chemical shift is in terms of parts per million (ppm). A reference signal is chosen, and the difference between the position of the signal of interest and that of the reference is termed as chemical shift. Essentially, the frequency of the sample is subtracted from the frequency of the reference and divided by the spectrometer's frequency.

1.2.4   Overview of the instruemnt

Magnet: A magnet is made up of an alloy which is made into a wire wrapped into a coil and has current passing through it. It generates the magnetic field which allows the splitting of the energy levels. The liquid helium cools the wire reducing the resistance to nearly zero. The liquid helium dewar is insulated by a vaccum chamber. There is a liquid nitrogen reservoir which is insulated by another vaccum chamber. A bore hole extends through the center. The sample probe and shim coils are located in the bore hole (see figure 1.3).

 Probe: A probe is a part of the instrument which accepts the sample, sends the radiofrequency energy into the sample, and detects the current emerging from the
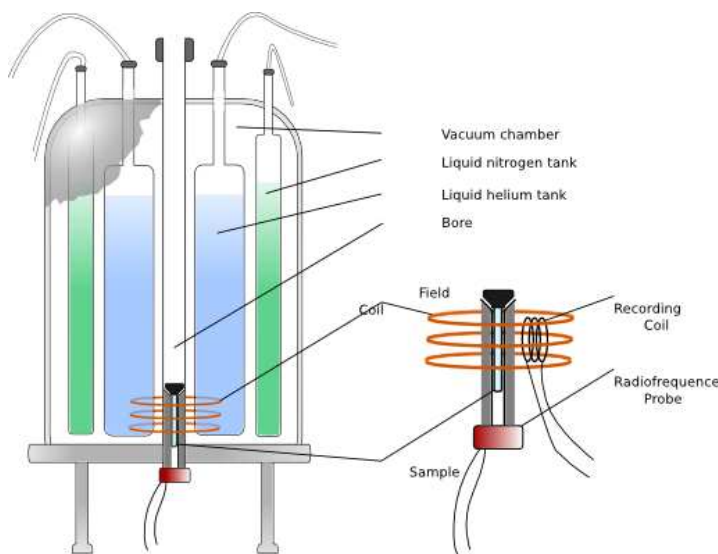
Figure 1.3: An overview of the NMR instrumentation.[16]

sample. The RF coil, sample spinner and gradient coils are contained within the sample probe.

RF coils: They create the B_1 field which is perpendicular to the B_0 field and rotate the net magnetisation in a pulse sequence.

Gradient coils: These coils produce the gradient in the magnetic field of the instrument (B_0) required to perform experiments like diffusion measurements (DOSY).

Shim coils: To acquire a good quality spectrum, the magnetic field should be homogeneous all over the sample. Shimming is the process of adjusting the inhomogeneity in the magnetic field with the help of shim coils. To shim the sample, we make changes to the shim values and observe the lock intensity until maximum intensity is reached. Samples with exactly same volume and same ionic strength will have the same shim values.

Lock: It is important to keep the magnetic field stable and homegeneous during the acquisition for good resolution of the spectrum. For this, the spectrometer

has a lock system which corrects the drift in the magnetic field by monitoring the absorption frequency of the solvent's deuterium resonance. It then makes minor changes in the magnetic field to keep the resonance frequency constant.

1.2.5 Acquisition parameters

Data acquisition requires some parameters to be set before acquiring the FID signal. These are important to improve signal-to-noise ratio (S/N ratio) and good resolution of the spectrum.

Spectrometer frequency: The RF pulse has a characteristic frequency which is called the spectrometer frequency (sfrq). It depends on the observed nucleus and the magnetic field of the spectrometer. The spectrometers are named for the frequency at which hydrogen atom resonates. A 400 MHz instrument means that hydrogen atoms will resonate at approximately 400 MHz.

Pulse width: A RF pulse is apllied which rotates the net magnetisation onto the yz plane. It is typically applied for few microseconds. For example, a pulse width of 11.25 μs leads to a $\pi/2$ pulse, then a pulse width of 22.5 μs will lead to a π pulse.

Recycle delay: It is time given to the system to relax back before the next pulse is applied. Without the delay, the nuclei will become saturated and there will be little or no signal. It is set as **d1** on Bruker and typically set as few seconds. The recycle delay should ideally be more than five times of T_1. For example, the fast relaxing nuclei such as ^{17}O and ^{51}V, the d1s range from 0.01 - 0.2 s.

Acquisition time: The time taken by the instrument to acquire a spectrum is the acquisition time (**at**). The nucleus is also relaxing during this time. So if the

acquisition time is long, the recycle delay can be reduced. The total time between each measurements is pw + at + d1.

Number of scans: The number of scans that we want to acquire is given to the instrument by the parameter **ns**. More scans will increase the S/N ratio.

Number of points: The **np** defines the number of points used to define the FID.

Spectral width: It is the total width of the spectrum. The spectral width (**sw**) is given in ppm to the instrument. The spectral width, acquisition time and the number of points are interrelated as:

$$at = \frac{np}{2sw} \tag{1.8}$$

$$res = \frac{1}{at} \tag{1.9}$$

where **res** is the resolution of the spectrum.

1.2.6   Processing parameters

Fourier transform: FID is time-domain data with intensity plotted as a function of time. Fourier transform converts the FID into frequency domain data. The frequency appears as a peak in the spectrum. The command for fourier transform is **ft** on Bruker.

Exponential multiplication: Prior to fourier transform, a window function is applied on FID which multiplies the FID by an exponential decay function emphasizing the data which mostly has the signal and not the data which contains noise. This improves the signal-to-noise considerably. This is applied by the command **em**. This exponential line broadening is set by a parameter called line broadening factor (**lb**). Larger LB means faster the decay of the exponential. However,

applying a very large line-broadening factor will decrease the resolution of the spectrum.

Phasing: After applying the window function and fourier transform, we see the peaks in the spectrum but they may be upside down or the shape may not be correct. So we apply phasing to the peaks so that all the peaks give the correct peak shape. **apk** is the command for automatic phase correction on Bruker. Once a FID is acquired, the command **efp** does all three (exponential multiplication, fourier transform and phasing).

Baseline correction: Baseline is the average of the noise in the spectrum and ideally, it should be a straight horizontal line. However, it drifts and sometimes there can be severe baseline distortions in the spectrum. The automatic baseline correction is done by the command **absd**.

1.2.7   Paramagnetic NMR as a tool

Nuclear magnetic resonance (NMR) is a powerful technique for *in situ* analysis of molecular dynamics. The Bloch equations (see equations 1.10-1.12) describe the time dependent evolution of the magnetic moments of susceptible nuclei in a magnetic field in a rotating frame within the framework of classical physics.[17] Here, u and v are the components of the transverse magnetisation, M_z corresponds to magnetization in the z-axis parallel with the static magnetic field ω_{rf}, T_1 and T_2 are the characteristic longitudinal and transverse relaxation times, respectively. ω_0 and ω_1 are the resonance frequency and the applied field, respectively.

$$\frac{d}{dt}u = -v(\omega_{rf} - \omega_0) - \frac{u}{T_2} \tag{1.10}$$

$$\frac{d}{dt}v = u(\omega_{rf} - \omega_0) - M_z \cdot \omega_1 - \frac{v}{T_2} \tag{1.11}$$

$$\frac{d}{dt}M_z = v \cdot \omega_1 - \frac{M_z - M_{z,\infty}}{T_1} \tag{1.12}$$

As shown by McConnell, the Bloch equations can be modified to account for chemical exchange,[18] an observation that was used by Swift and Connick to derive a model (See equation 1.13) for determining rates of exchange involving ligands bound to paramagnetic nuclei.[19] The exchange rates of coordinated solvent molecules with the bulk in paramagnetic complexes are estimated by following the resonance of ^{17}O nucleus of the free water molecule as a function of temperature.

$$\begin{aligned} \frac{1}{T_{2p}} &= \frac{\pi}{P_m}(\Delta\nu_{obs} - \Delta\nu_{solvent}) \\ &= \frac{P_m}{\tau_m}\left(\frac{T_{2m}^{-2} + (T_{2m}\tau_m)^{-1} + \Delta\omega_m^2}{(T_{2m}^{-1} + \tau_m^{-1})^2 + \Delta\omega_m^2}\right) \end{aligned} \tag{1.13}$$

In equation 1.13, $\frac{1}{T_{2p}}$ is the apparent T_2 which gets reduced in the presence of paramagnetic ion, and P_m is the molfraction of bound to free ligand. τ_m is the exchange time and k_m is the rate constant, where $\tau_m = \frac{1}{k_m}$. The $\Delta\nu_{obs} - \Delta\nu_{solvent}$ term is the experimentally observed difference in peak width of the uncoordinated exchanging ligand at half maximum in the presence and absence of the paramagnetic metal site. $\Delta\omega_m$ is the difference in resonance frequency of free and bound ligand.
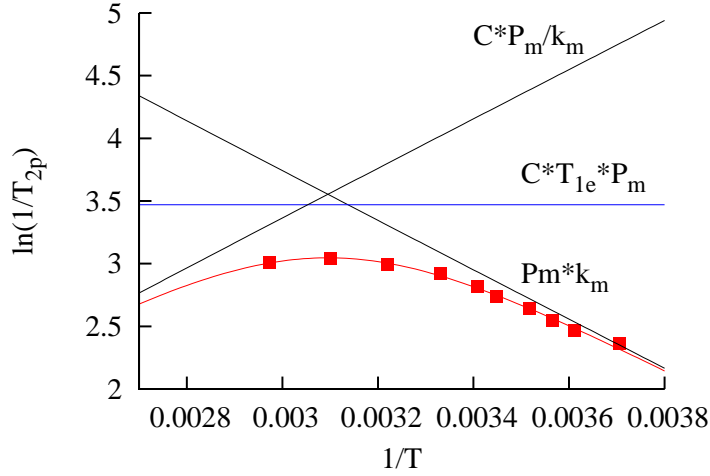
Figure 1.4: The reduced transverse relaxation, $1/T_{2p}$ as a function of inverse of temperature depicting three contributions $P_m k_m$, $P_m C/k_m$, $P_m C T_{1e}$.

At temperature and pH conditions for a particular paramagnetic ion, there is a region for which $T_{2m}^{-1} \gg \Delta\omega_M^2, \tau_m^{-1}$ such that Equation 1.13 reduces to: $\frac{1}{T_{2p}} = \frac{P_m}{\tau_m}$. This condition is also satisfied when signal of bound water to the paramagnetic ion is shifted from zero so that $\Delta\omega_M^2 \gg \frac{1}{T_{2,M}^2}, \frac{1}{\tau_m^2}$. Under these appropriate conditions, $\frac{1}{T_{2p}}$ is controlled by rate of chemical exchange.

However, it is common to fit the whole curve which is considered as sum of three lines as shown in fig. 1.4. In the case of Mn(II) complexes, the contribution from $\Delta\omega_m$ is negligible as they do not show any chemical shift. So, the equation 1.13 reduces to:

$$
\begin{aligned}
\frac{1}{T_{2p}} &= \frac{P_m}{\frac{1}{k_m} + T_{2M}} \\
&= \frac{P_m}{\frac{1}{k_m} + \frac{1}{C}\left(\frac{1}{T_{1e}} + k_m\right)}
\end{aligned}
\tag{1.14}
$$
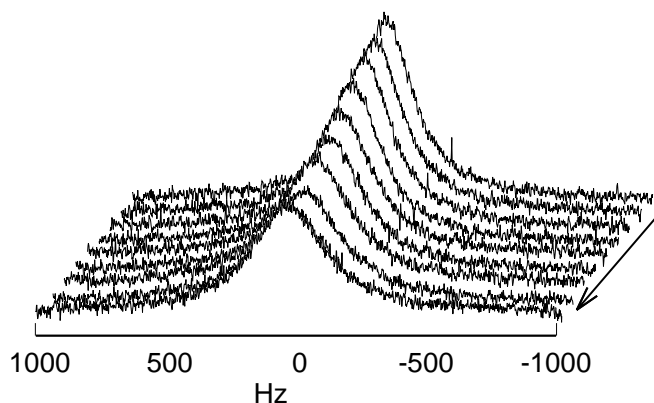
Figure 1.5: Increase in the ^{17}O NMR line-width of the bulk water signal with temperature when Mn(II)-POM is placed in a solution set at pH 3.2. The arrow shows the increase in temperature.

where, C is a temperature independent constant and depends on scalar coupling constant (A/h) and T_{1e} is electron relaxation time. For most compounds, the values of these parameters are unknown and their values are determined by fitting which adds to the source of error. For very long T_{1e}, the contribution from $P_m CT_{1e}$ becomes negligible, which adds complications in fitting this model. For $[Mn(H_2O)_6]^{2+}$ T_{1e} is known and reported as $1.25 \cdot 10^{-8}$ s by Ducommun et al.[20] However, for polyoxometalates T_{1e} is not known, and it is determined through fitting by varying T_{1e} and optimising $\Delta H^{\ddagger}$, $\Delta S^{\ddagger}$ and A/h.

1.2.8 DOSY NMR

Diffusion-ordered NMR spectroscopy is a useful method that provides the spectroscopic discrimination of different molecules in a complex mixture by measuring

the translational diffusion coefficients.[21] The measured diffusion coefficients are related to the particle size through Stokes-Einstein equation (see equation 1.15)

$$D = \frac{k_B}{6\pi\eta r} \tag{1.15}$$

where k_B is the Boltzmann's constant, T is the temperature, η is the viscosity of the solvent and r is the (hydrodynamic) radius of the molecule.

DOSY spectrum represents a two-dimensional matrix correlating the chemical shifts corresponding to different molecules in the solution on the horizontal axis to their diffusion coefficients on the vertical axis. The magnetic field is made to vary linearly over the sample tube. As the sample moves, the NMR signal is attenuated depending upon the diffusion time and the gradient length. The change in the NMR signal intensity as a function of gradient strength is described by

$$I = I_0 e^{-D\gamma^2 g^2 \delta^2 (\Delta - \delta/3)} \tag{1.16}$$

where I is the observed intensity, I_0 is the intensity at very small gradient value, D is the diffusion coefficient, γ is the gyromagnetic ratio of a nucleus (for example, ^{1}H - 267.513 $\cdot 10^6 \text{s}^{-1}\text{T}^{-1}$), g is the gradient strength, and Δ is the diffusion time.

For accurate diffusion measurement, it is very important that the temperature is stable all through the experiment and the sample is not spinning as this may lead to convection effects.

1.2.9 ^{17}O NMR spectroscopy

^{17}O NMR spectroscopy is an extremely powerful structural probe in oxygen-containing compounds including polyoxometalates. Oxygen is the most abundant and integral element in most of the complexes that it bonded to. The spectroscopic measurements using ^{17}O nucleus has not been exploited and used as other nuclei like ^{13}C, ^{1}H and ^{13}P owing to some of the limitations. The use of this technique was restricted by the low natural abundance coupled with quadrapolar relaxation of the ^{17}O nucleus.[22] However, advancement in NMR spectrometers and artificial enrichment of the compounds have proven to be instrumental in overcoming the limitations in the use of ^{17}O NMR spectroscopy.

The oxygen isotope (^{17}O) has a short delay time which leads to significant broadening of the signals and baseline distortions.[23] While the signals are broad, they are well separated as it has a very large shift range. This helps in assigning the signals as there is less overlap between the signals. Also, the measurements at higher temperature, using solvents with low viscosity and low concentrations of the sample can narrow down the line-widths significantly for better resolution.[24] Moreover, quadrupolar relaxation reduces the delay time considerably, and the signals are observed in much shorter time. Therefore, more scans can be acquired which enhances the signal intensity by increasing the signal-to-noise ratio. The limitation of broad signals can also be overcomed by fine tuning of the acquisition parameters.

The low natural abundance is compensated by artificially enriching the compounds using enriched water ($H_2^{17}O$). The tagging of the structural oxygens with the ^{17}O isotope can be done by two different ways. In the first approach, the

complex is synthesised in the presence of enriched water which is pre-enriching the complex. In another way, a complex can be enriched after synthesising it in normal water ($(H_2^{16}O)$). This is done by heating the complex in the presence of enriched water for a suitable period of time (post-enrichment).[25] The latter involves the exchange of structural ^{16}O oxygens with the bulk ^{17}O isotope. In some cases, the exchange can be very slow, and so the enrichment may not be complete. This is particularly relevant for oxygens bound to elements such as tungsten which are extremely slow in exchange. For such complexes, quantitative measurements may not be entirely possible, yet it may be used for qualitative purposes where the signals can be related to the different oxygen types present in the complex.

Interestingly, oxygens can be terminal (η=O) or bridging (μ_x-O where x can be 1-6). Each distinct oxygen resonates at a frequency different to the other. The terminal oxygens are most shifted downfield followed by the oxygen bound to two metals and so on. ^{17}O NMR spectroscopy has been widely used to monitor exchange rates between compounds and water including small complexes like ketones, metal-oxides belonging to first-group elements and polyoxometalates.[26, 27] The rates are measured by dissolving the enriched compound in unenriched water and following the decrease in signal intensity by NMR. In another way, the unenriched compound can be put in enriched water and the increase in signal intensity is monitored. The technique is also useful to study the labilities of bound ligands, most often water, in bulky sandwiched polyoxometalates such as Co^{II}-substituted $[Co_4(H_2O)_2(P_2W_{15}O_{56})_2]^{16-}$.[7]

In my research, I have used ^{17}O NMR spectroscopy for two purposes. In one approach, I have looked at the labilities of bound ligands in a polyoxotungstate with respect to the solvent, where both the ligand and the solvent is water (Chapter 2).

In another, I have looked at how the framework oxygens in polyoxoniobates interact with the solvent (Chapter 3). The key, in both the projects, has been to study the pH-dependent behaviour of these complexes using ^{17}O NMR spectroscopy.

1.3 Computational theory

The motivation behind the use of computational approach in chemistry is to estimate the experimental observations as close as possible. The rapid progress in computational resources have made the theoretical estimations possible at low cost and high accuracy. DFT has revolutionised the field of quantum chemistry by being user-friendly and sufficiently accurate.[28, 29] A DFT model is a theoretical method consisting of an exchange-correlation functional alongwith a basis set. Each unique pairing of a functional with a basis set represents a different approximation to the Schrödinger equation. For choosing a model, the two most important parameters to be considered are accuracy and cost.

1.3.1 Schrödinger equation

The Schrödinger equation was originally formulated by an Austrian physicist Erwin Schrödinger.[30] For a molecular system of N-electrons and M nuclei, the Schrödinger equation is

$$\hat{H}\Psi \;\; = \;\; E\Psi \tag{1.17}$$

where the Hamiltonian operator H is

$$\hat{H}\Psi \;=\; \hat{v}_{ext} + \hat{T} + \hat{V}_{ee} \tag{1.18}$$

and the wave function Ψ is

$$\Psi \;=\; \Psi(\vec{r_1}, \vec{r_2}, \vec{r_3}, ... \vec{r_N}) \tag{1.19}$$

The kinetic energy is given by,

$$\hat{T} \;=\; \frac{-1}{2} \sum_{i=1}^{N} \nabla_i^2 \tag{1.20}$$

the electron-electron repulsion operator which is Coloumb-interaction given by,

$$\hat{V}_{ee} \;=\; \sum \sum_{i<j} \frac{1}{r_{ij}} \tag{1.21}$$

the external potential due to the M nuclei by,

$$\hat{v}_{ext} \;=\; -\sum_{i=1}^{N} \sum_{A=1}^{M} \frac{Z_A}{|\vec{R_A} - \vec{r_i}|} \tag{1.22}$$

The indices i, j and A refer, respectively, to the electrons and the nucleus with charge Z_A. The solution to the Schrödinger equation is possible only for small systems while several simplifications are applied for solving the equation for large molecules. For example, a helium atom has two electrons with one being towards the nucleus and other farther away. Electrons do not exist in isolation but they are continuously interacting such that movement of one depends on the other.

Due to this interaction of repulsion between the electrons, the wave function gets distorted. Therefore, we need to construct a wavefunction in order to solve the Schrödinger equation using mathematical principles to make its calculation possible. Customising the parameters is necessary to approximate the wavefunction. The idea is to choose a wavefunction for which $\hat{H}$ is minimum. More parameters allow greater flexibility and give better approximation to the wavefunction.

One such simplification to the Schrödinger equation is the variational principle which gives the energy that is above the ground state.

Hartree developed a method that assumes that when the electrons move they create an overall effect of an average potential ($v_{eff.}$). This method does not consider each electron individually but an average effect of all the electrons in the system.[31, 32] Wavefunction based *ab initio* is a practical tool and widely used in predicting molecular structures for many systems.

Hohenberg and Kohn laid the foundation for Density Functional Theory which is another method to study many-electron systems. They proved in their first theorem that there is a unique ground state density for each external potential. Electron density can be used to identify the system.[33] This implies that the energy E is a functional of the electronic density of the ground state (i.e. for a given external potential v):

$$E = E_v[\rho] \tag{1.23}$$

Hohenberg and Kohn derived at the same time another theorem that states that the ground state energy is the lowest and for any other density, the energy will be

higher than the ground state energy.

$$E \leq E_v[\rho^t] \tag{1.24}$$

Density Functional Theory (DFT) owe its origin from Hohenberg-Kohn theorem which established the existence of a unique functional which describes the ground state and electron density exactly. Kohn and Sham followed the work and partitioned the electronic energy into several components.[34]

$$E = E^T + E^V + E^J + E^{XC} \tag{1.25}$$

where E^T is the kinetic energy, E^V is the external potential energy due to a classical external potential ν_{ext}, E^J is Coloumb-interaction energy and E^{XC} is the energy due to the self interaction of electrons.

$$E_{XC}[\rho] = E_x[\rho] + E_c[\rho] \tag{1.26}$$

where E_X is the exchange energy arising from the antisymmetry of the quantum mechanical wavefunction and E_C is the correlation energy originating from the correlation in the motion of the individual electrons. The functionals defining the exchange and the correlation components of the system are termed as exchange and correlation functionals, respectively.

There are different ways by which the electron density can be approximated in Density functional theory. One of the ways is an assumption that electron density is localised at one point and not uniformly distributed throughout the molecule.

The energy approximation by this method is called Local Density Approximation (LDA). An improvised version of LDA is Local Spin Density Approximation (LSD) where spin is considered. This method uses different orbitals for electrons with different spins. The local approximation is not able to reproduce the experimental data ss molecules do not resemble a uniform electron gas distribution.

Gradients of the density were introduced into the exchange and correlation functionals to account for the non-uniformity of the electron density. These methods are called Generalised Gradient Approximation (GGA). Some commonly used exchange functionals are Perdew-Wang functional (PW91) or Becke-88.[35, 36] Another way of improving the calculations is to combine the GGA functionals with *ab initio* results. This can be done by introducing a certain fraction of Hartree-Fock exchange in the exchange part of the functional. These are called hybrid functionals and are known to give better results. Commonly used exchange-correlation functionals are listed in table 1.1 and 1.2.

Table 1.1: Commonly used pure-DFT exchange-correlation functionals are listed below:

XC functional	Description	Authors	Year	Reference
B88	exchange	Becke	1988	[36]
PW91	exchange	Perdew, Wang	1991	[35, 37, 38]
PBE	exchange/correlation	Perdew, Burke, Ernzerhof	1996	[39, 40]
O	exchange	Handy	2001	[41, 42]
LYP	correlation	Lee, Yang, Parr	1988	[43, 44]
P86	correlation	Perdew	1986	[45]
MO6L	exchange/correlation	Truhlar and Zhao	2006	[46]

Apart from the use of large basis sets and hybrid functionals, relativistic effects become essential for the understanding of the physical and chemical properties of

Table 1.2: Commonly used hybrid and long-range XC functionals are listed below:

XC Functional	Description	Reference
B3PW91	hybrid with 20 % in PW91	[47]
PBE0	hybrid with 25 % HF exchange in PBE	[48]
B3LYP	hybrid with 20 % in LYP	[47]
MO6	hybrid	[49]
LC-ωPBE	long-range version of wPBE	[50, 51, 52]
CAM-B3LYP	long-range corrected version of B3LYP	[53]
wB97XD	long-range with dispersion	[54]

molecules when heavy metals are involved.[55] To obtain reliable computational results, time consuming relativistic effects are considered in ADF package by the means of zeroth-order regular approximation (ZORA).[56] Another important consideration to be taken while computing NMR chemical shifts is the presence of a solvation model. In most cases, NMR spectrum is collected in solution-state and chemical shifts are sensitive to the solvent used. Therfore, it is important that theoretical studies also take into account the solvation effects. Continuum solvation models like PCM or COSMO are efficient in incorporation of solvation effects in chemical calculations.[57, 58, 59] In these models, a solute is exposed to a continuous polarizable medium which resembles a sea of surrounding solvent molecules.

1.3.2   Basis sets

A basis set is a mathematical representation of a molecular orbital within a system which is important for theoretical calculations. Larger basis sets are more likely to approximate the orbitals by imposing less restrictions on the location of the electrons in space. Basis set assign a group of basis functions to each atom to approximate its orbitals. Minimal basis sets have minimum number of basis functions that are needed for each atom such as STO-3G (Slater-type orbitals).

To further increase the size of a basis set, more basis functions can be added per atom. Split valence basis sets have two (double zeta valence basis set) or three (triple zeta valence basis set) or more sets of basis function for each atom. Split valence basis sets allow the change in the size of the orbital but not their shape. This can be achieved by adding polarizing functions. A polarized basis set adds d-functions to the first and second row atoms and f functions to the transition metals. Thom Dunning pointed out the need for the correlation consistent basis sets.[60] cc-pVXZ means a Dunning correlation-consistent, polarized valence, X-zeta basis; X = D, T, Q, 5, 6, 7. Diffuse functions allow the orbitals to occupy a large region of space, and are particularly important for systems where electrons are held far from nucleus.[61] ECP basis sets (electron core potential) are basis sets which consider only the electrons in the valence shell such as lanl2dz.

1.4 Potentiometric Titrations

To determine the pH range in which the compound is stable, the amount of excess charge (z_e) per mole of analyte is plotted as a function of pH. The excess charge (z) is an uncompensated charge which is not accounted for by protons, hydroxides or counterions in the system. For each volume of acid and base added, we measure the concentration of free protons (by pH probe) and calculated the uncompensated charge, which is the difference between the concentration of the protons already present in the system and the concentration determined by pH probe. The target to this extra charge seems to be the analyte.

$$z = \frac{-([H^+] + [Na^+] - [ClO_4^-] - [OH^-])}{[POM_{Tot}]} \tag{1.27}$$

1.5   Overview of literature

1.5.1   Exchange of aquo ligands in polyoxotungstates

The water-exchange rate constants and thermodynamic parameters for first row transition metal ions have been experimentally investigated and discussed in detail by Swift *et al.* and later by Merbach *et al.*[19, 20] Merbach *et al.* used activation volume as a parameter to determine and classify reaction mechanisms using high pressure NMR spectroscopy.[20] The interchange reaction mechanism can be divided into associative (I_a) and dissociative (I_d) depending on whether bond making is more favorable or bond breaking. The decrease in ionic radii from Mn^{2+} to Ni^{2+} makes the entry of water molecule more and more difficult leading to gradual change in preference from associative in Mn^{2+} to dissociative in Co^{2+} and Ni^{2+}. The computational studies at *ab initio* level support experimental results and assign I_a mechanism to Mn^{2+} , whereas Co^{2+} and Ni^{2+} proceed via an I_d mechanism.[62, 63]

Swift *et al.* reported a rate of water-exchange in $[Mn(OH_2)_6]^{2+}$ at pH 1 as $3.1 \cdot 10^{7}$ s^{-1} ($\Delta H^{\ddagger}$ 33.9 kJ·mol^{-1} and $\Delta S^{\ddagger}$ 12.1 J·mol^{-1}·K^{-1}).[19] Merbach *et al.* reported rate, activation enthalpy and activation entropy as $2.1 \cdot 10^{7}$ s^{-1}, 33 kJ·mol^{-1} and 5.7 J·mol^{-1}·K^{-1}. While, Hunt *et al.* reported a rate of $2.3 \cdot 10^{7}$ s^{-1} at 298 K ($\Delta H^{\ddagger}$ 37 kJ·mol^{-1} and $\Delta S^{\ddagger}$ 21 J·mol^{-1}·K^{-1})[64], a recent study by Esteban-Gómez *et al.* determined a rate of $2.1 \cdot 10^{7}$ s^{-1} and activation enthalpy of 45.6 kJ·mol^{-1}.[65]

Hunt *et al.* investigated the effect of ligand substitution on lability of coordinated water molecules in manganese(II) complexes. Substitution of phenanthroline on manganese(II) slightly increased the rates of water-exchange , while NTA (nitriloacetate) and EDTA (ethylenediaminetetraacetic acid) ligands significantly

labilizes the coordinated aqua ligands with NTA ligand being most effective.[64, 66] van Eldik *et al.* reinvestigated seven-coordinated complex $[Mn(II)(edta)(H_2O)]^{2-}$ by variable temperature and variable pressure NMR and observed the same effect that Hunt reported. The interchange exchange mechanism in Mn(II)-EDTA points towards more dissociative mode based on positive and high activation entropy. The changeover in mechanism is also supported by pressure-dependent measurements with more positive activation volumes. This behaviour could be explained by the steric hindrance at the metal center caused by the chelating ligand which leaves little space for entering water molecule.[67]

Water exchange studies on two dinuclear seven coordinate manganese(II) complexes containing two pentaazamacrocyclic imine or amine-based subunits also show dissociative mode of interchange mechanism.[68] Unlike monomeric systems which have geminal aqua ligands, these complexes have two waters bound to different manganese(II) atoms. The data shows that the rates of water exchange, activation enthalpies and entropies are in the same range as compared to the corresponding monomeric mononuclear managanese(II) complexes. This shows that the two manganese centers do not communicate with each other and behave independent of each other.

Likewise, in more complex structures like functionalised polyoxometalates, the water ligands are well separated from each other and are bound to different manganese(II) nuclei. The solution chemistry of polyoxometalates is of importance in processes like redox catalysis. One of the main uses of these catalysts has been as oxidation catalysts.[69] For example, $[Fe_4(III)(H_2O)_2(PW_9O_{34})]^{10-}$ has been shown to catalyse oxidation of alkenes and geraniol with H_2O_2 as an oxidising agent.[9, 70] There's an inherent advantage to using fully inorganic catalysts such as these for

oxidation catalysis, as they don't contain any organic ligands that can be oxidised and cause degradation. On the other hand, the size and complexity of these clusters means that it's not always easy to fully characterise the active catalyst. The solvent-ligand exchange at the exposed metal center is a crucial part of any catalytic cycle.

In 1973, Weakley and co-workers[71] reported the first Keggin-derived divalent sandwich complexes of the formula $[M_4^{II}(H_2O)_2(PW_9O_{34})]^{10-}$ (M=Co(II), Cu(II), Zn(II), Mn(II)), and in 1983, Finke and Droege reported the first sandwich complexes of the Wells-Dawson type, $[M_4^{II}(H_2O)_2(P_2W_{15}O_{56})_2]^{16-}$ (M=Co(II), Cu(II), Zn(II)).[72] In these compounds, a sheet of four transition metal atoms are sandwiched between two large polyoxotungstate ligands. Only two of the sandwich metal atoms are exposed to the solvent, and bind one water ligand each.

Polyoxometalate sandwich compounds have been shown to function as oxidation catalysts.[69] For example, $[Fe_4^{III}(H_2O)_2(PW_9O_{34})]^{10-}$ has been shown to catalyse oxidation of alkenes and geraniol with H_2O_2 as an oxidising agent.[9, 70] Recently, the sandwich complex $[Co_4(H_2O)_2(PW_9O_{34})_2]^{10-}$ has been reported to be an active water oxidation catalyst at pH 8 in the presence of a large excess of $Ru(bpy)_3^{3+}$ and with the application of light.[3, 73]

The rates of exchange of the aqua ligands in $[Co_4(H_2O)_2(PW_9O_{34})_2]^{10-}$ at pH 5.4 is $k_{ex} = 1.5 \pm 0.3 \times 10^6 s^{-1}$ which is comparable to $Co(H_2O)_6^{2+}$ as well as the catalytically inactive $[Co_4(H_2O)_2(P_2W_{15}O_{56})_2]^{16-}$.[7] Given that the last complex has the largest stability range, this indicates that $[Co_4(H_2O)_2(PW_9O_{34})_2]^{10-}$ may not be a truly homogeneous catalyst. Indeed, Finke *et al.* have convincingly shown that at least under electrochemical conditions the active catalyst is colloidal cobalt.[74] A complicating factor in terms of providing a definitive an-

swer to whether the cobalt polyoxometalate complex is merely a source of colloidal cobalt or a catalyst in its own right is that the original reports by Hill *et al.* utilises a ratio of 1:1000 of $[Co_4(H_2O)_2(PW_9O_{34})_2]^{10-}$:$Ru(bpy)_3^{3+}$.

The coordinated water ligand in $[Co(II)(H_2O)(SiW_{11}O_{39}]^{6-}$ is more exposed to the bulk water than the sandwich complexes, with no hindering ligands surrounding the water binding sites. However, water-exchange measurements show that the rate of water exchange is one order of magnitude slower than $[Co(H_2O)_6]^{2+}$ and $[Co_4(H_2O)_2(PW_9O_{34})_2]^{10-}$. This is due to the short $Co-OH_2$ bond caused by elongation of Co-O bond trans to the water ligand which shifts the preference to more associative rather than dissociative. The structural differences in the ligands surrounding the water binding sites largely affects the labilities of the coordinated water molecules and also govern the interchange reaction mechanism.

This discovery of what appears to be an active fully inorganic water oxidation catalysts has attracted a lot of interest. However, the solution chemistry, in particular as a function of pH, is poorly understood except for for a handful of polyoxometalates, and the effect of polyoxometalate ligands on the fundamental reactivity of coordinated metal centres has not been investigated with few exceptions.[7, 8] There is thus a great need for basic data, in particular for polyoxometalate derivatives that contain metal sites that are environmentally acceptable for green catalysis, such as iron and manganese.

1.5.2 Exchange of structural oxygens with water in poly-oxoniobates

The solution chemistry of homoleptic isopolyoxoniobates is dominated by three species: the hexaniobate Lindqvist ion, $[Nb_6O_{19}]^{8-}$, which is stable above pH 9,[75] the decaniobate ion, $[Nb_{10}O_{28}]^{6-}$, which is stable between pH 6 and 8,[76] and the eicosaniobate ion, $[Nb_{20}O_{54}]^{8-}$, which has so far only been obtained in non-polar organic solvent.[77] In addition to these species, $[Nb_7O_{22}]^{9-}$ and $[Nb_{24}O_{72}]^{24-}$ have been observed when hydrolysing decaniobate in mildly alkaline solutions.[78, 79] $[Nb_{27}O_{76}]^{17-}$ and $[Nb_{32}O_{96}]^{32-}$ are also known, but it is not clear how they fit into the solution chemistry of niobates.[80]

Until recently, few heteropolyoxoniobates were known, and consisted mainly of hexaniobate derivatives of the form $[W_xNb_{6-x}O_{19}]^{(8-x)-}$ and of the Ti, Ge and Si species $[Ti_2Nb_8O_{28}]^{8-}$, $[GeNb_{12}O_{40}]^{16-}$, $[SiNb_{12}O_{40}]^{16-}$ and $[H_2Si_4Nb_{16}O_{56}]^{14-}$.[81] In the past five years, however, the number of heteropolyoxoniobates has increased many-fold to include $[TiNb_9O_{28}]^{7-}$, $[Ti_{12}Nb_6O_{44}]^{10-}$, $[FeNb_9O_{28}]^{8-}$, $[NiNb_9O_{28}]^{8-}$, $[Cr_2(OH)_4Nb_{10}O_{32}]^{8-}$, $[H_2MnNb_{10}O_{32}]^{8-}$, $[V_3Nb_{12}O_{42}]^{9-}$ and $[PV_2Nb_{12}O_{42}]^{9-}$.[82, 83, 84, 85, 86, 87]

Key to this has been the realisation that there's a hydrous form of niobium pentoxide that reacts under much milder conditions than the commercially available form of niobium pentoxide which needs to be activated using either concentrated hydrofluoric acid or molten potassium hydroxide. Using hydrothermal conditions – while still not mild by most standards – the pH can be manipulated with some precision, and stoichiometric amounts of reagents can be introduced. An additional discovery was the detrimental effect of having alkali metal cations present. Once

tetraalkyl ammonium cations were introduced instead, in the form of hydroxides, a much wider range of discrete heteropolyoxoniobate clusters could be accessed.

In the last century, rate of reactions at mineral surfaces were predicted by elucidating the mechanism of dissolution of $AlO_4Al_{12}(OH)_{24}(H_2O)_{12}{}^{7+}(aq)(Al_{13})$ (an aluminium polyoxocation) which was structurally similiar to aluminium oxide minerals [88]. Substitution at a single site by Ga(III) for Al(III) has surprisingly large effects on the rates of oxygen exchange while there is slight alteration in the structure[26].

Several of the iso- and heteropolyoxoniobates have been studied in terms of oxygen exchange. In all studies ^{17}O NMR was used to determine the rates. Briefly, the polyoxoniobate was synthesised using 40% $H_2{}^{17}O$ and then dissolved in isotopically normal water. By following the disappearance of the different NMR signals and comparing it with an intensity standard supplied in an insert, site specific reactivity information could be obtained.

Black *et al.* studied the reactivity of the hexaniobate Lindqvist ion as a function of pH.[13] The 19 oxygens in this molecule can be divided into three types: six terminal (η) oxygen atoms, 12 oxygen atoms forming bridges between two metal atoms (μ_2) and and one oxygen atom bridging between six metal atoms (μ_6). Counter-intuitively, for the mono-protonated species which dominates between pH 10 and 13.5, the μ_2 oxygen site exchanged faster than the terminal oxygen site. At either extreme in the pH range (below pH 11 and above pH 14, respectively) the rates of the η and μ_2 oxygens coalesced, which lead to the proposal of a 'pin-wheel' mechanism which involves all bridging oxygen atoms undergoing concerted partial dissociation so that they transform into η oxygens. Under no condition was the μ_6 oxygen found to exchange, showing that the molecule remained intact in solution.
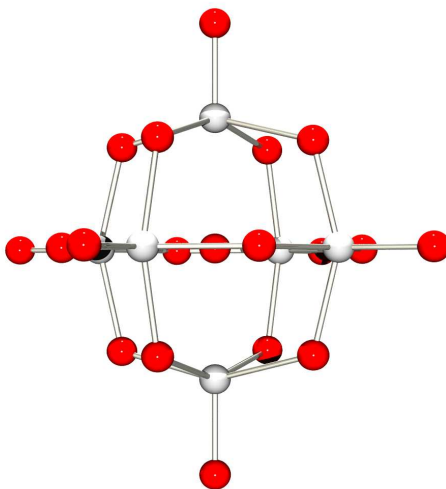
Figure 1.6: Structure of a hexaniobate ion, $[Nb_6O_{19}]^{8-}$.

Villa *et al.* later revised the findings of Black *et al.*, showing that borate and carbonate act as catalysts in the oxygen exchange process.[89] The observable effect was that the rates of exchange became very similar for both the η and μ_2 oxygens in the presence of borate and carbonate close to their respective pK_a, but not when biological buffers were used.

Villa *et al.* also studied the oxygen exchange in $[Nb_{10}O_{28}]^{8-}$ (decaniobate ion)(see figure 1.7), which can be considered as containing two condensed lacunary $[Nb_6O_{19}]^{8-}$ units.[90, 91] This molecule has 28 oxygens, eight of which are η, 12 of which are one of three types of μ_2, four of which are μ_3 and two of which are μ_6 type oxygens.

The decaniobate ion is stable at neutral pH and converts to other compounds outside a very narrow pH regime. The oxygen atoms in the decaniobate ion were found to undergo both base and acid promoted exchange, with the slowest exchange

happening in the middle of the stability region. Particularly, the three μ_2-O sites differ in the rates of isotopic exchange by a factor of 10^4. Importantly, at elevated pH (> 8.5) the rates of exchange increases until the pH is sufficiently high that the molecule dissociates into hexaniobate. However, as the processes of dissociation and exchange can be separated using NMR, it was found that prior to dissociation the presence of hydroxide ion labilises the entire molecule. The rates of exchange also increase at pH < 6.5. Here there's no evidence for any transformation of the decaniobate molecule, and the lower pH limit for the study was set by precipitation of the protonated ion.
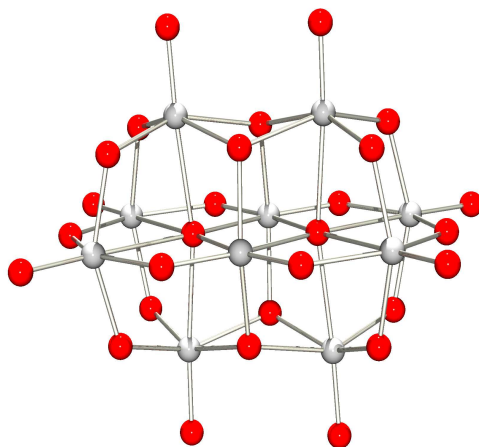
Figure 1.7: Structure of a decaniobate ion, $[Nb_{10}O_{28}]^{6-}$.

The reactivity of the decaniobate ion was compared with that of the mono- and di-substituted derivatives $[TiNb_9O_{28}]^{7-}$ and $[Ti_2Nb_8O_{28}]^{8-}$(see figure 1.8 and 1.9), respectively.[14, 92] In contrast with the behaviour of the decaniobate ion, isotopic oxygen exchange in the dititanoniobate,$[Ti_2Nb_8O_{28}]^{8-}$, ion is promoted

only by decreasing pH, and decreases steadily with increasing pH. In addition, the dititanoniobate ion does not dissociate even at pH as high as 13, but undergoes slow transformation into an unidentified species at low pH ($<$7.5). This would suggest that labilisation of the oxygen sites proceeds via protonation, unless there are base-promoted dissocation pathways present. The locii of protonation could not be unambiguously identified – while decreasing the pH affected the rates of exchange of the terminal Nb=O sites most, the shifts of the NMR signals from the two μ_2-oxygen sites in the equatorial plane were affected most. Empirically, the latter would be the expected protonation sites, as crystallography has shown μ_2 oxygens to be the favoured protonation locii in both the hexaniobate and the decavanadate ions,[76, 93] and one of the μ_2 oxygen sites holds the fastest exchanging atoms in the structure.

The successful synthesis of the monotitanoniobate ion, $[TiNb_9O_{28}]^{7-}$, in which only one of the central niobium atoms have been replaced by a titanium atom, allowed for probing the effect of substitution in a more subtle way. If effects of substitution are strictly local, then each side of the molecule should react as the decaniobate and dititanoniobate ions, respectively, whereas if effects are global the behaviour would be difficult to predict, but complex. The latter was observed. In the case of the monotitanoniobate ion degradation of the molecule, as detected by disappearance of the NMR signal from the inert μ_6 site, was seen at both low ($<$6) and high ($>$12) pH. This was accompanied by a general increase in oxygen exchange rates at pHs close to these dissociation zones, but in the intermediate region a more simple proton-assisted pathway dominated. More importantly, the substitution affected the relative rates of exchange of some of the oxygen sites on the opposite side to the substitution relative to relative rates of the corresponding

sites in the pure decaniobate and dititanoniobate ions, showing that substitutions do have global effects.
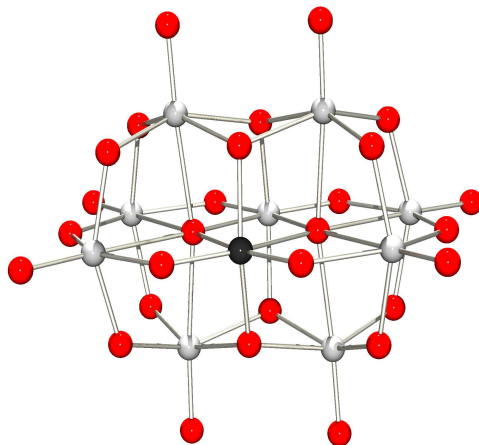
Figure 1.8: Structure of a monotitanodecaniobate ion, $[\text{TiNb}_9\text{O}_{28}]^{7-}$.

In large, complex ions such as polyoxometalates simple transition state theory invoking one-dimensional potential energy diagrams involving a single transition state are of little use. Instead, reaction pathways need to be found on a complex multidimensional surface, but such searches are at best costly, and often not meaningful. An alternative approach is to design calculations to probe key properties that are likely to affect key steps in the reaction. One such effort involved using density functional theory to probe the formation of metastable intermediates through the addition of hydroxide and hydronium (H_3O^+) ions to different metal sites in the decaniobate, monotitanoniobate and dititanoniobate ions.[94] The hydroxide affinities were negative (i.e. favoured) for all sites in the decaniobate ion, negative for some sites in the monotitanoniobate ion and positive for others, and
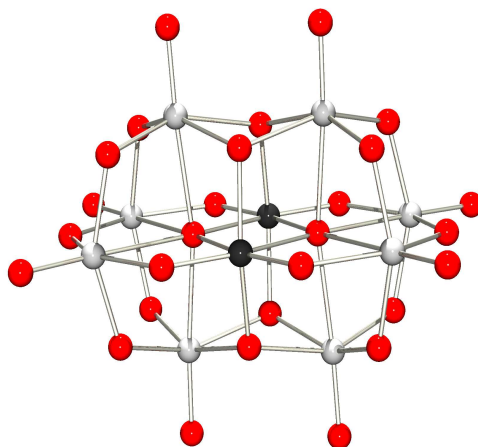
Figure 1.9: Structure of a dititanodecaniobate ion, $[Ti_2Nb_{10}O_{28}]^{8-}$.

positive for all sites in the dititanoniobate ion, supporting the observed pH depen-
dent behaviour of the rates of exchange, in which the rates decrease with increasing
pH for dititanoniobate and increase for decaniobate. The metastable intermediates
that formed computationally also pointed to a few specific sites of attack, includ-
ing the μ_2-oxygen atom on the short edge in the equatorial plane, which is a site
that is experimentally observed to be the fastest exchanging oxygen under most
conditions, and the shift of the NMR signal has been found to be quite sensitive
to the pH. Proton affinities were negative for all sites in all molecules. In addition
to showing that electrostatic forces play a large role in determining reactivity, the
calculations also supported the experimental observations with respect to specific
sites that may be involved in dissociation processes.

Johnson *et al.* studied the oxygen exchange in the silicotitanoniobate ion,
$[H_2Si_4Nb_{16}O_{56}]^{16-}$.[95] This large molecule has 19 nonequivalent oxygens and does

not resemble decametalate ion discussed above. There was a large variation in the ^{17}O NMR peak positions with changes in pH conditions. The μ_2-oxo and η-oxo sites experience larger shifts in peak positions than silicon-oxo region. Particularly, at pH 9, one of the μ_2-O site experience very large chemical shift moving upfield from δ=460 ppm to δ=389 ppm for reasons not known. A change in coordination number is expected from such a substantial chemical shift. The changes in positioning of peaks with pH is indicative of protonation of the molecule at certain sites. Thus the bridging oxygen sites could be considered as site of protonation which could affect the peak position of terminal oxygens as they lie close to them. The ^{17}O NMR signals of inert sites remain unchanged in pH range 8-13, indicating that molecule does not dissociate during isotope exchange. Considering the rates of oxygen-isotope exchange, all oxygen sites show similiar pH dependencies at a given pH in the region of 6 to 13. As pH decreases, protonation at the bridging oxygens enhances the isotopic exchange event for all the oxygen sites with terminal oxygens being most rapid.

The examples above demonstrate the difficulty in predicting the behaviour of complex metal oxides even when the system is well constrained, the structures are known with great confidence, and the rates of reactions are in a range where they can be conveniently observed under laboratory conditions. While it is not unexpected that μ_x type oxygen atoms should exhibit significantly different exchange rates as a function of x, one would not have expected a difference in rates of two orders of magnitude when all the oxygen sites are of the μ_2 type. We are also only slowly approaching a situation where we can start to device models to generate predictions. In order to confirm and improve these models, more data is needed.

1.5.3   DFT to predict NMR chemical shifts in polyoxometalates

In the past 25 years, modern computers with powerful hardware and advanced software have revolutionised the field of computational chemistry. The theoretical calculations are now possible even for large systems with minimal effort and cost, whereas few years back the chemists were only restricted to small systems. Density functional theory has provided an important contribution to the tremendous growth in the molecular orbital calculations, particularly for polyoxometalates. It is a simple and practical tool that is immensely helpful to the computational chemists beacause of its low computational cost and high efficiency. The methodology is rooted on Hohenberg-Kohn theorem, and is based on electron density approach to obtain the energy eigenvalue of the Schrödinger equation.

DFT methodology has shown impressive results for the prediction of molecular structures and NMR properties at low cost. Since, Kohn and Sham do not provide an exact exchange-correlation functional, the search for a functional that shows best results is mandatory. The hybrid functionals are more computationally time consuming than pure-DFT functionals but they give less errors. The use of large basis sets, hybrid functionals and inclusion of relativistic effects compensate for their cost by yielding improved results. The solvent effects by means of COSMO or PCM have also proven to be important in providing accurate prediction in nuclear shielding properties of POMs.[57, 96]

The need for theoretical calculations in polyoxometalate compounds stems from the fact that they are large clusters and display complex NMR spectrum. Chemical shifts show high sensitivity towards the surroundings of the nucleus so much

so that a slight change in the structure can lead to multiple resonances. It is straightforward to assign each chemical shift to the corresponding nuclei when symmetrical complexes are being studied, however that might not be the case for other complexes. The rapid progress in synthesis of mixed-metal coomplexes with intricate geometries display complex spectra which are difficult to interpret. The computational approaches provide a useful tool to help spectroscopists save some time and effort in decoding their spectra.

Many studies have been devoted to computation of NMR chemical shifts in polyoxometalates.[97, 98, 99] The first study was done on predicting [183]W NMR chemical shifts in Keggin complexes, but the results were unsatisfactory due to the use of ECP basis sets.[100, 97] Kortz *et al.* presented a successful set of calculations in predicting [183]W NMR chemical shifts in dilacunary polyoxotungstates.[98] Poblet and his co-workers present benchmark DFT based theoretical NMR predictions in chemical shifts of [183]W, ^{31}P and [17]O.[99, 101, 102] The calculations were done using a pure-DFT functional at TZP level for all the three nuclei and, in general, the predictions fairly match the observed data. Another important finding in these studies was that accurate NMR prediction is possible only when solvent effects and relativistic effects (for heavy nuclei) are considered.[98, 103] For [17]O chemical shift prediction, it was seen that pure-DFT functionals could not correlate all the oxygens with the experimental data very well. It should also be noted that the computational study related to prediction of [183]W chemical shifts was done mainly on symmetrical complexes which display one chemical shift. The goal of our research is to improvise on previous computational studies and assist POM chemists in detailing the structural conformations as well as the reaction dynamics theoretically.

1.6 Thesis Outline

Chapter 1 begins with the general introduction describing the importance and relevance of the work. It then progresses to discuss the theory behind the tools used which are mainly NMR and DFT. The overview of literature on all the projects is discussed in the last section.

Chapter 2 details the pH-dependent behaviour of paramagnetic sandwich polyoxometalate compounds. The potentiometric titrations on several paramagnetic complexes is presented together with a published paper on rates of exchange of bound waters in a Mn(II)-substituted paramagnetic Wells-Dawsons complex.

Chapter 3 discusses the exchange of structural oxygens with water in isostructural and isovalent polyoxometalates, $[PV_2Nb_{12}O_{42}]^{9-}$ and $[V_3Nb_{12}O_{42}]^{9-}$, differing by a single central atom. The effect of substitution and protonation on rates of oxygen exchange is examined.

Chapter 4 includes a published paper on predicting the ^{17}O NMR chemical shifts of wide range of polyoxometalates using density functional theory. The effects of basis sets and exchange-correlation functionals are explored to develop a methodology for accurate ^{17}O NMR shift prediction.

Chapter 5 addresses the computation of NMR chemical shifts of ^{31}P, ^{51}V, ^{183}W and ^{95}Mo nuclei in polyoxometalates using density functional theory. The study involves a scrutiny of different exchange-correlation functionals for each nucleus that gives best prediction.

Conclusion and Future work summarises the outcomes of the research work done and provides suggestions on the future work.

References

[1] Y. F. Song, R. Tsunashima, *Chem. Soc. Rev.* **2012**, *41*, 7384–7402.

[2] R. Sharma, J. Zhang, C. A. Ohlin, *Dalton Trans.* **2015**, *44*, 19068–19071.

[3] Q. Yin, J. M. Tan, C. Besson, Y. V. Gelatii, D. G. Musaev, A. E. Kuznetsov, Z. Luo, K. I. Hardcastle, C. L. Hill, *Science* **2010**, *328*, 342–345.

[4] M. T. Pope, *Heteropoly and isopoly oxometalates*, Springer Verlag, **1983**.

[5] N. Mizuno, K. Kamata, *Coord. Chem. Rev.* **2011**, *255*, 2358–2370.

[6] J. T. Rhule, C. L. Hill, D. A. Judd, R. F. Schinazi, *J. Mol. Catal. A: Chem.* **2007**, *262*, 1–242.

[7] C. A. Ohlin, S. J. Harley, J. G. McAlpin, R. K. Hockin, B. Q. Mercado, R. L. Johnson, E. M. Villa, M. K. Fidler, M. M. Olmstead, L. Spiccia, R. D. Britt, W. H. Casey, *Chem. Eur. J.* **2011**, *17*, 4408–4417.

[8] D. Lieb, A. Zahl, E. F. Wilson, C. Streb, L. C. Nye, K. Meyer, I. Ivanović-Burmazović, *Inorg. Chem.* **2011**, *50*, 9053–9058.

[9] X. Zhang, Q. Chen, D. C. Duncan, R. J. Lachiotte, C. L. Hill, *Inorg. Chem.* **1997**, *36*, 4381–4386.

[10] A. Estrada, I. Santos, M. Simoes, M. Neves, J. Cavaleiro, A. Cavaleiro, *Appl. Catal. A-Gen.* **2011**, *392*, 28–35.

[11] D. Fernandes, H. Carapuca, C. Brett, A. Cavaleiro, *Thin Solid Films* **2010**, *518*, 5881–5188.

[12] M. Nyman, *Dalton. Trans.* **2011**, *40*, 8049–8058.

[13] J. R. Black, M. Nyman, W. H. Casey, *J. Am. Chem. Soc.* **2006**, *128*, 14712–14720.

[14] E. M. Villa, C. A. Ohlin, J. R. Rustad, W. H. Casey, *J. Am. Chem. Soc.* **2009**, *131*, 16488 – 16492.

[15] http://www.process-nmr.com/.

[16] http://www.i2clipart.com/.

[17] F. Bloch, *Phys. Rev.* **1946**, *70*, 460–474.

[18] H. M. McConnell, *J. Chem. Phys.* **1958**, *28*, 430–431.

[19] T. J. Swift, R. E. Connick, *J. Chem. Phys.* **1962**, *37*, 307–320.

[20] Y. Ducommun, K. E. Newman, A. E. Merbach, *Inorg. Chem.* **1980**, *19*, 3696–3703.

[21] P. S., G. Absillis, F. J. Martin-Martinez, F. D. Proft, R. Willem, T. Prac-Vogt, *Chem. Eur. J.* **2014**, *20*, 5258–5270.

[22] C. J. Besecker, W. G. Klemperer, D. J. Maltbie, D. A. Wright, *Inorg. Chem.* **1985**, 1027–1032.

[23] W. G. Klemperer, *Angew. Chem. Int. Ed.* **1978**, *17*, 246–254.

[24] M. Filowitz, W. G. Klemperer, L. Messerle, W. Shum, *J. Am. Chem. Soc.* **1976**, 2345–2346.

[25] M. Filowitz, R. K. C. Ho, W. G. Klemperer, W. Shum, *Inorg. Chem.* **1979**, *18*, 93–103.

[26] W. Casey, B. Philips, *Geochim. Cosmochim. Ac.* **2001**, *65*, 705–714.

[27] C. A. Ohlin, E. M. Villa, J. C. Fettinger, W. H. Casey, *Angew. Chem. Int. Ed.* **2008**, *47*, 8251 – 8254.

[28] R. G. Parr, W. Yang, *Density Functional Theory of Atoms and Molecules*, Oxford University Press, **1989**.

[29] J. M. Seminario, Politzer, *Modern Density Functional Theory, A Tool for Chemistry*, Elsevier Science, **1995**.

[30] E. Schrödinger, *Ann. Physik* **1964**, *79*, 361–376.

[31] D. R. Hartree, *Proc. Cambridge Phil. Soc.* **1928**, *24*, 89.

[32] V. Fock, *Z. Physik* **1930**, *61*, 126.

[33] P. Hohenberg, W. Kohn, *Phys. Rev. B* **1964**, *136*, 864.

[34] W. Kohn, L. J. Sham, *Phys. Rev* **1965**, *140*, A1133.

[35] J. P. Perdew, J. A. Chevary, S. H. Vosko, K. A. Jackson, M. R. Pederson, D. J. Singh, C. Fiolhais, *Phys. Rev. B* **1992**, *46*, 6671–6687.

[36] A. D. Becke, *Phys. Rev. A* **1988**, *38*, 3098–3100.

[37] J. P. Perdew, J. A. Chevary, S. H. Vosko, K. A. Jackson, M. R. Pederson, D. J. Singh, C. Fiolhais, *Phys. Rev. B* **1993**, *48*, 4978.

[38] J. P. Perdew, K. Burke, Y. Wang, *Phys. Rev. B* **1996**, *54*, 16533–16539.

[39] J. P. Perdew, K. Burke, M. Ernzerhof, *Phys. Rev. Lett.* **1996**, *77*, 3865–3868.

[40] J. P. Perdew, K. Burke, M. Ernzerhof, *Phys. Rev. Lett.* **1997**, *78*, 1396.

[41] N. C. Handy, A. J. Cohen, *Mol. Phys.* **2001**, *99*, 403–412.

[42] W.-M. Hoe, A. Cohen, N. C. Handy, *Chem. Phys. Lett.* **2001**, *341*, 319–328.

[43] C. Lee, W. Yang, R. G. Parr, *Phys. Rev. B* **1988**, *37*, 785.

[44] B. Miehlich, A. Savin, H. Stoll, H. Preuss, *Chem. Phys. Lett.* **1989**, *157*, 200–206.

[45] J. P. Perdew, *Phys. Rev. B* **1986**, *33*, 8822–8844.

[46] Y. Zhao, D. G. Truhlar, *J. Chem. Phys.* **2006**, *125*, 194101.

[47] A. D. Becke, *J. Chem. Phys.* **1993**, *98*, 5648–5652.

[48] C. Adamo, V. Barone, *J. Chem. Phys.* **1998**, *108*, 664–675.

[49] Y. Zhao, D. G. Truhlar, *Theor. Chem. Acc.* **2008**, *120*, 215–241.

[50] O. A. Vydrov, G. E. Scuseria, *J. Chem. Phys.* **2006**, *125*, 234109.

[51] O. A. Vydrov, J. Heyd, G. E. Scuseria, *J. Chem. Phys.* **2006**, *125*, 074106.

[52] O. A. Vydrov, G. E. Scuseria, *J. Chem. Phys.* **2007**, *126*, 154109.

[53] T. Yanai, D. Tew, N. Handy, *Chem. Phys. Lett.* **2004**, *393*, 51–57.

[54] J.-D. Chai, M. Head-Gordon, *Phys. Chem. Chem. Phys.* **2008**, *10*, 6615–6620.

[55] E. V. Lenthe, E. J. Baerends, J. G. Snijders, *J. Chem. Phys.* **1993**, *99*, 4597–4610.

[56] F. Wang, T. Ziegler, E. V. Lenthe, S. V. Gisbergen, E. J. Baerends, *J. Chem. Phys.* **2005**, *122*, 204103.

[57] A. Klamt, *J. Chem. Phys.* **1995**, *99*, 2224–2235.

[58] A. Klamt, V. Jonas, *J. Chem. Phys.* **1996**, *105*, 9972–9981.

[59] S. Miertus, E. Scrocco, J. Tomasi, *Chem. Phys.* **1981**, *55*, 117–129.

[60] T. H. Dunning, *J. Chem. Phys.* **1989**, *90*, 1007–23.

[61] *gaussian*, `http://gaussian.com/`.

[62] R. F. P., *Helvetica Chimica Acta* **2000**, *83*, 3006–3020.

[63] H. H. Loffler, A. M. Mohammed, Y. Inada, S. Funahashi, *J. Comput. Chem.* **2005**, *127*, 1944–1949.

[64] M. Grant, H. W. Dodgen, J. P. Hunt, *Inorg. Chem.* **1971**, *10*, 71–73.

[65] Esteban-Gomez, *J. Am. Chem. Soc.* **2005**, *127*, 14085–14093.

[66] M. S. Zetter, M. W. Grant, E. J. Wood, H. W. Dodgen, J. P. Hunt, *Inorg. Chem.* **1972**, *11*, 2701–2706.

[67] J. Maigut, R. Meier, A. Zahl, R. Van Eldik, *J. Am. Chem. Soc.* **2008**, *130*, 14556–14569.

[68] D. Lieb, F. C. Friedel, M. Yawer, A. Zahl, F. W. Heinemann, I. Ivanović-Burmazović, *Inorg. Chem.* **2013**, *52*, 222–236.

[69] J. L. C. Sousa, I. C. M. S. Santos, M. M. Q. Simões, J. A. S. Cavaleiro, H. I. S. Nogueira, A. M. V. Cavaleiro, *Catal. Commun.* **2011**, *12*, 459–463.

[70] C. Wang, Y. Hua, Y. Tong, *Electrochim. Acta.* **2010**, *55*, 6755–6760.

[71] T. J. R. Weakley, H. T. Evans, J. S. Showell, C. M. J. Tourné, *J. Chem. Soc., Chem. Commun.* **1973**, *4*, 139–140.

[72] R. G. Finke, M. W. Droege, *Inorg. Chem.* **1983**, *22*, 1006–1008.

[73] Z. Huang, Z. Luo, Y. V. Geletii, J. W. Vickers, Q. Yin, D. Wu, Y. Hou, Y. Ding, *J. Am. Chem. Soc.* **2011**, *133*, 2068–2071.

[74] J. J. Stracke, R. G. Finke, *J. Am. Chem. Soc.* **2011**, *133*, 14872–14875.

[75] I. Lindqvist, *Ark. Kemi.* **1953**, *5*, 247–250.

[76] M. Nyman, T. M. Alam, F. Bonhomme, M. A. Rodriguez, C. S. Frazer, M. E. Welk, *J. Cluster Sci.* **2006**, *17*, 197–219.

[77] M. Maekawa, Y. Ozawa, A. Yagasaki, *Inorg. Chem.* **2006**, *45*, 9608–9609.

[78] R. P. Bontchev, M. Nyman, *Angew. Chem. Int. Ed.* **2006**, *45*, 6670–6672.

[79] J. Niu, P. Ma, H. Niu, J. Li, J. Zhao, J. Song, W. J, *Chem. Eur. J.* **2007**, *13*, 8739–8748.

[80] R. Tsunashima, D. L. Long, H. N. Miras, D. Gabb, C. P. Pradeep, L. Cronin, *Angew. Chem. Int. Ed.* **2010**, *49*, 113–116.

[81] M. Nyman, , F. Bonhomme, T. M. Alam, M. A. Rodriguez, B. R. Cherry, J. L. Krumhansl, T. M. Nenoff, A. M. Sattler, *Science* **2002**, *297*, 996–998.

[82] M. Nyman, L. J. Criscenti, F. Bonhomme, M. A. Rodriguez, R. T. Cygan, *J. Solid State Chem.* **2003**, *176*, 111–119.

[83] J. Son, C. A. Ohlin, W. H. Casey, *Dalton Trans.* **2012**, *41*, 12674–12677.

[84] J. Son, C. A. Ohlin, R. L. Johnson, Y. Ping, W. H. Casey, *Chem. Eur. J.* **2013**, *19*, 15191–5197.

[85] J. Son, C. A. Ohlin, W. H. Casey, *Dalton Trans.* **2013**, *42*, 7529–7533.

[86] J. Son, C. A. Ohlin, E. C. Larson, Y. Ping, W. H. Casey, *Eur. J. Inorg. Chem.* **2013**, 1748–1753.

[87] J. Son, J. Wang, F. E. Osterloh, P. Yub, W. H. Casey, *Chem. Commun.* **2014**, *50*, 836–838.

[88] W. Casey, B. Philips, M. Karlsson, S. Nordin, J. Nordin, D. Sullivan, S. Neugebauer-Crawford, *Geochim. Cosmochim. Ac.* **2000**, *64*, 2951–2964.

[89] E. M. Villa, C. A. Ohlin, W. H. Casey, *Chem. Eur. J.* **2010**, *16*, 8631–8634.

[90] E. M. Villa, C. A. Ohlin, E. Balogh, T. M. Anderson, M. D. Nyman, W. H. Casey, *Angew. Chem. Int. Ed.* **2008**, *47*, 4844 – 4846.

[91] E. M. Villa, C. A. Ohlin, E. Balogh, T. M. Anderson, M. D. Nyman, W. H. Casey, *Am. J. Sci.* **2008**, *308*, 942 – 953.

[92] E. M. Villa, C. A. Ohlin, W. H. Casey, *Amer. J. Sci.* **2010**, *310*, 629–644.

[93] V. W. Day, W. C. Klemperer, C. Schwartzlb, *J. Am. Chem. Soc.* **1987**, *109*, 6030–6044.

[94] J. R. Rustad, W. H. Casey, *Nature Mater.* **2012**, *11*, 223–226.

[95] R. L. Johnson, E. M. Villa, C. A. Ohlin, J. R. Rustad, W. H. Casey, *Chem. Eur. J.* **2011**, *17*, 9359–9367.

[96] J. Tomasi, B. Mennucci, R. Cammi, *Chem. Rev.* **2005**, *105*, 2999–3093.

[97] A. Bagno, M. Bonchio, A. Sartorel, G. Scorrano, *Chem. Phys. Chem.* **2003**, *4*, 517–519.

[98] N. Vankova, T. Heine, U. Kortz, *Eur. J. Inorg. Chem.* **2009**, 5102–5108.

[99] L. Vilá-Nadal, J. P. Sarasa, A. Rodríguez-Fortea, J. Igual, L. Kazansky, J. P. Poblet, *Chem. Asian. J.* **2010**, *5*, 97–104.

[100] A. Bagno, G. Scorrano, *Acc. Chem. Res.* **2000**, *33*, 609–616.

[101] M. Pascual-Borrás, X. López, A. Rodríguez-Fortea, E. R. Errington, J. P. Poblet, *Chem. Sci.* **2014**, *5*, 2031–2042.

[102] M. Pascual-Borrás, X. López, J. P. Poblet, *Phys. Chem. Chem. Phys.* **2015**, *17*, 8723–8731.

[103] T. T. Nguyen, J. Jung, X. Trivelli, J. Treébosc, S. Cordier, Y. Molard, C. J. Pollés, Pickard, J. Cuny, R. Gautier, *Inorg. Chem.* **2015**, *54*, 7673–7683.

Chapter2:

pH-dependent reaction dynamcis of paramagnetic sandwich polyoxometalates

Introduction

This chapter addresses the dynamics of reactions involving bound aquo ligands in the paramagnetic polyoxometalate moeities. The transition metal substituted sandwich complexes were studied in view of determining their pKa values and kinetic parameters of water exchange at metal site. As discussed in chapter 1, these complexes have two bulky polyoxotungstate lignads sandwiching a metal sheet of four transition metals bound to which are two aquo ligands. The two bound water molecules exchange with the bulk solution, the rates of which were compared at different pH using the paramagnetic line-broadening of the ^{17}O NMR signal using Swift and Connick formalism.[1]

To determine the pKa and stability of the complexes, potentiometric titrations were done on five complexes. Out of these five, three were Wells-Dawsons sandwich complexes given by Finke ($[M_4(H_2O)_2(P_2W_{15}O_{56})_2]^{16-}$, where M=Fe(III), Ni(II), Zn(II) and Mn(II)), and the other two were Keggin derived Weakley complexes, $[Mn_4(H_2O)_2(PW_9O_{34})_2]^{10-}$ and $[Mn_4(H_2O)_2(VW_9O_{34})_2]^{10-}$.[2, 3] Table 1 compares the pKas of different transition metal substituted Wells-Dawsons sandwich complexes.
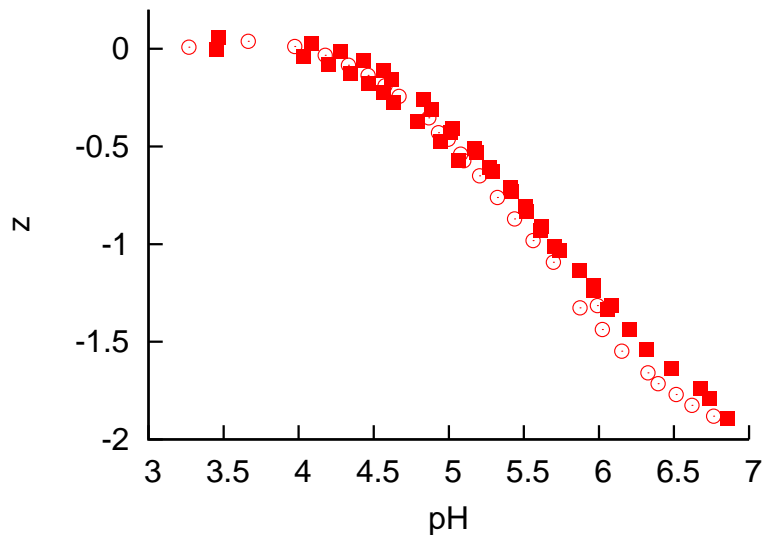
Figure 1: Excess charge (z) per mole of $[Fe_4(II)(H_2O)_2(P_2W_{15}O_{56})_2]^{16-}$ as a function of pH. The blue line indicates a fitted pKa of 5.0.

Ruhlmann *et al.* assigns two pKas at pH 3.2-3.6 and pH 5.0-5.6 for Mn, Fe, Co, Cu, Zn and Cd derivatives of $[M_4(H_2O)_2(P_2W_{15}O_{56})_2]^{16-}$ to water ligands bound at the central metal core.[6] In contrast, our results show a pka between 3 and 4 for Mn(II) derivative and it seems to be consistent from different techniques. Also, for Fe(III) derivative, we calculate a pKa of 5.0 from potentiometric titrations which

h

Table 1: Fitted pKa of different transition-metal substituted complexes of the formula, $[M_4(H_2O)_2(P_2W_{15}O_{56})_2]^{16-}$

Metal	fitted pKa	figure	exchange-kinetics
Zn	5.36	2	diamagnetic
Fe	5.0	1	too slow
Ni	-	3a	not stable
Co		refer [4]	successful
Mn	4.2	refer [5]	successful
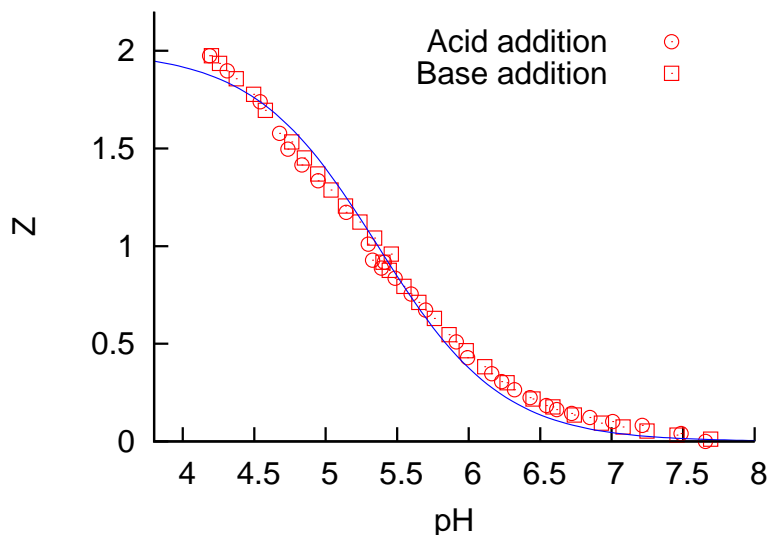
Figure 2: Excess charge (z) per mole of $[Zn_4(III)(H_2O)_2(P_2W_{15}O_{56})_2]^{16-}$ as a function of pH. The blue line indicates a fitted pKa of 5.36.

too differs from their value, but matches with estimated pka of 5.2 by Keita *et al.*[7] In our opinion, they incorrectly assign similiar pka value for all the complexes as it is unlikely that different metals bound to the same ligand will behave in the same manner.

It has been reported in a previous study that nickel(II)-substituted complex $[Ni_4(H_2O)_2(P_2W_{15}O_{56})_2]^{16-}$ degrades during titration which is evident from our data as well (see fig. 3a).[6] While, iron(III)-complex was stable over a wide pH range (pH 3 -7) with a fitted pKa of 5.0, however no broadening of ^{17}O NMR signal with respect to reference was seen within a temperature range of 270-285 K. The aqua ligands attached in the corresponding monomeric ion, $[Fe^{III}(H_2O)_6]^{3-}$, also exchange at a very slow rate of $1.6 \cdot 10^2$.[8] It can be assumed that the exchange of bound ligands in the iron (III)- polyoxometalate might be at a comparable rate, and hence could not be measured by spectroscopic technique. The zinc analogue

also displays similar acid-base chemistry as its other paramagnetic equivalents yielding a pKa of 5.36. The above mentioned three complexes were not taken further for water-exchange measurements.

The z-plot of other two manganese complexes with Keggin-derived polyoxo-tungstate ligands ($[Mn_4(H_2O)_2(PW_9O_{34})_2]^{10-}$ and $[Mn_4(H_2O)_2(VW_9O_{34})_2]^{10-}$) showed hysteresis even when subjected to a slight pH change (fig. 3b and 3c). In cobalt analog, Ohlin *et al.* has also seen that smaller complex, $[Co_4(H_2O)_2(PW_9O_{34})_2]^{10-}$, is less stable as compared to the bulkier complex, $[Co_4(H_2O)_2(P_2W_{15}O_{56})_2]^{16-}$.[4] The presence of the tungstate ligands $[P_2W_{15}O_{56}]^{12-}$ stabilise the metal sheet leading to complexes which have wider pH stablity region than complexes with substituted Keggin ligands $[PW_9O_{34}]^{9-}$.

Ohlin *et al.* provide a detailed study on the rates of exchange of bound waters on the cobalt substituted sandwich complexes. It was seen that the rates of exchange in the two cobalt (II)-polyoxometalates under study, $[Co_4(H_2O)_2(PW_9O_{34})_2]^{9-}$ and $[Co_4(H_2O)_2(P_2W_{15}O_{56})_2]^{16-}$, were unaffected by pH, and the rates were comparable to the corresponding hexaaqua ion ($[Co^{II}(H_2O)_6]^{2-}$ (as discussed in chapter 1).[4]

We investigated the pH dependent behaviour of manganese-substituted Wells-Dawsons sandwich complex and compared it with its monomeric species which is published in the journal article:

R. Sharma, J. Zhang and C. A. Ohlin, *Dalton Transaction*, **2015**, 44, 19068-19071.

Another interesting finding from this comparative study is that all four substituted complexes (Co(II), Mn(II), Zn(II) and Fe(II)) show a two proton protonation
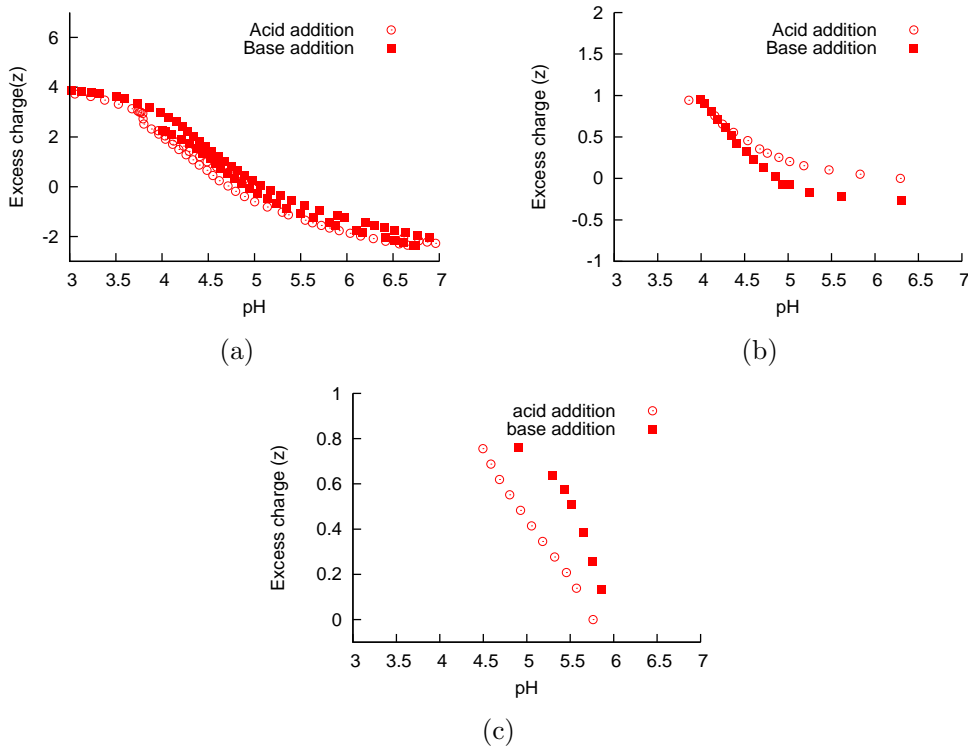
Figure 3: (a),(b), (c): Excess charge (z) per mole of $[Ni_4(II)(H_2O)_2(P_2W_{15}O_{56})_2]^{16-}$, $[Mn_4(II)(H_2O)_2(PW_9O_{34})_2]^{10-}$ and $[Mn_4(II)(H_2O)_2(VW_9O_{34})_2]^{10-}$, respectively as a function of pH.

process with slightly different pKas. We believe that this protonation is likely to be associated with the polyoxotungstate ligands. The reason behind this statement is the vast difference in the pKas of the corresponding hexaaqua ions of these species. We wished to investigate the exact locus of protonation, and so we did ^{1}H-solid-state NMR experiments on the diamagnetic Zn analog.

The proton at low pH is too difficult to be observed even by solid-state NMR beacuse of the huge water signal in the vicinity. In [1]H-^{1}H correlation experiment, a small peak next to the water signal shows the presence of an additional -OH moeity in the complex. Moreover, ^{31}P-^{1}H hetronuclear NMR data shows that this

proton is bound to the phosphorus at -6 ppm (see figure 4). From the previous characterisation of the complex, we know that this signal corresponds to the phosphorus atom proximal to the zinc metal cations in the structure.[2] The results do not provide much information about the distance between the phosphorus and the hydrogen atom in the complex which would have been the key to finding the exact oxygen of protonation. Certainly, this work opens up the scope for future computational studies to solve the experimental problem.
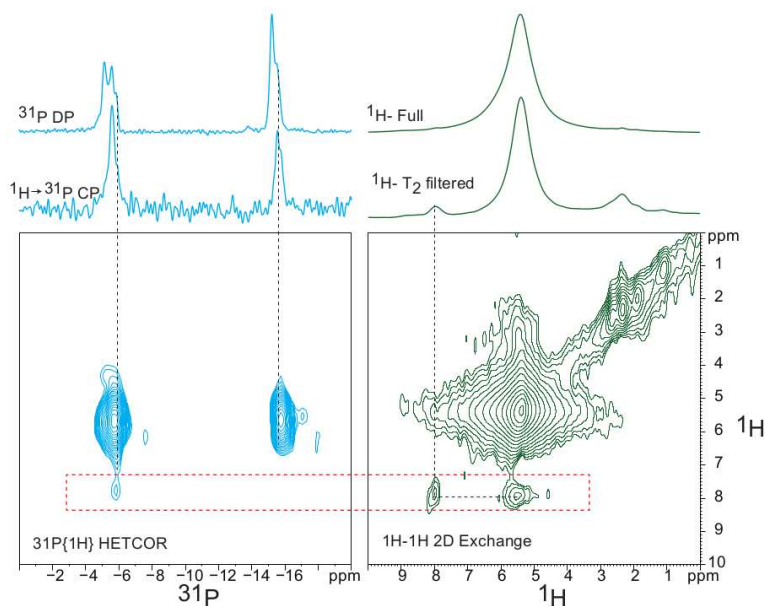
Figure 4: 2D ^{1}H-^{1}H and ^{31}P^{1}H solid-state NMR spectra of $[Zn_4(III)(H_2O)_2(P_2W_{15}O_{56})_2]^{16-}$ at pH 3.5.

References

[1] T. J. Swift, R. E. Connick, *J. Chem. Phys.* **1962**, *37*, 307–320.

[2] R. G. Finke, M. W. Droege, *Inorg. Chem.* **1983**, *22*, 1006–1008.

[3] T. J. R. Weakley, H. T. Evans, J. S. Showell, C. M. J. Tourné, *J. Chem. Soc., Chem. Commun.* **1973**, *4*, 139–140.

[4] C. A. Ohlin, S. J. Harley, J. G. McAlpin, R. K. Hockin, B. Q. Mercado, R. L. Johnson, E. M. Villa, M. K. Fidler, M. M. Olmstead, L. Spiccia, R. D. Britt, W. H. Casey, *Chem. Eur. J.* **2011**, *17*, 4408–4417.

[5] R. Sharma, J. Zhang, C. A. Ohlin, *Dalton Trans.* **2015**, *44*, 19068–19071.

[6] L. Ruhlmann, R. Canny, R. Contant, R. Thouvenot, *Inorg. Chem.* **2002**, *41*, 3811–3819.

[7] B. Keita, I. M. Mbomekalle, Y. W. Lu, L. Nadjo, P. Berthet, T. M. Anderson, C. L. Hill, *Eur. J. Inorg. Chem.* **2004**, *17*, 3462–3475.

[8] F. A. Dunand, L. Helm, A. E. Merbach, *Advances in Inorg. Chem.* **1983**, *54*, 1–69.

COMMUNICATION

pH-Dependent solution dynamics of a manganese(II) polyoxometalate, $[Mn_4(H_2O)_2(P_2W_{15}O_{56})_2]^{16-}$, and $[Mn(H_2O)_6]^{2+}$†

Rupali Sharma, Jie Zhang and C. André Ohlin*

The aqueous reaction dynamics of the manganese(II)-functionalised Wells–Dawson polyoxometalate $[Mn_4(H_2O)_2(P_2W_{15}O_{56})_2]^{16-}$ has been determined as a function of pH using variable temperature ^{17}O NMR, and compared with that of the well-studied monomeric manganese(II) hexa-aqua ion, $[Mn(H_2O)_6]^{2+}$. While the rate of aquo–ligand exchange on the hexa-aqua ion remains independent of pH in the range 3.2–6.0, the rate of water exchange of the polyoxometalate ion varies by a factor of fifteen, from $1.98 \times 10^7 \text{ s}^{-1}$ at pH 3.2 to $1.3 \times 10^6 \text{ s}^{-1}$ at pH 6.0. This decrease in the rate of exchange correlates with the deprotonation of the polyoxometalate framework.

Metal oxides are important in many fields, for example as heterogeneous catalysts in industrial applications, as metal oxide clusters in enzymes, and in the form of minerals in nature, many of which are simple transition metal (hydr)-oxides. As most of these are solids, one of the most important reactions that they undergo occurs at the solid–solvent interface, for example in the form of interaction with water such as weathering or dissolution. Because it is often difficult to get information about reactions involving solids at a level of resolution that allows for site specific characterisation, a significant part of our knowledge about the reactivity of metal oxides and hydroxides comes from the use of discrete molecules as models.

One of the simplest classes of models is made up of the metal hexa-aqua ions, and the determination of water exchange rates on such ions has been the subject of extensive literature.[1–4] However, ions with geminal water ligands do not adequately represent most mineral surfaces, where the aquo ligands are generally well separated, and it is thus desirable to use different ligands to modulate the coordination environment. In addition, as has been pointed out elsewhere, the literature lacks pH dependent data, even for the simplest metal aquo ions.[5]

Polyoxometalates (POMs), metal oxides comprising discrete oxide clusters of group 5 and 6 metals in their highest oxidation states, are arousing a lot of interest due to their potential in a wide range of fields, for example as catalysts, resins and drugs. They are also, however, of interest as molecular models for reactions involving water and minerals, but only the niobates have seen extensive use in this capacity and only to study the lability of framework oxygen atoms.[6–9] To the best of our knowledge, there are only two studies which have looked at the dynamics of water ligands bound to isolated metal centres in functionalised POMs. These studies looked at the water exchange reactions involving $[Co_4(H_2O)_2(B-\alpha-PW_9O_{34})_2]^{10-}$,[10,11] $\alpha\beta\beta\alpha$-$[Co_4(H_2O)_2(P_2W_{15}O_{56})_2]^{16-}$,[10,11] and $[Co(H_2O)SiW_{11}O_{36}]^{6-}$,[11] using the paramagnetic nuclear magnetic resonance techniques described by Swift and Connick.[1,2,12]

We here introduce the first example of the ^{17}O NMR based[1,2] determination of the water exchange rate on a manganese(II)-functionalised POM, $Na_{15}H[\alpha\beta\beta\alpha-Mn_4(H_2O)_2(P_2W_{15}O_{56})_2]\cdot70H_2O$ (see Fig. 1), as a function of temperature and pH, and also present the first study of pH dependent water exchange rates for the manganese(II) hexa-aqua ion. All experimental and theoretical details are provided in the ESI.†
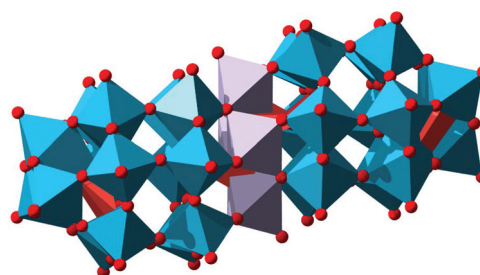
School of Chemistry, Monash University, Victoria, Australia.
E-mail: andy.ohlin@monash.edu
†Electronic supplementary information (ESI) available: Syntheses, determination of pH stability, NMR spectroscopy, and data reduction. See DOI: 10.1039/C5DT03138A

Fig. 1 Structure of $\alpha\beta\beta\alpha$-$[Mn_4(H_2O)_2(P_2W_{15}O_{56})_2]^{16-}$. Tungsten, oxygen, phosphorous and manganese atoms are shown in blue, red, orange and purple, respectively.

To determine the pH stability range of **1** the complex was titrated back and forth by alternating addition of acids and bases. The pH stability range was found to be limited to pH 3–7 as hysteresis was observed outside this range, and a plot of the excess charge, z_e, *vs.* pH constructed using eqn (S4)† showed a two-proton protonation event, with a fitted pK_a of 4.4 ± 0.0(2) (see Fig. 2A). UV/VIS spectroscopic data, which were acquired in the absence of background salt, likewise exhibited a pH-dependent behaviour in transitioning from a dark yellow to a paler yellow, corresponding to weakened O–W CT,[13] on acidification, with a fitted pK_a of 3.5 ± 0.1 (Fig. 2B). The ^{31}P NMR signal from the distal phosphorous centre in the ligand also showed a pH dependent behaviour with irreversible breakdown indicated below pH 3, with a pK_a of 4.0 ± 0.2 (Fig. 2C). No protonation events were observed for the [Mn(H$_2$O)$_6$]$^{2+}$ ion in this range, in accordance with the reported pK_a of 10.6.[14]

Note that these results differ somewhat from those of Ruhlmann *et al.*,[15] who found two pK_as each for the Mn, Fe, Co, Cu, Zn and Cd derivatives of [M(II)$_4$(H$_2$O)$_2$(P$_2$W$_{15}$O$_{56}$)$_2$]$^{16-}$ at pH 3.2–3.6 and 5.0–5.6, and attributed them all to the aquo–ligands bound to the heterometal centres. We find it surprising that ions as different as Cu(II) (pK_a of [Cu(H$_2$O)$_6$]$^{2+}$

ca. 7.3–8.0) and Mn(II) (pK_a of [Mn(H$_2$O)$_6$]$^{2+}$ *ca.* 10.6),[14] would exhibit such similar pK_as solely by virtue of being complexed to the same ligand. Instead, the observed pK_a is most likely associated with protonation of the polyoxotungstate ligands, as supported by the observation of two simultaneous protonation events which indicates that the two loci are identical but located distantly enough from one another so that protonation at one of the sites does not affect the pK_a of the other.

The rates of exchange of the aquo ligands in [Mn(H$_2$O)$_6$]$^{2+}$ and **1** were determined as a function of temperature and pH (see Table 1). We took a two-fold approach to calculate the activation parameters: the first approach, method 1, was to calculate the parameters by focussing only on the region where $\frac{1}{T_{2p}} \approx P_m k_m$,[12] and the second approach, method 2, involved fitting the data using eqn (1),[1] which is applicable for manganese species with a negligible signal shift and a long T_{1e}. The chief weakness with the first approach is the difficulty in objectively delimiting the linear region, and, more significantly, that $1/T_{2p}$ is approximate to, but not exactly equal to, $P_m k_m$. The consequence is that $\Delta H^{\ddagger}$ and $\Delta S^{\ddagger}$ are somewhat underestimated.
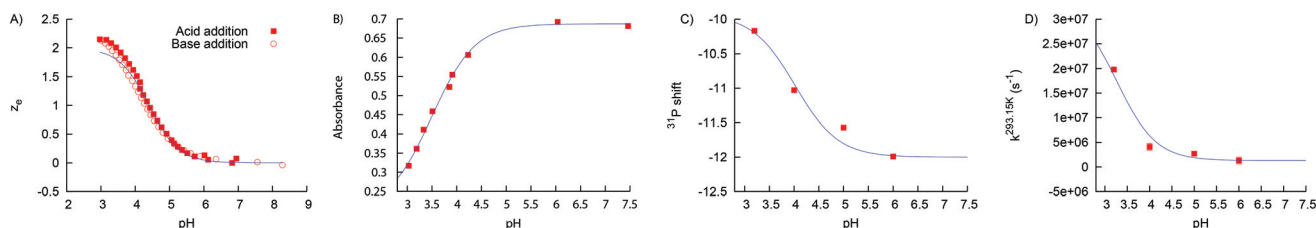
Fig. 2 (A) The excess charge (z_e) plot of **1** as a function of pH as the complex was titrated first with HClO$_4$ and then with NaOH. Acid addition is shown by filled squares and base addition is indicated using empty circles. The fitted line indicates the expected z_e for pK_a 4.4 ± 0.0(2). (B) Absorbance at 400 nm as a function of pH. The fitted line indicates the change in absorbance with pH for pK_a 3.5 ± 0.1. (C) ^{31}P NMR signal of distal phosphorus as a function of pH. The fitted line indicates the change in the shift with a pK_a 4.0 ± 0.2. (D) $k^{293.15 \text{ K}}$ as a function of pH. The fitted line is based on a simple protonation speciation model, with pK_a 3.3 ± 0.2.

Table 1 Kinetic and rate parameters of water-exchange in [Mn(H$_2$O)$_6$]$^{2+}$ and **1** calculated from temperature dependent ^{17}O NMR spectroscopy at different pH values

pH	$k_m^{293.15 \ a}$ [10^7 s^{-1}]	$\Delta H^{\ddagger}$ [kJ mol^{-1}]	$\Delta S^{\ddagger}$ [J mol^{-1} K^{-1}]	A/h [MHz]	Ref.
[Mn(OH$_2$)$_6$]$^{2+}$					
3.2	1.34 ± 0.02 (1.22 ± 0.02)	35 ± 1 (30 ± 1)	13 ± 4 (−6 ± 4)	6.17 ± 0.06	
4.0	1.65 ± 0.02 (1.21 ± 0.02)	38 ± 1 (31 ± 2)	22 ± 3 (−4 ± 5)	6.15 ± 0.05	
5.0	1.38 ± 0.02 (1.25 ± 0.02)	35 ± 1 (29 ± 2)	11 ± 4 (−11 ± 7)	6.17 ± 0.06	
6.0	1.86 ± 0.02 (1.31 ± 0.02)	33 ± 1 (26 ± 3)	7 ± 5 (−20 ± 11)	6.15 ± 0.07	
1^b	3.1	33.9	12.1	9.2	Swift *et al.*[1,2]
1–2^c	2.1 ± 1.7	32.9 ± 1.3	5.7 ± 5.0	5.3 ± 0.5	Ducommun *et al.*[4]
3	2.2 ± 0.6	32.2 ± 0.4	3.8 ± 1.7	5.4 ± 0.3	Zetter *et al.*[16]
4.3	2.7 ± 6.2	36.8 ± 4.2	20.9 ± 12.6	4.4	Grant *et al.*[3]
1					
3.2	1.98 ± 0.01 (1.16 ± 0.01)	28 ± 1 (19 ± 2)	−10 ± 3 (−44 ± 9)	3.06 ± 0.01	
4.0	0.41 ± 0.00 (0.38 ± 0.00)	30 ± 1 (21 ± 1)	−14 ± 4 (−49 ± 3)	1.44 ± 0.01	
5.0	0.27 ± 0.00 (0.18 ± 0.00)	31 ± 2 (25 ± 2)	−15 ± 8 (−41 ± 7)	1.05 ± 0.02	
6.0	0.13 ± 0.00 (0.11 ± 0.00)	44 ± 4 (41 ± 2)	21 ± 14 (12 ± 7)	1.04 ± 0.02	

Activation parameters were obtained using eqn (1) (method 2). Values in parentheses were obtained by fitting only the linear region (method 1; eqn (S12)). ^{a} Calculated from difference in line-width at 293.15 K with and without a paramagnetic ion (method 1: eqn (S12); method 2: eqn (S16)). ^{b} [HClO$_4$] given as 0.1 M. ^{c} [HClO$_4$] given as 0.06–0.1 M.

As T_{1e} and A/h are covariants, and eqn (1) gets progressively decoupled from T_{1e} as it increases, we used the value of 1.25×10^{-8} s determined by Ducommun et al. for the hexa-aqua ion rather than fitting it.[4] However, a value of 5.25×10^{-8} s was chosen for **1** via fitting, as there was no literature value available. See the ESI† for details.

$$\frac{1}{T_{2p}} = \frac{P_m}{\dfrac{1}{k_m} + \dfrac{1}{B\left(\dfrac{A}{h}\right)^2}\left(\dfrac{1}{T_{1e}} + k_m\right)} \quad (1)$$

The rates of exchange are calculated by the difference in line-width at 293.15 K using eqn (S16).† The widths of ^{17}O NMR signals are well determined and fitted such that the errors in rates are almost negligible. As seen from the rate data, the exchange of an aquo–ligand on the manganese hexa-aqua ion is insensitive to pH, as would be expected from the known pK_a of ca. 10.6.[14] The $\Delta H^{\ddagger}$ and $\Delta S^{\ddagger}$ are consistently lower for method 1 than method 2, as would be expected from not accounting for the contribution of A/h and T_{1e}. For method 2, activation parameters and A/h are consistent with the literature.

In contrast, the rates of water exchange involving complex **1** depend strongly on pH, with a fifteen-fold increase in the rate moving from pH 6.0 to pH 3.2. The change in rates with pH is consistent with the pK_as determined from potentiometric titration and UV/VIS measurements, and a very crude pK_a of 3.3 ± 0.3 was obtained by fitting the rates against a simple speciation model (Fig. 2D). Looking at the data from method 2, the $\Delta H^{\ddagger}$ increases somewhat with pH, whereas $\Delta S^{\ddagger}$ is constant within an error, with the exception at pH 6.0.

It is important to note that whereas the values of absolute rates and the activation parameters vary with the method chosen to fit the data, the same trends are observed. Whereas the values from method 2 agree better with the literature – as this is the approach taken in previous studies – it is troubling that the choice of T_{1e}, contrary to the common perception, has a very large influence on the determined $\Delta H^{\ddagger}$, $\Delta S^{\ddagger}$ and A/h values for $10^{-9} < T_{1e} < 10^{-7}$ s, as shown in Fig. S11 and S12.† This is a particular problem for species such as Mn(II) where $\Delta \omega_m$ is too small to aid in the independent determination of A/h, and where the temperature stability region is limited, as in the case of **1**.

The cause of the increase in rates of exchange with pH is not immediately clear. As discussed, the locus of protonation is very unlikely to be an aquo–ligand, but is instead on the polyoxotungstate ligand. Whether the locus is close to the Mn–OH$_2$ moiety and affecting the solvent shell near the aquo–ligand, or farther away and causing a change in rates solely via the decrease in charge on the polyoxotungstate ligand, is difficult to resolve. However, the observation that the pH-driven change in rates is accompanied by a change in the magnitude of the O–W charge transfer suggests the latter. It should also be noted that there are likely many protonation states of similar energies, rendering protons effectively deloca-

lised over the ligand. An intriguing observation is the lack of pH dependence of the rates for the cobalt(II) analogue of **1**, $[\text{Co}_4(\text{H}_2\text{O})_2(\text{P}_2\text{W}_{15}\text{O}_{56})_2]^{16-}$,[10] in spite of the similar protonation behaviour. Without a more systematic study of the entire series of transition metal substituted clusters it is difficult to know how well the observations for monomeric aqua species in terms of associative and dissociative mechanisms translate to these highly substituted systems.[17]

Finally, it is important to note that the pK_a is associated with the labilisation of **1**. Below pH 3.0, ^{31}P NMR, potentiometric titrimetry and UV/VIS data all show decomposition of the molecule. However, the reversible z_e-plot shows unequivocally that the molecule is intact in the pH range (3.2–6.0) where the dynamic NMR study was executed, and the rate data show that the rate of exchange of the bound water ligands increases at least fifteen-fold as the pH approaches the pK_a. The increase in the rate can thus not be due to the release of Mn(II). This behaviour, where sites in a molecule become labile to exchange as the pH is approaching the unstable regime, has recently also been demonstrated for a uranyl peroxo-hydroxide cluster.[18]

Conclusions

In conclusion, this study provides the results of the first pH dependent study of the exchange involving a manganese hexa-aqua ion and confirmed that it is pH independent, and presents the first rate data for a manganese-containing POM. We have also re-interpreted the previous pK_a values for **1**. Significantly, we have demonstrated that even protonation events that are not directly associated with bound aquo–ligands can have dramatic impacts on the lability of such ligands. These observations are important when considering the reactivity of extended metal-oxide surfaces where the reactivity of a site on one type of crystal face or kink site may have regional or global effects, and affect the reactivity of neighbouring but different types of sites.

Acknowledgements

Notes and references

1 T. J. Swift and R. E. Connick, J. Chem. Phys., 1962, **37**, 307–320.

2 T. J. Swift and R. E. Connick, J. Chem. Phys., 1964, **41**, 2553.

3 M. Grant, H. W. Dodgen and J. P. Hunt, Inorg. Chem., 1971, **10**, 71–73.

4 Y. Ducommun, K. E. Newman and A. E. Merbach, Inorg. Chem., 1980, **19**, 3696–3703.

5 H. A. Gazzaz, E. Ember, A. Zahl and R. van Eldik, *Dalton Trans.*, 2009, 9486–9495.

6 E. M. Villa, C. A. Ohlin, E. Balogh, T. M. Anderson, M. D. Nyman and W. H. Casey, *Angew. Chem., Int. Ed.*, 2008, **47**, 4844–4846.

7 E. M. Villa, C. A. Ohlin, J. R. Rustad and W. H. Casey, *J. Am. Chem. Soc.*, 2009, **131**, 16488–16492.

8 E. M. Villa, C. A. Ohlin and W. H. Casey, *J. Am. Chem. Soc.*, 2010, **132**, 5264–5272.

9 R. L. Johnson, E. M. Villa, C. A. Ohlin, J. R. Rustad and W. H. Casey, *Chem. – Eur. J.*, 2011, **17**, 9359–9367.

10 C. A. Ohlin, S. J. Harley, J. G. McAlpin, R. K. Hockin, B. Q. Mercado, R. L. Johnson, E. M. Villa, M. K. Fidler, M. M. Olmstead, L. Spiccia, R. D. Britt and W. H. Casey, *Chem. – Eur. J.*, 2011, **17**, 4408–4417.

11 D. Lieb, A. Zahl, E. F. Wilson, C. Streb, L. C. Nye, K. Meyer and I. Ivanović-Burmazović, *Inorg. Chem.*, 2011, **50**, 9053–9058.

12 S. J. Harley, C. A. Ohlin and W. H. Casey, *Geochim. Cosmochim. Acta*, 2011, **75**, 3711–3725.

13 X. Zhang, Q. Chen, D. C. Duncan, R. J. Lachiotte and C. L. Hill, *Inorg. Chem.*, 1997, **36**, 4381–4386.

14 J. Burgess, *Metal ions in solution*, John Wiley and Sons, New York, USA, 1978.

15 L. Ruhlmann, C. Costa-Coquelard, J. Canny and R. Thouvenot, *Eur. J. Inorg. Chem.*, 2002, **4**, 975–986.

16 M. S. Zetter, G. Y.-S. Lo, H. W. Dodgen and J. P. Hunt, *J. Am. Chem. Soc.*, 1978, **100**, 4430–4436.

17 L. Helm and A. E. Merbach, *Chem. Rev.*, 2005, **105**, 1923–1959.

18 R. Johnson, C. A. Ohlin, K. Pellegrini and P. Burns, *Angew. Chem., Int. Ed.*, 2013, **52**, 7464–7467.

Supporting information:
pH-dependent solution dynamics of a manganese(II) polyoxometalate, $[\mathrm{Mn_4(H_2O)_2(P_2W_{15}O_{56})_2}]^{16-}$, and $[\mathrm{Mn(H_2O)_6}]^{2+}$.

Rupali Sharma[1], Jie Zhang[1], and C. André Ohlin[1]

[1]School of Chemistry, Monash University, Victoria, Australia

1

Contents

Figure S1: ATR FT-IR spectrum of $Na_{15}H[Mn_4(H_2O)_2(P_2W_{15}O_{56})_2]\cdot70\,H_2O$. The spectrum was acquired on a Cary 640 FT-IR instrument.

1 Synthesis and characterisation of $\mathbf{Na_{15}H[Mn_4(H_2O)_2(P_2W_{15}O_{56})_2]\cdot70}$ $\mathbf{H_2O}$ (1)

$Na_{12}[\alpha-P_2W_{15}O_{56}]\cdot24H_2O$ was synthesised according to literature.[1] $\alpha\beta\beta\alpha$-$Na_{15}H[Mn_4(H_2O)_2(P_2W_{15}O_{56})_2]\cdot70$ H_2O (**1**) was synthesised according to a published procedure.[2] Briefly, $Mn(NO_3)_2\cdot4H_2O$ (2.5 mmol, 0.63 g) was dissolved in NaCl(aq) (1 M, 50 ml). $Na_{12}P_2W_{15}O_{56}$ (1 mmol, 4 g) was added very slowly, and the mixture heated at 60°C until a transparent solution was obtained. The solution was warm filtered through paper to remove any insoluble solids and then left at room temperature to crystallise. The crystals obtained were isolated, washed repeatedly with cold NaCl(aq) (2 M) solution on a medium frit with suction, until the filtrate was colourless. The compound was dried in a desiccator at room temperature.

Elemental analyses were carried out by Galbraith Laboratories, Inc. (Knoxville, TN). Elemental analysis calculated (found) for **1**: Na 3.76 (3.72), P 1.26 (1.33), Mn 2.33 (2.37), W 59.1 (59.5) %w/w.

Thermogravimetric analysis, performed on a Mettler Toledo TGA TSC 1, indicated 70 crystal waters per cluster molecule. The ATR FT-IR (fig. 1) agreed with the literature.[2]

A cyclic voltammogram was recorded of an N_2 purged solution of **1** (0.97 mM) at pH 4.0 (0.1 M CH_3COONa, 0.1 M CH_3COOH; 0.05 M Na_2SO_4) using a three-electrode set up (Ag/AgCl in 3 M NaCl reference; glassy carbon working electrode; Pt wire counter electrode) with a scan rate of 20 mV s^{-1} (see figure S2). The obtained voltammogram agrees with literature.[3] There is no evidence of irreversible waves which would indicate free $[Mn(H_2O)_6]^{2+}$.

^{31}P NMR spectra were acquired on a Bruker DPX 300 (7.05 T, ^{31}P 121.49 MHz) spectrometer equipped with a 5 mm broadband probe. The ^{31}P chemical shifts were measured at 298 K and calibrated against an external H_3PO_4(85 %) reference.

2 Determination of pH stability

2.1 Potentiometric titration

A sample **1** (3.89 mM, 5 ml, 0.1 M $NaClO_4$) was titrated on a Metrohm 736 GP Titrino from the self-buffering pH (6.82) to pH 2.97 using $HClO_4$ (111 mM, 0.1 M $NaClO_4$). The burette was then changed to

3
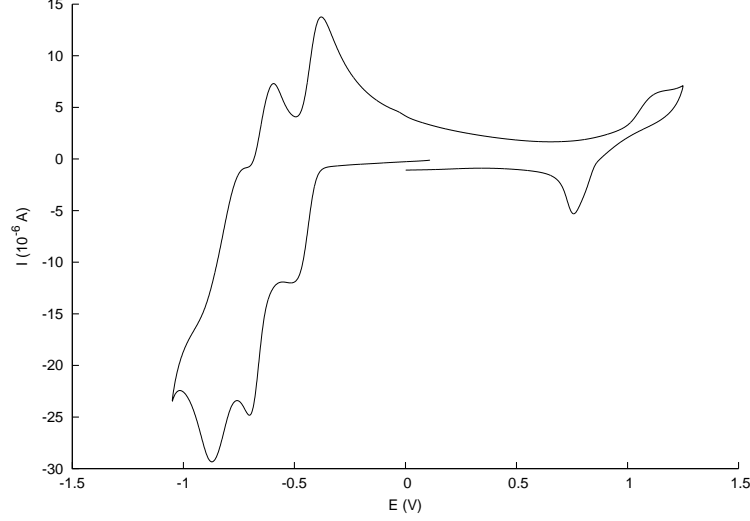
Figure S2: Cyclic voltammogram of **1**. W(IV)/W(V) waves on the left and Mn(II)/Mn(III) waves on the right. Initial scan direction left. See section 1 in text for details.

NaOH (101 mM, 0.1 M NaClO$_4$) and the sample was titrated back to pH 8.29.

The amount of uncompensated excess charge per mol of **1**, z_e, was plotted as a function of pH. The z_e value can be calculated from the complete mass-charge balance of the titrated NaClO$_4$/HClO$_4$ system.[4] Briefly, for a pH active, multiply charged species (M^{n-}), the total concentration of M, M_{tot} is the sum of M in all the possible protonation states (eq. S1). z_{tot} is the sum of all the charges in the system (eq. S3), and should be exactly zero if all charges are accounted for. For a multiprotic acid where the pK$_a$s are unknown, z_M, the sum of all the charge contributed by M in its different protonation states, is unknown (eq. S3). As $z_{tot} \equiv 0$, by defining $z_e = \frac{z_M}{[M_{tot}]}$, we can calculate the **variation** in the excess uncompensated charge per molecule (eq. S4). We can thus see protonation events, although the exact protonation state may not be known.

$$M_{tot} = [M^{n-}] + [HM^{(n-1)}] + [H_2M^{(n-2)}] + ... \tag{S1}$$

$$z_{tot} = [Na^+] + [H^+] - [OH^-] - [ClO_4^-] + (-n) \cdot [M^{n-}] + (-(n-1) \cdot [M^{-(n-1)}] + ... \tag{S2}$$

$$= [Na^+] + [H^+] - [OH^-] - [ClO_4^-] + z_M \tag{S3}$$

$$z_e = -\frac{[Na^+] + [H^+] - [OH^-] - [ClO_4^-]}{[M_{tot}]} \tag{S4}$$

The stable pH region for **1** was defined as the region where the z_e curves overlapped, which was pH 3-7 (fig. 2A). A pK$_a$, 4.4±0.0(2), was determined by fitting the z_e values to equation S10 (see eq. S5-S9 for derivation).

4
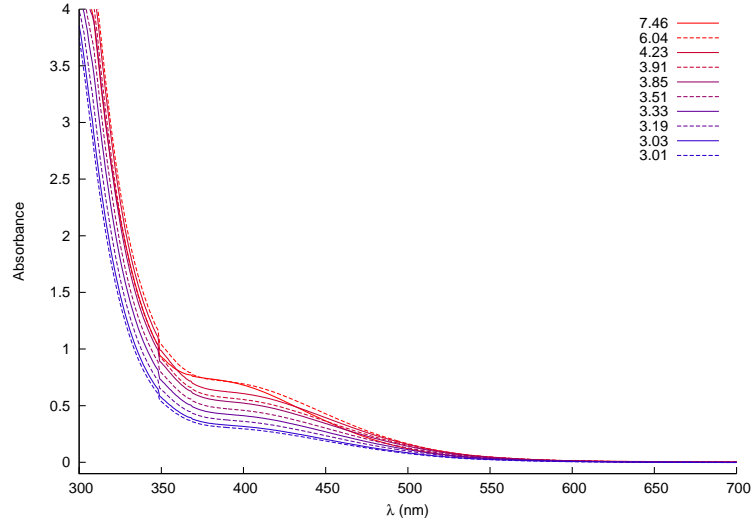
Figure S3: Successive absorption spectra of **1** as a function of pH. Absorbance decreases as pH shifts from basic to acidic conditions (Blue – more acidic. Red – more alkaline).

$$K_a = \frac{[H][A]}{[HA]} \tag{S5}$$

$$K_a = \frac{[H][x_A]}{1 - x_A} \Leftrightarrow \tag{S6}$$

$$x_A = \frac{K_a}{[H] + K_a} \tag{S7}$$

$$x_A = \frac{10^{-pK_a}}{10^{-pH} + 10^{-pK_a}} \tag{S8}$$

$$z_e = (1 - x_A)z_{HA} + x_A z_A \tag{S9}$$

$$z_{HA} = 0$$

$$z_e = z_A \frac{10^{-pK_a}}{10^{-pH} + 10^{-pK_a}} \tag{S10}$$

2.2 UV/VIS titration

3.0 ml aliquots of a 162 μM solution of **1** were pH adjusted using 0.1 M HClO$_4$ and 0.1 M N(CH$_3$)$_4$OH. The UV/VIS spectra were collected on a Cary Bio 300 and corrected for dilution (see fig. S3). No background salt was used.

A pK$_a$, 3.4±0.0(2), was determined by fitting the absorbance to $Abs_{obs,400nm} = (1 - x_A)Abs_{HA,400nm} + x_A Abs_{A,400nm}$ (*c.f.* eq. S9). See figure 2B.

3 ^{17}O NMR spectroscopy

3.1 Data acquisition

Samples for rate measurements contained 0.5 mM [Mn(H$_2$O)$_6$][NO$_3$]$_2$ or 1.94 mM **1**, and the pH was set using HClO$_4$ or NaOH. All solutions contained 0.1 M NaClO$_4$, used isotopically normal water unless otherwise

5

specified, and were spiked with 5 μl 20%-^{17}O enriched water per 500 μl. Spectra were collected on a Bruker DRX 400 instrument (9.4 T, ^{17}O 54.26 MHz) using a $\pi/2$ pulse width (11.25 μs), 256 repetitions and with a 0.5 s recycle delay. The temperature was set to 270–336 K, and was recorded using a T-type thermocouple inserted into a dummy sample. The instrument was shimmed using an external 0.1 M NaClO$_4$ D$_2$O sample. Reference samples were made up using 0.1 M NaClO$_4$ and the pH was adjusted to match the sample. Line widths were fitted using a Lorentzian function. The results are tabulated in tables S1-S8.

Table S1: ^{17}O NMR line widths of the bulk water signal in the presence of 1.94 mM **1** in 0.1 M NaClO$_4$ at pH 3.2.

T (K)	Reference width (Hz)	Sample width (Hz)
274.15	92.37±1.32	239.37±1.16
276.40	85.49±1.12	248.56±1.10
277.85	77.08±0.99	249.27±1.18
281.10	75.45±0.99	262.17±1.24
285.90	61.38±0.76	278.12±1.5
289.55	57.16±0.65	290.03±1.76
293.15	50.03±0.58	306.95±1.81
298.95	43.57±0.47	326.66±2.07
309.75	39.52±0.42	326.66±2.11
315.10	31.06±0.31	310.90±2.02

Table S2: ^{17}O NMR line widths of the bulk water signal in the presence of 1.94 mM **1** in 0.1 M NaClO$_4$ at pH 4.0.

T (K)	Reference width (Hz)	Sample width (Hz)
274.15	87.35±1.26	135.23±0.48
276.40	86.57±1.15	133.10±0.41
277.85	81.33±1.03	133.23±0.45
281.10	73.6±0.91	129.08±0.49
285.90	63.05±0.79	128.43±0.46
289.55	56.05±0.68	130.56±0.47
293.15	51.47±0.6	135.38±0.50
298.95	44.27±0.50	138.23±0.54
309.75	40.07±0.43	140.87±0.59
304.30	35.72±0.38	141.44±0.68
315.10	31.44±0.31	137.71±0.66
319.35	29.09±0.29	138.35±0.62
324.10	26.28±0.25	134.4±0.65

3.2 Data processing

$$\frac{1}{T_{2p}} = \pi(\Delta\nu_{obs} - \Delta\nu_{solvent}) \tag{S11}$$

$$= P_m k_m \left[\frac{\frac{1}{(T_{2m})^2} + \frac{k_m}{T_{2m}} + \Delta\omega_m^2}{\left(\frac{1}{T_{2m}} + k_m\right)^2 + \Delta\omega_m^2} \right] \tag{S12}$$

6

Table S3: ^{17}O NMR line widths of the bulk water signal in the presence of 1.94 mM **1** in 0.1 M NaClO$_4$ at pH 5.0.

T (K)	Reference width (Hz)	Sample width (Hz)
275.40	93.5±0.99	112.35±0.44
281.25	76.04±0.73	101.54±0.3
287.20	63.04±0.59	98.02±0.28
293.15	55.33±0.45	95.82±0.27
298.15	46.95±0.37	96.06±0.27
303.30	45.31±0.36	100.28±0.28
310.80	38.27±0.28	98.16±0.28
320.55	31.80±0.24	95.31±0.30
332.95	25.78±0.19	94.81±0.31

Table S4: ^{17}O NMR line widths of the bulk water signal in the presence of 1.94 mM **1** in 0.1 M NaClO$_4$ at pH 6.0.

T (K)	Reference width (Hz)	Sample width (Hz)
284.05	95.43±1.01	109.83±0.28
287.02	86.68±0.92	103.02±0.36
293.15	75.19±0.74	99.08±0.29
298.15	64.14±0.64	97.31±0.29
303.30	57.13±0.52	101.42±0.27
310.80	47.36±0.41	100.2±0.29
320.55	39.65±0.33	99.15±0.28
332.95	32.31±0.28	100.16±0.32

Exchange rates were determined using the formalism developed by Swift and Connick.[5] Briefly, Swift and Connick described the complex relationship between the line-width of the bulk water ^{17}O NMR signal in the presence of paramagnetic aquo-complexes, and the ratio of bound to free water (P_m), the rate of exchange (k_m), the transverse relaxation rate of the oxygen in the bound water (T_{2m}), and the difference in resonance frequency between the oxygen in the bulk water and the bound ligand $\Delta\omega_m$ (eq. S12).[5, 6] Crucially, they recognised that in temperature regions where the relaxation is rapid and controlled by the change in precessional frequency ($\Delta\omega_m \gg \frac{1}{T_{2m}}$) or where T_{2m} relaxation is fast and $\frac{1}{T_{2p}}$ is dominated by exchange ($\frac{1}{T_{2m}} \gg \Delta\omega_m$), then equation S12 is reduced to $\frac{1}{T_{2p}} \approx P_m k_m$ (see eq. S13, with k_m dependent on temperature according to the Eyring-Polanyi equation).[7] However, it is common to attempt to fit the full temperature region, but this requires that a number of other variables are known, such as the paramagnetic shift ω_m, the scalar coupling constant $\frac{A}{h}$, and the electronic longitudinal relaxation, T_{1e}, which in turn are temperature dependent and relying on other factors. For most compounds these variables aren't known, and their values are determined by curve fitting which then becomes an additional potential source of error. Because all rate data in a Swift-Connick type experiment are derived, the results must thus be treated critically.

$$\frac{1}{T_{2p}} \quad \approx \quad P_m k_m \tag{S13}$$

In the current case, for species with long T_{1e}, such as manganese(II), $\Delta\omega_m$ is very small, and eq. S15 can be derived,[5] where $B = \frac{2^2\pi^2}{3}S(S+1)$ and S=5/2.[6] In cases where there's a substantial shift in the bulk signal position with temperature this can be used to determine $\frac{A}{h}$ independently of T_{1e}, and T_{1e} can be

7

Table S5: ^{17}O NMR line widths of the bulk water signal in the presence of 0.50 mM $[Mn(OH_2)_6]^{2+}$ in 0.1 M NaClO$_4$ at pH 3.2.

T (K)	Reference width (Hz)	Sample width (Hz)
276.70	89.86±1.22	183.42±0.75
280.40	71.35±1.01	182.85±0.97
284.20	66.11±0.86	205.77±1.00
289.80	58.31±0.75	233.52±1.24
293.15	51.78±0.61	260.94±1.50
300.15	43.23±0.47	307.74±2.00
310.45	35.48±0.39	351.25±2.53
322.30	29.07±0.30	379.88±3.01
336.10	24.21±0.24	349.86±2.83

Table S6: ^{17}O NMR line widths of the bulk water signal in the presence of 0.50 mM $[Mn(OH_2)_6]^{2+}$ in 0.1 M NaClO$_4$ at pH 4.0.

T (K)	Reference width (Hz)	Sample width (Hz)
276.70	88.81±1.23	180.72±0.76
280.40	73.10±1.03	181.90±1.03
284.20	66.96±0.83	205.17±1.04
289.80	57.10±0.70	227.72±1.30
293.15	51.74±0.59	259.51±1.52
300.15	43.70±0.50	296.34±2.03
310.45	35.82±0.37	369.71±2.46
322.30	28.73±0.28	374.89±2.98
336.10	24.21±0.28	332.50±2.78

determined either via fitting or by noting that the largest value for $\frac{1}{T_{2p}}$ is dependent only on $\frac{A}{\hbar}$ and T_{1e}.[8] That is, however, not the case for **1**, where the is no observable bulk water signal shift with temperature.

$$\frac{1}{T_{2p}} \quad = \quad \frac{P_m}{\frac{1}{k_m} + T_{2m}} \tag{S14}$$

$$= \quad \frac{P_m}{\frac{1}{k_m} + \frac{1}{B\left(\frac{A}{\hbar}\right)^2}\left(\frac{1}{T_{1e}} + k_m\right)} \tag{S15}$$

Note that for very long T_{1e} ($T_{1e} > 10^{-6}$), $\frac{1}{B(\frac{A}{\hbar})^2 T1e} \approx 0$, decoupling the equation from T_{1e}, which adds complications in fitting using this model as the sensitivity to T_{1e} varies with the value.

For $Mn(H_2O)_6^{2+}$ we used T_{1e} $1.25 \cdot 10^{-8}$s, as reported by Ducommun et al.[9] However, for **1** T_{1e} is not known, and so it was attempted to determine it through fitting by varying T_{1e} and optimising $\Delta H^{\ddagger}$, $\Delta S^{\ddagger}$ and $\frac{A}{\hbar}$ (see figures S4-S7). Only for pH 4.0 was a minimum for the RMS value found, at T_{1e} $5.25 \cdot 10^{-8}$s.

8

Table S7: ^{17}O NMR line widths of the bulk water signal in the presence of 0.50 mM $[Mn(OH_2)_6]^{2+}$ in 0.1 M $NaClO_4$ at pH 5.0.

T (K)	Reference width (Hz)	Sample width (Hz)
276.70	86.91±1.17	186.70±0.70
280.40	71.76±1.14	190.92±0.96
284.20	68.17±0.87	209.00±1.02
289.80	60.65±0.74	234.12±1.25
293.15	52.25±0.61	266.67±1.54
300.15	44.78±0.49	304.89±1.89
310.45	36.84±0.39	363.54±2.41
322.30	29.16±0.29	374.53±2.93
336.10	24.19±0.23	352.31±2.59

Table S8: ^{17}O NMR line widths of the bulk water signal in the presence of 0.50 mM $[Mn(OH_2)_6]^{2+}$ in 0.1 M $NaClO_4$ at pH 6.0.

T (K)	Reference width (Hz)	Sample width (Hz)
276.70	97.82±1.44	213.08±0.57
280.40	80.88±1.16	215.38±0.72
284.20	74.14±0.95	213.24±0.77
289.80	64.05±0.84	250.46±0.85
293.15	59.85±0.72	285.25±1.23
300.15	48.80±0.57	315.31±1.38
310.45	40.32±0.45	368.25±1.74
322.30	32.67±0.34	380.64±2.08
336.10	26.73±0.28	352.22±1.78

3.3 Calculation of rate using difference in line-width with and without paramagnetic ion

$$\pi(\Delta\nu_{obs.} - \Delta\nu_{solvent}) = \frac{P_m}{\frac{1}{k_m} + \frac{1}{B\left(\frac{A}{h}\right)^2}\left(\frac{1}{T_{1e}} + k_m\right)} \Leftrightarrow \tag{S16}$$

$$\frac{P_m}{\pi(\Delta\nu_{obs.} - \Delta\nu_{solvent})} = \frac{1}{k_m} + \frac{1}{B\left(\frac{A}{h}\right)^2}\left(\frac{1}{T_{1e}} + k_m\right)$$

$$km = -\frac{\left(\sqrt{(T_{1e}^2(\frac{A}{h})^4 B^2 X^2 - 2T_{1e}(\frac{A}{h})^2 BX - 4T_{1e}^2(\frac{A}{h})^2 B + 1)} - T_{1e}(\frac{A}{h})^2 BX + 1\right)}{2T_{1e}} \tag{S17}$$

where X $= \frac{P_m}{\pi(\Delta\nu_{obs.} - \Delta\nu_{solvent})}$

9

3.4 Error propagation

The rates are affected by variability in two parameters: $\frac{A}{h}$ and $\Delta\nu$ (or X). Assuming that they are uncorrelated, the uncertainity in rates is given by:

$$\delta km = \sqrt{\left(\frac{\partial km}{\partial(\frac{A}{h})}\right)^2 \cdot \left(\delta(\frac{A}{h})\right)^2 + \left(\frac{\partial km}{\partial X}\right)^2 \cdot (\delta X)^2} \tag{S18}$$

where, δ represents uncertainities. After taking partial derivatives,

$$\frac{\partial km}{\partial(\frac{A}{h})} = \frac{T_{1e}(\frac{A}{h})^3 B^2 X^2 - 2T_{1e}(\frac{A}{h})B - (\frac{A}{h})BX}{\sqrt{(T_{1e}^2(\frac{A}{h})^4 B^2 X^2 - 2T_{1e}(\frac{A}{h})^2 BX - 4T_{1e}^2(\frac{A}{h})^2 B + 1)}} - \frac{B(\frac{A}{h})X}{2} \tag{S19}$$

$$\frac{\partial km}{\partial X} = \frac{T_{1e}(\frac{A}{h})^4 B^2 X - (\frac{A}{h})^2 B}{2\sqrt{(T_{1e}^2(\frac{A}{h})^4 B^2 X^2 - 2T_{1e}(\frac{A}{h})^2 BX - 4T_{1e}^2(\frac{A}{h})^2 B + 1)}} - \frac{(\frac{A}{h})^2 B}{2} \tag{S20}$$
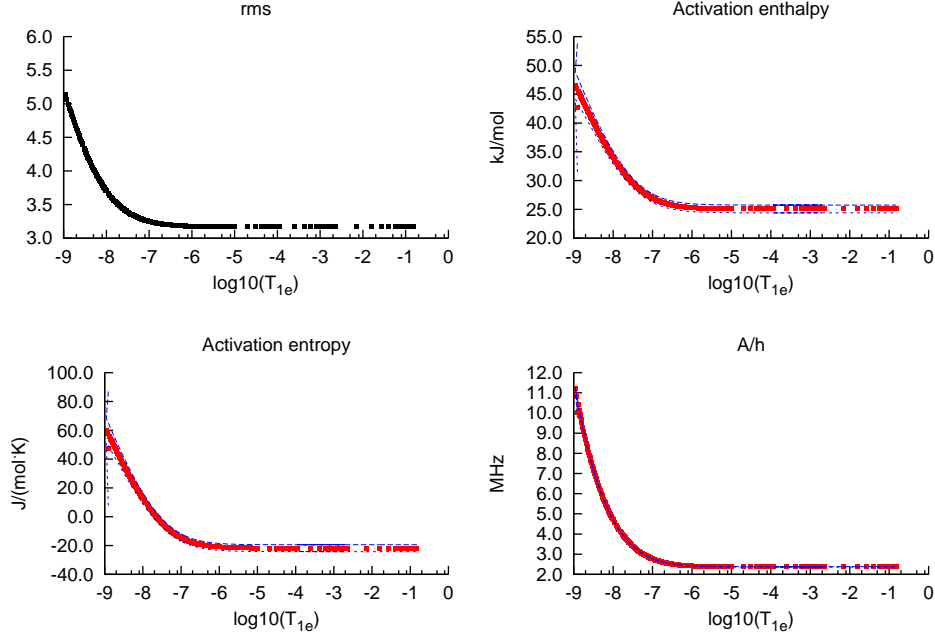
Figure S4: Fitting variables for the data of **1** at pH 3.2. Top left: Root of mean square of residual of $\frac{1}{T_{2p}}$ as a function of T_{1e}. Top right: $\Delta H^{\ddagger}$ as a function of T_{1e}. Bottom left: $\Delta S^{\ddagger}$ as a function of T_{1e}. Bottom right: $\frac{A}{h}$ as a function of T_{1e}. The dotted blue lines indicate the $\pm$ error for each variable.

10
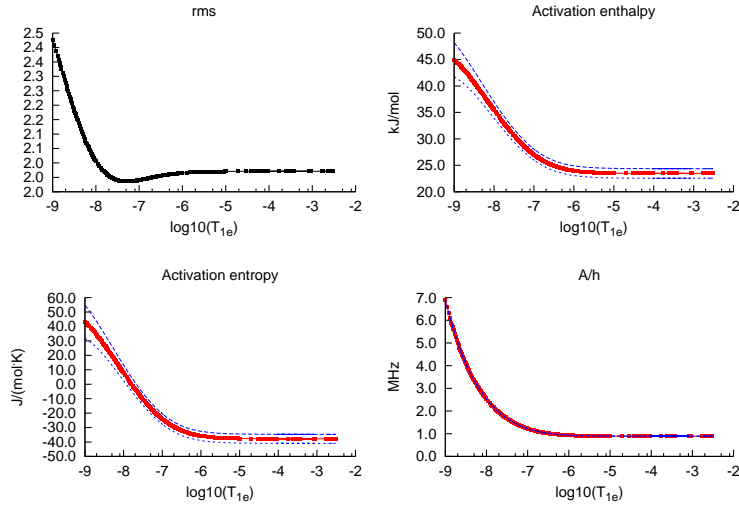
Figure S5: Fitting variables for the data of **1** at pH 4.0. Top left: Root of mean square of residual of $\frac{1}{T_{2p}}$ as a function of T_{1e}. The minimum is at T_{1e} $5.25 \cdot 10^{-8}$ s. Top right: $\Delta H^{\ddagger}$ as a function of T_{1e}. Bottom left: $\Delta S^{\ddagger}$ as a function of T_{1e}. Bottom right: $\frac{A}{h}$ as a function of T_{1e}. The dotted blue lines indicate the $\pm$ error for each variable.
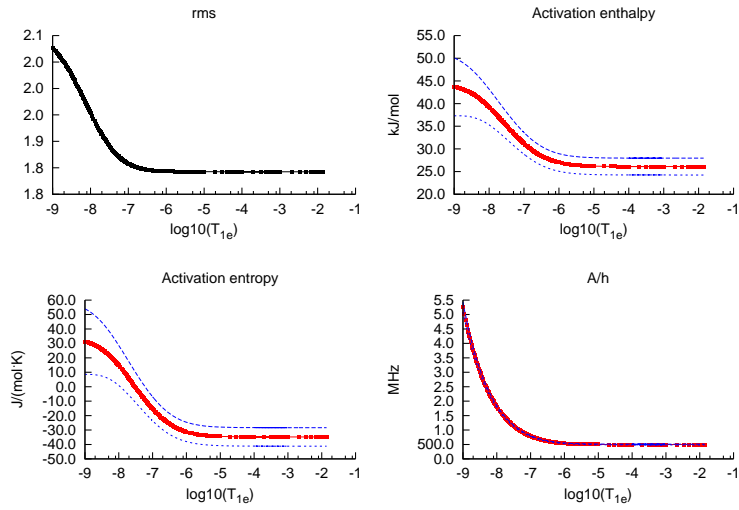
Figure S6: Fitting variables for the data of **1** at pH 5.0. Top left: Root of mean square of residual of $\frac{1}{T_{2p}}$ as a function of T_{1e}. Top right: $\Delta H^{\ddagger}$ as a function of T_{1e}. Bottom left: $\Delta S^{\ddagger}$ as a function of T_{1e}. Bottom right: $\frac{A}{h}$ as a function of T_{1e}. The dotted blue lines indicate the $\pm$ error for each variable.

11
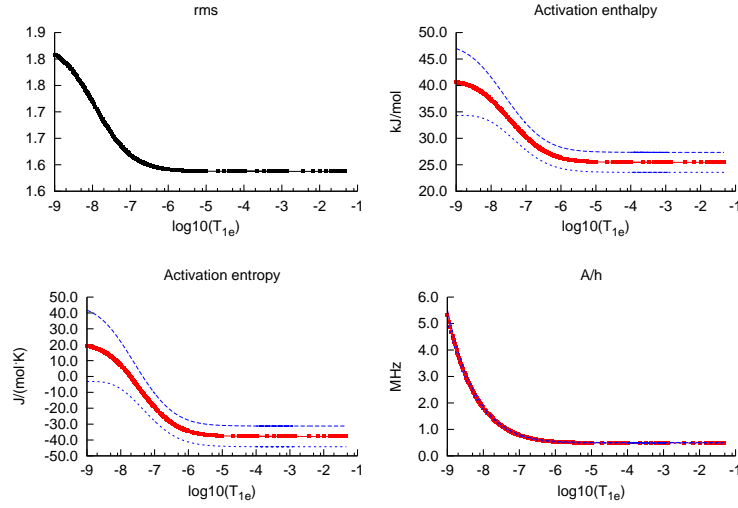
Figure S7: Fitting variables for the data of **1** at pH 6.0. Top left: Root of mean square of residual of $\frac{1}{T_{2p}}$ as a function of T_{1e}. Top right: $\Delta H^{\ddagger}$ as a function of T_{1e}. Bottom left: $\Delta S^{\ddagger}$ as a function of T_{1e}. Bottom right: $\frac{A}{h}$ as a function of T_{1e}. The dotted blue lines indicate the $\pm$ error for each variable.
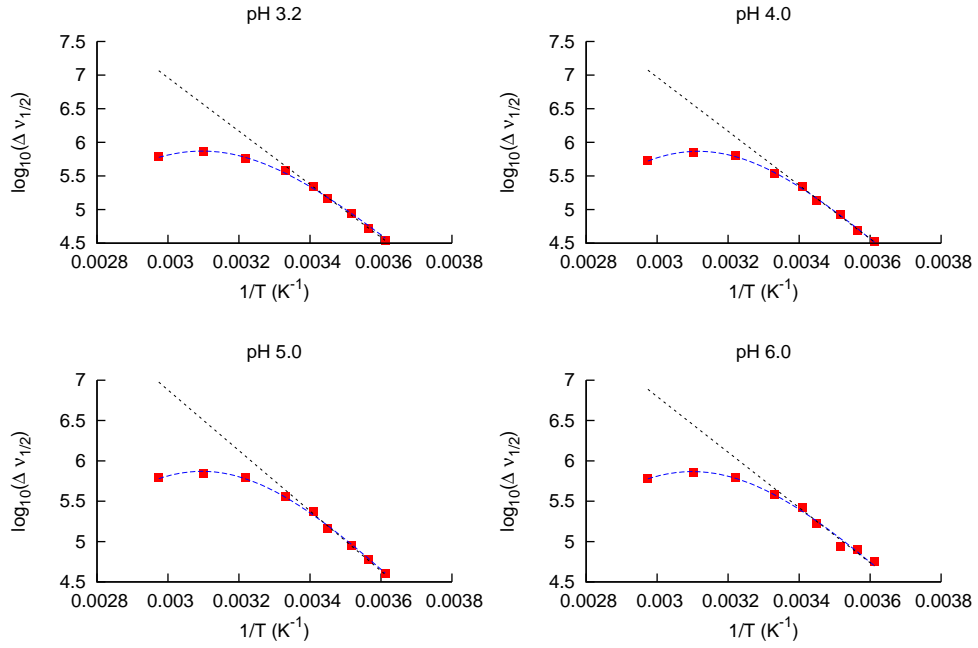
Figure S8: VT NMR data for $[\mathrm{Mn(H_2O)_6}]^{2+}$ at different pH. Blue dotted line shows best fit using eq. S15. Black dotted line shows best fit using equation S13. Top left: pH 3.2. Top right: pH 4.0. Bottom left: pH 5.0. Bottom right: pH 6.0.

12
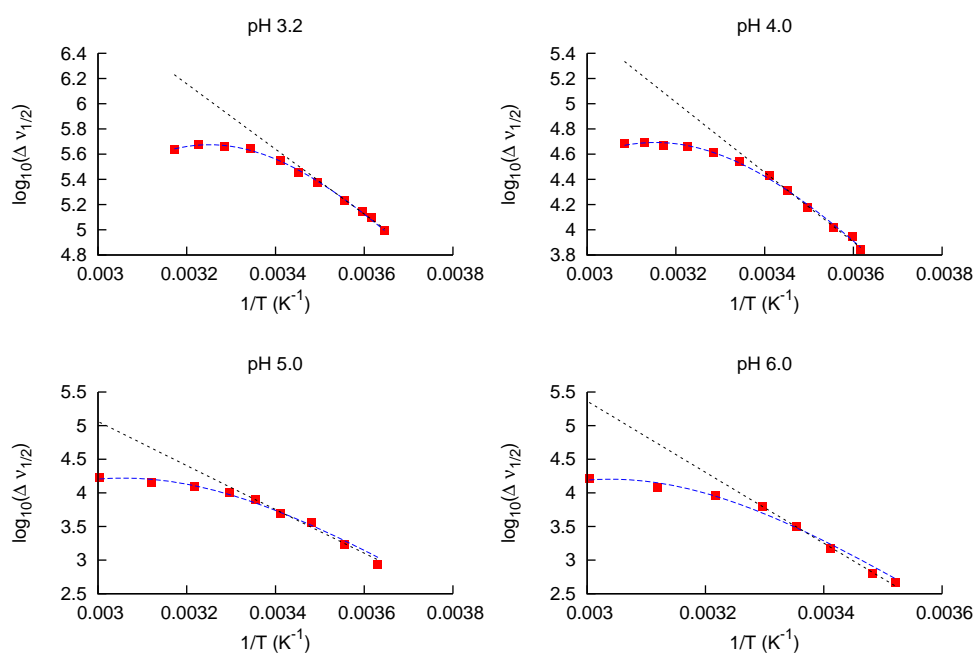
Figure S9: VT NMR data for **1** at different pH. Blue dotted line shows best fit using eq. S15. Black dotted line shows best fit using equation S13. Top left: pH 3.2. Top right: pH 4.0. Bottom left: pH 5.0. Bottom right: pH 6.0.

13

References

[1] R. Contant, *Inorg. Synth.* **1990**, *27*, 104–108.

[2] C. J. Gómez-García, J. J. Borrás-Almenar, E. Coronado, L. Ouahab, *Inorg. Chem.* **1994**, *33*, 4016–4022.

[3] L. Ruhmann, C. Costa-Coquelard, J. Canny, R. Thouvenot, *Eur. J. Inorg. Chem.* **2002**, *4*, 975–986.

[4] C. A. Ohlin, S. J. Harley, J. G. McAlpin, R. K. Hockin, B. Q. Mercado, R. L. Johnson, E. M. Villa, M. K. Fidler, M. M. Olmstead, L. Spiccia, R. D. Britt, W. H. Casey, *Chem. Eur. J.* **2011**, *17*, 4408–4417.

[5] T. J. Swift, R. E. Connick, *J. Chem. Phys.* **1962**, *37*, 307–320.

[6] T. J. Swift, R. E. Connick, *J. Chem. Phys.* **1964**, *41*, 2553.

[7] S. J. Harley, C. A. Ohlin, W. H. Casey, *Geochim. Cosmochim. Acta* **2011**, *75*, 3711–3725.

[8] M. S. Zetter, M. W. Grant, E. J. Wood, H. W. Dodgen, J. P. Hunt, *Inorg. Chem.* **1972**, *11*, 2701–2706.

[9] Y. Ducommun, K. E. Newman, A. E. Merbach, *Inorg. Chem.* **1980**, *19*, 3696–3703.

14

Chapter3:

Effect of substitution on oxygen isotope-exchange rates in isovalent and isostructural complexes, $[PVNb_{12}O_{42}]^{9-}$ and $[V_3Nb_{12}O_{42}]^{9-}$

Abstract

The oxygen-exchange process in nanometer-sized complexes such as polyoxometalates provides a molecular level insight into reactions occuring at other extended oxides such as minerals. We compare the rates of isotope-exchange between structural oxygens of two isostructural and also isovalent Keggin-type heteropolyanions, $[PV_2Nb_{12}O_{42}]^{9-}$ and $[V_3Nb_{12}O_{42}]^{9-}$ with water. The two ions have the same Keggin niobium framework with two vanadyl caps differing only by a single central atom (P^V or V^V). The size of the ion, $[PV_2Nb_{12}O_{42}]^{9-}$, was calculated using ^{31}P diffusion-ordered spectroscopy and pKa(s) for each ion was determined by potentiometric titrations. The rates of oxygen exchange were investigated by monitoring the decrease in the intensity of the ^{17}O NMR signal as the enriched ion equilibrates with the bulk aqueous solution. Oxygen-isotope exchange is sensitive to the metal bonded (V, P or Nb), type of bonding (η-O or μ_x-O) and pH. At any given pH, the oxygens bound to vanadium atoms exchange faster than the oxygens bound to phosphorus atoms followed by niobium atoms. Also, the terminal oxygens react more rapidly

than doubly bonded μ_2-oxygens with rates differing by a factor of 10^2-10^4, yet all the oxygen sites show a unanimous response to changes in the pH enviornment. Interestingly, the replacement of a single central atom, which leads to only subtle structural differences, can cause substantial changes in the pH stabilities of the anions and reactivities of all framework oxygens. We also show that protonation at one oxygen site can accelerate the overall oxygen-exchange process.

1   Introduction

The reactivities at different oxygen sites in polyoxometalates are key to understanding the dissolution processes of oxides such as minerals. The principal interaction between a mineral surface and water can be probed by looking at the oxygen-exchange between the mineral and the aqueous medium. Polyoxoniobates, the niobium based oxides, have allowed chemists to investigate isotope-exchange reactions in polyoxometalates as their rates can be measured on a time scale suited for measurements in the laboratory. The literature has already been discussed in detail in chapter 1 (Introduction). To summarise, there are two well known structures in the polyoxoniobate library: the Lindqvist ion (hexaniobate, $[\text{Nb}_6\text{O}_{19}]^{8-}$) and the decaniobate ion ($[\text{Nb}_{10}\text{O}_{28}]^{6-}$). Both have been studied in the past for isotope-exchange reactions.[1, 2] These nanometer-sized clusters with different types of oxygen sites displayed complex pH-dependent reaction dynamics. The Lindqvist ion (see fig. 1) is a highly symmetrical structure with three oxygen sites of which the central μ_6-oxygen is inert. The isotope-exchange processes for the terminal and μ_2-oxo sites proceed at similar rates

when the molecule is either completely protonated or deprotonated, however coordination with protons at the bridging oxo site enhances the rates of μ_2-O(H) much more than the terminal oxygen sites. In the case of decaniobate (see fig. 2), there are
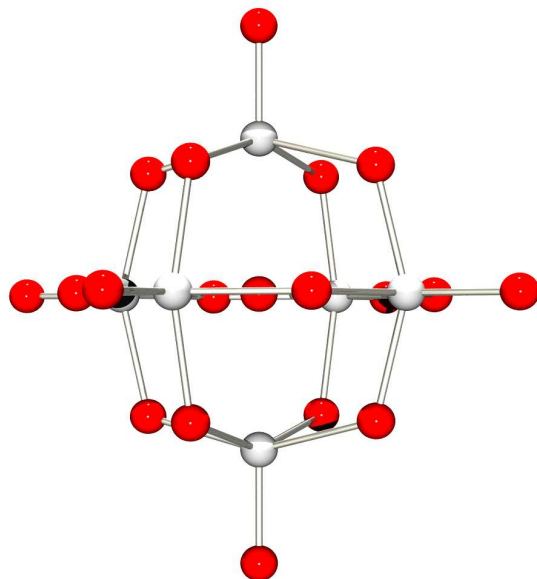
Figure 1: Structure of a Lindqvist ion, $[\text{Nb}_6\text{O}_{19}]^{8-}$.

28 oxygen atoms which display seven distinct sites and the isotope-exchange process at all the oxygen sites respond to pH in the same way. One of the bridging μ_2-oxo sites exchanges faster than the terminal oxo sites and is faster than other μ_2-oxo sites by a factor of 10^4. There is a slow dissociation of the molecule to form hexaniobate and possibly a tetramer above pH 8.5 which is evident from the arrival of a new signal in the ^{17}O NMR spectrum.[2, 3]

The study was taken further by including derivatives of the decaniobate ion where one or two central atoms are replaced by Ti(IV) yielding mono- or di-titanodecaniobate ions. These three decametalate structures are isostructural but not isovalent. Substi-
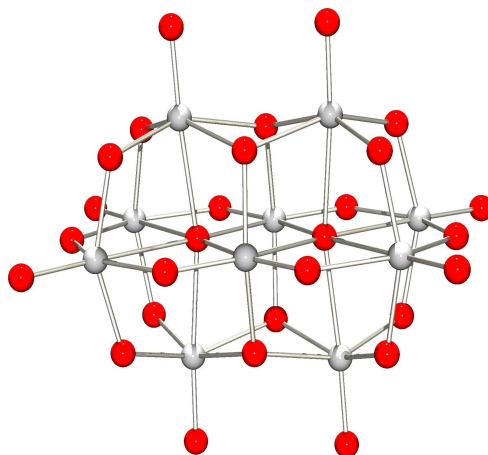
Figure 2: Structure of a decaniobate ion, $[Nb_{10}O_{28}]^{6-}$.

tution had a huge impact on the reactivities of all the oxygens such that the rates of exchange decrease with increasing pH in $[Ti_2Nb_8O_{28}]^{8-}$ where there is rapid exchange at low pH enviornment and the complex is much more stable than its parent ion at high pH. While, the mono-substituted ion, $[TiNb_9O_{28}]^{7-}$, shows a different trend in reactivity where the rates increased at both high and low end of the pH scale. Notably, substitution not only affects the oxygens close to the substituted atom but also other oxygens which lie far from the substitution.[4] These studies show that the rates of isotope-exchange are prone to subtle changes in the molecule like substitution and protonation. Moreover, the overall charge on the molecule plays an important role in determining the pH-dependent pattern of oxygen-exchange reactions.

Another series of popular anions in polyoxometalate library are the Keggin ions which find extensive applications in the fields of catalysis. They have the general

formula $[XM_{12}O_{42}]^{q-}$ where M = Mo(VI), W(VI) or Nb(V) and X is a heteroatom.[5] While there is a plethora of polyoxomolybdates and polyoxotungstates, the oxygen-exchange is particularly studied in polyoxoniobates as the oxygens bound to the niobium atoms are slow enough to exchange within a time scale of few minutes to few months. They provide a convenient way of monitoring of the ^{17}O NMR signals and therefore, measurements of rates of exchange. To date, the isotope-exchange studies have not been devoted to even pure keggin anions. We here investigate oxygen-isotope exchange reactions in two isostructural and isovalent Keggin-type polyoxoniobates, $[PV_2Nb_{12}O_{42}]^{9-}$ (complex **1**) and $[V_3Nb_{12}O_{42}]^{9-}$ (complex **2**), which only differ by a single central atom (see fig. 3).
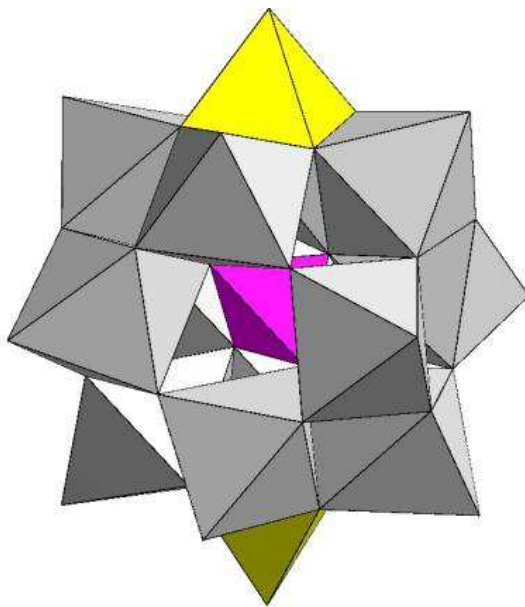
Figure 3: Structure of a $[PV_2Nb_{12}O_{42}]^{9-}$ ion. The niobium atoms are shown in grey, vanadium in yellow and phosphorus in purple. In the vanadium analogue, $[V_3Nb_{12}O_{42}]^{9-}$, the central atom is vanadium.

The complexes under study have a niobium framework analogous to Keggin ions with two vanadyl groups attached on top and bottom. The complex $[PV_2Nb_{12}O_{42}]^{9-}$ has a tetrahedral phosphate as a central moeity while $[V_3Nb_{12}O_{42}]^{9-}$ has the central site occupied by a vanadium atom. Interestingly, it has been seen that the two complexes show a large variation in their pH stabilities. The vanadium analogue has a pH stable region of pH 6.5 - pH 9, while phosphorus as a central atom stabilises the structure with a wider stability region of pH 5 - pH 10.[6, 7] We extend this work and examine their pKa values by performing potentiometric titrations and compare the rates of isotope-exchange process between the structural oxygens and water.

2   Experimental

2.1   pH measurements

Biological buffers used for NMR measurements at 0.05 M concentration with a background salt of 0.1 M TMACl (tetramethylammonium chloride) are: MES (2-(N-morpholino)ethanesulfonic acid) at pH 5.55 and pH 6.05; PIPES (piperazine-N,N'-bis(2-ethanesulfonic acid)) at pH 6.55 and pH 7.05; HEPES (4-(2-hydroxyethyl)-1-peprazineethanesulfonic acid) at pH 7.56, pH 8.05 and pH 8.3; CHES (N-Cyclohexyl-3-aminopropanesulfonic acid) at pH 8.9; CAPS (N-cyclohexyl-3-aminopropanesulfonic acid) at pH 9.9. The pH of the solutions were adjusted by 1 M TMAOH solution which already contained 0.1 M TMACl.

2.2 Potentiometric titrations

The titrations were carried out on a Metrohm GP Titrino auto-titrator. 5 ml of each complex at a concentration of 4 mM was titrated back and forth by a standardised acid (HCl) and a base (NaOH). The excess charge (z) was calculated at each addition of an acid or a base to determine the stability and the pKa(s) of the complexes. The concentration of acid and base used for titration was 0.099 M and 0.103 M, respectively. All the solutions contained 0.1 M TMACl as a background salt. The solutions were always deaerated thoroughly by bubbling nitrogen for at least 20 minutes and kept under nitrogen atmosphere throughout the experiment. The solution was also stirred continuously during the experiment for homogeneity in the sample. The gnuplot script used to generate the z-plot can be seen in listing L2 in Appendix.

2.3 Computational details

The structures were optimised using Gaussian 09 rev. D.01 with implicit solvation using polarizable continuum model (PCM).[8, 9] The exchange-coorelation functional used was PBE0. The basis sets employed were cc-pvtz for oxygen and phosphorus atoms while lanl2dz(K-) was used for niobium and vanadium atoms. For NMR calculations, PBE0/def2-tzvp method was used. The x, y, z coordinates of the structures are summarised in table 1 and table 2 in Appendix.

2.4   NMR spectroscopy

All the NMR spectra reported were recorded in solution-phase on a Bruker DRX 400 MHz (9.4 T, ^{31}P 161.976 MHz; ^{51}V 105.246 MHz; ^{17}O 54.243 MHz) equipped with a 5 mm broadband probe with a pulse width of 11.25 μs ($\pi/2$). The temperature on the instrument was measured by two different ways. First, the copper-constantan theromocouple (Type T) was inserted into the sample tube and the apparatus was slowly placed inside the spectrometer. The tube was allowed to sit in the instrumemt for at least 5 minutes and then the temperature was checked. The temperature on the instrument was calibrated until the temperature on the thermocouple showed 35±0.1°C.

The ^{31}P and ^{51}V spectra were calibrated against external references of 85 % H_3PO_4 in D_2O (set at 0 ppm) and NH_4VO_3 in D_2O for ^{51}V (set as -580 ppm). The ^{51}V spectra were collected at 298 K with a recycle delay of 0.2 s. For each sample 1000 acqusitions were obtained. ^{31}P spectra were obtained using a recycle delay of 2 s acquiring 100 scans per sample.

All the isotope-exchange solution-state ^{17}O NMR experiments were done on a series of samples at different pH and a temperature of 308 K. All the measurements were taken using a pulse width of 11.25 μs ($\pi/2$) and a recycle delay of 0.01 s. 2500-10000 acquisitions were obtained per sample to achieve good signal-to-noise ratios. The sample is prepared by dissolving 5 mM of enriched complex in a 0.5 ml buffered normal ^{16}O water with 0.1 M TMACl as background salt in an eppendorf. Each sample is then immediately transferred to a NMR tube with a $TbCl_3$ insert and placed on the spectrometer for acquisition. The lock and shim is done on a reference

prior to running the sample. The reference is a buffered D_2O solution with 0.1 M TMACl background salt and a $TbCl_3$ insert. All the buffers used for preparing the sample already contain 0.1 M TMACl as a background salt. The ^{17}O NMR peaks are reported relative to the bulk water signal at 0 ppm.

As the enriched complex with all the oxygen sites tagged with ^{17}O isotope is dissolved in an isotopically normal buffered solution, all the oxygen sites in the molecule begin to exchange with the bulk solution at a given rate. The decrease in the intensity of each signal was monitored with time to calculate isotope-exchange rates. A series of such experiments were done by changing the pH covering the entire pH stability range of these complexes. ^{51}V and ^{31}P spectra were taken at every step to ensure that the complex is intact.

^{31}P DOSY NMR data was acquired on a non-spinning sample at a temperature of 298 K using the *stebpgp1s* pulse program. Gradient strength differs from 0.963 G cm^{-1} to 36.31 G cm^{-1} with 16 gradient steps. 80 scans per gradient strength were acquired to ensure good signal-to-noise ratio. The gnuplot script to generate the DOSY plot is listed in listing L1 in Appendix.

3   Results

3.1 ^{31}P DOSY NMR

Diffusion-ordered spectroscopy was used as a tool to determine the size of the complex, $[PV_2Nb_{12}O_{42}]^{9-}$. Table 1 summarises the parameters used to set up the experiment and table 2 tabulates the intensities of the ^{31}P NMR signal as a function of

gradient strength. The data is fitted using the gnuplot script (Appendix 1)[10] to give a diffusion coefficient of $2.67 \cdot 10^{-10}$ m^{2}s^{-1} (as shown in figure 4). Considering the molecule to be spherical, the radius of the ion was calculated using Stokes-Einstein equation:

$$D \;=\; \frac{k_B T}{6 \pi \eta r} \tag{1}$$

where D is the diffusion coefficient of the molecule, η is the viscosity of the water ($8.9 \cdot 10^4$ Pa s), k_B is the Boltzmann's constant, T is the temperature and r is the solvodynamic radius of the molecule. The radius of the molecule calculated from the diffusion experiment is 9.183 ± 0.1Å, which is larger but comparable to the computed radius of the complex. The computed cavity volume and the radius of the complex is 907.776 Å^3 and 6.008 Å, respectively. The difference in the experimentally estimated radius might be because of the presence of the counterions and solvation shell.

Table 1: Parameters used to set up the ^{31}P DOSY experiment in complex **1**

Parameter	Description	Value
gpz6	Gradient strength	2 % - 95%
p30	Gradient length ($\delta/2$)	2500 μs
d20	Diffusion time (Δ)	0.1 s
d21	Longitudinal eddy current delay	0.02 s
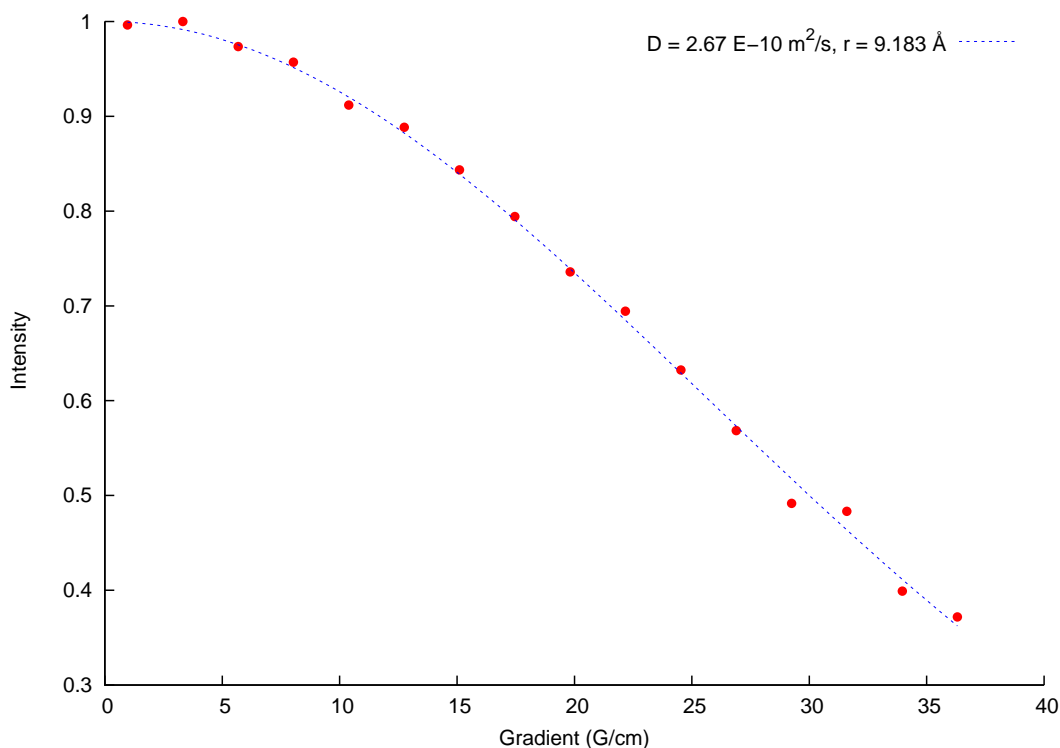
Figure 4: Change in intensity of the ^{31}P signal in complex **1** as a function of gradient strength. The dotted line shows the fit to give the diffusion coefficient and the radius of the molecule.

3.2   Potentiometric titration

The pH stability of both the complexes has already been established by UV-Vis spectroscopy and ^{51}V spectroscopy by Jungho *et al.*[6, 7] The complex **1** is stable between pH 5 - 10, while the vanadium analogue is less stable with the stability region between pH 6.5 - pH 9. We performed the potentiometric titrations to confirm the pH stability and to determine the pKa(s) of the two complexes. The excess charge, z, was determined at each addition of an acid and a base. The equation for calculation

Table 2: Relative intensity of the ^{31}P signal as a function of gradient strength.

No.	Gradient (G/cm)	Relative Intensity
1	0.963	0.996
2	3.320	1.000
3	5.677	0.974
4	8.033	0.957
5	10.39	0.912
6	12.75	0.888
7	15.10	0.844
8	17.46	0.794
9	19.82	0.736
10	22.17	0.694
11	24.53	0.632
12	26.89	0.568
13	29.25	0.492
14	31.60	0.483
15	33.96	0.399
16	36.31	0.372

of z is given as:

$$z = -\frac{([H^+] + [TMA^+] - [Cl^-] - [OH^-])}{[POM_{Tot}]} \tag{2}$$

Both the complexes show a similar trend in the titration. Figure 5 shows the plot of excess charge (z) as a function of pH for complex **1**. The data shows a two step protonation event with two fitted pka(s): $pKa_1 = 9.12\pm0.02$ and $pKa_2 = 5.79\pm0.03$. As the pH increases from pH 8 to pH 10, the complex gets deprotonated by 1.5 protons and there is a perfect overlap between the z values. There is an uptake of one more proton in increasing the acidity from pH 7 to pH 5 (see fig. 5). The less stable complex, **2**, protonates once between its stable region (pH 6.5 - pH 9)

with a fitted pKa of 8.15±0.04 (refer fig. 6). We observe some disparity in z values between pH 6 to pH 8 in complex **1** and for complex **2**, the z values show much larger divergence between the addition of an acid and a base. However, we do not see any changes in the ^{51}V and ^{31}P NMR spectra in their pH stability region.
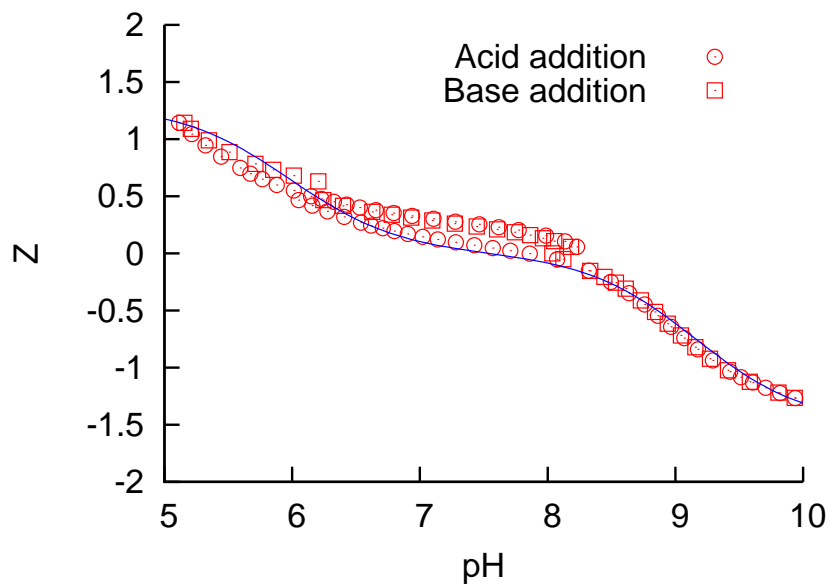
Figure 5: The excess charge, z, on complex **1** plotted as a function of pH. The blue line indicates two fitted pKas of 9.12±0.02 and 5.79±0.03.
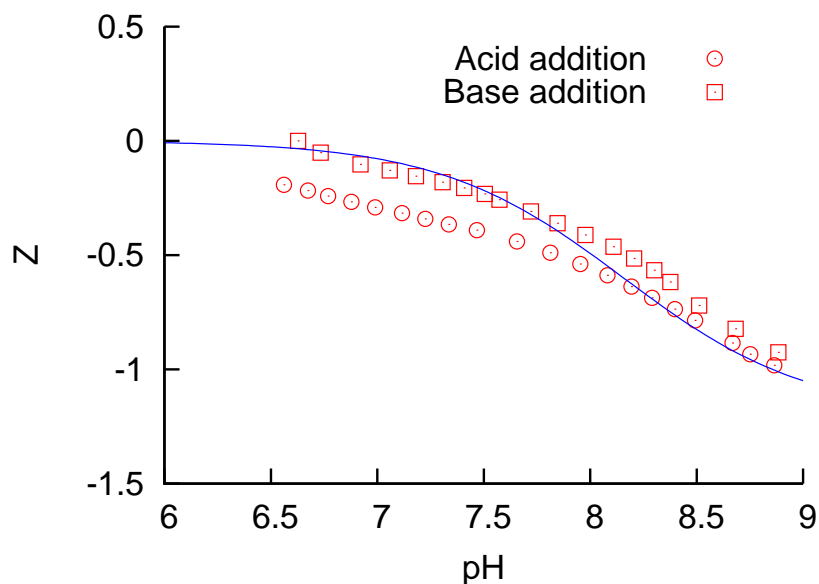
Figure 6: Excess charge, z, on complex **2** as a function of pH. The blue line indicates a fitted pKa of 8.15±0.04.

3.3 ^{17}O NMR spectroscopy

The two anions have 42 oxygen atoms with eight distinct oxygen sites, four of which are central μ_4-oxygens bound to phosphorus (or vanadium) and three niobium atoms (site P or V), two types of 8 μ_3-oxygens bound to two niobium atoms and one vanadium atom (site A and B), two types of 16 μ_2-oxygens which are bound to two niobium atoms (site C and D), twelve terminal oxygens bound to niobium atoms (site E) and two terminal oxygens bound to the capping vanadium atoms (site F) (see figure 7).
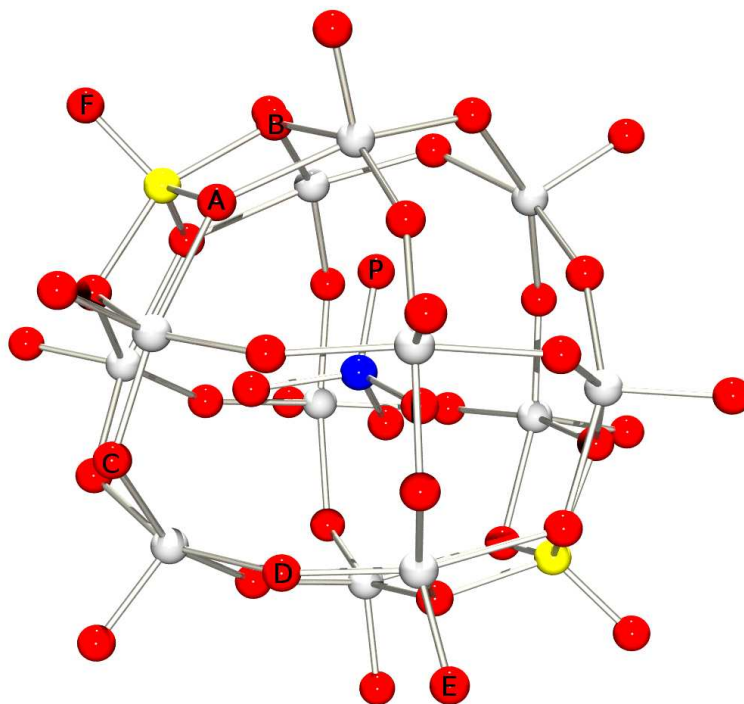
Figure 7: Structure of a $[PV_2Nb_{12}O_{42}]^{9-}$ ion labelled with different oxygen sites. The vanadium atoms are shown in yellow, phosphorus in blue, niobium in grey and red circles show oxygen atoms. In isostructural complex, $[V_3Nb_{12}O_{42}]^{9-}$, the central phosphorus atom is replaced with a vanadium atom.

A pure Keggin ion is a symmetrical ion which displays four chemical shifts corresponding to a central μ_4-O site, two bridging μ_2-O sites and a terminal oxo site.[11] In the complexes under study, the capping vanadium atoms are an addition to the highly symmetrical Keggin structure which distorts the symmetry of the ion. The dissolution of the ^{17}O enriched complex **1** shows six distinct signals in the integrated ratio of 3:2:2:1:1:1 (left-to-right) which is in accordance with the stiochiometry (see figure 8), while the vanadium analogue displays only five signals. The chemical shift for the two terminal oxygens bound to two capping vanadium atoms was not seen in

both these complexes. In the vanadium analogue, the chemical shift for the oxygens
bound to the central vanadium atom was also not observed. These oxygens equili-
brate with the bulk solution rapidly that the NMR signal could not be observed, and
therefore their rates could not be determined. The observed signals were assigned
on the basis of computed NMR shifts. The clusters were optimised at PBE0/cc-pvtz
(H-Ar), lanl2dz (K-) level and the NMR chemical shift were calculated using PBE0
with def2-tzvp basis set.[12] Table 3 summarises the observed and the computed
NMR chemical shifts for all the peaks in both the complexes. The two isostruc-
tural anions share the same stiochiometry and the assignment of the signals, yet the
chemical shifts are different in the two ranging from 4-15 ppm. Theoretically, the
twelve terminal oxygens show two different computed shifts at 693.4 ppm and 701.8
ppm while experimentally one chemical shift was observed at 667.2 ppm in complex
1. The complex **2** also shows one signal at 679.5 ppm, however according to the
integrated area, the shift corresponds to eight oxygen atoms. This means that the
other four oxygens in complex **2** exchanged with the solution before the spectrum
was acquired. The two μ_3 signals, in both, were broad which may be because of the
asymmetry associated with these atoms as vanadium is a quadrupolar nucleus. The
signals were acquired with more scans for clear identification (see fig. 9).
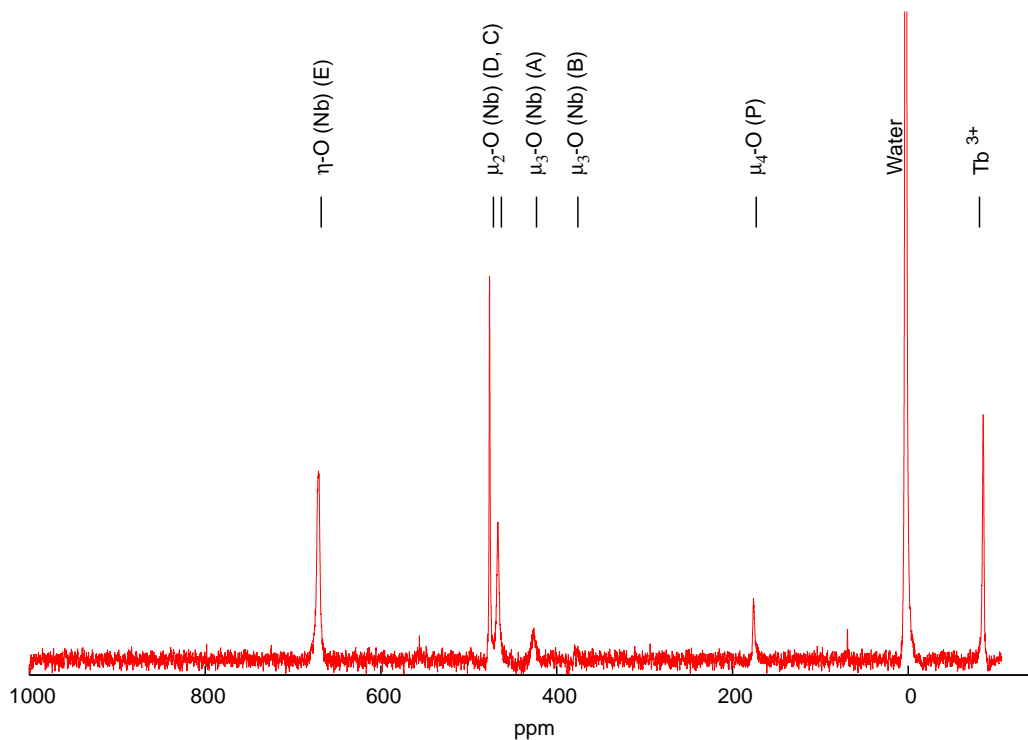
Figure 8: Distinct ^{17}O NMR signals seen in complex $[PV_2Nb_{12}O_{42}]^{9-}$ (**1**) at pH 9.9. The signals are assigned on the basis of theoretical estimation. The ratio of the signals was 3:2:2:1:1:1 (left-to-right). The signal for two terminal vanadium oxygen was not observed. The μ_3-O signals were too broad to be clearly seen in 5000 scans.

101
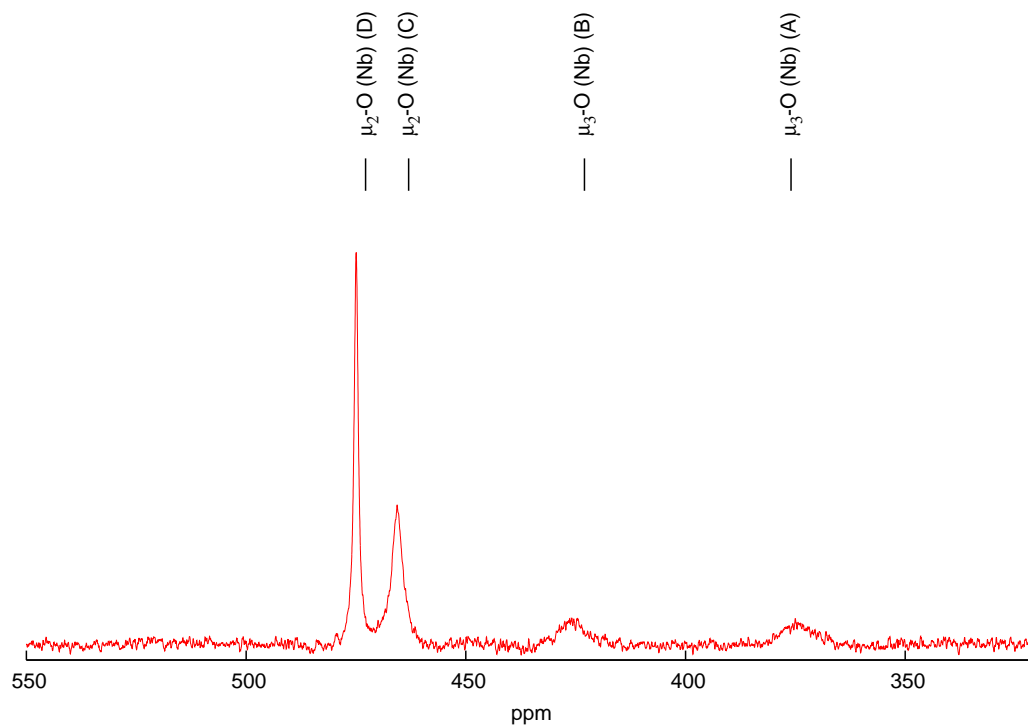
Figure 9: Four bridging oxygen sites in complex **1** at pH 9.9. The broad signals corresponding to μ_3-O where each oxygen is bonded to two niobium atoms and one vanadium atom are clearly shown in this figure.

Table 3: Computed and Observed ^{17}O NMR shifts of complexes **1** and **2**. The details of computations are given in the experimental section.

Oxygen atom	[PV$_2$Nb$_{12}$O$_{42}$]$^{9-}$ (**1**)		[V$_3$Nb$_{12}$O$_{42}$]$^{9-}$ (**2**)	
	Computed	**Observed (ppm)**	**Computed**	**Observed (ppm)**
P	100.7841	174.9	-	-
A	365.5372	372.3	389	368.4
B	409.7709	423.2	436	438.4
C	446.6743	463.3	460	472.9
D	474.5405	472.6	488	478.8
E (4 oxygens)	693.4687	667.2	682	
(8 oxygens)	701.8104	667.2	694	679.5
F	979.6028	not observed	975	not observed
V (central)	-	-	572	not observed

The intensity of all the ^{17}O NMR signals decrease exponentionally with time and the integrated areas of each peak were fit using equation 1 as a function of time to yield rates of isotope-exchange.

$$I \;=\; I_0 e^{-k \cdot t} \tag{3}$$

where I_0 is the initial intensity at time 0 and t is the time in seconds. The rate constant, k, is given in s^{-1}.

The value of rate constant vary for different oxygen sites at a given pH and varies considerably for each oxygen site at different pH. At any pH, the order of reactivity is F (η-O (V)) > P (μ_4-O (P)) > E (η-O (Nb)) > D (μ_2-O (Nb)) $\geqslant$ C (μ_2-O (Nb)) > A,B (μ_3-O (Nb)). The fastest oxygens (site F) were too fast to be seen in the ^{17}O NMR spectrum, and the slowest oxygens (site A and B) were not investigated because of the extreme broadness of the signals and prolonged exchange process.

Broadly, the isotope-exchange process for all the oxygen sites is slowest at the very basic end of the pH stability region (pH 10) and promoted by increasing proton concentration in the solution. For example, in complex **1**, the exchange of terminal oxygens bound to niobium (site E) is faster by a factor of 10^2 in moving from pH 9.9 to pH 7.04 (see fig. 10 and table 4). Figure 8 and 9 show the integrated areas of signals corresponding to site C and D as a function of time at different pH. We see a steady increase in the rates of isotope-exchange for all the sites near the first protonation event, between pH 8 and pH 10, where rates increase by an order of magnitude at sites E and D (refer fig. 10). Interestingly, site D which corresponds to eight oxygens display one chemical shift on the NMR spectrum but shows two different rates from pH 8.05 - pH 5.55 which differ by a factor of 10^2. For this reason, we split the exchange rates as D1 (red dots) and D2 (orange dots) as shown in fig. 10. The data is also fitted as a sum of the two rate equations (refer eq. 4):

$$I \quad = \quad I_{0(1)}e^{-k_1 \cdot t} + I_{0(2)}e^{-k_2 \cdot t} \tag{4}$$

Table 5 summarises the rates of isotope-exchange for the bridging oxygens in complex **1**. Increasing the acidity further from basic pH 8 to neutral pH 7, we do not see any change in the excess charge of the molecule yet the rates of exchange at site E and site D1 are accelerated substantially (see fig. 5 and fig. 10). Above pH 7, the oxygen exchange at site E is rapid enough for rates to be determined, while the rates for site D show a steady increase from pH 7.04 to pH 6.05 and then a sharp rise from pH 6.05 to pH 5.55 near the second pKa of 5.79. Site C shows steady increments in exchange rates in the entire pH region (pH 5 - pH 10).
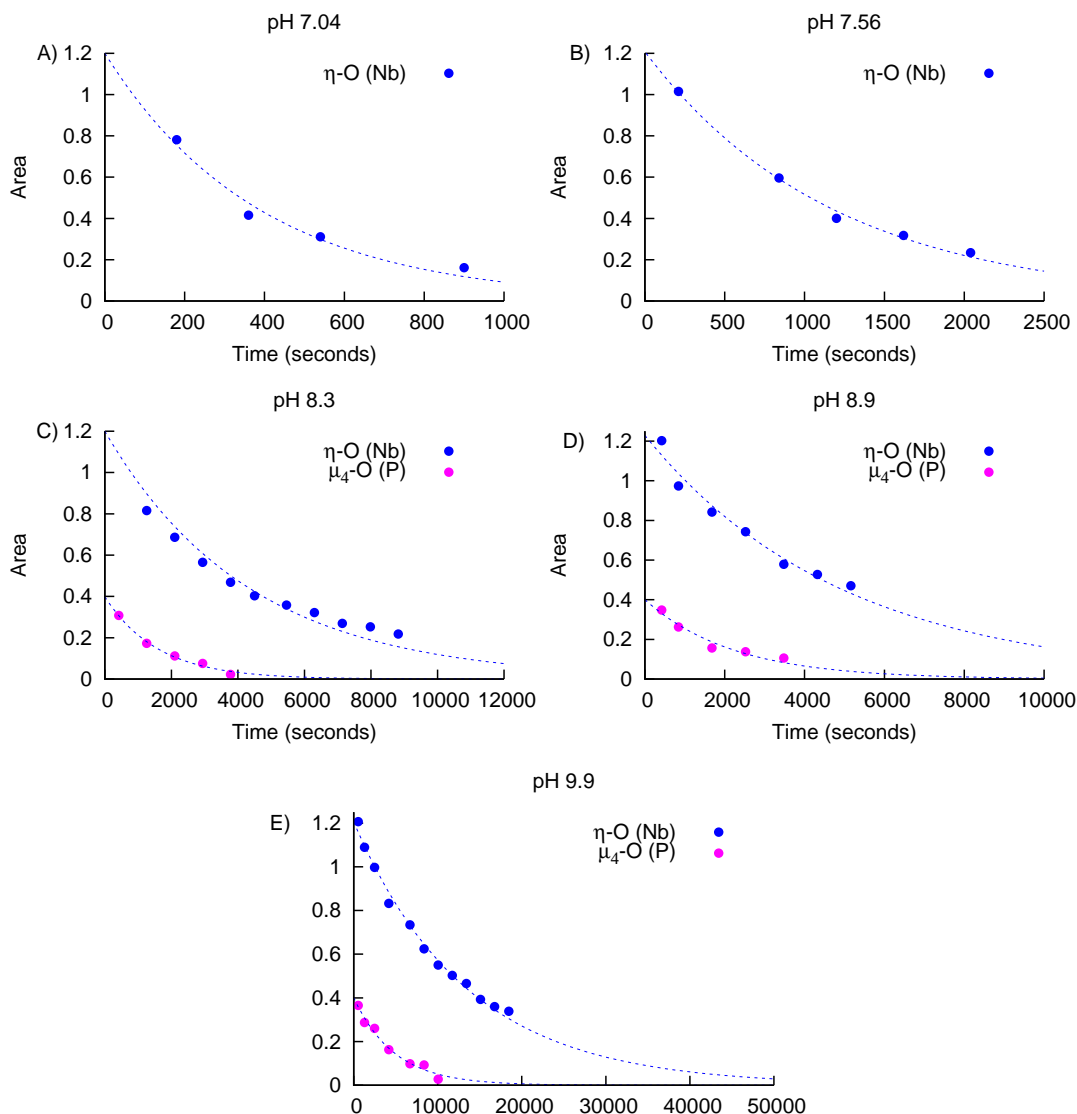
Figure 10: Change in the intensity (integrated area) of ^{17}O NMR peaks from pH 7.04 - 9.9 at 308 K for complex **1**. The blue and pink dots show the integrated areas for the peak at 667.2 ppm which corresponds to twelve η-O (Nb) and for the peak at 174.9 ppm which corresponds to four central oxygens bonded to phosphorus. The areas are normalised against an external reference ($TbCl_3$) to account for instrumental fluctuations. The areas are further normalised to yield a ratio of 1.2 and 0.4 for 12 Nb-O and 4 P-O, respectively, for ease of comparison. The exponential decrease in intensity as a function of time is fitted using first order rate law (shown as dotted blue lines) to give the rates of isotope-exchange.
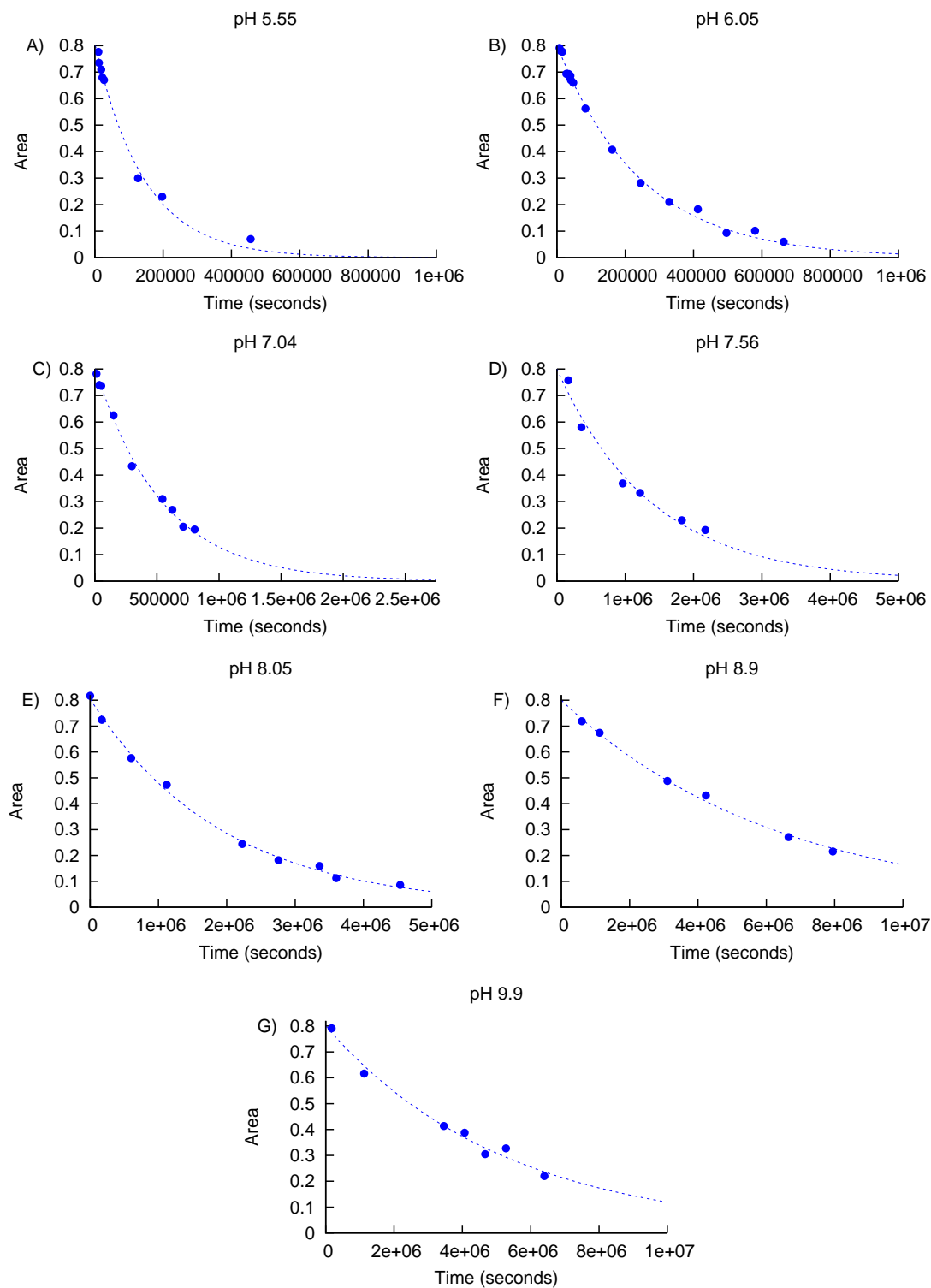
Figure 11: Change in the intensity (integrated area) of ^{17}O NMR peak at 463 ppm corresponding to μ_2-O (site C) from pH 5.55 - 9.9 at 308 K for complex **1**. The areas are normalised against an external reference ($TbCl_3$) and further normalised to yield a ratio of 0.8. The dotted line represents the fit to the rate law.
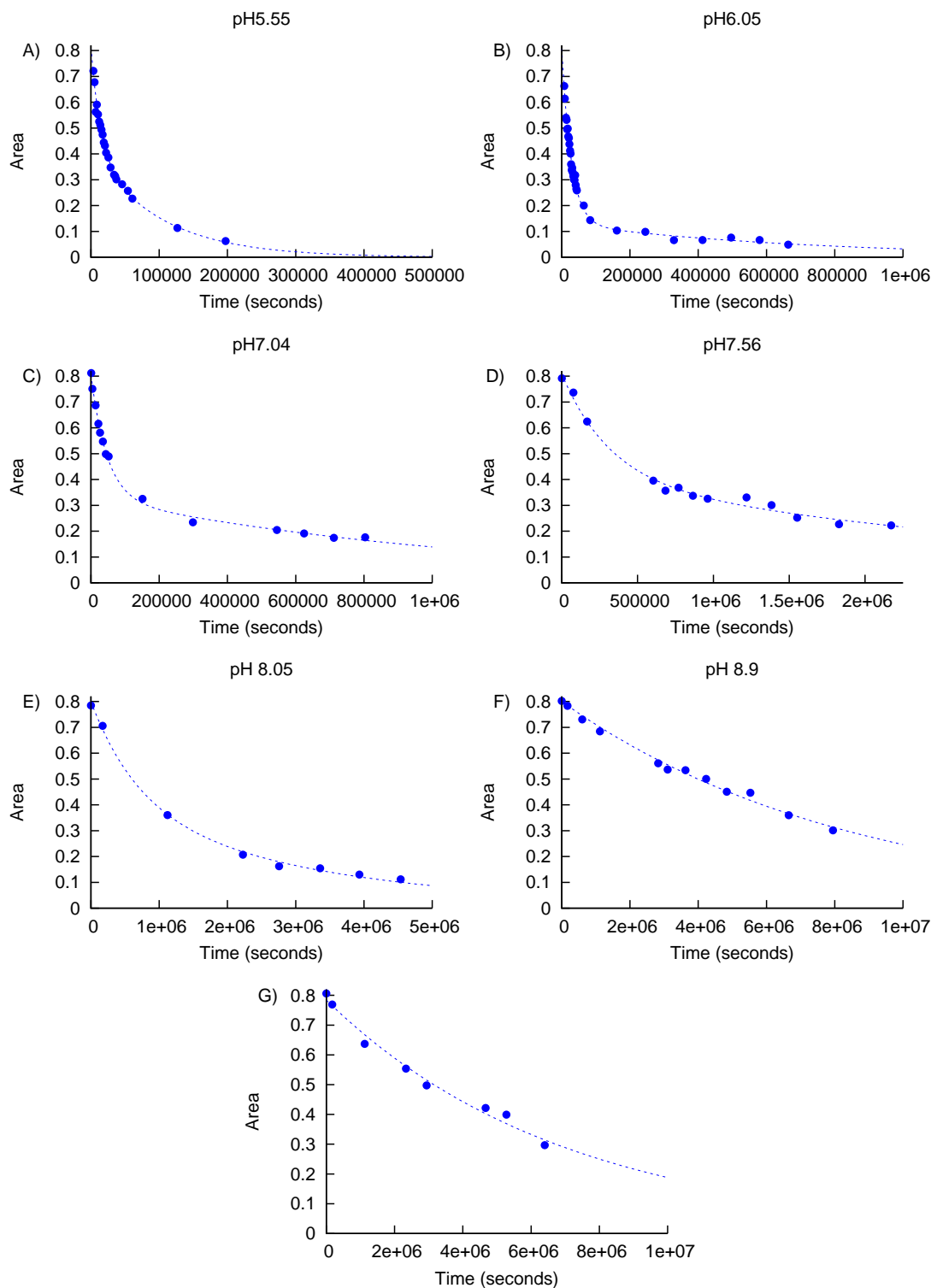
Figure 12: Change in the intensity (integrated area) of ^{17}O NMR peak at 472 ppm corresponding to μ_2-O (D) from pH 5.55 - 9.9 at 308 K for complex **1**. The areas are normalised against an external reference (TbCl$_3$) and further normalised to yield a ratio of 0.8. From pH 5.55 - 8.05, the oxygens represent one chemical shift yet two different rates and so the dotted line represents the sum of the fits (according to eq. 4) between this pH regime. For pH 8.94 and 9.95, the data is fitted using a single rate law.
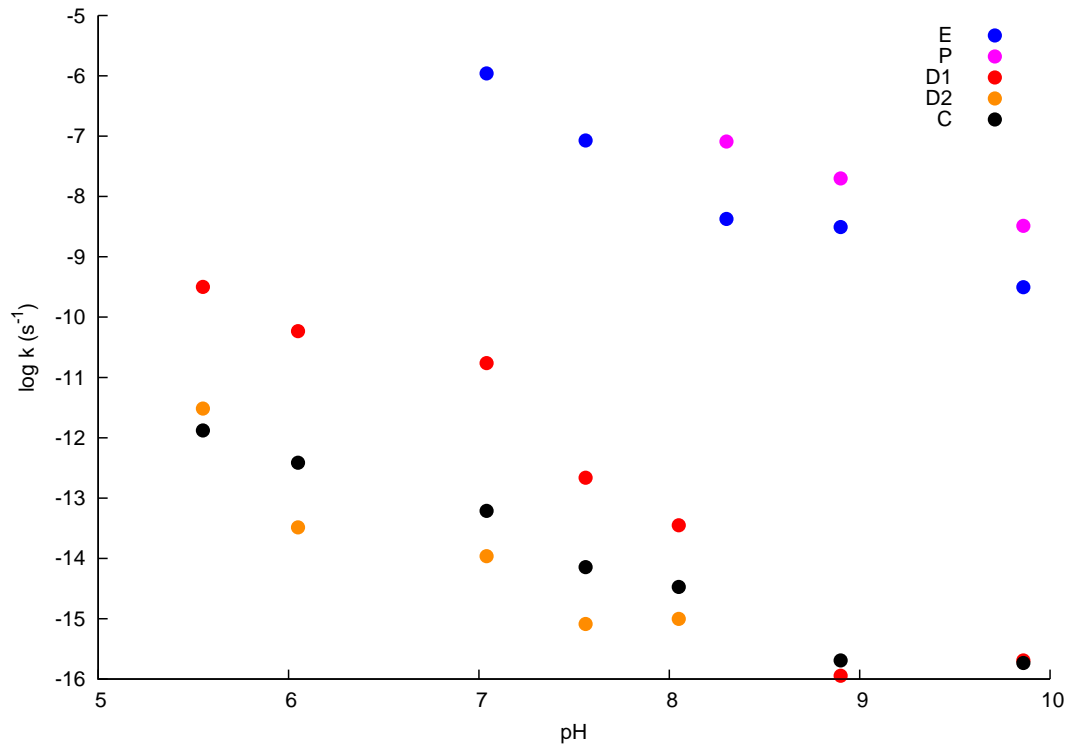
Figure 13: Rates of oxygen-isotope exchange for all the oxygens of complex **1** as a function of pH at 308 K.
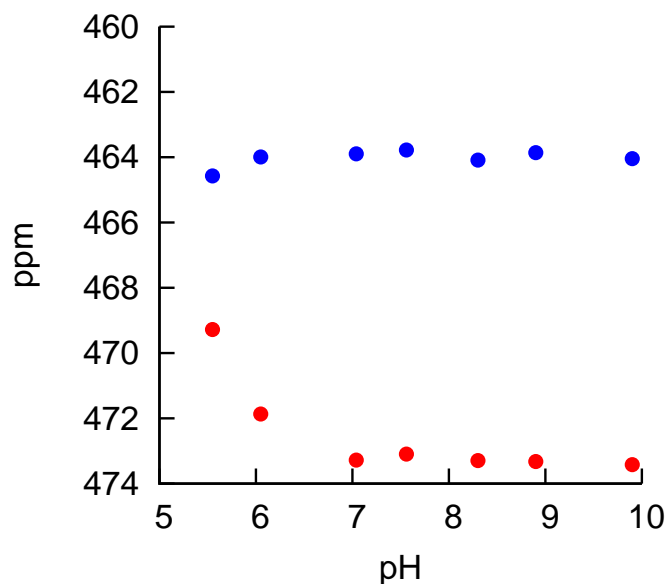
Figure 14: Change in ^{17}O NMR chemical shifts corresponding to the μ_2-oxygens in complex **1** as a function of pH.

Table 4: Rates of oxygen-isotope exchange for the terminal oxygens as a function of pH for complex **1** at 308 K.

pH	E (η-O)	P (μ_4-O)
7.0	$(2.58\pm0.4)\cdot10^{-3}$	-
7.5	$(8.94\pm0.37)\cdot10^{-4}$	-
8.3	$(2.31\pm0.10)\cdot10^{-4}$	$(6.18\pm0.53)\cdot10^{-4}$
8.9	$(2.02\pm0.17)\cdot10^{-4}$	$(4.52\pm0.69)\cdot10^{-4}$
9.9	$(7.45\pm0.24)\cdot10^{-5}$	$(2.06\pm0.19)\cdot10^{-4}$

Table 5: Rates of oxygen-isotope exchange for the bridging oxygens as a function of pH for complex **1** at 308 K.

pH	D1 (μ_2-O)	D2 (μ_2-O)	C (μ_2-O)
5.55	$(7.50\pm1.38)\cdot10^{-5}$	$(9.97\pm1.53)\cdot10^{-6}$	$(6.94\pm0.42)\cdot10^{-6}$
6.05	$(3.60\pm0.19)\cdot10^{-5}$	$(1.39\pm0.33)\cdot10^{-6}$	$(4.06\pm0.11)\cdot10^{-6}$
7.04	$(2.12\pm0.18)\cdot10^{-5}$	$(8.63\pm1.24)\cdot10^{-7}$	$(1.83\pm0.06)\cdot10^{-6}$
7.56	$(3.17\pm0.09)\cdot10^{-6}$	$(2.80\pm1.04)\cdot10^{-7}$	$(7.19\pm0.07)\cdot10^{-7}$
8.05	$(1.44\pm0.06)\cdot10^{-6}$	$(3.05\pm1.1)\cdot10^{-7}$	$(5.18\pm0.15)\cdot10^{-7}$
8.9	$(1.19\pm0.04)\cdot10^{-7}$	-	$(1.53\pm0.08)\cdot10^{-7}$
9.9	$(1.43\pm0.08)\cdot10^{-7}$	-	$(1.90\pm0.1)\cdot10^{-7}$
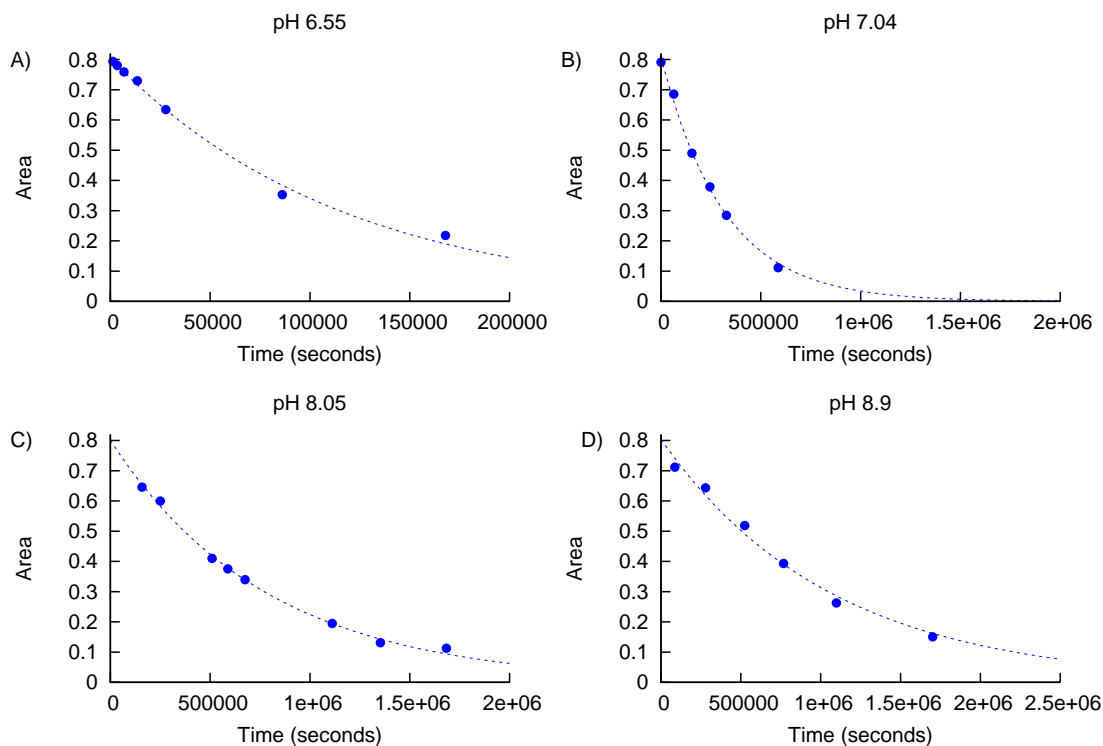
Figure 15: Rates of oxygen-isotope exchange of oxygens corresponding to site D in complex **2** as a function of pH at 308 K.

Figure 15 shows the decrease in the intensity of the ^{17}O NMR signal corresponding to oxygen site D in complex **2**. The bridging oxygens at site D show a steady increase in rates as a function of pH (see fig. 16 and table 6). The rate data was fitted to give a pKa of 6.98±0.05. However, we will consider the pKa obtained from z-plot (pKa = 8.15±0.04) to be more accurate because the data for rates of exchange is incomplete towards low pH for full fit to yield an accurate pKa. The bridging oxygens of the same type (μ_2-O) at site C are comparatively much slower to exchange and did not show any decline in the ^{17}O NMR signal in one month. The exchange was not monitored due to lack of time. The terminal oxygens at site E exchange faster than oxygen atoms at site D by a factor of 10^2. At pH 7, the rate of exchange at site E is $7.6 \cdot 10^{-4}$ s^{-1} while rates could not be measured at pH 6.55 because of the fast exchange at low pH.
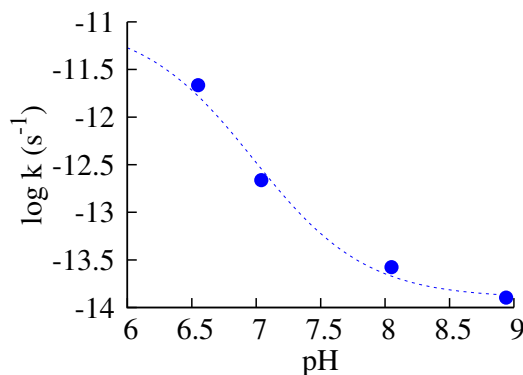
Figure 16: Rates of oxygen-isotope exchange of oxygens corresponding to site D in complex **2** as a function of pH at 308 K. The blue dotted line shows a fitted pKa of 6.98±0.05.

Table 6: Rates of oxygen-isotope exchange for all the oxygens as a function of pH for complex **2** at 308 K.

pH	D (μ_2-O)
6.55	$(8.59\pm0.4)\cdot10^{-6}$
7.04	$(3.17\pm0.13)\cdot10^{-6}$
8.05	$(1.27\pm0.04)\cdot10^{-6}$
8.9	$(9.22\pm0.87)\cdot10^{-7}$

4   Discussion

Understanding the fundamental reactivity of oxides is incomplete without the detailed knowledge of their distinct fragments. The reactivities at each individual site can not be deciphered by bulk studies alone. Therefore, the microscopic investigations of these discrete clusters are important to provide geochemists a comprehensive view of minerals. We studied two nanosized clusters as a whole by potentiometric titrations which gives an outline of their behaviour towards changes in pH enviornment. We also probed the reactivity of each individual site by ^{17}O NMR spectrocopic measurements of isotope-exchange rates. The total effect observed for a structure is a culmination of the interactive and cooperative behaviour at each site. The study shows that all the oxygen sites react in the same way to changes in the outside enviornment such as pH. The sites may be entirely different, from being bonded to different types or number of metals to being more or less exposed to the solution, but they all respond to a situation unanimously. The oxygens bound to vanadium (capping or central) exchange relatively rapidly at all pH values while the exchange for bridging μ_4-oxygens bound to phosphorus could be monitored above pH > 8.3. This confirms the general concept that isotope-exchange of niobates is slow enough

to be measurable even for the most rapid oxygens. Moreover, the increase in the proton concentration in the solution enhances the lability of all the oxygens.

The substitution of a single atom can have substantial effect on the reactivity of the entire molecule as well as the reactivities at each oxygen site.[4] Casey *et. al.* have discussed the dramatic effect of single-atom substitution on isotope-exchange rates in a recent review.[13] In the complexes studied above, the two sites of the same type (μ_2-O) are structurally analogous and display close chemical shifts which are *ca.* 10 ppm apart. Yet, the rates of isotope-exchange at these sites differ by an order of magnitude in complex **1** (see figure 17) and much higher in complex **2**. In complex **2**, the site D exchanges completely while the site C remains fully tagged (see fig. 18). The chemical shifts and the labilities for two-coordinated oxygens at two sites differ considerably despite very similar bond Nb-O distances. We propose the factor contributing to the drift in chemical shift and the marked difference in the rates to be the bond angle (Nb-O-Nb). The bi-dentate oxygens at site D become more bent (Nb-O-Nb angle of 126.480°) than oxygens at site C with a bond angle of 151.163° in complex **1**, and it seems probable that the shift for site D arises from the decrease in the Nb-O-Nb angle. It has already been seen, in complexes like $[V_{10}O_{28}]^{6-}$ and $[PV_{14}O_{42}]^{9-}$, that the ^{17}O NMR shifts shift downfield when M-O-M becomes bent.[14]

Another isostructural bi-capped Keggin structure, $[PV_{14}O_{42}]^{9-}$, is stable in a very narrow pH range between pH 1.3 - pH 6. The pH-dependencies of [51]V NMR chemical shifts reveal the protonation sites to be the uncapped bridging μ_2- oxygens.[15, 16] Polyoxometalates are prone to get protonated at bridging oxo sites, which is generally

the trend evident in clusters like hexaniobate and decaniobate ions. Although, the precise site of protonation in the Keggin-type ions studied here is unclear, however the slight change in chemical shift at site D (see figure 11) together with the marked increase in rates of exchange indicate the protonation site to be the bridging oxygens at site D. Such responses to pH enviornment has been seen earlier in isostructural decametalate structures where all oxygens display similar pH-dependencies and similar oxygen sites display large differences in exchange rates. These isostructural complexes had different overall charge which also governed their pH-dependent pattern, while our study shows that even the isovalent substituted complexes exhibit large differences in their response to pH.
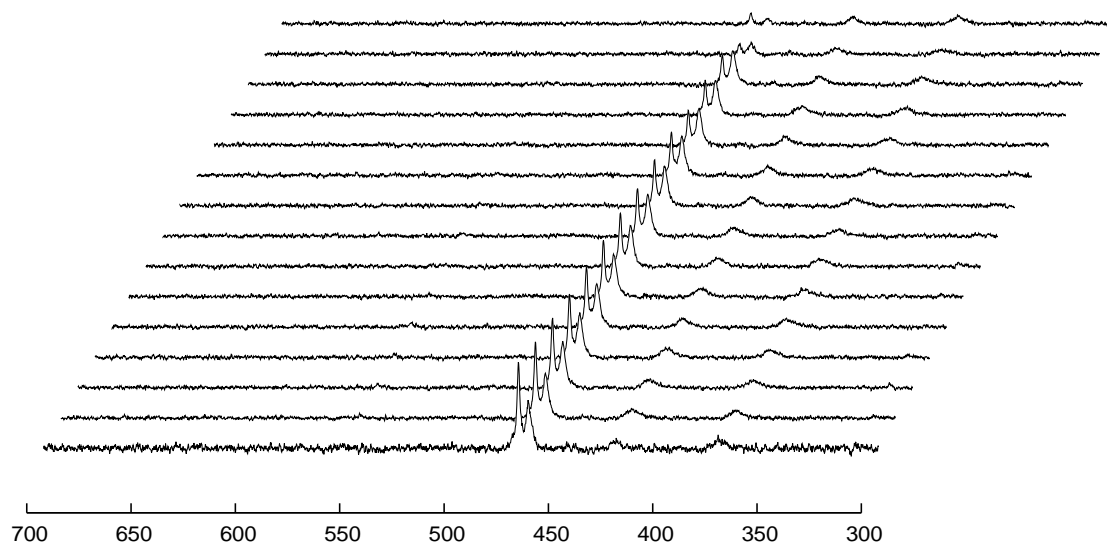
Figure 17: The decrease in the intensity of the peaks corresponding to μ_2-O (Nb) signals in the complex **1**. Both the signals corresponding to site C and site D decrease at a similar rate with time.
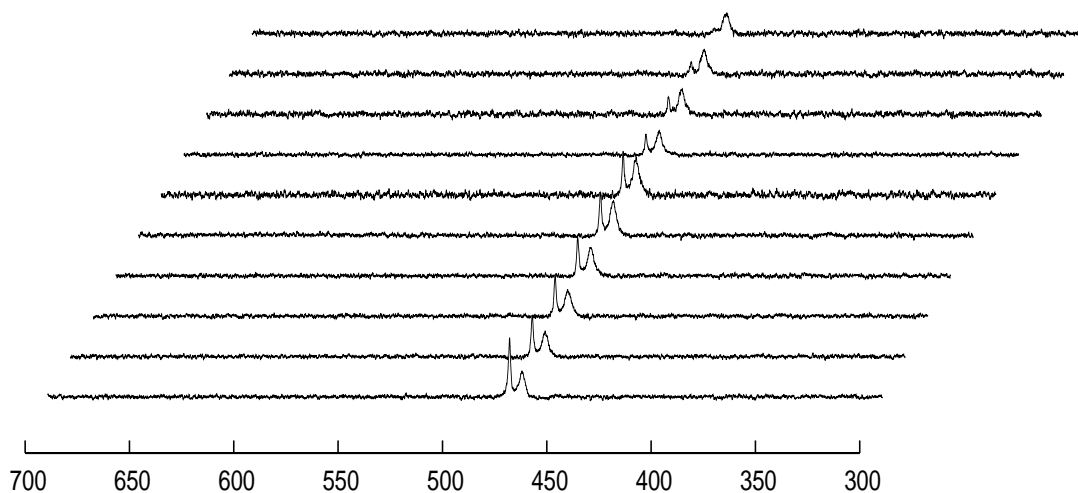
Figure 18: The decrease in the intensity of the peaks corresponding to μ_2-O (Nb) signals in complex **2**. The signal corresponding to site D decreases much rapidly than signal corresponding to site C.

5   Conclusions

We investigated the effect of substitution on reactivity of the molecule as a whole and the reactivities of individual oxygen sites in two Keggin-type polyoxoniobates. The isostructural complexes with the same overall charge differing only by a single-atom, show considerable variation in their response to changes in pH enviornment. The vanadium oxo sites are more labile than phosphorus oxo sites followed by niobium. Within the niobium oxo sites, η-O are more rapid compared with the bridging μ_2-oxo sites. Protonation enhances the rates for all oxygen sites in the molecule with the sites E and D being affected the most. The excess charge and the isotope-exchange rates follow a very similar trend as a function of pH indicating that each individual site acts

in an interactive and cooperative manner. Likewise, the dynamics of mineral oxides at solid-solvent interface often involves nanosized sites, the reactivities of which need to be investigated at microscopic level for a complete grasp of mineral dissolution reactions.

References

[1] J. R. Black, M. Nyman, W. H. Casey, *J. Am. Chem. Soc.* **2006**, *128*, 14712–14720.

[2] E. M. Villa, C. A. Ohlin, E. Balogh, T. M. Anderson, M. D. Nyman, W. H. Casey, *Angew. Chem. Int. Ed.* **2008**, *47*, 4844 – 4846.

[3] E. M. Villa, C. A. Ohlin, E. Balogh, T. M. Anderson, M. D. Nyman, W. H. Casey, *Am. J. Sci.* **2008**, *308*, 942 – 953.

[4] E. M. Villa, C. A. Ohlin, J. R. Rustad, W. H. Casey, *J. Am. Chem. Soc.* **2009**, *131*, 16488 – 16492.

[5] M. A. Fedotov, R. I. Maksimovskaya, *J. Struc. Chem.* **2006**, *47*, 952–978.

[6] J. Son, C. A. Ohlin, R. L. Johnson, Y. Ping, W. H. Casey, *Chem. Eur. J.* **2013**, *19*, 15191–5197.

[7] J. Son, C. A. Ohlin, E. C. Larson, Y. Ping, W. H. Casey, *Eur. J. Inorg. Chem.* **2013**, 1748–1753.

[8] M. J. Frisch, G. W. Trucks, H. B. Schlegel, *Gaussian 09 Revision D.01* **2009**, 7384–7402.

[9] J. Tomasi, B. Mennucci, R. Cammi, *Chem. Rev.* **2005**, *105*, 2999–3093.

[10] T. Williams, C. Kelly, *gnuplot*, `http://sourceforge.net/projects/gnuplot/`.

[11] M. Filowitz, R. K. C. Ho, W. G. Klemperer, W. Shum, *Inorg. Chem.* **1979**, *18*, 93–103.

[12] R. Sharma, J. Zhang, C. A. Ohlin, *Phys. Chem. Chem. Phys.* **2016**, *18*, 8235–8241.

[13] W. H. Casey, J. R. Rustad, *New J. Chem.* **2016**, *40*, 898–905.

[14] A. T. Harrison, O. W. Howarth, *J. Chem. Soc. Dalton Trans.* **1985**, 1953–1957.

[15] A. Selling, I. Andersson, L. Pettersson, C. M. Schramm, S. L. Downey, J. H. Grate, *Inorg. Chem.* **1994**, *33*, 3141–3150.

[16] R. Kato, A. Kobayashi, Y. Sasaki, *Iorg. Chem.* **1982**, *21*, 240–246.

Chapter 4

Predicting ^{17}O NMR chemical shifts of polyoxometalates using density functional theory

This chapter addresses the prediction of ^{17}O NMR chemical shifts of a wide range of polyoxometalates using methods based on density functional theory. The main objective of predicting the chemical shifts is to assign the experimentally observed signals. Since, oxygen can be terminal (η=O) or bridging (μ_x-O where x can be 1-6), each type of oxygen atom shows up as a distinct signal with intensity of each signal corresponding to the number of oxygen atoms. It is straightforward if all the sites are observed in the ^{17}O NMR spectrum or the degree of isotopic enrichment of all the sites are equal so that assignment can be confirmed by integration. However, in cases where all the oxygen sites are not observed which could be due to incomplete enrichment of some oxygen sites or fast exchange of some oxygen atoms with the solvent, the assignment of the signals is challenging. For a computational method to be useful, it needs to predict the correct ordering of the observable signals and the correct distance between them. The absolute chemical shift can then be predicted using linear regression. An added issue when computing the shifts is that it is often impossible to know the absolute protonation state of the molecule in solution.

Density functional theory is an appealing computational tool to predict the NMR chemical shifts in these metal complexes with high accuracy. In this work, different exchange-correlation functionals, basis sets and variation in amount of Hartree-Fock exchange were explored for geometry optimisations and NMR calculation to select the best method for predicting structures and chemical shifts.

For accurate NMR predictions, there is a need to optimise the POM geometries. The optimisations are important, firstly, because the crystal structure can not always be deter-

mined. Secondly, the complexes attain much more symmetric conformations in solution and since, experimentally determined chemical shifts are measured in solution state, it is imperative to employ calculations on optimised geometries. The decaniobate ion, $[Nb_{10}O_{28}]^{6-}$ was chosen as a model complex to develop a computational method that gives best results. In general, the hybrid-DFT functionals performed better than the pure-DFT functionals. While, dispersion-corrected functionals were at par with the hybrid functionals, they are relatively computationally costly. The PBE0 was selected as a functional of choice for both geometry optimisations and NMR calculations. Using PBE0/def2-tzvp for NMR calculations on 33 PBE0/cc-pvtz (H-Ar), lanl2dz (K-) optimised heterogeneous polyoxometalates with 179 ^{17}O NMR signals, an excellent correlation was achieved between the observed and predicted chemical shifts.

In addition, in complex, $[H_xNb_6O_{19}]^{(8-x)}$, protonation induced pH-dependent shifts were reproduced accurately. It is a tri-protic ion which gets protonated at μ_2-O sites yet all the other oxygen atoms show a pH-dependent drift in chemical shift. The method accurately predicted the shift progress as a function of pH.

More details of the work can be seen in the attached manuscript:

Rupali Sharma, Jie Zhang and C. André Ohlin, *Phys. Chem. Chem. Phys.*, **2016**, 18, 8235-8241.

PAPER

Predicting ^{17}O NMR chemical shifts of polyoxometalates using density functional theory†

Rupali Sharma, Jie Zhang and C. André Ohlin*

We have investigated the computation of ^{17}O NMR chemical shifts of a wide range of polyoxometalates using density functional theory. The effects of basis sets and exchange–correlation functionals are explored, and whereas pure DFT functionals generally predict the chemical shifts of terminal oxygen sites quite well, hybrid functionals are required for the prediction of accurate chemical shifts in conjunction with linear regression. By using PBE0/def2-tzvp//PBE0/cc-pvtz(H-Ar), lanl2dz(K-) we have computed the chemical shifts of 37 polyoxometalates, corresponding to 209 ^{17}O NMR signals. We also show that at this level of theory the protonation-induced pH dependence of the chemical shift of the triprotic hexaniobate Lindqvist anion, $[H_xNb_6O_{19}]^{(8-x)}$, can be reproduced, which suggests that hypotheses regarding loci of protonation can be confidently tested.

Polyoxometalates, polyanionic metal oxide clusters of group V and VI elements,[1,2] have generated a lot of interest as catalysts, as bioactive molecules, and as homogeneous models for understanding the behaviour of heterogeneous metal oxides such as minerals at the solvent–solid interface.[3–5]

The latter application is very attractive as it offers site-specific information about the dynamic behaviour of the molecule, something which may be impossible to achieve when working with heterogeneous materials. As such, ^{17}O NMR has proven to be a powerful method for providing details of the rates of exchange between different metal oxide oxygen sites and water, and has revealed a broad range of reactivities exhibited by oxygen sites in even small homoleptic isopolyoxometalate clusters.[6–10] The tunability of polyoxometalates *via* targeted substitution has further highlighted the profound effects even small structural or compositional changes can have on the solution dynamics of these molecules. In most cases, due to the low natural abundance of ^{17}O,[11] successful acquisition of ^{17}O NMR spectra depends on the artificial enrichment of the oxygen sites in the molecule, either by synthesising the molecule using enriched water, or by heating the already-prepared molecule in enriched water and allowing the isotopic tag to be introduced through solvent exchange (post-enrichment) with varying degrees of success.

Either way, achieving site-specific information is predicated on the ability to accurately assign ^{17}O NMR signals to the different sites in the model molecule. To this end, computational

modelling is an attractive tool, and even high-end desktop computers are now fast enough to be able to carry out a range of computational experiments on nanometer-sized polyoxometalates at acceptable levels of theory.

Density functional theory (DFT) has proven to be a versatile tool for predicting molecular and spectroscopic properties owing to its lower computational cost relative to correlated methods, and greater flexibility and no need for parametrisation relative to semi-empirical methods.[12,13] As DFT does not inherently account for electron exchange and correlation, accurate computation of molecular properties relies on the use of exchange and correlation (XC) functionals. Pure generalized gradient approximation (GGA) DFT functionals such as BP86 have historically been well known in inorganic chemistry as they are not particularly computationally demanding. However, to cancel out the self-interaction error in DFT, a specific amount – typically 25% – of Hartree–Fock (HF) exchange can be included in the exchange part of the XC functional. XC functionals that include exact HF exchange, such as B3LYP, are referred to as hybrid functionals as they include both the electron density (as DFT does) and the exact wave function (as HF theory does). Different forms of hybrid functionals have been dominating the computational field for the past twenty years since successfully implemented by Becke,[14] but are computationally more demanding than pure GGA DFT functionals. In general, by careful selection of the appropriate XC functional for the intended application, DFT-based predictions can be made to yield excellent agreement with experimental observations.

A landmark paper recently published by Pascual-Borrás *et al.* investigated the use of DFT to compute ^{17}O NMR chemical shifts in organic solvents of a series of 15 mostly Lindqvist-ion-based polyoxometalates.[15] The preferred method involved

School of Chemistry, Monash University, 3800 Melbourne, Victoria, Australia. E-mail: andy.ohlin@monash.edu

† Electronic supplementary information (ESI) available: Numerical data for select figures, effects of basis sets, optimised geometries, computed shifts, literature shifts *etc.* See DOI: 10.1039/c5cp07766d

This journal is © the Owner Societies 2016

120

Phys. Chem. Chem. Phys., 2016, **18**, 8235–8241 | 8235

optimising the structures at PBE/tz2p with relativistic effects introduced by the zeroth order regular approximation (ZORA) with scalar correction, and computing the NMR shift using the gauge including atomic orbital (GIAO)[16] method at OPBE/tzp with ZORA and spin–orbit coupling. The computations were carried out using the Amsterdam Density Functional (ADF) package,[17] and accounted for solvation implicitly *via* COSMO. The authors found that while the shifts of terminal oxygen sites could be quite accurately predicted, multiple bonded oxygen sites were less amenable to prediction. In addition, a bug related to the computation of the spin–orbit part of the chemical shielding is present in all versions of ADF from 2008 to 2013,[18] which may have affected the results provided by Pascual-Borrás *et al.* as well as a few other publications on NMR shift computations of different nuclei in polyoxometalates.[19,20] We thus decided to revisit their observations and, if possible, improve them in terms of the power of predicting accurate ^{17}O NMR shifts.

In order for a predictive method to be at all useful, it needs at a minimum to predict the correct relative ordering of the ^{17}O NMR signals from the different oxygen sites in the molecule (criterion 1) so that signals that are observed to appear upfield relative to other signals are predicted to do so. However, as it is sometimes not possible to obtain signals from all sites *e.g.* due to difficulties with enriching inert oxygen sites during post-enrichment and unambiguous assignment is thus complicated, a predictive method should also be able to yield the correct chemical shift distance between the signals (criterion 2), and ideally the correct absolute chemical shift (criterion 3). The last criterion is less important if criteria 1 and 2 are fulfilled, as linear correction can be applied to correct systematic errors in the predictive method. Finally, the method should be easy to implement in commonly available computational packages (criterion 4).

We have re-investigated the use of density functional theory to predict the chemical shift of ^{17}O NMR signals in polyoxometalates. Emphasis has been on finding a computationally affordable method so that even fairly large polyoxometalates can be subjected to computation, yet while retaining sufficient predictive accuracy that the method is useful. We have thus focused on using the Gaussian computational package, as it is popular, fast and generally available, and have looked at a range of common exchange/correlation functionals and basis sets. Our focus here will not be on the theoretical basis of these types of computations, which is covered in excellent detail by Pascual-Borrás *et al.*, but is instead on the development of a prescriptive method that is easy to implement for researchers with little experience in computational chemistry.

Experimental details

All computations were carried out using Gaussian 09 rev. D.01,[21] with implicit solvation using the polarizable continuum model (PCM).[22] Basis sets were obtained from the basis set exchange.[23,24] Pure d and f functions were requested. Nuclear shielding was calculated using the GIAO method,[16] and calibrated

against the computed shift for the oxygen atom signal in water to give a chemical shift. Unless otherwise indicated the typical shift computation was carried out at PBE0[25]/def2-tzvp[26] using a structure optimised at PBE0/cc-pvtz (H-Ar),[27,28] lanl2dz (K-);[29] the notation used to indicate this in the present work is PBE0/def2tzvp//PBE0/cc-pvtz(H-Ar), lanl2dz (K-) where lanl2dz denotes that it was used for all elements with atomic numbers equal to or higher than potassium. XC functionals used also include PBE,[30,31] BP86,[32,33] PW91,[34,35] mPW91,[36] OPBE,[37,38] M06L,[39] B3LYP,[40–43] M06,[39] lc-ωPBE,[44] ωB97XD[45] and CAM-B3LYP.[46] The shifts of equivalent oxygen sites were averaged to yield a single shift. This was also done in the computations on the protonated compounds. Proton-dependent shifts were extracted from the published figure[6] using WebPlotDigitizer.[47] We use μ_n to indicate oxygen sites that bond to *n* different metal atoms, and η to indicate oxygen sites that bond to a single metal atom *i.e.* a terminal oxygen. Crystal structures of Nb_{10}, $TiNb_9$ and Ti_2Nb_8 were obtained from the literature, and are supplied as Cartesian coordinates in the ESI.† [48–50] ^{17}O NMR signal data were obtained from the literature (see ESI† for details).[6,11,51–62]

Results

We first focussed on a series of tetramethylammonium niobate ions –$[Nb_{10}O_{28}]^{6-}$ (Nb_{10}), $[TiNb_9O_{28}]^{7-}$ ($TiNb_9$) and $[Ti_2Nb_8O_{28}]^{8-}$ (Ti_2Nb_8; Fig. 1) – that exhibit spectra that do not change significantly with different pH in their stability ranges so that protonation of the molecules does not have to be accounted for.[7–9,51] This, coupled with well-understood solution dynamics, makes this admittedly structurally narrow set of test molecules ideal for method development.

The accurate prediction of chemical shifts necessitates the use of accurate molecular geometries. We thus first investigated a selection of XC functionals in the optimisation of $[Nb_{10}O_{28}]^{6-}$ and $[Ti_2Nb_8O_{28}]^{8-}$ using cc-pvtz (H-Ar) and lanl2dz (K-) and out of necessity compared the optimised structures with crystal structure geometries (Fig. 2). $TiNb_9$ was omitted at this stage due to partial occupancies in its crystal structure distorting the observed bond distances. While most exchange correlation functionals performed similarly, the hybrid functional PBE0 and the long range-range corrected CAM-B3LYP and LC-ωPBE functionals yielded smaller mean and maximum absolute errors in computed bond distances relative to the crystal structures. Because of the high computational cost of,
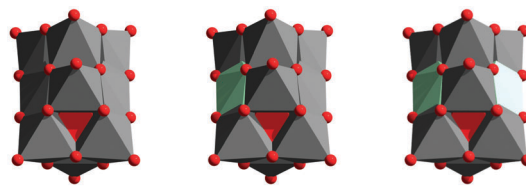

Fig. 1 $[Nb_{10}O_{28}]^{6-}$ (left), $[TiNb_9O_{28}]^{7-}$ (middle) and $[Ti_2Nb_8O_{28}]^{8-}$ (right). Niobium, oxygen and titanium indicated by grey, red and green, respectively.
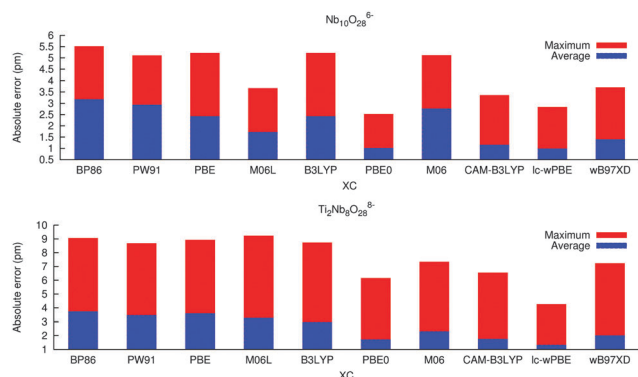
121

Fig. 2 Maximum absolute error (red) and average absolute error (blue) in predicted vs. crystal structure bond distances of Nb_{10} (top) and Ti_2Nb_8 (bottom). Geometries were optimised using the indicated XC functionals and lanl2dz(K-) and cc-pvtz (H-Ar). The data are given in Table S2 (ESI†).

in particular, CAM-B3LYP, we settled on PBE0 as the functional of choice for geometry optimisation.

Using the structure of $[Nb_{10}O_{28}]^{6-}$ optimised at PBE0/cc-pvtz(H-Ar), lanl2dz(K-) we explored different XC functionals together with the def2-tzvp basis set in the computation of the ^{17}O NMR chemical shifts (Fig. 3). Here, a few trends were clear. Firstly, pure GGA DFT functionals over-predict the shifts of multiple bonded μ_n-oxygen atoms, but – with the exception of M06L – still fare quite well in predicting the shift of terminal, η-oxygen sites. In contrast, hybrid functionals give a similar error for all oxygen sites, regardless of the oxygen type, and thus
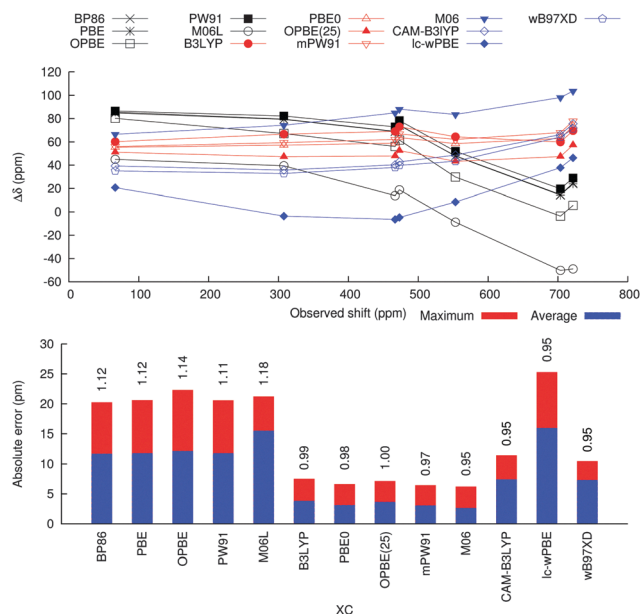
Fig. 3 Top: Error in predicted shift vs. observed shift for different exchange correlation functionals for Nb_{10}. Pure DFT functionals are indicated in black and hybrid functionals are indicated in red. Functionals with long-range correction are given in blue. Bottom: Absolute maximum and average errors in predicted shifts vs. observed shifts after linear regression has been applied. The numbers above the bars indicate the regressed slope. OPBE(25) indicates OPBE with 0.75 OPT exchange and 0.25 HF exchange. The data are given in Table S3 (ESI†).

produce an apparent constant systematic error. This observation allowed us to apply linear correction via linear regression, which further highlighted the difference in performance by the different classes of functionals. Again, PBE0 performed very well, ranking just after mPW91 and M06 based on maximum and average errors, and gave a scaling factor close to unity, which indicated that it fulfils criterion 2 better than either mPW91 or M06 do. We also found that for the Nb_{10} ion the combination of cc-pvtz(H-Ar) and lanl2dz(K-) in the optimisation step outperformed cc-pvdz-(H-Ar) and lanl2dz(K-), def2-svp, and def2-tzvp with regards to the shift predicted at PBE0/def2-tzvp (Fig. S1, ESI†), but that def2-tzvp gave a more constant systematic error than cc-pvtz(H-Ar) and lanl2dz(K-) in the shift calculation step (Fig. S2, ESI†). Similar trends with respect to the use of XC functionals in the shift computation stage were observed when using the determined crystal structures directly without optimisation (Fig. S3, ESI†). Whereas the latter approach is attractive for very large molecules where structural optimisation would be time consuming, care needs to be taken when there are partial occupancies in the structure as this will distort bonds. Also, crystallographically determined bonds to protons are abnormally short, and such bonds would have to be optimised computationally.

Investigating the performance of PBE0/def2-tzvp on structures optimised using other XC functionals (Fig. S4, ESI†) confirmed that PBE0/def2-tzvp//PBE0/cc-pvtz(H-Ar), lanl2dz (K-) yielded the best results in terms of constant systematic errors, with the pure GGA functionals now leading to over-estimated shifts of the terminal oxygen sites. However, given the similarity in the errors of the predicted shifts, the key to good shift prediction is really the use of a hybrid functional such as PBE0 in the shift computation stage as all the tested XC functionals appear to perform quite well in terms of structure optimisation. We thus decided to use PBE0 for both structure optimisation and NMR shift computations in the remainder of the study.

The good performance of the pure GGA functionals with respect to predicting the chemical shift of terminal oxygen sites and the consistent error in the predicted chemical shifts by the hybrid functionals focused our attention on the specific influence of the Hartree–Fock exchange. Substituting part of the PBE exchange with HF exchange led to a decrease in errors in the predicted shifts of multiple bonded oxygen sites, such as
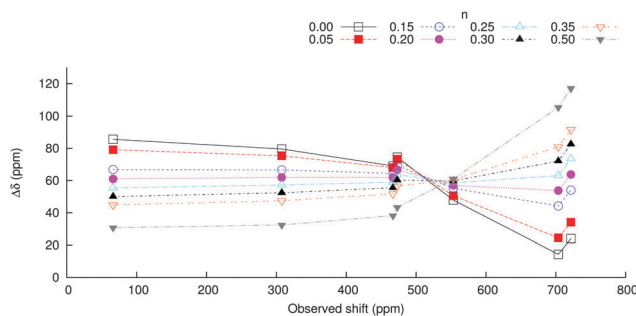
Fig. 4 Error in predicted shift vs. observed shift with varying amounts of HF exchange included in the XC functional for Nb_{10}. The functional used was $n HF_x + (1 - n) PBE_x + PBE_c$. For $n = 0$ and $n = 0.25$ the functionals are identical to PBE and PBE0, respectively. The data are given in Table S4 (ESI†).

μ_6-O, but an increase in errors in the predicted shift of the terminal η-O sites (Fig. 4 and Fig. S5, ESI†). When the ratio of
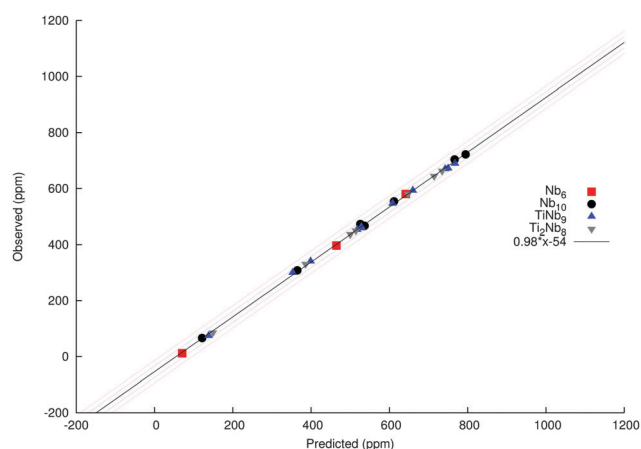

Fig. 5 Non-regressed computed shifts *vs.* observed shifts for Nb_{10}, $TiNb_9$ and Ti_2Nb_8 at PBE0/def2-tzvp//PBE0/cc-pvtz(H-Ar), lanl2dz(K-). The black line has a slope of 0.98 and an intercept of −54 ppm (r^2 0.999). The blue and red lines indicate regressed offsets of 10 and 20 ppm, respectively.

HF exchange to PBE exchange was 1 : 3 ($n = 0.25$) the error in the predicted shift was similar for all oxygen sites. The same trend was observed for PW91 (Fig. S6, ESI†). In light of this, it is interesting to briefly revisit the trends shown in Fig. 3 as n is 0.27 and 0.20 for M06 and B3LYP respectively, and 0.25 for mPW91, OPBE(25) and PBE0. In contrast to the plain hybrid functionals, the range-corrected functionals CAM-B3LYP, lc-ωPBE and ωB97XD also incorporate 65–100% ranged HF exchange, which may explain the increasing error for terminal oxygen sites. There is thus no need to adjust the amount of HF exchange included in most standard hybrid functionals as they will give a fairly constant amount of error across the spectral range.

Computing the shifts of all oxygen sites in Nb_{10}, $TiNb_9$ and Ti_2Nb_8 at PBE0/def2-tzvp//PBE0/cc-pvtz(H-Ar), lanl2dz(K-) and comparing them to the corresponding observed shifts, a slope of 0.98 and an intercept of −54 ppm are obtained, with a coefficient of determination of 0.999(4) (Fig. 5). The predictive power of the method is thus excellent for the structurally and chemically homogeneous Nb_{10}, $TiNb_9$ and Ti_2Nb_8 test set.

Expanding the study to include 37 structurally and chemical heterogeneous polyoxometalates with 209 observed ^{17}O NMR
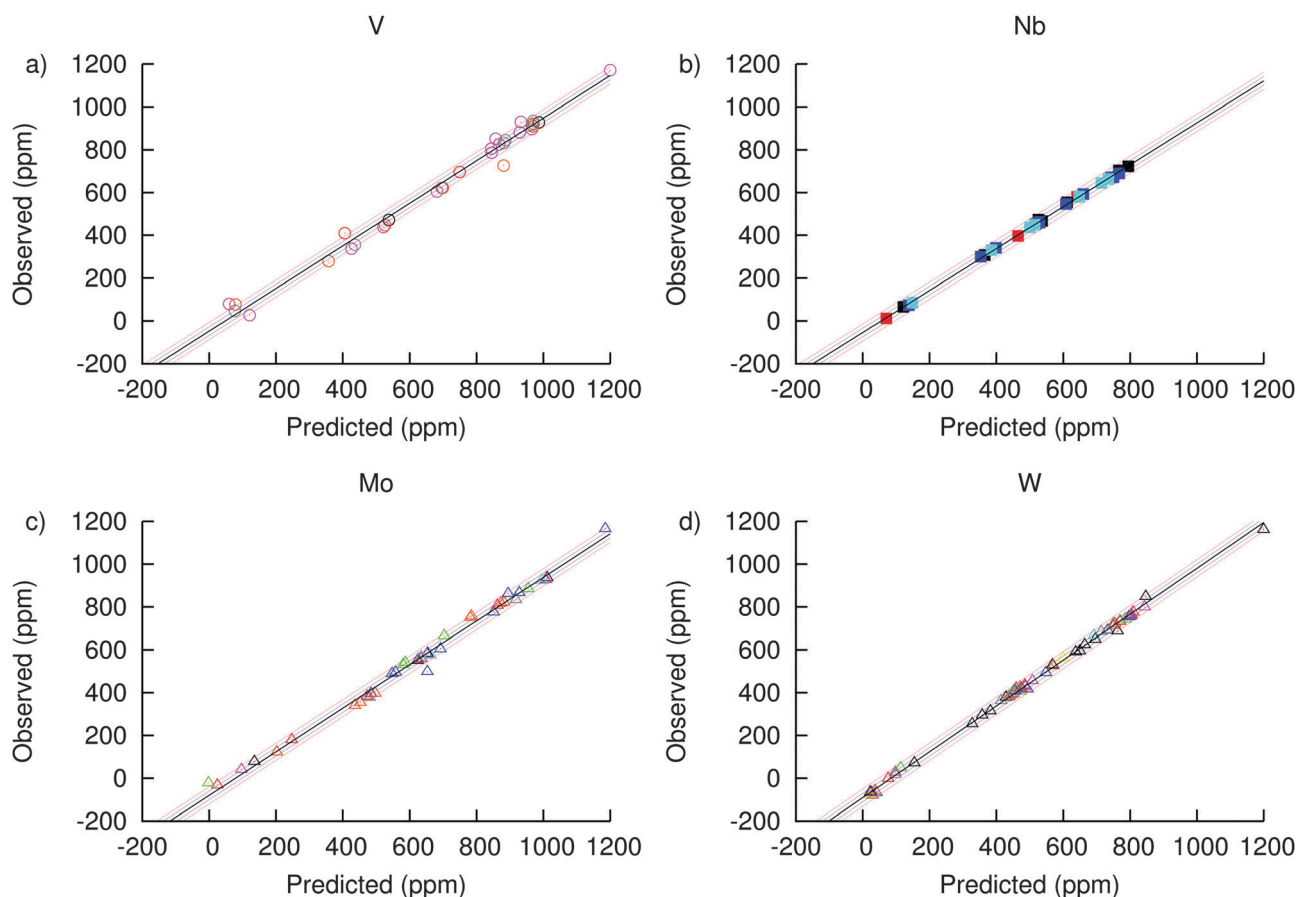
Fig. 6 Predicted non-regressed shifts *vs.* observed chemical shifts for different classes of compounds. Top left: Polyoxovanadates (Tables S5 and S6, ESI†); the black line has a slope of 1.00 with an intercept of −47 ppm and r^2 of 0.989. Top right: Polyoxoniobates (Tables S7 and S8, ESI†); the black line has a slope of 0.98 with an intercept of −54 ppm and r^2 of 0.999. Bottom left: Polyoxomolybdates (Tables S11 and S12, ESI†); the black line has a slope of 1.01 with an intercept of −74 ppm and r^2 of 0.992. Bottom right: Polyoxotungstates (Tables S13 and S14, ESI†); the black line has a slope of 1.06 with an intercept of −85 ppm and r^2 of 0.998. For polyoxotantalates the slope, intercept and coefficient of determination are 1.10, −96 and 0.991, respectively (not shown). The blue and red lines indicate regressed offsets of 10 and 20 ppm, respectively.

8238 | *Phys. Chem. Chem. Phys.*, 2016, **18**, 8235–8241

123

This journal is © the Owner Societies 2016

signals (see ESI† for details) shows that the method works well in general, but also that different offsets and slopes are obtained depending on which group 5 or 6 element dominates the group (Fig. 6). It is clear that the predictive power for the polyoxovanadates in particular is quite poor compared to the other elements. We speculate that this may be due to the vanadate species being present in various states of protonation whereas the structures used in the computations are not protonated. This is certainly true for the di- and tetra-metavanadates and decavanadates which would be protonated under most conditions where they would be observed by NMR. This may also explain the relatively poor correlation for the molybdates, as our test set by necessity included a range of protic molybdic acids as well as two molybdovanadates. The correlation for tungstates is better, and while the test set also includes polytungstic acids, it also contains species that were acquired in non-protic solvents such as aceto-nitrile. Either way, combining computed *vs.* observed data for all members of the test set a slope of 1.02, the intercept of −71 ppm and r^2 of 0.993 was obtained (Fig. S7, ESI†). This demonstrates that although the chemical shifts of some compounds are predicted less well than others – possibly due to protic chemistry – overall the performance is very good and there is an improvement over the correlation seen using ADF and OPBE/tzp//PBE/tz2p and including computationally costly relativistic effects, where coefficients of determination of 0.96 and 0.98 were obtained when polyoxo-vanadates were included and excluded, respectively.[15]

An important problem in the study of large multiprotic molecules such as polyoxometalate clusters is the question of the locus or loci of protonation. ^{17}O NMR is a potentially powerful tool for resolving the location of solution state proto-nation *in situ* as the shift of different sites should change with protonation. However, as has been observed for the hexaniobate Lindqvist ion, $[Nb_6O_{19}]^{8-}$, protonation doesn't necessarily just affect the shift of a single oxygen site.[6] In the hexaniobate ion the shifts corresponding to all sites – μ_6-O, μ_2-O and η-O – are affected by protonation. The effect is opposite for the η and μ_6 oxygen atoms relative to the μ_2 oxygen atoms; however, the latter are shifted downfield by *ca.* 22 ppm while the former move upfield by 50 and 20 ppm, respectively. If the locus of protona-tion were assigned based on the magnitude of the shift alone, the η oxygen would have been the suspected site of protonation, although the upfield shift would have counter-indicated it as a protonation site. Either way, for the hexaniobate ion the protonation site is well-known from crystal structures, and is the μ_2 oxygen,[63] as is generally the case with homoleptic isopolyoxometalates. The first three pK_a are also known.[64]

The hexaniobate ion is thus a good test case for computing protonation-induced pH-dependent shifts. We optimised all possible diprotonated and triprotonated isomers, and for each protonation state selected the lowest energy one (Fig. S8 and Table S15, ESI†) and computed the corresponding chemical shift. The speciation diagram was simulated (listings S1 and S2, and Fig. S9, ESI†) and used to scale the contribution to the observed shift of each species as a function of pH (Fig. 7).

The shifts of the η-oxygen site are predicted well, whereas the predicted shifts for the other two sites are consistently
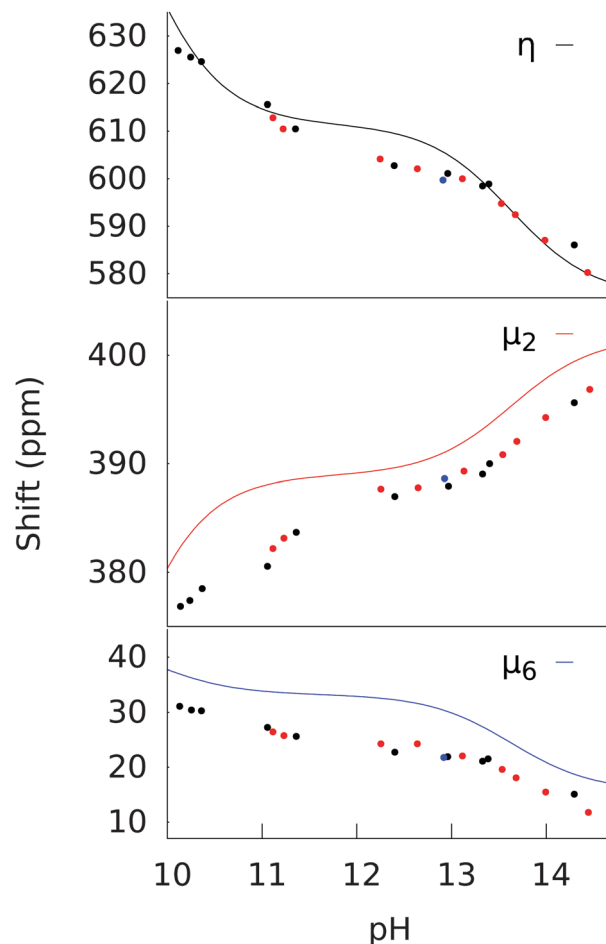
Fig. 7 Prediction of pH-dependent ^{17}O NMR shifts of the different oxygen sites in the $H_x[Nb_6O_{19}]^{(8-x)-}$ molecule. Experimental shifts (Tables S16–S18, ESI†) at 277 K, 298 K and 303 K are given as black, red and blue circles, respectively. Predicted shifts are scaled by 0.98 and then offset by −54 ppm, and are given as black, red and blue lines for the η, μ_2 and μ_6 oxygen signals, respectively.

overestimated by *ca.* 10 ppm. However, the shape and magnitude of the pH-dependence are in all cases accurately predicted. This indicates that it is possible to accurately simulate the effect of protonation and, importantly, test hypotheses about the locus of protonation using PBE0/def2-tzvp//PBE0/cc-pvtz (H–Ar), lanl2dz (K-), with the main limiting factor being the large number of structures that may need to be optimized for polyprotic systems and not the predictive power of the method itself.

Conclusions

We have implemented and demonstrated the computation of ^{17}O NMR shifts of a wide range of polyoxometalates using Gaussian 09 and PBE0/def2-tzvp//PBE0/cc-pvtz (H–Ar), lanl2dz (K-) with implicit solvation through the polarizable continuum model. At this level of theory the structures of polyoxometalates with over 100 atoms can be optimized on even a fast desktop computer and the corresponding ^{17}O NMR shifts are predicted with good precision and accuracy.

The method also fulfils the four criteria that we believe are required for a method to be useful to the wider polyoxometalate community, namely it should be able to predict the correct order of appearance of the NMR signals, correct relative shifts, and correct absolute shifts – although this required linear regression – and should be able to do this in a widely used computational package.

In addition, we have demonstrated how the protonation-induced pH-dependent shifts are reproduced well at this level of theory, with the essential features of the pH-dependent behaviour captured, as demonstrated using $H_x[Nb_6O_{19}]^{(8-x)-}$. Importantly, the method accurately reproduces the shifts of all the oxygen atoms in the structure, in spite of protonation being limited to the μ_2-oxygen sites.

It is possible that variations in the combination of basis sets, XC functionals and solvation models may yield even better correlation between observed and predicted shifts; however, to the authors it appears that the key to predicting accurate chemical shifts is the ability of hybrid functionals to a site-independent systematic error coupled with linear regression to compensate for this.

We are also in the process of exploring whether these effects hold true for the computation of chemical shifts of other nuclei of interest, such as ^{31}P, ^{51}V, ^{95}Mo and ^{183}W.

Acknowledgements

References

1 M. T. Pope and A. Müller, *Angew. Chem., Int. Ed.*, 1991, **30**, 34–48.

2 Y.-F. Song and R. Tsunashima, *Chem. Soc. Rev.*, 2012, **41**, 7384–7402.

3 C. A. Ohlin, E. M. Villa, J. R. Rustad and W. H. Casey, *Nat. Mater.*, 2010, **9**, 11–19.

4 J. R. Rustad and W. H. Casey, *Nat. Mater.*, 2012, **11**, 223–226.

5 W. H. Casey, *Environ. Chem.*, 2015, **12**, 1–19.

6 J. R. Black, M. Nyman and W. H. Casey, *J. Am. Chem. Soc.*, 2006, **128**, 14712–14720.

7 E. M. Villa, C. A. Ohlin, E. Balogh, T. M. Anderson, M. D. Nyman and W. H. Casey, *Angew. Chem., Int. Ed.*, 2008, **47**, 4844–4846.

8 E. M. Villa, C. A. Ohlin, J. R. Rustad and W. H. Casey, *J. Am. Chem. Soc.*, 2009, **131**, 16488–16492.

9 E. M. Villa, C. A. Ohlin and W. H. Casey, *J. Am. Chem. Soc.*, 2010, **132**, 5264–5272.

10 R. L. Johnson, E. M. Villa, C. A. Ohlin, J. R. Rustad and W. H. Casey, *Chem. – Eur. J.*, 2011, **17**, 9359–9367.

11 W. G. Klemperer, *Angew. Chem., Int. Ed. Engl.*, 1978, **17**, 246–254.

12 W. Kohn, A. D. Becke and R. G. Parr, *J. Phys. Chem.*, 1996, 12974–12980.

13 C. J. Cramer and D. G. Truhlar, *Phys. Chem. Chem. Phys.*, 2009, **11**, 10757–10816.

14 A. D. Becke, *J. Chem. Phys.*, 1993, **98**, 1372–1377.

15 M. Pascual-Borrás, X. López, A. Rodríguez-Fortea, R. J. Errington and J. M. Poblet, *Chem. Sci.*, 2014, **5**, 2031–2042.

16 K. Wolinski, J. F. Hilton and P. Pulay, *J. Am. Chem. Soc.*, 1990, **112**, 8251–8260.

17 SCM, Amsterdam Density Functional package, http://www.scm.com.

18 SCM, *ADF 2014 Release Notes*, http://www.scm.com/Doc/Doc2014/Background/Updates/page10.html.

19 N. Vankova, T. Heine and U. Kortz, *Eur. J. Inorg. Chem.*, 2009, 5102–5108.

20 M. Pascual-Borrás, X. López and J. M. Poblet, *Phys. Chem. Chem. Phys.*, 2015, **17**, 8723–8731.

21 M. J. Frisch, G. W. Trucks and H. B. Schlegel, *et al.*, *Gaussian 09 Revision D.01*, Gaussian Inc., Wallingford CT, 2009.

22 J. Tomasi, B. Mennucci and R. Cammi, *Chem. Rev.*, 2005, **105**, 2999–3093.

23 D. Feller, *J. Comput. Chem.*, 1996, **17**, 1571–1586.

24 K. L. Schuchardt, B. T. Didier, T. Elsethagen, L. Sun, V. Gurumoorthi, J. Chase, J. Li and T. L. Windus, *J. Chem. Inf. Model.*, 2007, **47**, 1045–1052.

25 C. Adamo and V. Barone, *J. Chem. Phys.*, 1999, **110**, 6158–6159.

26 F. Weigend and R. Ahlrichs, *Phys. Chem. Chem. Phys.*, 2005, **7**, 3297–3305.

27 T. H. J. Dunning, *J. Chem. Phys.*, 1989, **90**, 1007–1023.

28 D. E. Woon and T. H. J. Dunning, *J. Chem. Phys.*, 1993, **98**, 1358–1371.

29 P. J. Hay and W. R. Wadt, *J. Chem. Phys.*, 1985, **82**, 284–310.

30 J. P. Perdew, K. Burke and M. Ernzerhof, *Phys. Rev. Lett.*, 1996, **77**, 3865–3868.

31 J. P. Perdew, K. Burke and M. Ernzerhof, *Phys. Rev. Lett.*, 1997, **78**, 1396.

32 A. D. Becke, *Phys. Rev. A: At., Mol., Opt. Phys.*, 1988, **38**, 3098–3100.

33 J. P. Perdew, *Phys. Rev. B: Condens. Matter Mater. Phys.*, 1986, **33**, 8822–8824.

34 J. P. Perdew, J. A. Chevary, S. H. Vosko, K. A. Jackson, M. R. Pederson, D. J. Singh and C. Fiolhais, *Phys. Rev. B: Condens. Matter Mater. Phys.*, 1992, **46**, 6671–6687.

35 J. P. Perdew, J. A. Chevary, S. H. Vosko, K. A. Jackson, M. R. Pederson, D. J. Singh and C. Fiolhais, *Phys. Rev. B: Condens. Matter Mater. Phys.*, 1993, **48**, 4978.

36 C. Adamo and V. Barone, *J. Chem. Phys.*, 1998, **108**, 644–675.

37 N. C. Handy and A. J. Cohen, *Mol. Phys.*, 2001, **99**, 403–412.

38 W.-M. Hoe, A. Cohen and N. C. Handy, *Chem. Phys. Lett.*, 2001, **341**, 319–328.

39 Y. Zhao and D. G. Truhlar, *Theor. Chem. Acc.*, 2008, **120**, 215–241.

40 A. D. Becke, *J. Chem. Phys.*, 1993, **98**, 5648–5652.

8240 | *Phys. Chem. Chem. Phys.*, 2016, **18**, 8235–8241

125

This journal is © the Owner Societies 2016

41 C. Lee, W. Yang and R. G. Parr, *Phys. Rev. B: Condens. Matter Mater. Phys.*, 1988, **37**, 785–789.

42 B. Mielich, A. Savin, H. Stoll and H. Preuss, *Chem. Phys. Lett.*, 1989, **157**, 200–206.

43 S. H. Vosko, L. Wilk and M. Nusair, *Can. J. Phys.*, 1980, **58**, 1200–1211.

44 O. A. Vydrov and G. E. Scuseria, *J. Chem. Phys.*, 2006, **125**, 234109.

45 J.-D. Chai and M. Head-Gordon, *Phys. Chem. Chem. Phys.*, 2008, **10**, 6615–6620.

46 T. Yanai, D. Tew and N. Handy, *Chem. Phys. Lett.*, 2004, **393**, 51–57.

47 A. Rohatgi, *WebPlotDigitizer*, http://arohatgi.info/WebPlotDigitizer/.

48 C. A. Ohlin, E. M. Villa and W. H. Casey, *Inorg. Chim. Acta*, 2009, **362**, 1391–1392.

49 C. A. Ohlin, E. M. Villa, J. C. Fettinger and W. H. Casey, *Dalton Trans.*, 2009, 2677–2678.

50 M. Nyman, L. J. Criscenti, F. Bonhomme, M. A. Rodriguez and R. T. Cygan, *J. Solid State Chem.*, 2003, **176**, 111–119.

51 W. G. Klemperer and K. A. Marek, *Eur. J. Inorg. Chem.*, 2013, 1762–1771.

52 M. Filowitz, R. K. C. Ho, W. g. Klemperer and W. Shum, *Inorg. Chem.*, 1979, **18**, 93–103.

53 A. D. English, J. P. Jesson, W. G. Klemperer, T. Mamouneas, L. Messerle, W. Shum and A. Tramontano, *J. Am. Chem. Soc.*, 1975, **97**, 4785–4786.

54 W. G. Klemperer and W. Shum, *J. Am. Chem. Soc.*, 1978, 4891–4893.

55 R. I. Maksimovskaya and N. N. Chumachenko, *Polyhedron*, 1987, **6**, 1813–1821.

56 R. I. Maksimovskaya and K. G. Burtseva, *Polyhedron*, 1985, **4**, 1559–1562.

57 R. I. Maksimovskaya and M. A. Fedotov, *J. Struct. Chem.*, 2006, **47**, 1559–1562.

58 R. I. Maksimovskaya and G. M. Maksimov, *Inorg. Chem.*, 2011, **50**, 4725–4731.

59 L. P. Tsiganok, A. B. Vishnikin and R. I. Maksimovskaya, *Polyhedron*, 1989, **8**, 2739–2742.

60 C. J. Besecker, W. G. Klemperer, D. J. Maltbie and D. A. Wright, *Inorg. Chem.*, 1985, **24**, 1027–1032.

61 R. J. Errington, S. S. Petkar, P. S. Middleton, W. McFarlane, W. Clegg, R. A. Coxall and R. W. Harrington, *Dalton Trans.*, 2007, 5211–5222.

62 D. C. Duncan and C. L. Hill, *RSC Adv.*, 2014, **4**, 7094–7103.

63 T. Ozeki, T. Yamase, H. Naruke and Y. Sasaki, *Bull. Chem. Soc. Jpn.*, 1994, **67**, 3249–3253.

64 N. Etxebarria, L. A. Fernandez and J. M. Madariaga, *Dalton Trans.*, 1994, 3055–3059.

Supporting information:
Predicting ^{17}O NMR chemical shifts of polyoxometalates using density functional theory.

Rupali Sharma[1], Jie Zhang[1], and C. André Ohlin[1]

[1]School of Chemistry, Monash University, Victoria, Australia

School of Chemistry, Monash University, Victoria 3800 Australia

1

Contents

List of Tables

2

List of Figures

3

Listings

4

Table S1: Abbreviations used in the Supporting Information.

Abbreviation	Explanation
ACN	Acetonitrile
Aq.	Water
DCM	Dichloromethane
Nb_{10}	$[Nb_{10}O_{28}]^{6-}$
TBA	Tetrabutylammonium
$TiNb_9$	$[Ti_2Nb_8O_{28}]^{7-}$
Ti_2Nb_8	$[Ti_2Nb_8O_{28}]^{8-}$
TMA	Tetramethylammonium

Table S2: Maximum absolute error and average absolute error in predicted vs crystal structure bond distances of Nb_{10} and Ti_2Nb_8 for different exchange correlation functionals. Geometries were optimised using the indicated XC functionals and lanl2dz (Ti, Nb) and cc-pvtz (O).

Molecule	Functional	Maximum absolute error (pm)	Average Absolute Error (pm)
Nb_{10}	BP86	5.51	3.18
	PW91	5.10	2.93
	PBE	5.21	2.42
	M06L	3.66	1.72
	B3LYP	5.21	2.42
	PBE0	2.52	1.01
	M06	5.11	2.76
	CAM-B3LYP	3.35	1.15
	lc-ωPBE	2.83	0.99
	ωB97XD	3.70	1.39
Ti_2Nb_8	BP86	9.05	3.73
	PW91	8.67	3.46
	PBE	8.92	3.60
	M06L	9.22	3.27
	B3LYP	8.73	2.97
	PBE0	6.15	1.72
	M06	7.33	2.30
	CAM-B3LYP	6.54	1.75
	lc-ωPBE	4.25	1.32
	ωB97XD	7.22	2.01

5
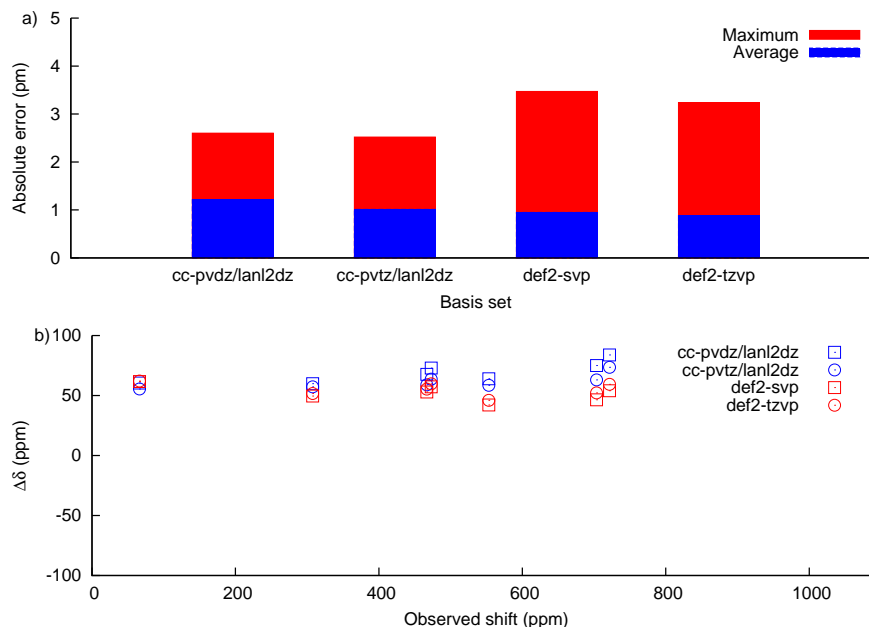
Figure S1: a) Maximum (red) and average (blue) absolute errors in calculated bond distances relative to the crystal structure for $[Nb_{10}O_{28}]^{6-}$ for different basis sets. b) Error in calculated, non-regressed shift vs observed shift for structures of $[Nb_{10}O_{28}]^{6-}$ optimised using PBE0 and cc-pvdz(H-AR),lanl2dz (K-, blue circles), cc-pvtz (H-Ar), lanl2dz (K-) (blue squares), def2-svp (red circles) and def2-tzvp (red squares). The NMR shifts were all calculated using PBE0/def2-tzvp with PCM (water). The maximum and absolute errors for the linearly regressed vs observed shifts are 7.45 and 4.01 (cc-pvdz/lanl2dz), 6.61 and 3.10 (cc-pvtz/lanl2dz), 7.45 and 4.02 (def2-svp), and 8.62 and 4.18 (def2-tzvp) ppm, respectively
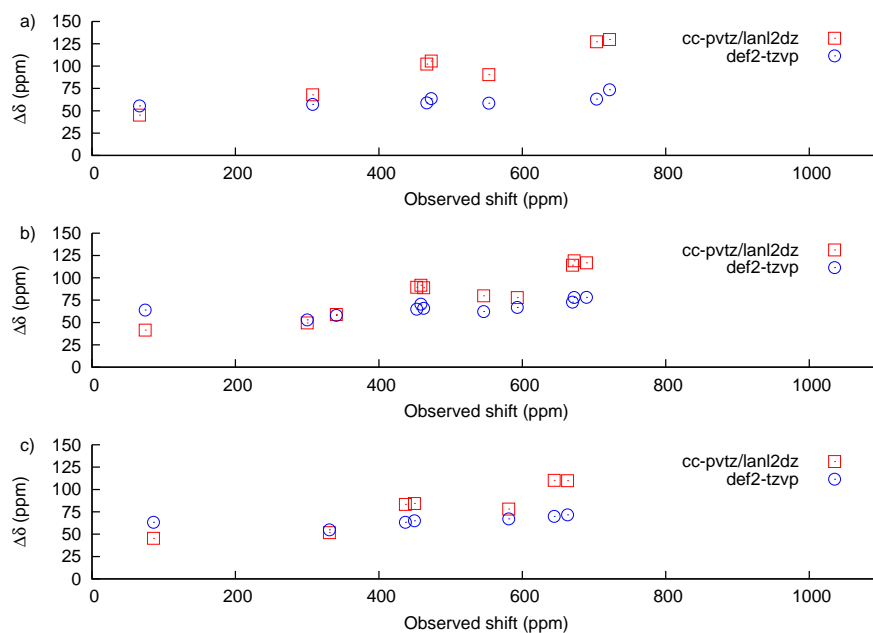
Figure S2: Effect of the basis set in the NMR shift calculation on the calculated non-regressed ^{17}O NMR chemical shift of $[Nb_{10}O_{28}]^{6-}$ (a), $[TiNb_9O_{28}]^{7-}$ (b) and $[Ti_2Nb_8O_{28}]^{8-}$ (c). cc-pvtz/lanl2dz indicates that cc-pvtz was used for H-Ar and lanl2dz for all elements from K and above. All shift calculations were done using PBE0 and with implicit solvation using PCM (water), and using a structure optimised using PBE0, and cc-pvtz (H-Ar) and lanl2dz (K-).

Table S3: Absolute maximum (AME) and average errors (AAE) in predicted shifts vs observed shifts for Nb_{10} after linear regression has been applied. Slope and intercept for the regression that has been applied is also indicated. OPBE(25) indicates OPBE with 0.75 PBE exchange and 0.25 HF exchange.

Entry	Functional	AME (ppm)	AAE (ppm)	Slope	Intercept (ppm)	r^2
1	BP86	20.22	11.67	1.12	-117	0.996
2	PBE	20.58	11.77	1.12	-118	0.996
3	OPBE	22.28	12.14	1.14	-115	0.996
4	PW91	20.55	11.77	1.11	-118	0.996
5	M06L	21.19	15.48	1.18	-86	0.994
6	B3LYP	7.49	3.81	0.99	-63	0.999(6)
7	PBE0	6.61	3.10	0.98	-51	0.999(7)
8	OPBE(25)	7.11	3.62	1.00	-48	0.999(6)
9	mPW91	6.43	3.04	0.97	-51	0.999(7)
10	M06	6.19	2.61	0.95	-57	0.999(8)
11	CAM-B3LYP	11.41	7.40	0.95	-23	0.999
12	lc-ωPBE	25.27	15.94	0.95	8.7	0.994
13	ωB97XD	10.45	7.29	0.95	-19	0.999

7
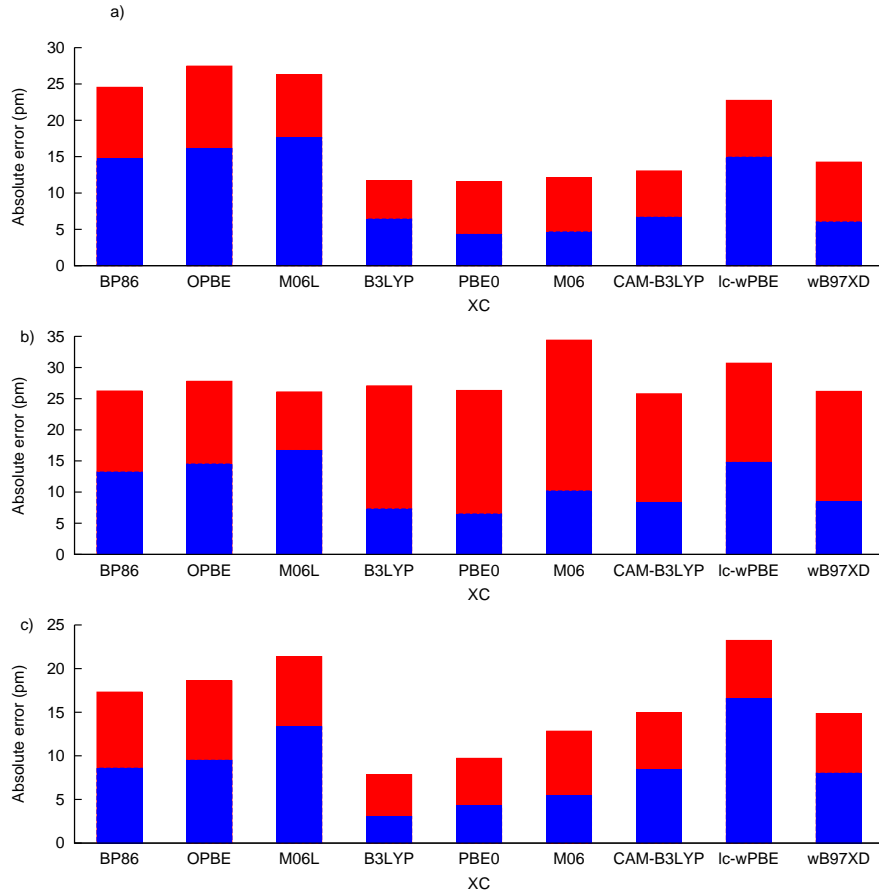
Figure S3: Maximum (red) and average (blue) absolute errors in calculated, linearly regressed ^{17}O NMR shifts using the crystal structures of $[Nb_{10}O_{28}]^{6-}$ (a), $[TiNb_9O_{28}]^{7-}$ (b) and $[Ti_2Nb_8O_{28}]^{8-}$ (c). Note that the large errors for $[TiNb_9O_{28}]^{7-}$ is due to the crystal structure being symmetric because of averaging of bond parameters from each central metal sites having 50% Ti/50% Nb occupancy. Note that the shifts were computed using cc-pvtz(H-Ar), lanl2dz(K-) and not def2-tzvp.

Table S4: ^{17}O NMR shifts in ppm relative to water of $[Nb_{10}O_{28}]^{6-}$ computed with different amounts of exact HF exchange used with the PBE exchange/correlation functional, where $XC=n \cdot HF_X + (1-n) \cdot PBE_x + PBE_c$. PBE_x is the exchange functional of the PBE XC and PBE_c is the correlation one. All computations used the structure optimised at PBE0/cc-pvtz(H-Ar), lanl2dz (K-) and were performed with def2-tzvp.

n	A (Nb_6O)	B (Nb_3-O)	C (Nb_2-O)	D (Nb_2-O)	E (Nb_2-O)	F (Nb=O)	G (Nb=O)
Experimental	66.28	307.63	466.85	472.97	553.3	703.51	721.52
0.00	151.8693	387.1852	535.9396	547.5211	601.1162	717.8359	745.5329
0.05	145.4058	383.0118	534.8875	546.2284	603.8797	727. 9502	755.6541
0.15	133.1047	374.1881	531.2756	542.2933	608.4974	747.6751	775.5414
0.20	127.2832	369.5711	528.7474	539.6810	610.3316	757.2367	785.2517
0.25	121.6874	364.8398	525.7640	536.6640	611.8384	766.5670	794.7706
0.30	116.3049	360.0098	522.3527	533.2634	613.0110	775.6402	804.0718

8
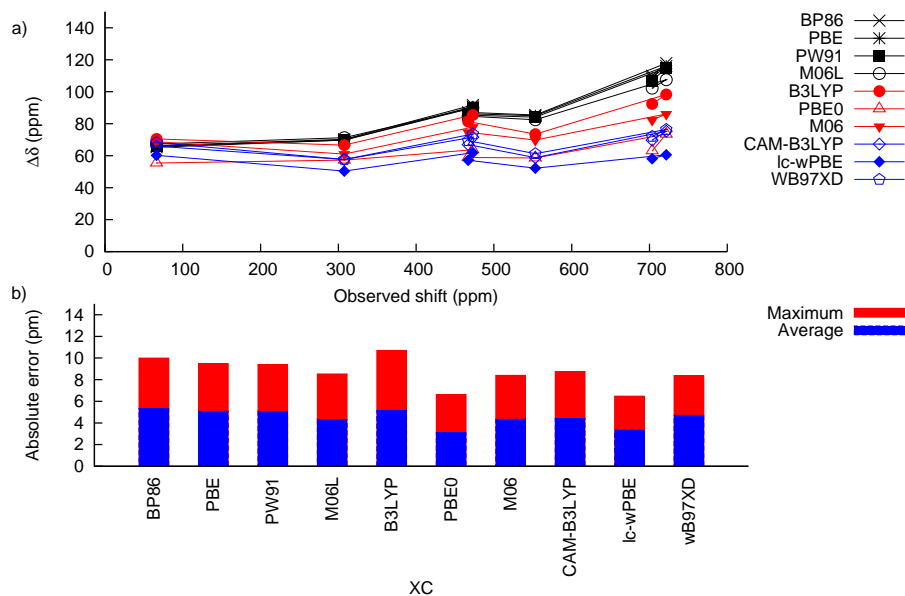
Figure S4: Computation of the ^{17}O NMR chemical shift of $[Nb_{10}O_{28}]^{6-}$ as a function of exchange correlation functional used to optimise the structure in conjunction with cc-pvtz (H-Ar) and lanl2dz (K-). All NMR shifts were were calculated using PBE0/def2-tzvp. a) Error in computed shift as a function of observed shift. Non-hybrid DFT functionals in black, hybrid DFT functionals in red and long-range corrected functionals in blue. b) Maximum and average error in computed shift as a function of exchange correlation functional.

9
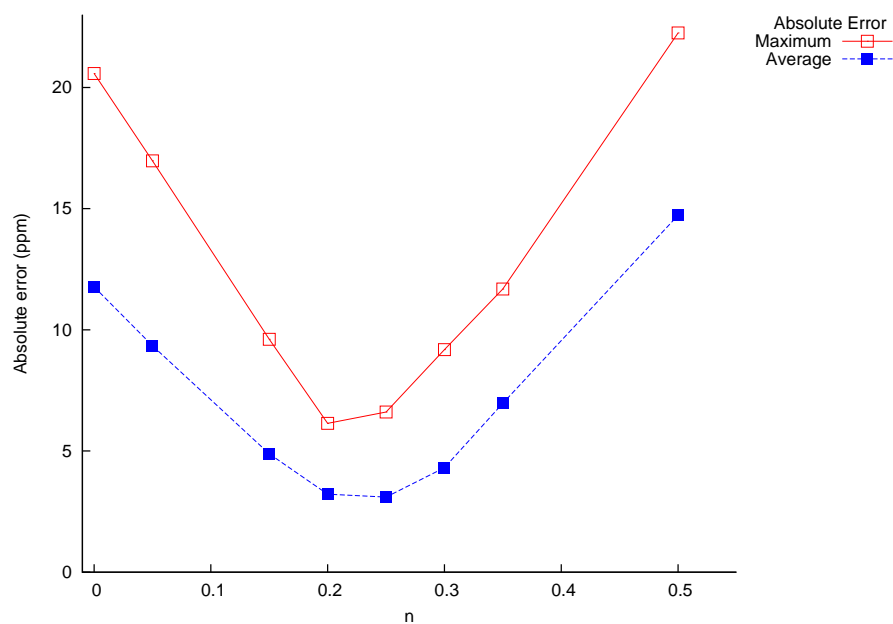
Figure S5: a) Effect on the maximum and average error in the calculated linearly regressed ^{17}O NMR chemical shift of $[Nb_{10}O_{28}]^{6-}$ of varying the HF-exchange-to-PBE-exchange ratio using n in the exchange correlation functional XC=n·HF$_{ex}$+(n-1)·PBE$_{ex}$)+PBE$_{corr}$. For the pure PBE GGA n=0.0. For the hybrid functional PBE0 n=0.25. All shift calculations were done using def2-tzvp and implicit solvation using PCM (water) with the structure optimised at PBE0/ccpvtz(H-Ar), lanl2dz (K-).

10

Table S5: Experimentally determined ^{17}O NMR shifts of polyoxovanadates. The lettering indicates different oxygen sites, the type of which are specified in parentheses. See original publication for assignment. Data used in regression is indicated with *.

Entry	Anion	A μ_6-O	B μ_3-O	C μ_2-O	D μ_2-O	E μ_2-O	F η-O (V)	G η-O (V)	H OV$_5$M	I OV$_2$M	J OM$_3$	K VOM	L OM	Cation, Solvent [Ref.]
1*	$[V_2O_7]^{4-}$			405			696							[Na]$^+$, Aq.^{b} [1]
2*	$[V_4O_{12}]^{4-}$			472			928							[Na]$^+$, Aq., pH 7 [1]
3	$[V_{10}O_{28}]^{6-}$	63	397	765	790	895	1140	1150						[Na]$^+$, Aq. pH 5.4 [2]
4		72	378	759	803	904	1160^a							[Na]$^+$, Aq. pH 4.5 [3]
5		67	396	764	790	898	1150^a							[Na]$^+$, Aq. pH 5.0 [3]
6		63	400	764	786	895	1146^a							[Na]$^+$, Aq. pH 5.5 [3]
7*		62	406	766	780	893	1143^a							[Na]$^+$, Aq. pH 6.0 [3]
8	$[V_9MoO_{28}]^{5-}$	27	436	786(C,C') 822(C")	801	895(E,E')	1153(F,F') 1169(F"')	1190	80	342		604	880	[Na]$^+$, Aq., pH ca 5-7^b [2]
9*		27.6	438.7	786(C,C') 825(C")	806	896.8 930.1(E')	1143(F,F') 1180(F")	1170.8 1191(G')	80.2	337.2		604.4	881.4	[Na]$^+$, Aq., pH ca 6-7^b [4]
10	$[HV_9MoO_{28}]^{4-}$	41.4	410.1	720 835.7	846.3 835.7	917.9 936	1187 1200	1200 1206.7	74.7	343.6		614.2	896.1	[Na]$^+$, Aq., pH ca 2^b [4]
11*	cis-$[V_8Mo_2O_{28}]^{4-}$	77.2	446.7	726	832	909.2	1165	1207			279.4	622	922.2	[Na]$^+$, Aq., pH ca 1.5^b [4]
12*	$trans$-$[V_8Mo_2O_{28}]^{4-}$	47.2		845	832	935	1198	1220			355.1	622	916	[Na]$^+$, Aq., pH ca 1.5^b [4]

^{a} Only one η-O signal was observed. ^{b} pH not explicitly indicated.

Table S6: Computed non-regressed ^{17}O NMR shifts of polyoxovanadates at PBE0/def2-tzvp//PBE0/cc-pvtz(H-Ar), lanl2dz(K-).

Entry	Anion	A μ_6-O	B μ_3-O	C μ_2-O	D μ_2-O	E μ_2-O	F η-O (V)	G η-O (V)	H OV$_5$M	I OV$_2$M	J OM$_3$	K VOM	L OM
1	$[V_2O_7]^{4-}$			405.7491			749.4465						
2	$[V_4O_{12}]^{4-}$			537.6781			986.4810						
3	$[V_{10}O_{28}]^{6-}$	72.9847	488.7242	822.8857	826.8696	923.8887	1168.6345	1165.2453					
4	$[V_9MoO_{28}]^{5-}$	121.0328	521.3673	845.4758, 845.2809(C,C') 868.0003(C")	843.9845	966.0855 932.6064(E')	1209.914, 1224.859(F,F') 1203.304(F")	1199.772 1219.654(G')	59.5768	425.9279		681.4618	929.3352
5	cis-$[V_8Mo_2O_{28}]^{4-}$	78.7002	526.2462	881.2569	881.9060	968.3087	1259.2853	1262.0740			357.5316	699.1630	970.5933
6	$trans$-$[V_8Mo_2O_{28}]^{4-}$	77.2633		886.7252	882.3726	969.5609	1260.1363	1260.6463			436.2515	695.8877	965.6687

Table S7: Experimentally determined ^{17}O NMR shifts of polyoxoniobates. The lettering indicates different oxygen sites, the type of which are specified in parentheses. See original publication and figures S10-S11 for assignment. Data used in regression is indicated with *.

Entry	Anion	A (μ_6-O)	B (μ_3-O)	C (μ_2-O)	D (μ_2-O)	E (μ_2-O)	G (η-O)	F (η-O)	Cation, Solvent [Ref.]
1	$[Nb_6O_{19}]^{8-}$	29		392		607			[K]$^+$, Aq., pH 14 [5]
2		20		386		594			Aq.,^{a} pH 13 [6]
3*		11.8		396.8		580.3			[K]$^+$, Aq., pH 14.4 (see tables S16-S18) [7]
5		37		382		612			[K]$^+$, Aq., pH 11, [OH]$^-$/[Nb$_6$O$_{19}$]$^{8-}$=3 [8]
6		36		383		612			[K]$^+$, Aq., pH 11, [OH]$^-$/[Nb$_6$O$_{19}$]$^{8-}$=4 [8]
7		29		393		612			[K]$^+$, Aq., pH 13, [OH]$^-$/[Nb$_6$O$_{19}$]$^{8-}$=10 [8]
8		38		378		635			TMA, Aq., pH 11, [OH]$^-$/[Nb$_6$O$_{19}$]$^{8-}$=3 [8]
9		38		380		631			TMA, Aq., pH 11, [OH]$^-$/[Nb$_6$O$_{19}$]$^{8-}$=4 [8]
10		32		391		612			TMA, Aq., pH 13, [OH]$^-$/[Nb$_6$O$_{19}$]$^{8-}$=10 [8]
11	$[Nb_{10}O_{28}]^{6-}$	66.425	307.939	467.055	472.738	553.717	703.598	722.067	TMA, Aq. pH 5.5 [9]
12		66.033	308.218	466.623	472.959	553.922	703.879	722.184	TMA, Aq. pH 6.1 [9]
13		66.017	307.497	466.606	472.943	553.201	703.862	721.463	TMA, Aq. pH 6.6 [9]
14		66.017	307.497	466.606	472.943	553.201	703.862	721.463	TMA, Aq. pH 7.12 [9]
15		66.262	307.741	466.850	473.186	554.148	704.105	721.705	TMA, Aq. pH 7.51 [9]
16		66.377	307.857	466.967	473.303	553.562	703.519	721.823	TMA, Aq. pH 8.1 [9]
17		66.017	308.201	466.606	472.943	553.201	703.862	722.167	TMA, Aq. pH 8.5 [9]
18		66.377	307.857	466.967	473.303	553.562	703.519	721.823	TMA, Aq. pH 9.1 [9]
19*		66.050	308.234	466.640	472.976	553.939	703.896	722.201	TMA, Aq. pH 9.6 [9]
20	$[TiNb_9O_{28}]^{7-}$	74.920	300.399 341.101 (B')	452.760 458.523 (C')	462.845	546.770 592.514 (E')	673.557 670.676 (G')	691.206	TMA, Aq. pH 6.54[9]
21		74.559	300.399 340.740 (B')	452.760 458.883 (C')	462.845	546.409 592.874 (E')	673.196 670.315 (G')	690.125	TMA, Aq. pH 7.05[9]
22		74.920	299.679 338.219 (B')	452.760 458.163 (C')	461.764	547.130 590.713 (E')	676.798 673.557 (G')	692.287	TMA, Aq. pH 7.92[9]
23		74.920	300.399 341.101 (B')	453.120 458.883 (C')	462.845	546.770 593.594 (E')	673.917 671.036 (G')	690.486	TMA, Aq. pH 8.95[9]
24		74.920	300.399 341.101 (B')	453.120 458.883 (C')	462.845	546.770 594.594 (E')	673.557 670.675 (G')	690.486	TMA, Aq. pH 9.96[9]
25		74.560	300.039 340.741 (B')	453.121 458.884 (C')	462.846	546.410 594.235 (E')	672.837 670.316 (G')	690.487	TMA, Aq. pH 10.98[9]
26		74.559	300.039 340.740 (B')	452.760 458.523 (C')	462.485	546.409 593.234 (E')	673.196 670.315 (G')	690.125	TMA, Aq. pH 11.63[9]
27		74.560	300.039 340.741 (B')	453.120 458.883 (C')	462.845	546.410 593.235 (E')	672.837 670.315 (G')	690.486	TMA, Aq. pH 12.47[9]
28		74.199	300.039 340.740 (B')	452.760 458.523 (C')	462.485	546.049 592.874 (E')	672.116 669.955 (G')	689.405	TMA, Aq. pH 13.25[9]
29	$[Ti_2Nb_8O_{28}]^{8-}$	101.934	331.735		451.678	555.773	666.712	680.399	TMA, Aq. pH 6.61 [9]
30		99.413	331.736		451.679	558.296	662.751	677.519	TMA, Aq. pH 7.15 [9]
31		97.972	332.096		451.319	561.177	661.310	676.438	TMA, Aq. pH 7.49 [9]
32*		89.327	328.854	431.508	449.158	575.225	652.666	669.234	TMA, Aq. pH 8.03 [9]
33		88.247	329.214	434.750	449.518	576.666	650.505	667.794	TMA, Aq. pH 8.52 [9]
34		87.887	329.575	435.471	449.518	577.746	649.424	666.713	TMA, Aq. pH 8.95 [9]
35		86.806	331.015	434.750	449.878	579.547	645.462	664.192	TMA, Aq. pH 9.43 [9]
36		85.725	330.655	436.191	449.158	580.267	644.381	663.111	TMA, Aq. pH 10.01 [9]
37		85.725	331.015	436.911	449.517	580.626	644.380	663.110	TMA, Aq. pH 10.45 [9]
38*		85.725	331.015	436.911	449.518	580.988	644.381	663.111	TMA, Aq. pH 10.79 [9]

^{a} Counterion not indicated.

12

Table S8: Computed non-regressed ^{17}O NMR shifts of polyoxoniobates at PBE0/def2-tzvp//PBE0/cc-pvtz(H-Ar), lanl2dz(K-).

Entry	Anion	A (μ_6-O)	B (μ_3-O)	C (μ_2-O)	D (μ_2-O)	E (μ_2-O)	F (η-O)	G (η-O)
1	$[Nb_6O_{19}]^{8-}$	70.7060		464.7897		641.7471		
2	$[Nb_{10}O_{28}]^{6-}$	121.6874	364.8398	536.6640	525.7640	611.8384	794.7706	766.5670
3	$[TiNb_9O_{28}]^{7-}$	138.1742	352.9244 (B)	528.4199 (C')	517.6431	608.2108 (E)	767.5604	742.7352 (G')
			398.3550 (B')	529.1051 (C)		659.8050 (E')		750.1919 (G)
4	$[Ti_2Nb_8O_{28}]^{8-}$	148.9896	385.9111	514.4733	500.1411	648.0585	734.7198	714.2441

13

139

Table S9: Experimentally determined ^{17}O NMR shifts of polyoxotantalates. The lettering indicates different oxygen sites, the type of which are specified in parentheses. See original publication and figures S10-S11 for assignment. Data used in regression is indicated with *.

	Anion	A (μ_6-O)	B (μ_3-O)	C (μ_2-O)	D (μ_2-O)	E (μ_2-O)	F (η-O)	G (η-O)	Cation, Solvent [Ref.]
1*	$[Ta_6O_{19}]^{8-}$	-39	328				478		K$^+$, Aq., pH 14 [5]
2		-41	329				476		Aq.,^{a} pH 13 [6]
3*	$[Ta_{10}O_{28}]^{6-}$	26	249	398	385	461	591	571	TBA, Aq./ACN^b[8]

^{a} Counterion not indicated. ^{b} pH not indicated.

Table S10: Computed non-regressed ^{17}O NMR shifts of polyoxotantalates at PBE0/def2-tzvp//PBE0/cc-pvtz(H-Ar), lanl2dz(K-).

	Anion	A (μ_6-O)	B (μ_3-O)	C (μ_2-O)	D (μ_2-O)	E (μ_2-O)	F (η-O)	G (η-O)
1	$[Ta_6O_{19}]^{8-}$	71.8385	371.5893				525.3828	
2	$[Ta_{10}O_{28}]^{6-}$	121.5488	305.6237	433.3515	417.6975	498.6297	652.0944	624.0150

Table S11: Experimentally determined ^{17}O NMR shifts of polyoxomolybdates. The lettering indicates different oxygen sites, the type of which are specified in parentheses. See original publication and figures S10-S11 for assignment. Data used in regression is indicated with *.

	Anion	A μ_6-O	B OMo_3	C OMo_2	D OMo_2	E OMo_2	F (η-O (Mo))	G (η-O (Mo))	H MOMo	I OM_2	J (η-O (M))	Cation, Solvent [Ref.]
1*	$[Mo_6O_{19}]^{2-}$	-32		559			927					TBA, DMF [5, 10]
2				563			933					TBA, ACN [5]
3*	$[VMo_5O_{19}]^{3-}$	-22		541	531		885		665		1200	TBA, ACN [5]
4*	$[V_2Mo_4O_{19}]^{4-}$			489	498		862		604		1165	[Na]$^+$, Aq. [2]
5*	$[TeMo_6O_{24}]^{6-}$		180	383			807					[Na]$^+$, Aq. pH 5.8 [5]
6*	$[H_6AlMo_6O_{24}]^{3-}$			378			833					[Na]$^+$, Aq. pH 4.1 [5]
		μ_4-O										
7	$[Mo_7O_{24}]^{6-}$	123	338	400	758		821					[Na]$^+$, Aq. pH 5.5 [11]
8		123	335	395	757		814					[Na]$^+$, Aq. pH 5.5 [5]
9		123	340	398	759		824					[NH$_4$]$^+$, Aq. pH 5.4 [5]
10*		122	340	397	750		817(F)					[NH$_4$]$^+$, Aq.,^{a} [12]
			354		757		824(F',F")					
11*	$\alpha-[Mo_8O_{26}]^{4-}$		495	396	775		866					TBA, ACN, [5, 10]
12*	$\beta-[Mo_8O_{26}]^{4-}$	56	296	425	743		866	900(F',F",F"')				TBA, ACN [5, 10]
13*	$[PMo_{12}O_{40}]^{3-}$	78		583	550		936					TBA, ACN [5]
14*	$[SiMo_{12}O_{40}]^{4-}$	41		580	555		928					TBA, ACN [5]
15*	$[GaMo_{12}O_{40}]^{5-}$			575	568		923					[H]$^+$, Aq. [13]

^{a} pH not given.

Table S12: Computed non-regressed ^{17}O NMR shifts of polyoxomolybdates at PBE0/def2-tzvp//PBE0/cc-pvtz(H-Ar), lanl2dz(K-).

	Anion	A μ_6-O	B OMo_3	C OMo_2	D OMo_2	E OMo_2	F $(\eta\text{-}O\ (Mo))$	G $(\eta\text{-}O\ (Mo))$	H $MOMo$	I OM_2	J $(\eta\text{-}O\ (M))$
1	$[Mo_6O_{19}]^{2-}$	24.1773		634.4282			1006.6900				
2	$[VMo_5O_{19}]^{3-}$	-2.1462		587.1757	580.6522		955.1359		703.6874		1278.9114
3	$[V_2Mo_4O_{19}]^{4-}$			547.4077	653.1606		894.5740		692.2472		1185.3398
4	$[TeMo_6O_{24}]^{6-}$		247.2371	472.8190			862.6313				
5	$[H_6AlMo_6O_{24}]^{3-}$			480.4051			918.2591				
		μ_4-O									
6	$[Mo_7O_{24}]^{6-}$	202.1697	436.1738	497.0060	781.1074		873.1187(F)	833.9954			
			452.7282		785.1972		882.3631(F',F")				
7	$\alpha-[Mo_8O_{26}]^{4-}$		557.6329	483.9945	850.9894		928.0600				
9	$[PMo_{12}O_{40}]^{3-}$	134.9841		653.2265	622.8281		1011.6802				
10	$[SiMo_{12}O_{40}]^{4-}$	96.4548		651.1499	625.8577		1007.1545				
11	$[GaMo_{12}O_{40}]^{5-}$			662.4293	634.1072		995.0366				
		μ_5-O									
8	$\beta-[Mo_8O_{26}]^{4-}$	124.3076	410.3020	499.3071	802.7165		932.7817(F) 917.3511(F') 926.5983(F") 955.9130(F"')	962.4964			

16

142

Table S13: Experimentally determined ^{17}O NMR shifts of polyoxotungstates. The lettering indicates different oxygen sites, the type of which are specified in parentheses. See original publication and figures S10-S11 for assignment. Data used in regression is indicated with *.

	Anion	A μ_6-O	B OW$_3$	C OW$_2$	D OW$_2$	E OW$_2$	F (η-O (W))	G (η-O (W))	W-O-M	OM$_2$	(η-O (M))	Cation, Solvent [Ref.]
1*	[W$_6$O$_{19}$]$^{2-}$	-81		413			772					TBA, DMF [14, 5]
2*	[NbW$_5$O$_{19}$]$^{3-}$	-67	392	394			730	732	456		799	TBA, ACN [15]
3*	[TaW$_5$O$_{19}$]$^{3-}$	-73	93	394			731	733	420		666	TBA, ACN [15]
4*	[VW$_5$O$_{19}$]$^{3-}$	-75	395	389			731		562		1217	TBA, ACN [14, 5]
5*	[TiW$_5$(OMe)O$_{18}$]$^{3-}$	-58	380	390			713	721	525			TBA, ACN [16]
6*	[SnW$_5$(OMe)O$_{18}$]$^{3-}$	17	363	383			684	720	395			TBA, ACN [17]
7*	[Nb$_2$W$_4$O$_{19}$]$^{4-}$		374				691		435(H,H')	493	753	TBA, ACN [15]
8*	[V$_2$W$_4$O$_{19}$]$^{4-}$	-65	371	384			687		530(H,H')	848	1162	TBA, ACN [14]
9*	[W$_{10}$O$_{32}$]$^{4-}$	-6	430	416			762					TBA, ACN [5]
		-1.6	434	421	423		765	732				TBA, ACN [18]
		A μ_4-O										
10*	[W$_7$O$_{24}$]$^{6-}$	71	254 295	314	590	595	648(F,F',F'')	624				[Na]$^+$, Aq.^{a} [12]
11*	[BW$_{12}$O$_{40}$]$^{5-}$	49		410			740					[Na]$^+$, Aq., pH 6.5-7.0^a [19]
12*	[PW$_{12}$O$_{40}$]$^{3-}$			431	405		769					TBA, Aq.^{a} [5]
		68		429	410		770					TBA, ACN [20]
13*	[SiW$_{12}$O$_{40}$]$^{4-}$	27		427	405		761					TBA, ACN [5, 20]
14*	[GaW$_{12}$O$_{40}$]$^{5-}$			417	410		756					[H]$^+$, Aq.^{a} [21, 20]

^{a} pH not given or not explicitly given.

Table S14: Computed non-regressed ^{17}O NMR shifts of polyoxotungstates at PBE0/def2-tzvp//PBE0/cc-pvtz(H-Ar), lanl2dz(K-).

	Anion	A μ_6-O	B OW_3	C OW_2	D OW_2	E OW_2	F (η-O (W))	G (η-O (W))	H W-O-M	I OM_2	J (η-O (M))
1	$[W_6O_{19}]^{2-}$	27.1091		471.6662			807.2543				
2	$[NbW_5O_{19}]^{3-}$	26.6769		447.3100			768.7669		507.8898		843.8781
3	$[TaW_5O_{19}]^{3-}$	33.2494		448.4662			768.0084		469.9926		692.2944
4	$[VW_5O_{19}]^{3-}$	19.1239		448.8332			769.9133		599.8506		1264.4884
5	$[TiW_5(OMe)O_{18}]^{3-}$	36.7791		437.2122	444.0949		748.4535	755.1191	570.8406		
6	$[SnW_5(OMe)O_{18}]^{3-}$	97.7043		414.1766	438.8812		713.5677	750.2890	451.0481		
7	$[Nb_2W_4O_{19}]^{4-}$	40.6921		429.1183			732.5865		485.6050 483.5458	547.9321	796.4729
8	$[V_2W_4O_{19}]^{4-}$	22.8015		428.8062			846.7756		563.4016 556.4016(H')	762.6024	1199.6009
9	$[W_{10}O_{32}]^{4-}$	75.7722		458.9297	473.5959	484.6224	770.3677	803.9238			
		μ_4-O									
10	$[W_7O_{24}]^{6-}$	153.9535	327.3486 357.6217	381.8083	637.3061	649.9097	699.0286 692.4312(F',F'')	664.5313			
11	$[BW_{12}O_{40}]^{5-}$	113.2042		450.9616	471.4723		785.5085				
12	$[PW_{12}O_{40}]^{3-}$	135.8173		455.1303	487.9224		805.3313				
13	$[SiW_{12}O_{40}]^{4-}$	97.4293		453.5796	486.0730		803.9524				
14	$[GaW_{12}O_{40}]^{5-}$			455.6311	493.4255		801.1723				

18

144
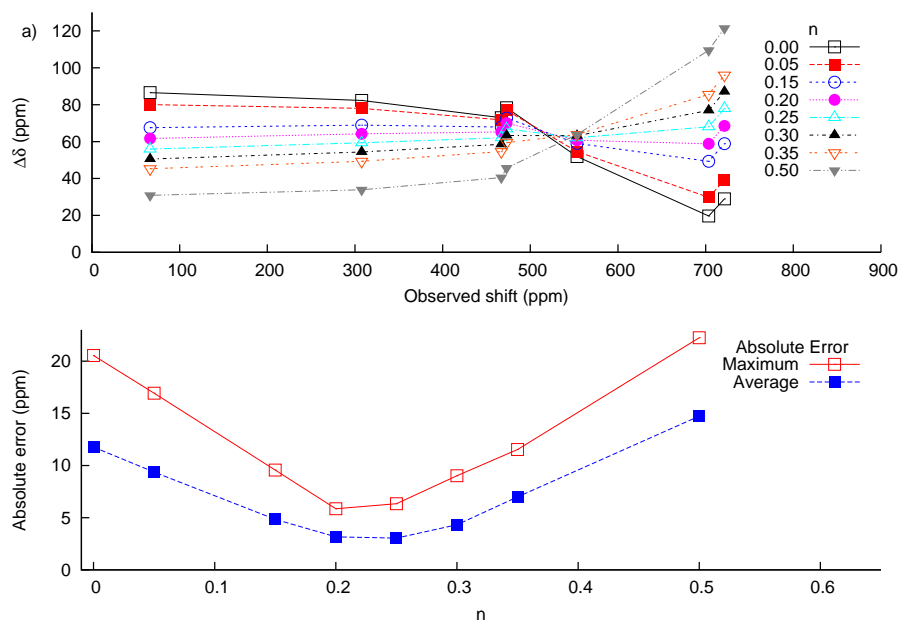
Figure S6: Effect on the calculated non-regressed ^{17}O NMR chemical shift of $[Nb_{10}O_{28}]^{6-}$ of varying the HF-exchange-to-PW91-exchange ratio using n in the exchange correlation functional $XC=n\cdot HF_{ex}+(n-1)\cdot PW91_{ex})+PW91_{corr}$, and b) effect on the maximum and average error in the calculated linearly regressed ^{17}O NMR chemical shift. All shift calculations were done using def2-tzvp and with implicit solvation using PCM (water), and using a structure optimised at PBE0/cc-pvtz(H-Ar), lanl2dz(K-).

```matlab
K=[10^(-9.35)  10^(-9.92)  10^(-13.63)];
h=logspace(-9,-14,100);
Ctot=1.0;
species=speciation(K,h,Ctot);
plot(-log10(h),species(:,:))
```

Listing S1: control.m

```matlab
function curve=speciation(k,h,ctot)
  k=[1 k];

  for n=1:size(k,2)
    knew(n,1)=prod(k(1,1:n),2);
    hnew(n,:)=h.^(n-1)';
  end
  vector=(knew'./hnew');
  c=vector(:,2);
  c=ctot./sum(vector,2);
  curve=[c.*vector];
end
```

Listing S2: speciation.m

19

Table S15: Computed non-regressed ^{17}O NMR shifts in ppm of protonated and unprotonated structures of $[\text{Nb}_6\text{O}_{19}]^{8-}$ at PBE0/def2-tzvp//PBE0/cc-pvtz(H-Ar), lanl2dz(K-). The different isomers are listed in the same order as in figure S8. The lowest energy isomers at pbe0/def2-tzvp are marked with bold; $\Delta\epsilon$ is given relative to the lowest energy isomer for each protonation state.

Entry	Number of protons	δ μ_6-O	δ μ_2-O	δ η=O	ϵ (a.u.)	$\Delta\epsilon$ (kcal)
1	0	**71**	**465**	**642**	-1772.79383817	0
2	1	**89**	**452**	**679**	-1773.32865682	0
3	2	100	438	715	-1773.84487818	0.4391
4		99	437	714	-1773.84142771	2.6043
5		105	442	718	-1773.83768080	4.9555
6		105	442	720	-1773.83737179	5.1494
7		**98**	**439**	**722**	-1773.84557801	0
8		97	438	722	-1773.84547981	0.0616
9		105	439	721	-1773.8406571	3.0879
10		107	439	720	-1773.84094689	2.9060
11	3	109	421	757	-1774.3391972	5.3238
12		111	423	759	-1774.3388020	5.5718
13		**99**	**415**	**757**	-1774.3476813	0
14		111	426	757	-1774.33818085	5.9616
15		103	422	758	-1774.34387887	2.3860
16		106	422	749	-1774.34226680	3.3976
17		120	430	762	-1774.32708771	12.923
18		121	430	762	-1774.32677228	13.120
19		112	422	756	-1774.34242317	3.2995
20		120	430	762	-1774.32713339	12.894
21		112	422	755	-1774.34196575	3.5865
22		120	430	762	-1774.32712675	12.898
23		111	425	755	-1774.33816727	5.9701
24		109	423	754	-1774.33525822	7.7955
25		110	430	776	-1774.32831278	12.154
26		110	422	758	-1774.33525822	7.7955
27		112	422	755	-1774.34200367	3.5627
28		122	441	780	-1774.31576440	20.028
29		120	430	762	-1774.32712033	12.902
30		112	422	756	-1774.34242370	3.2992
31		120	430	762	-1774.32708035	12.927
32		121	430	762	-1774.32677621	13.118
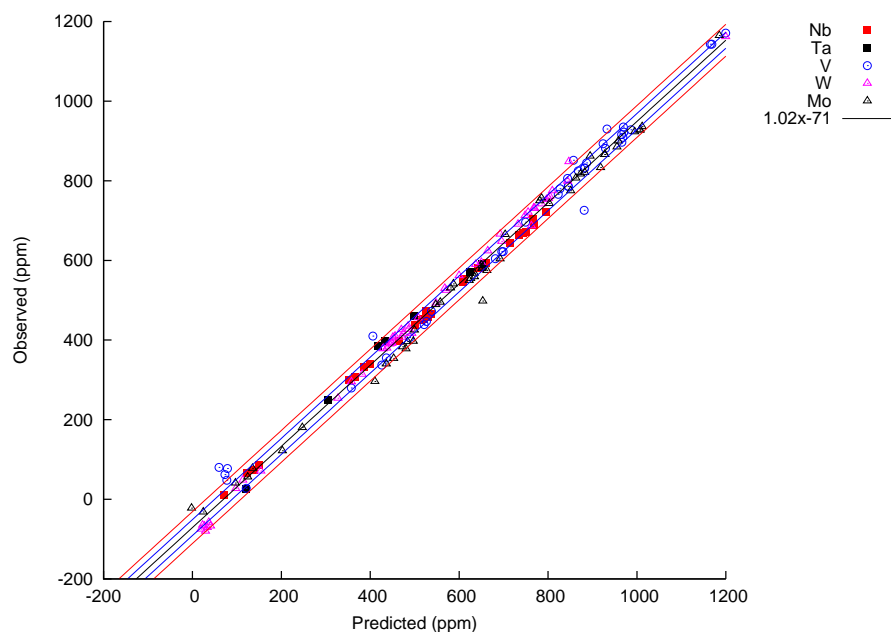
Figure S7: Predicted vs observed ^{17}O NMR chemical shifts for all the compounds in the test set. The coefficient of determination is 0.993.

Table S16: Extracted chemical shifts for the η-oxygen site in the hexaniobate ion as a function of pH. The data was extracted from figure 4 in Black *et al.*, *J. Am. Chem. Soc.*, **2006**, *128*, 14712-14720.

Temperature (K)	pH	Shift (ppm)
277	10.11	626.96
	10.25	625.58
	10.36	624.61
	11.06	615.64
	11.35	610.52
	12.39	602.79
	12.96	601.13
	13.33	598.51
	13.39	598.92
	14.30	586.08
298	11.11	612.87
	11.22	610.52
	12.25	604.17
	12.64	602.10
	13.11	600.03
	13.52	594.78
	13.67	592.43
	13.98	587.04
	14.43	580.28
303	12.91	599.75

21
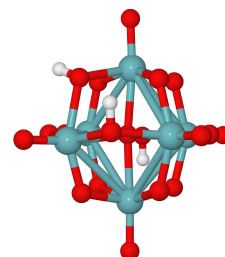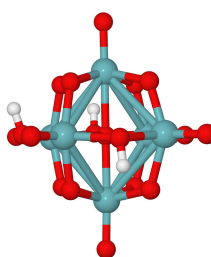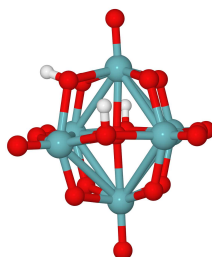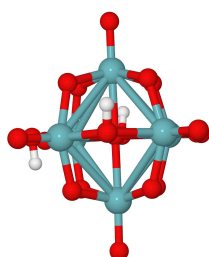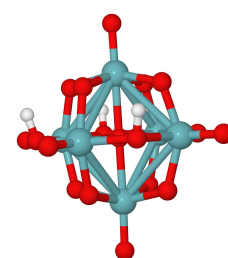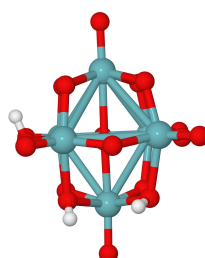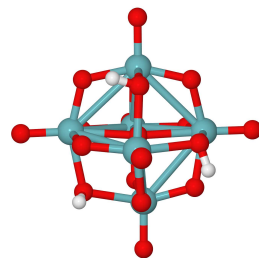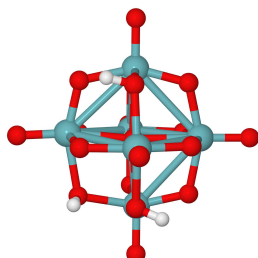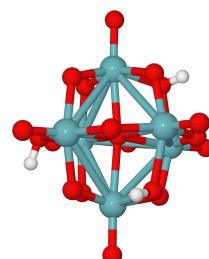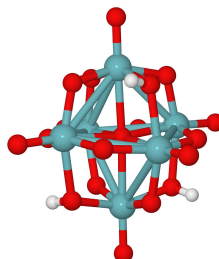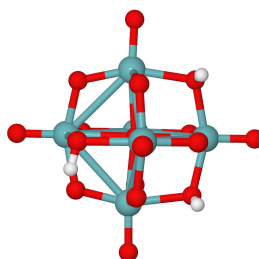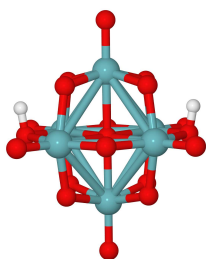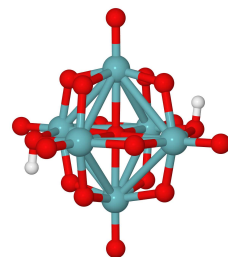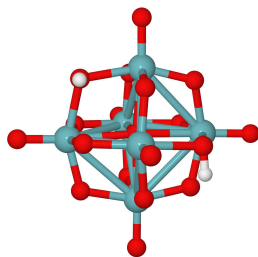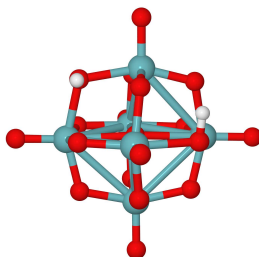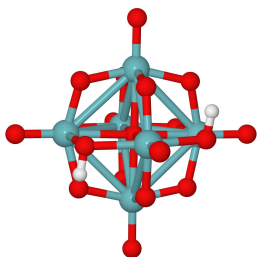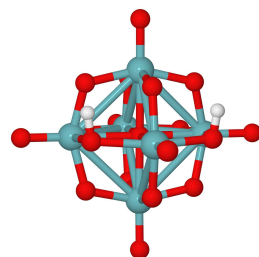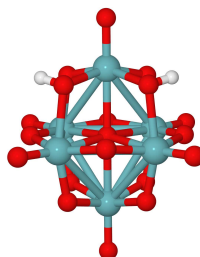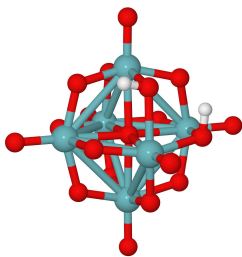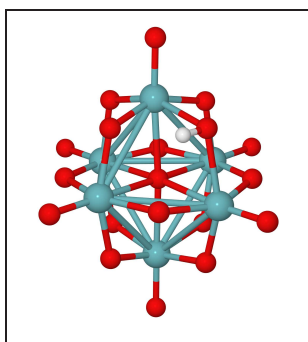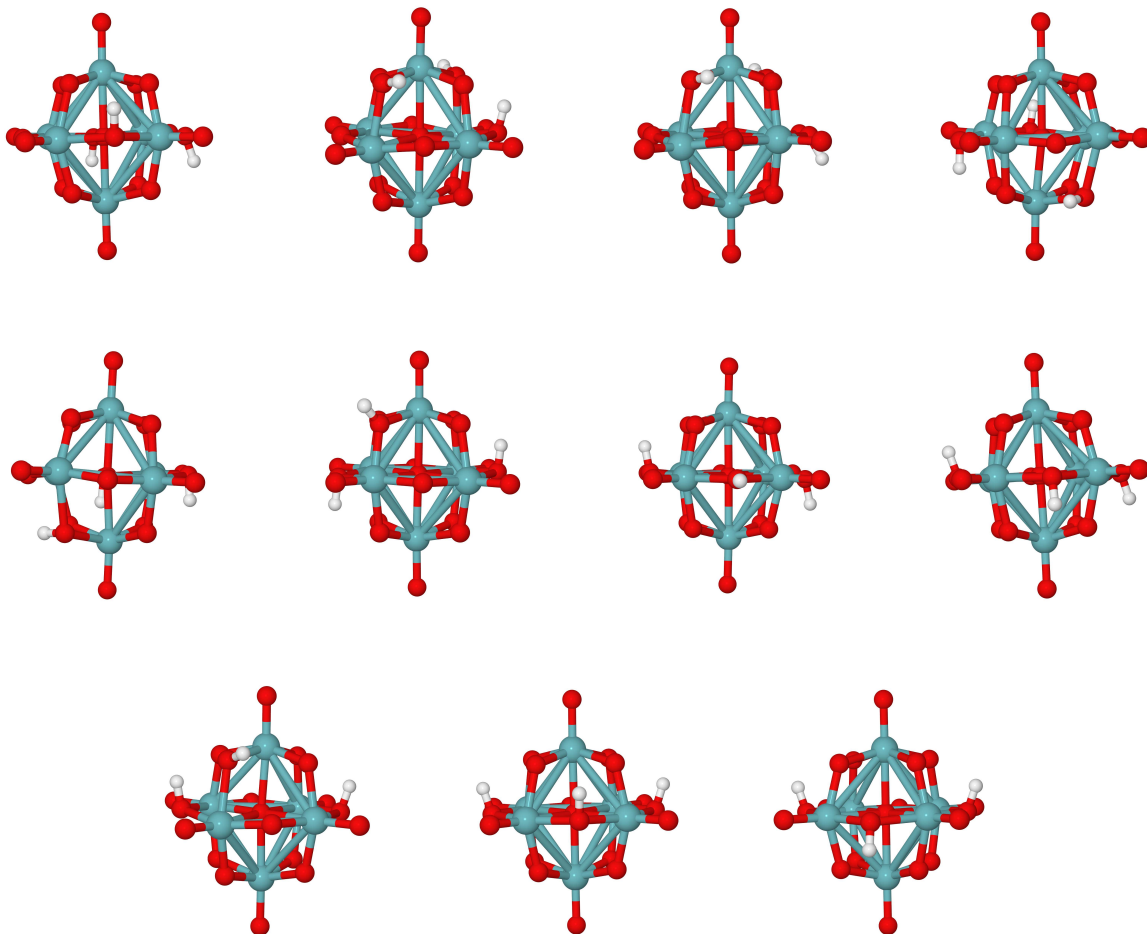
Figure S8: The lowest energy isomers for each protonation state are framed. From left to right, top row (energy in parenthesis): $[HNb_6O_{19}]^{7-}$ (-1773.32865682 a.u.), $[H_2Nb_6O_{19}]^{6-}$ (-1773.84487818 a.u.), $[H_2Nb_6O_{19}]^{6-}$ (-1773.84142771 a.u.) and $[H_2Nb_6O_{19}]^{6-}$ (-1773.8376808 a.u.). Second row: $[H_2Nb_6O_{19}]^{6-}$ (-1773.83737179 a.u.), $[H_2Nb_6O_{19}]^{6-}$ (-1773.84557801 a.u.), $[H_2Nb_6O_{19}]^{6-}$ (-1773.84547981 a.u.) and $[H_2Nb_6O_{19}]^{6-}$ (-1773.8406571 a.u.). Third row: $[H_2Nb_6O_{19}]^{6-}$ (-1773.84094689 a.u.), $[H_3Nb_6O_{19}]^{6-}$ (-1774.3391972 a.u.), $[H_3Nb_6O_{19}]^{6-}$ (-1774.338802 a.u.) and $[H_3Nb_6O_{19}]^{6-}$ (-1774.3476813 a.u.). Fourth row: $[H_3Nb_6O_{19}]^{6-}$ (-1774.33818085 a.u.), $[H_3Nb_6O_{19}]^{6-}$ (-1774.34387887 a.u.), $[H_3Nb_6O_{19}]^{6-}$ (-1774.34226680 a.u.) and $[H_3Nb_6O_{19}]^{6-}$ (-1774.32708771 a.u.). Fifth row: $[H_3Nb_6O_{19}]^{6-}$ (-1774.32677228 a.u.), $[H_3Nb_6O_{19}]^{6-}$ (-1774.34242317 a.u.), $[H_3Nb_6O_{19}]^{6-}$ (-1774.32713339 a.u.) and $[H_3Nb_6O_{19}]^{6-}$ (-1774.34196575 a.u.). Sixth row: $[H_3Nb_6O_{19}]^{6-}$ (-1774.32712675 a.u.), $[H_3Nb_6O_{19}]^{6-}$ (-1774.33816727 a.u.), $[H_3Nb_6O_{19}]^{6-}$ (-1774.33525822 a.u.) and $[H_3Nb_6O_{19}]^{6-}$ (-1774.32831278 a.u.). Seventh row: $[H_3Nb_6O_{19}]^{6-}$ (-1774.33525822 a.u.), $[H_3Nb_6O_{19}]^{6-}$ (-1774.34200367 a.u.), $[H_3Nb_6O_{19}]^{6-}$ (-1774.31576440 a.u.) and $[H_3Nb_6O_{19}]^{6-}$ (-1774.32712033 a.u.). Eighth row: $[H_3Nb_6O_{19}]^{6-}$ (-1774.34242370 a.u.), $[H_3Nb_6O_{19}]^{6-}$ (-1774.32708035 a.u.) and $[H_3Nb_6O_{19}]^{6-}$ (-1774.32677621 a.u.)

23
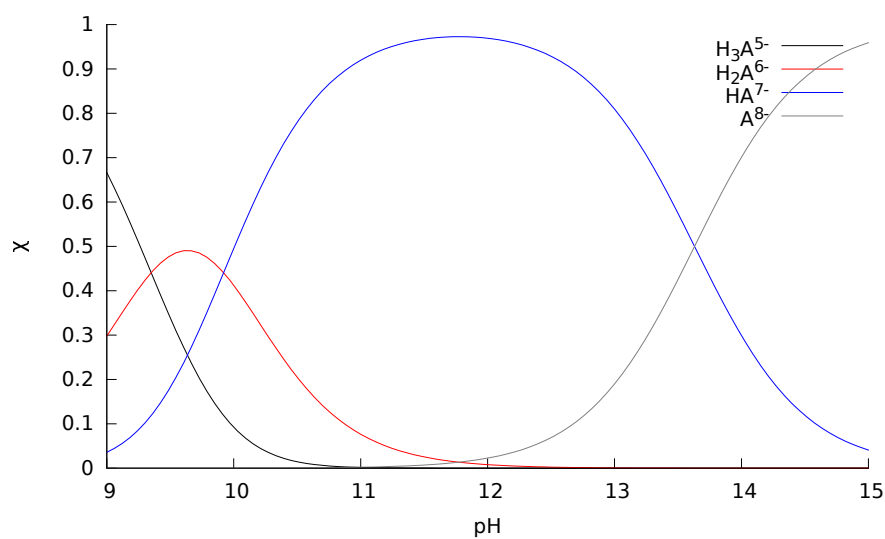
Figure S9: Speciation of the hexaniobate Lindqvist ion as a function of pH simulated using the Octave code in listings S1 and S2.

Table S17: Extracted chemical shifts for the μ_2-oxygen site in the hexaniobate ion as a function of pH. The data was extracted from figure 4 in Black *et al.*, *J. Am. Chem. Soc.*, **2006**, *128*, 14712-14720.

Temperature (K)	pH	Shift (ppm)
277	10.14	376.85
	10.24	377.40
	10.37	378.49
	11.06	380.55
	11.36	383.70
	12.40	386.99
	12.97	387.95
	13.33	389.04
	13.40	390.00
	14.30	395.62
298	11.11	382.19
	11.23	383.15
	12.25	387.67
	12.65	387.81
	13.13	389.32
	13.54	390.82
	13.69	392.05
	13.99	394.25
	14.46	396.85
303	12.93	388.63

24

Table S18: Extracted chemical shifts for the μ_6-oxygen site in the hexaniobate ion as a function of pH. The data was extracted from figure 4 in Black *et al.*, *J. Am. Chem. Soc.*, **2006**, *128*, 14712-14720.

Temperature (K)	pH	Shift (ppm)
277.00	10.13	31.10
	10.25	30.41
	10.36	30.27
	11.06	27.26
	11.36	25.62
	12.40	22.74
	12.96	21.92
	13.33	21.10
	13.39	21.51
	14.30	15.07
298.00	11.11	26.44
	11.23	25.75
	12.25	24.25
	12.64	24.25
	13.11	22.05
	13.53	19.59
	13.68	18.08
	13.99	15.48
	14.44	11.78
303.00	12.92	21.78

25
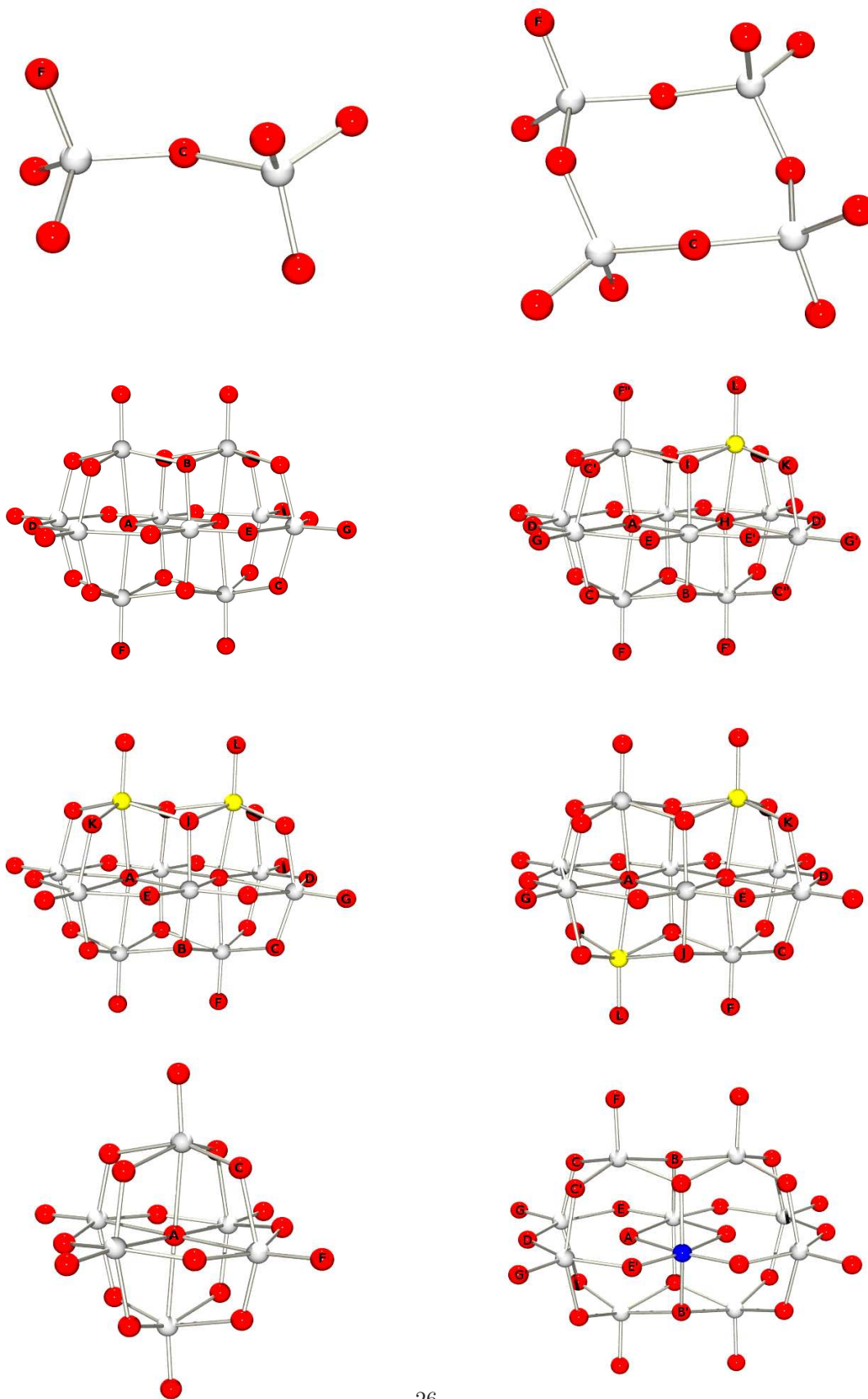
Figure S10: Key I to oxygen types referred to in tables S5-S14. Row 1, left: $[V_2O_7]^{4-}$. Right: $[V_4O_{12}]^{4-}$. Row 2, left: $[M_{10}O_{28}]^{x-}$. Right: $[V_9MoO_{28}]^{5-}$. Row 3, left: cis–$[V_8Mo_2O_{28}]^{4-}$. Right: trans–$[V_8Mo_2O_{28}]^{4-}$. Row 4, left: $[M_6O_{19}]^{x-}$. Right: $[TiNb_9O_{28}]^{7-}$.
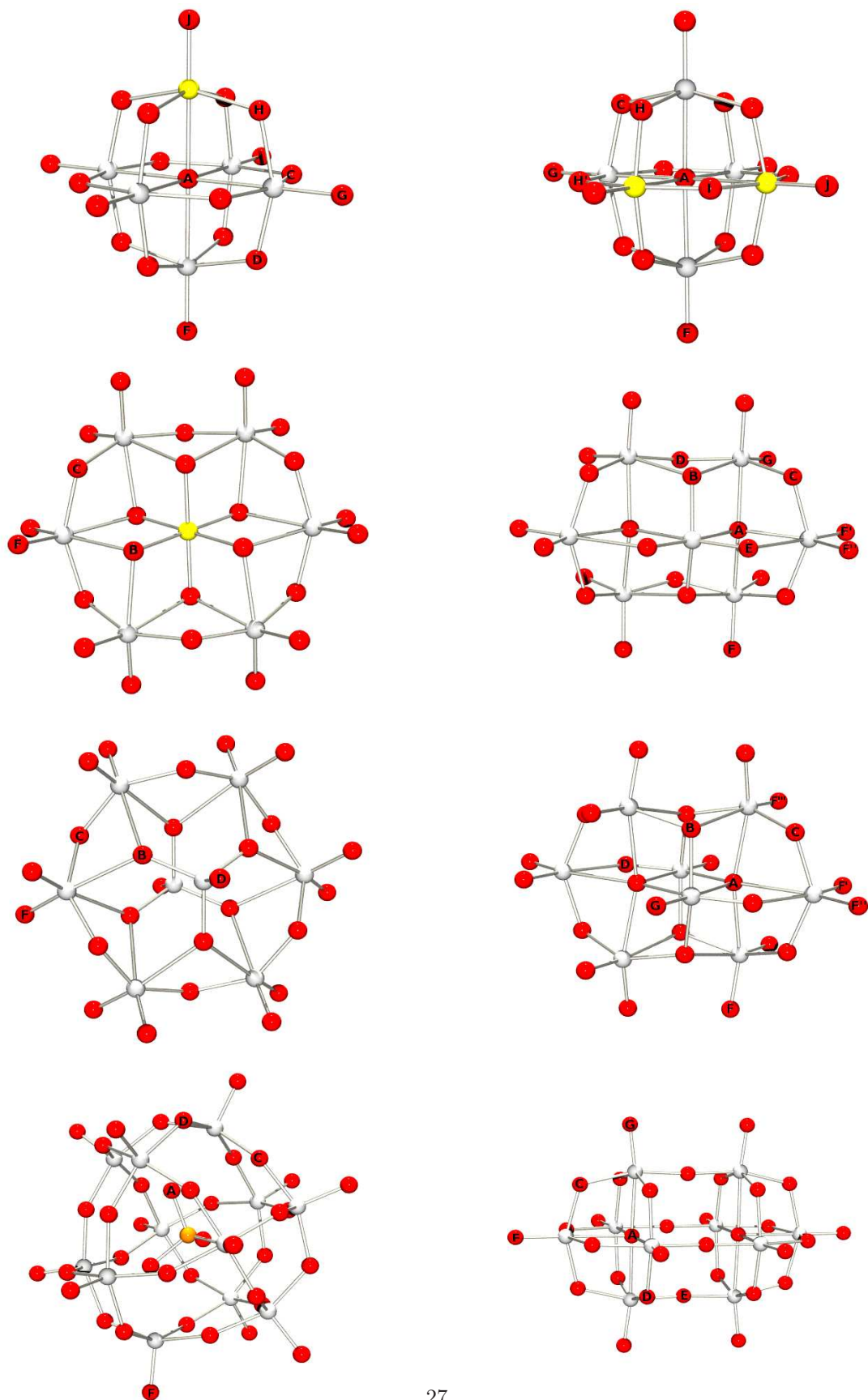
Figure S11: Key II to oxygen types referred to in tables S5-S14. Row 1, left: $[M'M_5O_{19}]^{x-}$ and $[M'(OMe)M_5O_{18}]^{x-}$. Right: $[M'_2M_4O_{19}]^{x-}$. Row 2, left: $H_n[M'Mo_6O_{24}]^{x-}$. Right: $[M_7O_{24}]^{6-}$. Row 3, left: $\alpha-[Mo_8O_{26}]^{4-}$. Right: $\beta-[Mo_8O_{26}]^{4-}$. Row 4, left: $[M'M_{12}OO_{40}]^{x-}$. Right: $[W_{10}O_{32}]^{4-}$.

References

[1] E. Heath, O. W. Howarth, *J. Chem. Soc., Dalton Trans.* **1981**, *5*, 1105–1110.

[2] R. I. Maksimovskaya, N. N. Chumachenko, *Polyhedron* **1987**, *6*, 1813–1821.

[3] W. G. Klemperer, W. Shum, *J. Am. Chem. Soc.* **1977**, *99*, 3544–3545.

[4] O. W. Howarth, *J. Chem. Soc., Dalton Trans.* **1989**, *10*, 1915–1923.

[5] M. Filowitz, R. K. C. Ho, W. G. Klemperer, W. Shum, *Inorg. Chem.* **1979**, *18*, 93–103.

[6] A. D. English, J. P. Jesson, W. G. Klemperer, T. Mamouneas, L. Messerle, W. Shum, A. Tramontano, *J. Am. Chem. Soc.* **1975**, *97*, 4785–4786.

[7] J. R. Black, M. Nyman, W. H. Casey, *J. Am. Chem. Soc.* **2006**, *128*, 14712–14720.

[8] W. G. Klemperer, K. A. Marek, *Eur. J. Inorg. Chem.* **2013**, 1762–1771.

[9] E. M. Villa, Personal communication.

[10] W. G. Klemperer, *Angew. Chem. Int. Ed. Engl.* **1978**, *17*, 246–254.

[11] W. G. Filowitz, M. Klemperer, W. Messerle, L.and Shum, *J. Am. Chem. Soc.* **1976**, *98*, 2345–2346.

[12] R. I. Maksimovskaya, K. G. Burtseva, *Polyhedron* **1985**, *4*, 1559–1562.

[13] L. P. Tsiganok, A. B. Vishnikin, R. I. Maksimovskaya, *Polyhedron* **1989**, *8*, 2739–2742.

[14] W. G. Klemperer, W. Shum, *J. Am. Chem. Soc.* **1978**, 4891–4893.

[15] C. J. Besecker, W. G. Klemperer, D. J. Maltibie, D. A. Wright, *Inorg. Chem.* **1985**, *24*, 1027–1032.

[16] R. J. Errington, S. S. Petkar, P. S. Middleton, W. McFarlane, W. Clegg, R. A. Coxall, R. W. Harrington, *Dalton Trans.* **2007**, 5211–5222.

[17] B. Kandasamy, C. Wills, W. McFarlane, W. Clegg, R. W. Harrington, Rodríguez-Fortea, J. M. Poblet, P. G. Bruce, R. J. Errington, *Chem. Eur. J.* **2012**, *18*, 59–62.

[18] D. C. Duncan, C. L. Hill, *RSC Adv.* **2014**, *4*, 7094–7103.

[19] R. I. Maksimovskaya, G. M. Maksimov, *Inorg. Chem.* **2011**, *50*, 4725–4731.

[20] R. I. Maksimovskaya, M. A. Fedotov, *J. struc. Chem.* **2006**, *47*, 1559–1562.

[21] L. P. Kazansky, M. A. Fedotov, *Izv. Akad. Nuak SSSR, Ser. Khim.* **1988**, *9*, 2000–2003.

28

Chapter5
A DFT approach for calculation of ^{51}V, ^{183}W, ^{95}Mo and ^{31}P NMR shifts in polyoxometalates

Abstract

We employ density functional theory for predicting NMR chemical shifts of four different nuclei (^{31}P, ^{51}V, ^{183}W and ^{95}Mo) in a wide range of polyoxometalates with a view to interpret complex experimental measurements. The impact of exchange-correlation functional on the predictive capability of chemical shifts was investigated. We find that the accurate prediction of NMR chemical shifts benefit from the use of hybrid functionals and bigger basis sets together with linear regression. Moreover, the inclusion of implicit solvation model for all nuclei and the incorporation of relativistic effects for heavy metals, ^{183}W and ^{95}Mo, are nearly mandatory for computing chemical shifts close to the observed results. The ^{51}V chemical shifts are predicted best at SAOP/TZP level, while PBE0/TZP is required for accurate computation of ^{183}W NMR shifts in asymmetrical and mixed-metal complexes. For 14 polyoxovanadates with 33 ^{51}V signals and 18 polyoxotungstates with 66 ^{183}W signals, we achieve a good agreement between the experimental and predicted results. We found a large discrepancy in the predicted and observed ^{95}Mo chemical shifts, yet the relative ordering of the signals was accurately predicted. Using PBE0/def2-tzvp for computing ^{31}P chemical shifts in seven Keggin complexes, an average absolute error

of 0.34 ppm was obtained. The study demonstrates that computations may not be able to estimate the observed results precisely, yet they provide a mock spectrum which, at best, resembles experimental spectrum.

1 Introduction

Polyoxometalates are discrete clusters of group 5 and 6 elements in their highest oxidation states.[1] Metal-oxide structures with only one type of transition metal such as Mo, W, V, or Nb constitute isopolyanions, while heteropolyanions consisting of mixed metals are widely applied in the field of catalysis and as model compounds for understanding of solution dynamics of minerals.[2] The first heteropolyanion to be solved using X-ray diffraction analysis was α-$[PW_{12}O_{40}]^{3-}$ by Keggin in 1934, and from then the complexes of general formula $[XM_{12}O_{40}]^{q-}$ are widely known as Baker-Figgis-Keggin structures where X= B, Al, Ga, Si, Ge, P, As or V. The transition element M, by definition, is Mo, W, V, Ta or Nb.[3]

NMR spectroscopy is a powerful tool for structural characterisation of polyoxometalates, and also useful in studying their complex reaction dynamics in aqueous solution.[4, 5, 6] The non-equivalent atoms in each complex display different chemical shifts on the NMR spectrum which are extremely sensitive to the structural parameters and the environmental changes. Each nucleus carries distinct information which supports or complements the information from other nuclei and taken together they reveal the structural aspects of a complex which is sometimes unachievable by any other technique.
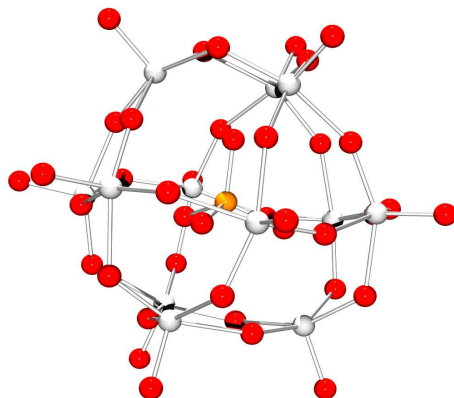
Figure 1: Structure of a Keggin molecule, $[XW_{12}O_{40}]^{q-}$. The tungsten atoms are shown in grey, red circles denote oxygen atoms and the central orange atom (X) can be P, Si, Ga and B.

Several properties of metal nuclei must be taken into account for NMR data to be useful, and the two most important are natural abundance and sensitivity. The use of NMR for heavy metals is hampered by factors like low gyromagnetic ratio, sensitivity or quadrupolar relaxation. Amongst the four heavy metals, Mo, W, V and Nb, ^{51}V is the most abundant and widely-used NMR active nucleus, followed by tungsten. ^{51}V NMR spectroscopy is a very informative method in characterising the compounds particularly in mixed metal complexes with niobium or molybdenum which are difficult to be seen by NMR spectroscopy. The quadrupolar ^{51}V nucleus gives broad signals, but allows spectroscopic measurements in very dilute solutions because of its high abundance. Significant amount of data is available for chemical shifts of ^{183}W nucleus (14.4 % natural abundance, I = 1/2), spanning ca. 8000 ppm.[7] Despite the low sensitivity of this nucleus, high resolution can be achieved

with the use of high-field spectrometers. The molybdenum nucleus has two active NMR isotopes, ^{95}Mo and ^{97}Mo. ^{95}Mo is generally preferred over the latter as it has lower quadrupolar moment than ^{97}Mo.[8] ^{93}Nb NMR is not used as the signals are too broad which makes the spectrum not very informative.

The assignment of each resonance to the corresponding atom can be straightforward if the complex is symmetrical with fewer unique atoms or the resonances are of different intensities. However, a variety of complexes have been reported which have low symmetry or have multiple heavy metals incorporated in them such that the NMR spectrum is sufficiently complicated. A potentially simple solution to this problem is to look for alternative methods that can help in interpretation of complex NMR spectra.

The application of Density functional theory (DFT) in predicting NMR chemical shifts is a powerful method even for large compounds like polyoxometalates.[9, 10, 11] Various routes have been taken within DFT for calculation of shielding of NMR active nuclei by tuning the computational parameters such as basis sets and exchange-correlation functionals, in order to achieve high level of accuracy at comparatively low cost. Pure-DFT functionals have been largely used for computing NMR properties in these bulky complexes owing to their advantage of being less computationally demanding.[11, 12] While hybrid functionals are also essentially pure-DFT functionals, they also include a certain fraction of Hartree-Fock exchange in their exchange part which makes them more expensive. Our group has recently published a detailed study on the influence of Hartree-Fock exchange in predicting ^{17}O NMR shifts in a wide range of polyoxometalate compounds.[13] It is seen that the hybrid functionals

compensate for their high cost by yielding less and systematic errors in calculated chemical shifts than pure-DFT functionals. Implicit solvation is also key to getting energy levels right for anions. For this reason, it is important to use a solvation model like COSMO or PCM in which the solute molecule is immersed in a cavity of a continuous medium.[14, 15] Therefore, as NMR predictions rely heavily on the choice of computational parameters, by modelling these parameters wisely, DFT can be very useful in providing theoretical guidance to experimental observations.

A DFT method was applied on gas-phase optimised geometries of glycolate oxoperoxo and dioxo vanadium(V) complexes and ^{51}V NMR chemical shifts were calculated at PW91/IGLO level. The theoretical NMR chemical shifts even on isolated molecules showed good agreement with the experimental values. Another important finding was that the ^{51}V chemical shifts may not be affected severely by the structural modifications far from the nucleus, but they are extremely sensitive to the V=O bond lengths in these complexes.[16] In the case of POMs, the first attempt to compute ^{51}V chemical shifts was probably made recently by Kortz *et al.* in 2009.[9] The calculations were performed on a platinum (1V)-containing polyoxovanadate, $[H_2PtV_9O_{28}]^{5-}$ using the ADF[17] package including relativistic effects by zeroth-order regular approximation (ZORA)[18] and spin-orbit corrections in both gas and aqueous phase. It was seen that the solvent effects significantly improve the quality of the computed NMR shifts at least in the case of POMs. It was seen that the pure-DFT functional BP was inadequate in predicting ^{51}V NMR chemical shifts and the model functional, SAOP, yielded much better results.[19] The mean average error in the calculations performed at the same level of theory in aqueous phase dropped

from 108 ppm by using BP functional to 12 ppm with SAOP.[9] Since the work was done only on one complex with four vanadium signals, any further data is highly desirable.

The DFT based calculations on NMR shifts in atoms like tungsten and molybdenum are more challenging, particularly in polyoxometalates, because of their large size and strong influence of relativistic effects. Bagno *et al.* first computed [183]W chemical shifts in small complexes including a Keggin heteropolyoxotungstate, α-$[PW_{12}O_{40}]^{3-}$.[7] [183]W chemical shifts calculated at B3LYP/lanl2dz level with PM3 geometry showed poor correlation (slope = 0.0367), while the good quality of fit ($r^2 = 0.998$) indicates that the error in the calculations by using ECPs is large yet systematic. The results suggested the importance of a bigger basis set and the inclusion of relativistic effects for accurate predictions of nuclear shielding in tungsten nucleus. Later, the study was revisited using ADF scheme incorporating the relativistic effects by means of ZORA.[17] The calculations were applied on three systems: Lindqvist-type POMs, monosubstituted Keggin POM α-$[Ru(DMSO)PW_{11}O_{39}]^{5-}$ and monolacunary Keggin POM α-$[PW_{11}O_{39}]^{7-}$. The average error in calculated [183]W chemical shifts in the Lindqvist-type complexes (see fig. 2 for structure), after regression, is 12 ppm with a slope of 1.3 and an intercept of 175. The complex, α-$[Ru(DMSO)PW_{11}O_{39}]^{5-}$, has six distinct signals which yield a correlation line with a slope of 0.6 and an intercept of 65. The ordering of the six signals was accurately reproduced except for two close signals (differing by 11 ppm). The lacunary complex, α-$[PW_{11}O_{39}]^{7-}$, has a vacant site which may be occupied by a couterion. The experimental NMR spectrum spans only 53 ppm and of all six signals, only one with half

the intensity can be assigned. The spectrum was calculated by either considering the complex to be an isolated ion or an ion pair where Li^+ occupies the lacuna. The predicted spectrum from latter model fits well with the experimental results. These studies highlight the potential of chemical shift calculations for assigning ^{183}W NMR spectrum in polyoxometalates.
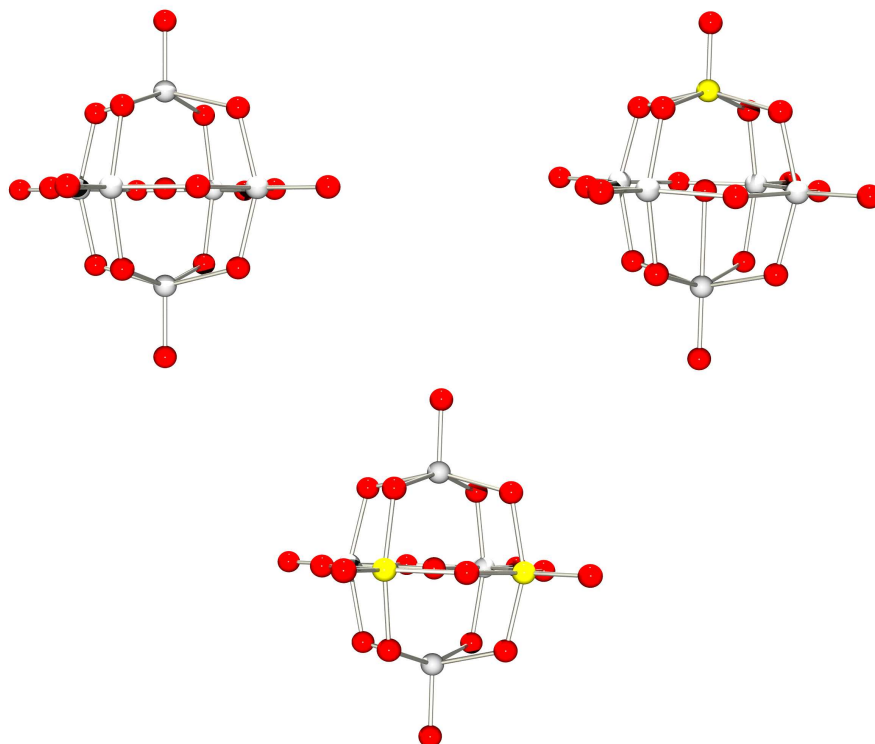
Figure 2: Structure of a Lindqvist ion, $[W_6O_{19}]^{2-}$ and its mono- and di-substituted derivatives, $[VW_5O_{19}]^{3-}$ and $[V_2W_4O_{19}]^{4-}$. The tungsten atoms are shown in grey, vanadium atoms in yellow and the red circles denote oxygen atoms.

Kortz *et al.* computed ^{183}W NMR chemical shifts in dilacunary polyoxotungstates with the general formula, γ-$[XMW_{10}O_{36}]^{7-}$, where X = Si or Ge and M = Li^+, Na^+ or K^+.[9] The ten tungsten atoms display three distinct resonances in the ratio of 4:4:2.

The calculations were done at BP/ZORA level on the isolated ion (γ-$[GeW_{10}O_{36}]^{8-}$), and on the complex where K^+ is placed in the center of the lacuna (γ-$[KGe_{10}O_{36}]^{7-}$). The calculated spectrum for the γ-$[KGe_{10}O_{36}]^{7-}$ agrees better with the experimental spectrum with the correct ordering and the distance between the signals. Moreover, the presence of a solvent molecule in the vicinity of the lacuna further improves the correlation of the computed shifts with the experimental observations with a mean average error of only 5 ppm. They showed that for computing ^{183}W chemical shifts in lacunary complexes, one also needs to consider the position of the counterion and the solvent.

The calculations presented by Poblet *et al.* show best correlation, by far, with the experimental measurements in polyoxotungstates which include Keggin anions, a Dawson anion (α-$[P_2W_{18}O_{62}]^{6-}$), $[W_6O_{19}]^{2-}$ and $[W_{10}O_{32}]^{4-}$. A test set of highly symmetrical Keggin anions (α-$[XW_{12}O_{40}]^{q-}$ where X = B, Al, Ga, Si, Ge, P, As and Zn) was chosen and different approaches (basis set, spin-orbit corrections and solvent effects) were taken to obtain a method that yields smallest mean absolute arror.[20] The ADF scheme was chosen with the spin-orbit corrections at ZORA and the solvent effects by COSMO using the BP functional. The results show that the ^{183}W NMR chemical shifts can be predicted well if the NMR chemical shift calculations are done on a QZ4P optimised structures using TZP basis set, including the spin-orbit corrections and the solvent effects. They achieved a mean average error of 7.3 ppm with an ideal slope of unity for 24 ^{183}W signals.

Although ^{95}Mo NMR is an attractive tool as a structural probe in polyoxometa-lates, very few theoretical studies have been devoted to the calculation of NMR pa-

rameters which restricts the interpretation of the complex experimental spectrum.[8, 21] As per our knowledge, no study has been reported on polyoxometalates to date. One recent report on the calculation of ^{95}Mo chemical shifts was done recently on $[Mo_6X_{14}]^{2-}$ (X=Cl, Br, I) clusters. The calculations were done with extended TZ2P and QZ4P basis sets, and BP functional. Similar to the results observed for tungsten, prediction of NMR chemical shifts in molybdenum nucleus is reproducible provided enough basis sets and relativistic effects are considered. The solvent effects induced by continuum solvation model can improve the predictive capability by as much as $\sim$ 100 ppm, while the ordering is conserved even without the solvent effects. The study reveals that predicting ^{95}Mo NMR shifts in these clusters depend strongly on computational approach, geometries and solvent effects.[21] DFT computations of ^{95}Mo NMR parameters in molybdenum hexacarbonyl also emphasise the strong influence of the choice of computational parameters like basis sets, XC functional and relativistic corrections on estimation of NMR chemical shifts. The study also shows that for $Mo(CO)_6$, hybrid functionals perform better than pure-DFT functionals especially for the computations of isotropic parameters.[8]

Poblet *et al.* present a study on computation of ^{31}P NMR sifts exploring the influence of density functional and basis set on accurate prediction in polyoxometalates. The calculations were done in ADF package with the inclusion of relativistic corrections (ZORA) and solvent effects (COSMO). They found that use of pure-DFT functional PBE is sufficient to predict ^{31}P NMR shifts in the complexes under study and adding further computational cost by using hybrid functionals do not improve the results. The NMR calculations using PBE/TZP method on several polyoxomet-

alates optimised with OPBE/TZ2P yield a AAE (average absolute error) of 0.57 ppm.

Buhl and Kaup concluded in a recent review that no universal computational method can be given for computation of NMR properties.[22] In general, NMR prediction in transition metals benefit from the use of hybrid functionals and those of third row require scalar relativistic effects. Hence, a preliminary computational study has to be carried out for each nucleus to determine the most suitable computational approach. With this in mind, we present DFT calculations on the ^{31}P, ^{51}V, ^{183}W and ^{95}Mo NMR chemical shifts using the ADF code[17] with the inclusion of relativistic effects by ZORA[18] and the solvent effects by means of COSMO. This is the first detailed study on computation of ^{51}V chemical shifts in polyoxometalates including versatile vanadium-containing POMs. For computing ^{183}W chemical shifts, we include asymmetric complexes in our study which pose a greater challenge in interpretation of experimental measurements. Asymmetric complexes like Keggin-type heteropolyoxotungstates with general formula $[MXW_{11}O_{39}]^{q-}$ display six resonances which span a close range of ~ 100 ppm and the assignment of these solely depend on empirical criteria. We decided to focus the calculations on these substituted Keggin complexes, also including the well-known symmetric clusters like Lindqvist and pure Keggin anions to evaluate the importance of XC functional in computation of ^{183}W NMR shifts. We also investigate the prediction of ^{95}Mo chemical shifts in polyoxometalates which has not been done so far. Moreover, ^{31}P chemical shifts were calculated in Keggin complexes, and compared with the experimental data.

2 Computational details

NMR measurements are mostly taken in solution state and complexes attain much more symmetric conformations in solutions than in solid state. NMR chemical shifts, particularly for heavy metals, are extremely sensitive to geometrical parameters and solvent effects. Therefore, it is imperative to employ calculations on optimised POM geometries. All the investigated POMs were optimised with the hybrid PBE0 functional which has a 0.25 proportion of Hartree-Fock exchange included in the exchange part. Previously, we have optimised the geometries for a wide range of polyoxometalates using Gaussian 09 rev. D.01,[23] with the polarizable continuum model (PCM)[24] for DFT calculations on ^{17}O NMR shifts.[13] It was a practical and reasonable choice to continue with the NMR calculations on other nuclei with these geometries. The chosen geometries were optimised using PBE0 functional and basis sets used were: cc-pvtz (H-Ar) and ECP basis set lanl2dz (K-).

All the NMR shift calculations were performed using Density functional theory as implemented in either Gaussian 09 rev. D.01[23] or Amsterdam Density Functional (ADF 2014) code.[17] We calculated the ^{51}V NMR shifts in both gaussian and ADF package with PBE0 functional[25] using def2-tzvp[26] and TZP basis sets,[27] respectively. While other calculations were done using ADF 2014 package and solvent treatment was accomplished by means of the conductor-like screening model (COSMO).[15, 14] The ^{31}P NMR shifts were computed using PBE0/def2-tzvp in Gaussian 09 package and calibrated against nuclear shielding of $[PO_4]^{3-}$ in water at the same level of theory.

For heavy metals like tungsten and molybdenum, we carried out the calculations

in ADF incorporating the relativistic corrections by ZORA.[18, 28, 29] The exchange-correlation (XC) functionals used were BP[30, 31], PBE[32, 33], OPBE[34, 35], PW91[36, 37], B3LYP[38] and SAOP[19]. The calculations were done using the same solvent in which the experimental measurements were taken using a solvation model by means of COSMO.[15] The shifts of equivalent atoms were averaged to yield a single shift.

The chemical shift is determined as the difference between the nuclear shielding of the reference molecule and the shielding of the complex under study. The reference molecule for calculating ^{51}V chemical shifts is $[VO_4]^{2-}$ at the same level of theory. $[WO_4]^{2-}$ and $[MO_4]^{2-}$ ions were chosen as reference compounds for calculating ^{183}W and ^{95}Mo chemical shifts in polyoxometalates.

The computed shifts were correlated with the observed shifts via a fitted line, $\delta(\text{obs.}) = m\delta(\text{calc.}) + c$, where m is the slope and c is the intercept. The average (AAE) and maximum absolute error (MAE) was calculated by taking the average and maximum, respectively, of the absolute error in a set of computed shifts.

3 Results and discussion

3.1 Computation of $\delta(^{51}\text{V})$ in POMs

We computed the ^{51}V NMR chemical shifts using the DFT method PBE0/def-2tzvp on a test set of five optimised vanadium complexes. The complexes were primarily decavanadate ion, $[V_{10}O_{28}]^{6-}$, and its substituted derivatives (see fig. 3). The decavanadate ion has two central vanadiums, four equivalent equatorial atoms and

four apical atoms yielding three distinct resonances in the ratio of 1:2:2 in the ^{51}V

NMR spectrum.[39] Substitution of one vanadium atom with either molybdenum or

tungsten at the apical position yields a mono-substituted decavanadate structure,

$[V_9MoO_{28}]^{5-}$ or $[V_9WO_{28}]^{5-}$, which shows six resonances in the ratio of 2:2:2:1:1:1

as the three apical vanadium atoms become inequivalent.[40] The substitution at

two apical vanadium atoms gives a di-substituted decavanadate ion, $[V_8Mo_2O_{28}]^{5-}$

(see figure 3) which can have two isomers depending the substitution is on the same

side (cis) or opposite (trans). The calculations on these five complexes with 20 ^{51}V

signals using PBE0/def2-tzvp in Gaussian 09 showed unsatisfactory correlation with

a slope of 1.16 and r^2 of 0.974. This clearly indicated that we needed to explore more

exchange-correlation functionals for an appropriate computational methodology for

computing ^{51}V NMR shifts. Inspired by the excellent results achieved by Kortz *et*

al. (as discussed in introduction) where SAOP functional gives less mean absolute

error in the computed NMR chemical shifts of platinum-substituted decavanadate

ion, we decided to implement it on our test set in ADF package. Table 1 and figure

4 compares the calculated ^{51}V NMR shifts using PBE0/def2-tzvp in Gaussian 09,

PBE0/TZP in ADF and SAOP/TZP in ADF with the experimental chemical shifts.

It was seen that better agreement was achieved between experimental and observed

shifts when SAOP functional was employed with an ideal unity slope and a AAE of

3.55 ppm (see figure 4).
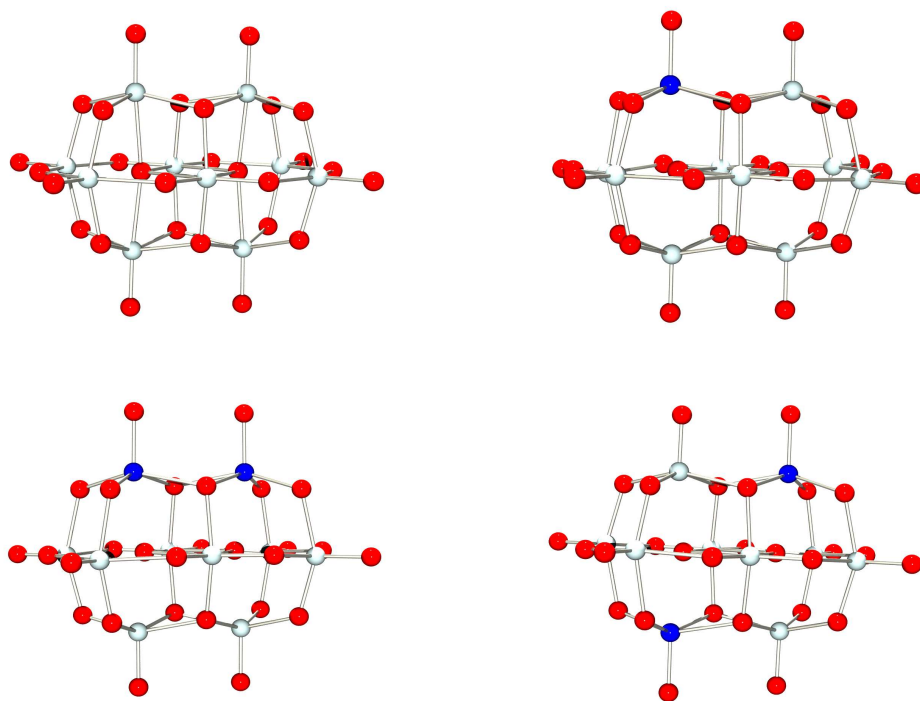
Figure 3: Structure of $[V_{10}O_{28}]^{6-}$ (top left), $[V_9MoO_{28}]^{5-}$ (top right), *cis*-$[V_8Mo_2O_{28}]^{4-}$ (bottom left) and *trans*-$[V_8Mo_2O_{28}]^{4-}$ (bottom right).

Table 1: Observed and calculated ^{51}V NMR chemical shifts using TZP basis set with different exchange-correlation functionals

Anion	Observed	SAOP(ADF)	PBE0 (G09)	PBE0 (ADF)	Ref.
$[V_{10}O_{28}]^{6-}$	-420	-344.32	-562.86	-558.23	[41, 40]
	-495	-408.5	-612.04	-610.61	
	-511	-419.77	-627.78	-628.4	
$-[V_9MoO_{28}]^{5-}$	-425	-344.87	-562.8889	-557.49	[40]
	-495.5	-417.23	-619.40	-617.87	
	-505	-426.06	-629.46	-628.62	
	-514.9	-432.1	-634.96	-635.39	
	-516.2	-432.1	-641.90	-640.85	
	-525.3	-441.11	-650.09	-651.27	
$-[V_9WO_{28}]^{5-}$	-424	-349.21	-566.33	-563.06	[41]
	-492	-417.35	-619.40	-617.70	
	-503	-425.39	-628.76	-627.12	
	-511	-434.45	-641.29	-644.63	
	-522	-438.99	-650.70	-651.82	
$trans$-$[V_8MoO_{28}]^{4-}$	-427	-345.6	-644.24	-560.59	[40]
	-505	-430.69	-631.0442	-629.19	
	-516.2	-437.65	-566.3146	-644.5	
cis-$[V_8Mo_2O_{28}]^{4-}$	-424	-344.62	-657.56	-557.72	[40]
	-505	-431.01	-630.49	-628.92	
	-525.5	-449.15	-562.61	-657.96	
Slope		1.01	1.16	1.09	
Intercept		-74.19	+228	+185.66	
r^2		0.986	0.974	0.979	
Average Error		3.55	4.79	5.02	
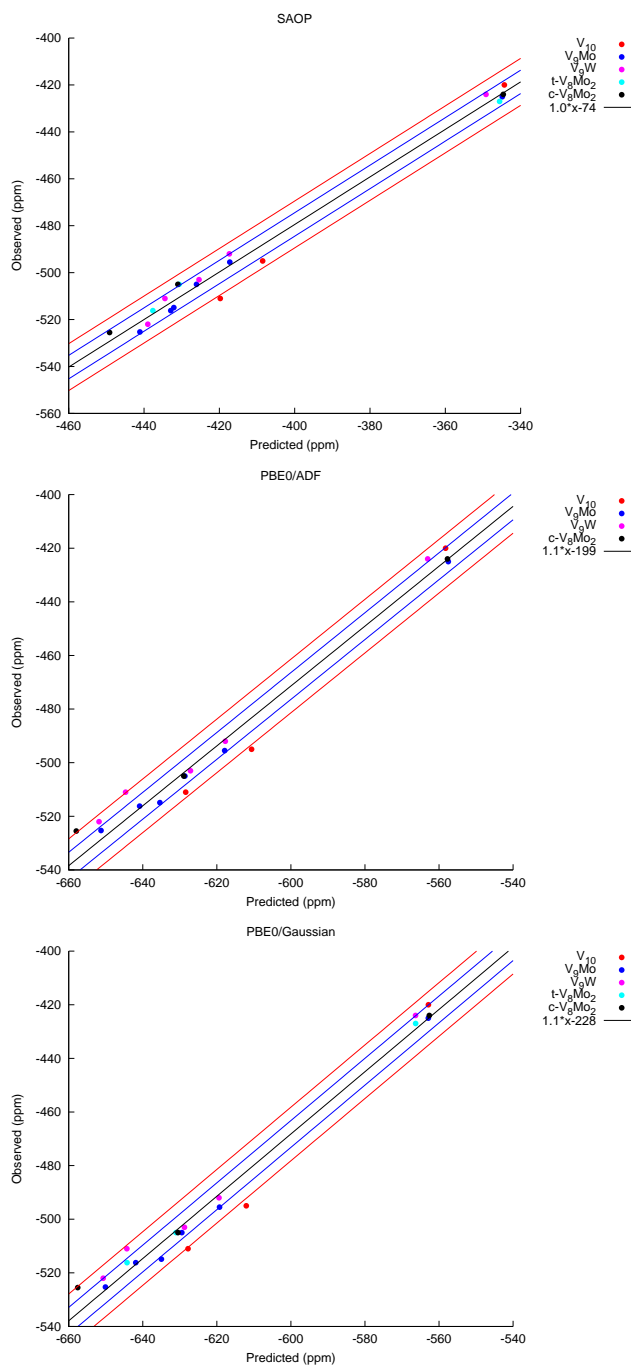
Figure 4: The black line indicates the correlation between observed and predicted NMR ^{51}V shifts for a test set of 5 polyoxovanadates with 20 ^{51}V signals. The NMR shifts are computed with top: SAOP/TZP (ADF); middle: PBE0/TZP (ADF); bottom: PBE0/def2-tzvp (Gaussian). The blue and red lines show the regressed line ± 5 ppm and ± 10 ppm, respectively.

Since SAOP is computationally costly, we explored other pure-DFT and hybrid functionals for computing ^{51}V chemical shifts on three complexes ($[V_{10}O_{28}]^{6-}$, $[V_9MoO_{28}]^{5-}$ and $[V_9WO_{28}]^{5-}$). The fitting parameters (slope, intercept, mean absolute error and maximum absolute error) obtained by computing chemical shifts in these three complexes using different functionals are compared in figure 5 and table 2. Both pure-DFT and hybrid functionals lack good correlation with the observed data. The SAOP functional outperforms all the others with the best fitting parameters (slope $= 1.05$, intercept $= 58.9$ ppm, $r^2 = 0.985$ and mean absolute error of 3.9 ppm, which is 2.1 % of shift range).

Table 2: The computed and observed ^{51}V NMR shifts using different exchange-correlation functionals in ADF package on a test set of three complexes.

Anion	BP	PBE	OPBE	PBE0	B3LYP	OPBE0	SAOP	Obs.	Ref.
$[V_{10}O_{28}]^{6-}$	-391.76	-395.38	-353.59	-558.23	-542.17	-525.15	-344.32	-420	[42, 40]
	-463.63	-466.18	-418.18	-610.61	-601.27	-571.21	-408.50	-495	
	-484.28	-486.95	-439.75	-628.40	-619.04	-590.61	-419.77	-511	
$[V_9Mo_{28}]^{5-}$	-393.05	-396.65	-353.93	-557.49	-542.86	-523.53	-344.88	-425	[40]
	-475.69	-478.06	-429.25	-617.87	-610.47	-577.73	-417.24	-495.5	
	-486.40	-488.62	-439.98	-628.62	-628.33	-588.36	-426.07	-505	
	-495.83	-498.46	-451.31	-635.39	-617.01	-596.90	-432.10	-514.9	
	-497.48	-499.70	-452.34	-640.85	-632.90	-602.92	-432.90	-516.2	
	-513.54	-515.85	-467.59	-651.27	-645.05	-612.42	-441.11	-525.3	
$[V_9WO_{28}]^{5-}$	-399.94	-403.53	-360.80	-563.07	-548.45	-528.72	-349.21	-424	[41]
	-475.50	-477.87	-429.01	-617.71	-610.11	-577.64	-417.35	-492	
	-483.77	-486.10	-437.44	-627.13	-620.11	-587.13	-425.40	-503	
	-504.86	-507.20	-459.49	-644.64	-637.47	-605.78	-434.45	-511	
	-513.59	-515.93	-467.64	-651.82	-645.04	-612.43	-438.89	-522	
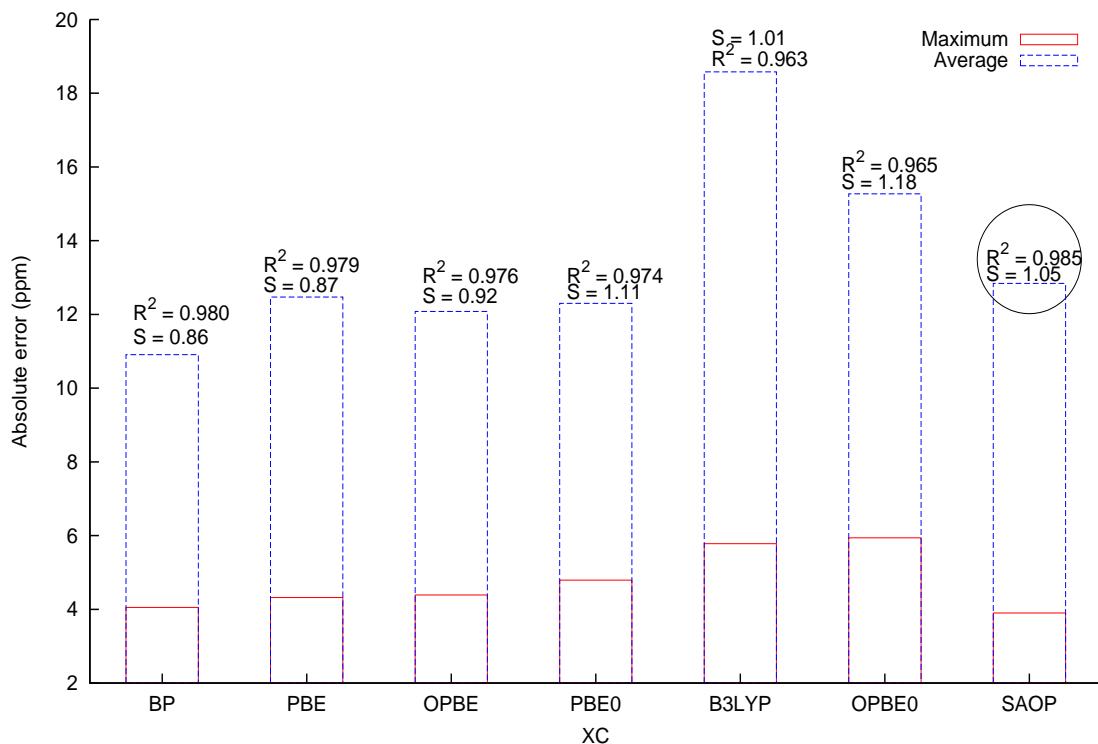
Figure 5: Comparison between different XC functionals for computing ^{51}V NMR shifts in a test set of three complexes ($[V_{10}O_{28}]^{6-}$, $[V_9MoO_{28}]^{5-}$, $[V_9WO_{28}]^{5-}$) with 14 ^{51}V signals. The NMR calculations were done using ADF package with solvent effects incorporated using COSMO. The circle shows the XC functional that displays best fitting parameters.

Calculations using DFT method SAOP/TZP extended to 14 polyoxovanadate complexes with 33 observed ^{51}V signals show a good agreement between theoretical predictions and experimental measurements (see figure 6). The 14 complexes are a mix of structurally diverse vanadium-containing polyoxometalate compounds that include substituted hexavanadate complexes ($[V_2Mo_4]^{4-}$, $[VMo_5]^{5-}$, $[V_2W_4]^{4-}$ and $[VW_5]^{5-}$), and decavanadate complex together with its five substituted derivatives. Also, we have included some mixed-metal complexes which are primarily Keg-

gin polyoxotungstates with one or two vanadium substitutions, such as $[BVW_{11}]^{6-}$, $[SiVW_{11}]^{5-}$ and $[SiV_2W_{10}]^{6-}$.[43] Table 3 presents the data on computed ^{51}V NMR shifts using SAOP/TZP and observed shifts of complexes apart from the test set. In figure 6, a plot between calculated and observed values for all the anions shows the correlation with a slope of 1.08, intercept of 51 ppm, r^2 of 0.889 and AAE of 9.53 ppm. The ^{51}V chemical shifts for vanadium-substituted polyoxotungstate complexes $[V_2W_4]^{4-}$, $[VW_5]^{5-}$,$[BVW_{11}]^{6-}$, $[SiVW_{11}]^{5-}$ and $[SiV_2W_{11}]^{4-}$ show poor correlation with the observed data. The r^2 is improved from 0.889 to 0.957 when the above mentioned five complexes are excluded from the plot. This demonstrates that the method might not give best results for certain complexes, but overall the performance of SAOP/TZP is good.

Table 3: Observed and predicted ^{51}V NMR shifts using SAOP/TZP method in ADF package, apart from the test set.

Anion	Predicted (ppm)	Observed (ppm)	Reference
$[VMo_5O_{19}]^{3-}$	-409.25	-502.00	[41]
$[V_9TeO_{28}]^{5-}$	-363.18	-449.00	[42]
	-392.57	-485.00	
	-419.30	-507.00	
	-423.83	-502.00	
$[V_2Mo_4O_{19}]^{4-}$	-411.84	-494.00	[44]
$[TeV_5Mo_3]^{5-}$	-405.59	-503.00	[42]
	-419.59	-520.00	
$[BVW_{11}O_{40}]^{6-}$	-455.12	-576.40	[43]
$[SiVW_{11}O_{40}]^{5-}$	-435.95	-550.80	[43]
$[SiV_2W_{10}O_{40}]^{6-}$	-441.04	-550.20	[43]
$[V_2W_4O_{19}]^{4-}$	-397.95	-510.50	[43]
$[VW_5O_{19}]^{3-}$	-404.58	-509.60	[43]

Figure 6: The black line indicates the correlation between observed and predicted NMR ^{51}V shifts for a test set of 14 polyoxometalates with 33 signals. The blue and red lines show the regressed line ± 10 ppm and ± 20 ppm, respectively. The mean absolute error (AAE) is 9.53 ppm.

3.2 Computation of $\delta(^{183}\textbf{W})$ in POMs

The next set of calculations were done on two classes of polyoxotungstates: the Lindqvist ion and the Keggin anion including their derivatives. The isopolyanions $[W_7O_{24}]^{6-}$ and $[W_{10}O_{32}]^{4-}$ were also included in the group. The Lindqvist ion is a highly symmetrical hexatungstate ion, $[W_6O_{19}]^{2-}$, with six equivalent tungsten cations which display one experimental chemical shift at $+59$ ppm.[10] The mono-

substituted Lindqvist anion, $[VW_5O_{19}]^{3-}$, shows two signals in the intensity ratio of 4:1 in the ^{183}W NMR spectrum,[43, 10] while the di-substituted anion, $[V_2W_4O_{19}]^{4-}$, shows two close resonances with equal intensity, corresponding to the cis isomer of the structure.[43, 45] The isopolyanion $[W_7O_{24}]^{6-}$ displays three resonances, one at extreme lower end (-179 ppm), second at -92 ppm and the third at a very positive resonance of +269 ppm.[44] The two lines on NMR spectrum of the complex $[W_{10}O_{32}]^{4-}$ appear at lower values of -25 ppm and -160 ppm.[10] The Keggin complexes have 12 equivalent tungsten atoms which display one chemical shift in the ^{183}W NMR spectrum. Between the different keggin molecules, the chemical shift is not changed much.[44] The substitution of one tungsten atom with another atom, such as vanadium, distorts the symmetry of the molecule to form complexes of general formula, $[XMW_{11}]^{q-}$ (where X is P, B or Si and M is V, Ti, Pb, Nb or Ta) (see figure 7). These substituted complexes now display six ^{183}W NMR signals. The ratio between the signals is 2:2:2:2:2:1 and span a range of ~ 100 ppm.[43] The assignment of these signals is purely on the basis of tungsten-tungsten atom connectivities.
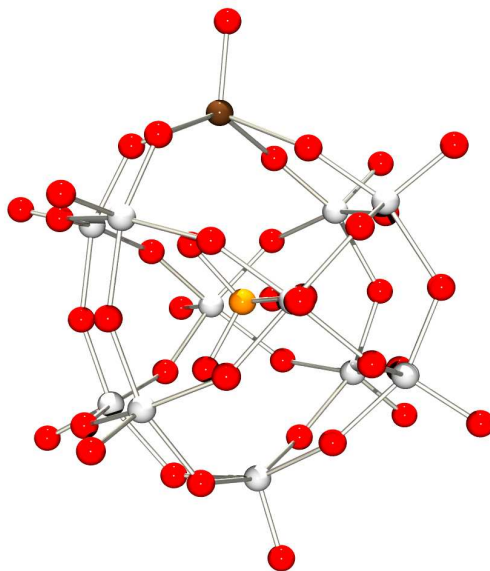
Figure 7: Structure of a mono-substituted Keggin molecule, $[XMW_{11}O_{40}]^{q-}$. The tungsten atoms are shown in grey, red circles denote oxygen atoms, the central orange atom is X (P or Si) and the brown circle shows the substituted atom M (Pb, Ta, Ti, V or Nb).

The benchmark calculations by Poblet *et al.* demonstrate that BP/TZP method is capable of reproducing experimental [183]W chemical shifts. The study included a series of symmetric Keggin complexes, a Lindqvist anion, a bulky Wells-Dawson anion $[P_2W_{18}O_{62}]^{6-}$ and $[W_{10}O_{32}]^{4-}$, which showed good correlation between experimental and observed measurements with a mean average error of 7 ppm.[20] We expanded the study to include the asymmetrical substituted complexes using the same functional (BP) in ADF package incorporating the relativistic (ZORA) and solvent effects (COSMO). Figure 8 shows the plot of observed versus BP/TZP calculated chemical shifts in 19 structurally diverse polyoxotungstate compounds. The

methodology failed to provide convincing estimation of chemical shifts in these com-
plexes with unsatisfactory fitting parameters (slope = 0.83, intercept = 133.8 and
r^2= 0.885). The results indicate that the pure-DFT functional, BP, can predict the
$\delta(^{183}W)$ for symmetrical complexes but falls short when asymmetrical complexes
are included. Moreover, the choice of XC functional is an important parameter in
any computational approach which can affect the predictive power of DFT based
approach considerably.
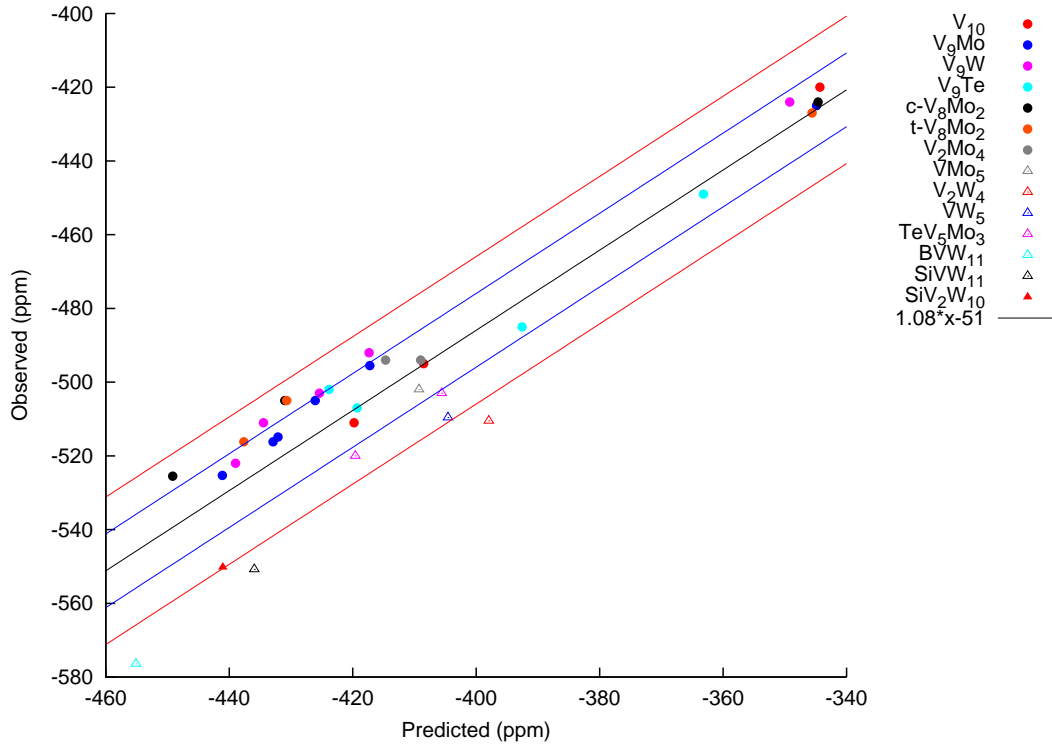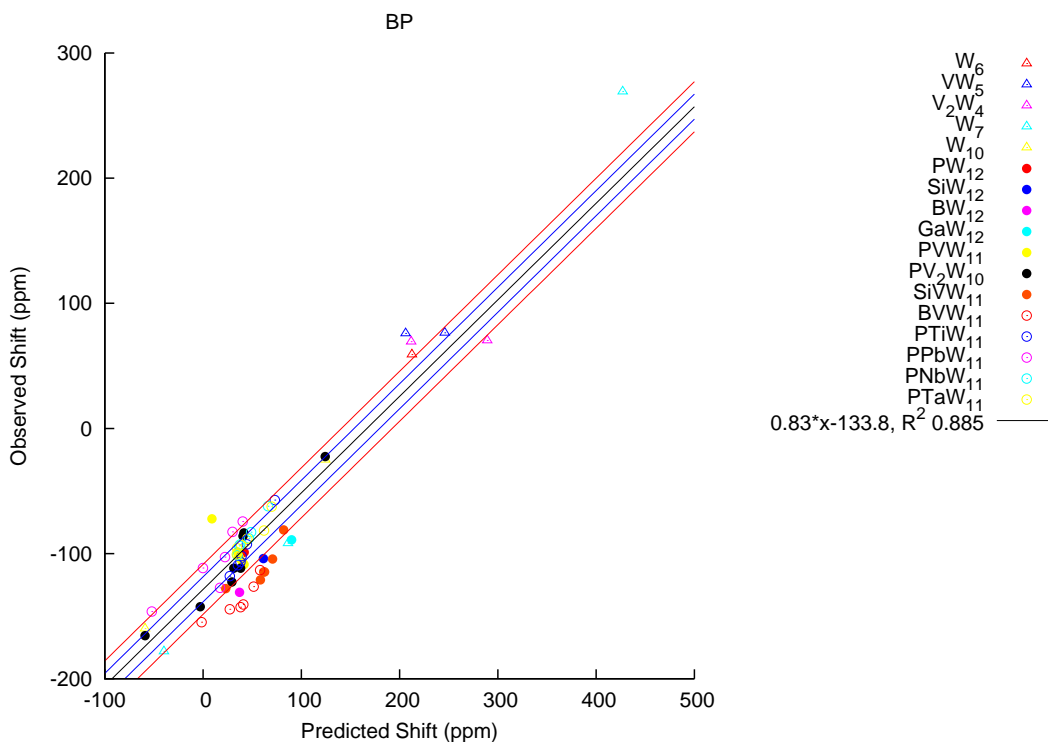

Figure 8: The black line indicates the correlation between observed and predicted
NMR ^{183}W shifts for a set of polyoxometalates with signals. The NMR shifts are
computed with ADF package using BP/TZP method. The blue and red lines show
the regressed line ±10 ppm and ±20 ppm, respectively. The average absolute error
is 17.39 ppm.

We compared different pure-DFT and hybrid-DFT XC functionals for computation of $\delta(^{183}W)$ in polyoxometalates, including the well-known symmetrical complexes like Lindqvist and Keggin ions in conjunction with their asymmetrical substituted counterparts that are more challenging in terms of complexity in signal assignment. Chemical shifts were computed using eight different XC functionals for a set of seven polyoxotungstates consisting of $[W_6O_{19}]^{2-}$, $[W_7O_{24}]^{6-}$, $[W_{10}O_{32}]^{4-}$, four Keggin anions with formula $[XW_{12}O_{40}]^{q-}$ (where X = P, Si, Ga, B) and a mono-substituted Keggin complex $[PVW_{11}O_{40}]^{4-}$.
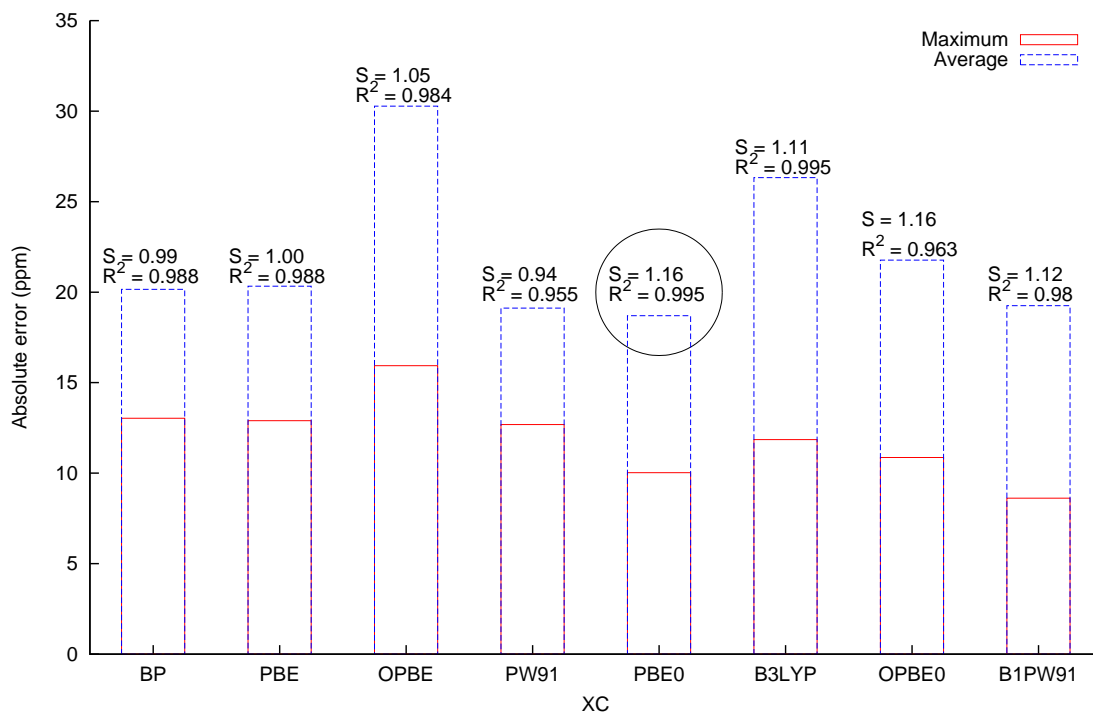
Figure 9: Comparison between different exchange-correlation functionals for computing ^{183}W NMR shifts in a test set of seven complexes. The NMR calculations were done with TZP basis set incorporating relativistic and solvent effects by ZORA and COSMO, respectively. The circle denotes the XC functional with best fitting parameters.

Figure 9 compares the fitting parameters (AAE, MAE, slope and r^2) in calculated ^{183}W chemical shifts, after linear regression, of the test set using eight XC functionals. Table 4 tabulates the predicted and observed ^{183}W NMR shifts using different XC functionals on the test set. All calculations were implemented in ADF scheme[17] with TZP basis set including relativistic effects and solvent effects by ZORA and COSMO, respectively.[18, 15] The pure-DFT functionals like BP and PBE gave good results with a unity slope and AAE of 13 ppm, however PBE0 yields a AAE of 10 ppm and excellent correlation (r^2 = 0.995). We have seen earlier in figure 8 that when more asymmetrical complexes are included in the study, the BP functional fails to give good estimates of observed shifts. Therefore, we settled with PBE0 as the functional of choice for predicting ^{183}W chemical shifts in polyoxometalates.

Table 4: The computed and observed ^{183}W NMR shifts using different exchange-correlation functionals with TZP basis set on a test set.

Anion	BP	PBE	OPBE	PW91	PBE0	B3LYP	OPBE0	B1PW91	Obs.	Ref.
$[W_6O_{19}]^{2-}$	212.59	202.14	189.41	204.58	140.38	169.02	116.07	143.41	59.00	[44]
$[PW_{12}O_{40}]^{3-}$	41.76	28.58	33.93	35.37	5.34	-0.37	-12.44	7.77	-99.00	[44]
$[BW_{12}O_{40}]^{5-}$	37.09	34.06	47.11	30.08	-33.32	32.35	-55.96	-32.14	-131.00	[44]
$[GaW_{12}O_{40}]^{5-}$	90.06	80.79	87.25	83.27	27.34	45.23	5.12	29.68	-89.00	[44]
$[SiW_{12}O_{40}]^{4-}$	61.40	53.24	63.25	54.18	14.66	22.45	-4.18	16.94	-104.00	[44]
$W_7O_{24}]^{6-}$	-39.84	-47.55	-45.22	-44.54	-59.17	-32.79	-82.71	-57.52	-178.20	[46]
	86.34	76.41	83.61	79.37	26.39	54.66	5.70	28.60	-91.80	
	426.96	414.00	403.14	418.30	323.15	368.65	287.77	325.58	269.20	
$[PVW_{11}O_{40}]^{4-}$	9.03	1.39	12.76	3.08	1.83	29.14	-49.41	4.34	-72.20	[43]
	34.85	27.31	40.02	28.87	-2.12	25.62	-20.92	0.04	-98.60	
	35.66	28.13	40.92	29.70	-2.92	24.87	-20.65	-0.66	-101.20	
	37.19	29.54	42.69	31.19	-3.49	23.91	-19.92	-1.17	-103.70	
	39.95	32.25	45.14	33.88	-3.84	23.78	-19.09	-1.76	-106.70	
	41.68	34.02	46.63	35.62	-31.80	-3.43	-15.28	-29.67	-108.70	

Further expanding the study, we computed the ^{183}W chemical shifts using PBE0/TZP method on a total of 18 polyoxotungstates with 66 ^{183}W signals (includes five hex-

ametalate anions of Lindqvist framework, four pure Keggin anions and seven mixed-metal complexes of Keggin origin, isopolyanions $[W_7O_{24}]^{6-}$, $[W_{10}O_{32}]^{4-}$)(see figure 10). We achieve an ideal slope of 1.01, an intercept of 97.32 ppm, r^2 of 0.95 and AAE of 13.03 ppm (2 % of chemical shift range of 600 ppm). Table 5 presents data on computed and observed ^{183}W NMR shifts of polyoxotungstates under study (excludes the test set). Considering a wide range of 600 ppm, inclusion of asymmetric complexes and a total of 66 signals, we have achieved a good agreement of the calculated shifts and the observed NMR shifts.
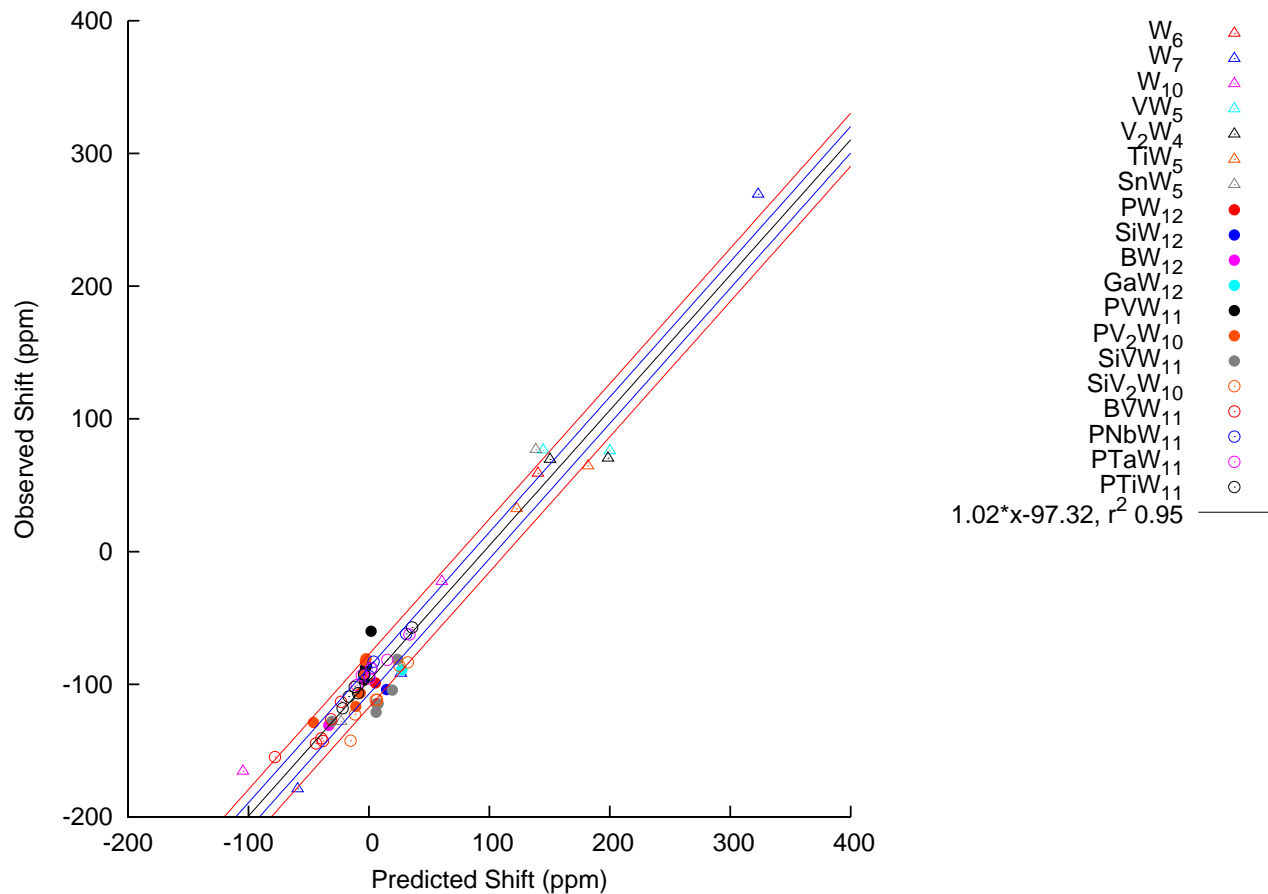
Figure 10: The black line indicates the correlation between observed and predicted NMR ^{183}W shifts for a set of 18 polyoxometalates with 66 signals. The NMR shifts are computed with ADF package using PBE0/TZP method. The blue and red lines show the regressed line ± 10 ppm and ± 20 ppm, respectively. The AAE and MAE is 13.03 ppm and 38.38 ppm, respectively.

Table 5: Predicted and observed ^{183}W NMR shifts using PBE0/TZP in 19 polyoxo-tungstate compounds with 66 signals

Anion	Predicted (PBE0) (ppm)	Predicted (BP) (ppm)	Observed (ppm)	Reference
$[V_2W_4O_{19}]^{4-}$	198.515	245.92	70.3	[43]
	150.34	211.69	69.4	
$[VW_5O_{19}]^{3-}$	200.06	245.92	75.9	[43]
	144.66	206.10	76.4	
$[TiW_5O_{19}]$	181.85	-	64.5	[47]
	122.755	-	32.2	
$[SnW_5O_{19}]$	138.575	-	76.9	[48]
$[W_{10}O_{32}]^{4-}$	60.5512	124.28	-22.5	[49]
	-104.57	-59.10	-165.6	
$[BVW_{11}O_{40}]^{6-}$	-23.10	58.02	-113.2	[43]
	-31.46	51.46	-126.4	
	-39.48	40.84	-140.7	
	-38.11	38.14	-142.8	
	-43.99	27.13	-144.5	
	-77.97	-1.46	-154.8	
$[SiVW_{11}O_{40}]^{5-}$	23.68	82.03	-81.1	[43]
	19.46	70.66	-104.3	
	7.67	62.55	-114.6	
	6.17	61.65	-114.6	
	5.93	58.26	-121	
	-30.79	23.11	-128	
$[PV_2W_{10}O_{40}]^{5-}$	-2.41	41.47	-80.8	[43]
	-2.99	40.46	-82.2	
	-3.58	31.36	-91.9	
	-7.17	38.23	-106.7	
	-10.93	29.26	-116.7	
	-46.02	-2.85	-128.8	
$[SiV_2W_{10}O_{40}]^{6-}$	32.30	-	-83.5	[43]
	25.24	-	-86	
	5.72	-	-111.7	
	6.65	-	-111.7	
	-11.53	-	-122.7	
	-15.26	-	-142.5	
$[PTaW_{11}O_{40}]$	33.57	69.81	-62.5	[50]
	15.23	61.96	-81.6	
	1.93	45.05	-88	
	-5.92	38.84	-93.2	
	0.59	34.53	-95.7	
	-10.18	34.35	-100.6	
$[PTiW_{11}O_{40}]^{5-}$	35.94	72.93	-57.2	[43]
	-3.98	44.59	-92.6	
	-11.78	39.26	-101.9	
	-8.91	38.00	-106.7	
	-16.69	35.40	-109.2	
	-21.86	27.18	-118	
$[PNbW_{11}O_{40}]$	30.99	66.17	-62.1	[50]
	3.95	48.87	-82.9	
	1.87	46.67	-87.8	
	-4.09	37.76	-92.7	
	0.185	36.78	-93.8	
	-8.34	34.84	-101.3	

3.3   Computation of $\delta(^{95}\text{Mo})$ in POMs

We computed ^{95}Mo chemical shifts in seven polyoxomolybdate clusters with nine ^{95}Mo signals. All our calculations were done within the ADF code of DFT scheme with TZP basis set incorporating the relativistic effects and solvent effects, as done earlier for computing ^{183}W chemical shifts. Chemical shifts were computed for a series of versatile anions that includes isoployanions like hexamolybdate ($[\text{Mo}_6\text{O}_{19}]^{2-}$), heptamolybdate ($[\text{Mo}_7\text{O}_{24}]^{6-}$), two isomers of octamolybdate (α-$[\text{Mo}_8\text{O}_{26}]^{4-}$ and β-$[\text{Mo}_8\text{O}_{26}]^{4-}$); two heteropoly Keggin anions ($[\text{PMo}_{12}\text{O}_{40}]^{3-}$ and $[\text{SiMo}_{12}\text{O}_{40}]^{4-}$) and a molybdenum-substituted decavanadate ion ($[\text{V}_9\text{MoO}_{28}]^{6-}$). Figure 11 compares the performance of different XC functionals for predicting the ^{95}Mo chemical shifts in these seven complexes with nine resonances in terms of slope, r^2, AAE and MAE, after applying linear regression. The study included four pure-DFT functionals: BP, PBE, OPBE and PW91 and four hybrid functionals such as PBE0, B3LYP, OPBE0 and B1PW91 and a model functional SAOP. The pure-DFT functionals, BP and PBE, yield a slope of 0.80 and r^2 of 0.935, while hybrid functionals like B3LYP and B1PW91 also offer similar slope of 0.85 and 0.88 with the correlation (r^2 = 0.94). SAOP yields a slope and r^2 of 0.946. Table 6 summarises the predicted and observed ^{95}Mo NMR shifts using different XC functionals on the test set. All the functionals give nearly same mean average error of 13-14 ppm. Figure 12 shows the correlation between computed and experimental ^{95}Mo NMR shifts for 11 molybdenum POMs with 13 ^{95}Mo signals and table 7 tabulates the observed and predicted chemical shifts for the complexes under study excluding the shifts for the test set.
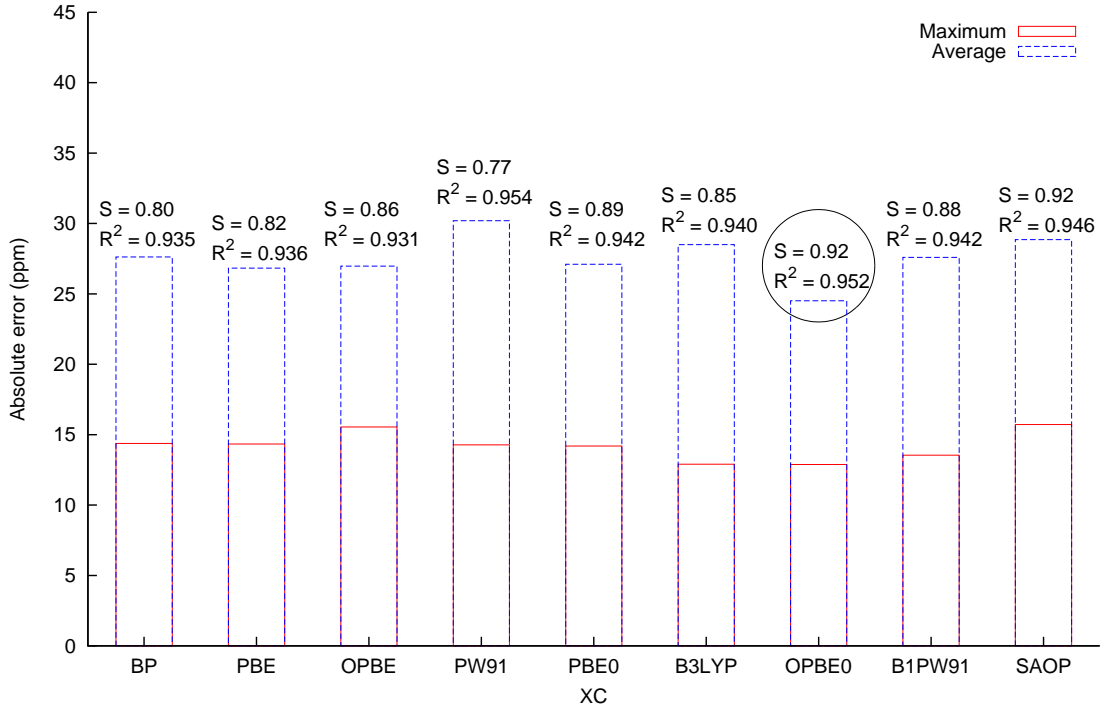
Figure 11: Comparison between different exchange-correlation functionals for computing ^{95}Mo NMR shifts in a test set of seven complexes. The NMR calculations were done with TZP basis set incorporating relativistic and solvent effects by ZORA and COSMO, respectively. The circle denotes the XC functional with best fitting parameters.

Table 6: The computed and observed ^{95}Mo NMR shifts using different exchange-correlation functionals on a test set.

Anion	BP	PBE	OPBE	PW91	PBE0	B3LYP	OPBE0	B1PW91	Observed	Reference
$[Mo_6O_{19}]^{2-}$	161.79	157.9	158.15	159.56	156.25	167.06	151.79	157.99	122	
$[Mo_7O_{24}]^{6-}$	75.96	72.23	63.54	74.27	82.65	93.34	54.38	83.89	36	[44]
	255.76	251.21	235.8	253.26	242.37	259.54	228.92	243.79	210	
$[PMo_{12}O_{40}]^{3-}$	43.79	41.51	43.25	42.21	38.31	47.19	36.48	39.32	16	[44]
$[SiMo_{12}O_{40}]^{4-}$	56.26	53.86	53.79	54.49	45.07	55.61	41.82	45.82	19	[44]
$\alpha-[Mo_8O_{26}]^{4-}$	-9.99	-10.80	-9.33	-10.03	-1.16	3.37	-4.06	-0.80	16	[44]
$\beta-[Mo_8O_{26}]^{4-}$	16.01	13.51	14.04	14.67	37.07	41.05	33.01	38.23	19	[44]
	136.6	131.68	125.00	133.73	118.82	132.95	107.96	120.96	109	
$[MoV_9O_{28}]^{5-}$	127.18	122.36	114.82	124.06	123.09	135.33	111.42	124.99	115	[44]

*All the shifts are in ppm

Table 7: Observed and predicted ^{95}Mo NMR shifts using PBE0/TZP for complexes other than the test set

Anion	Predicted (ppm)	Observed (ppm)	Reference
$[V_2Mo_4O_{19}]^{4-}$	183.225	130	[44]
$[TeMo_6O_{24}]^{6-}$	51.73	8	[42]
cis-$[V_8Mo_2O_{28}]^{6-}$	118.66	110	[40]
trans-$[V_8Mo_2O_{28}]^{6-}$	92.33	92.4	[40]

Overall, all the XC functionals give nearly the same results which indicates the error is inherent in the optimised geometries used for NMR chemical shift calculation. There is a large discrepancy between the absolute value of the calculated and the experimental shifts, yet the relative ordering of the signals was accurately predicted. Various reasons can be postulated, particularly the optimisation of geometries by ECP basis set and the deficiencies in calculation methods themselves (mainly XC functionals and basis set limitation). It can be inferred that possibly DFT, at this level of theory, is not enough to give accurate estimation of chemical shifts in the case of molybdenum nucleus. Despite the limitation, we can estimate the spectral region in which a signal should lie and the sequence of the ^{95}Mo signals and therefore, assign the resonances in complex anions.
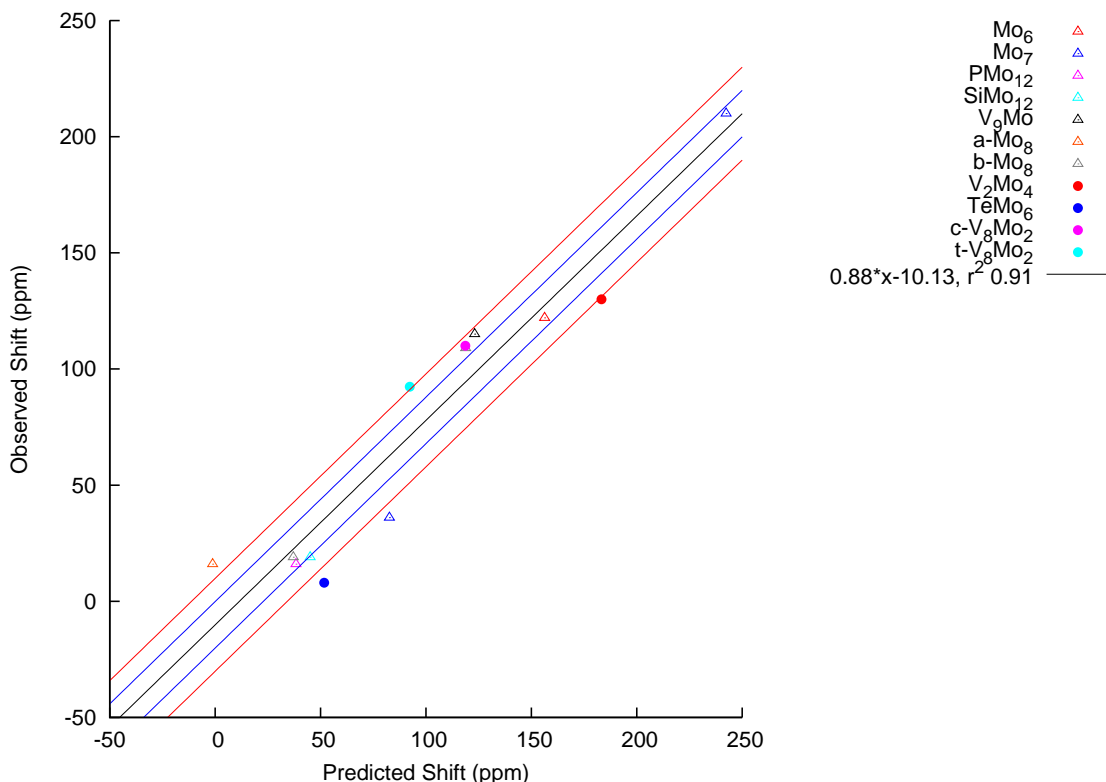
Figure 12: The black line indicates the correlation between observed and predicted NMR ^{95}Mo shifts for 11 polyoxomolybdates with 13 signals. The NMR shifts were computed using PBE0/TZP in ADF package. The blue and red lines show regressed line ± 10 ppm and ± 20 ppm, respectively. The AAE is 15.73 ppm and MAE is 27.39 ppm.

3.4   Computation of $\delta(^{31}\text{P})$ in POMs

We computed ^{31}P NMR shifts in sseven complexes which are either pure Keggin ions ($[\text{PX}_{12}\text{O}_{40}]^{3-}$ where X = W^{VI} or Mo^{VI} or their substituted derivatives ($[\text{PXW}_{11}\text{O}_{40}]^{q-}$ where X = V, Ti, Nb or Ta). The calculations were done using Gaussian 09 package with PBE0/def2-tzvp method. We achieve a correlation line with a slope of 2.53, an intercept of 0.24 , AAE of 0.34 ppm and r^2 of 0.977. Poblet *et al.* has computed

^{31}P NMR shifts in several polyoxometalates using pure-DFT functional PBE implemented in ADF package and achieved a linear regression coefficient (r^2) of 0.966 and a slope of -0.796. They also included scalar relativistic corrections by means of ZORA which add to the computational cost. However, we could achieve same level of computational results by using a commonly available program for computing ^{31}P NMR shifts although the use of hybrid functional, PBE0, leads to the calculations being more expensive.
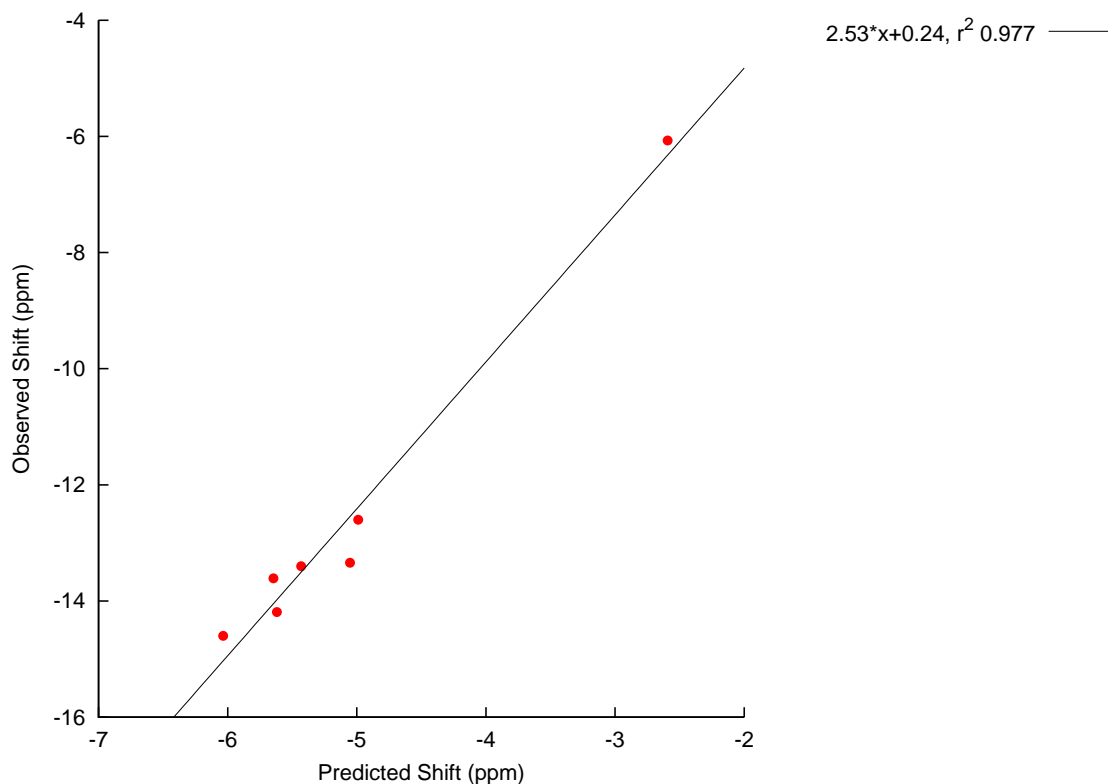
Figure 13: The black line indicates the correlation between observed and predicted NMR ^{31}P shifts for seven Keggin ions and their derivativest with seven ^{31}P NMR signals. The NMR shifts were computed using PBE0/def2-tzvp in Gaussian 09 package. The AAE and MAE is 0.34 ppm and 0.84 ppm, respectively.

Table 8: Observed and predicted ^{31}P NMR shifts using PBE0/def2-tzvp method in Gaussian 09 for seven Keggin ions and its substituted derivatives

Anion	Predicted (ppm)	Observed (ppm)	Reference
$[PW_{12}O_{40}]^{3-}$	-6.04	-14.60	[44]
$[PVW_{11}O_{40}]^{4-}$	-5.62	-14.19	[43]
$[PV_2W_{10}O_{40}]^{5-}$	-5.65	-13.61	[43]
$[PMo_{12}O_{40}]^{3-}$	-2.59	-6.07	[44]
$[PNbW_{11}o_{40}]$	-4.99	-12.60	[50]
$[PTaW_{11}O_{40}]$	-5.43	-13.40	[50]
$[PTiW_{11}O_{40}]^{5-}$	-5.05	-13.34	[43]

4   Conclusion

We have demonstrated that the predictive capability of DFT for computing NMR chemical shifts is highly affected by the choice of the density functional. There is no single functional that is applicable for computing NMR shifts for all nuclei, and probably for all molecules. We show that, in ADF package, SAOP/TZP and PBE0/TZP methods correctly predict the ^{51}V and ^{183}W NMR chemical shifts, respectively, for most of the vanadium- and tungsten-containing polyoxometalate species, including asymmetric Keggin clusters. The PBE0/def2-tzvp strategy using Gaussian 09 predicts the ^{31}P NMR shifts in Keggin complexes with accuracy. The prediction of ^{95}Mo NMR shifts lacks good agreement with the observed shifts and does not get better with the use of a hybrid functional. The present study shows that the DFT based calculations can estimate a general trend in the chemical shifts to complement complex NMR experimental measurements.

References

[1] Y. F. Song, R. Tsunashima, *Chem. Soc. Rev.* **2012**, *41*, 7384–7402.

[2] C. A. Ohlin, E. M. Villa, W. H. Casey, *Nature Mater.* **2010**, *11*, 223–226.

[3] J. F. Keggin, *Proc. Roy. Soc. L.* **1934**, 75–100.

[4] R. Sharma, J. Zhang, C. A. Ohlin, *Dalton Trans.* **2015**, *44*, 19068–19071.

[5] E. M. Villa, C. A. Ohlin, J. R. Rustad, W. H. Casey, *J. Am. Chem. Soc.* **2009**, *131*, 16488 – 16492.

[6] J. R. Black, M. Nyman, W. H. Casey, *J. Am. Chem. Soc.* **2006**, *128*, 14712–14720.

[7] A. Bagno, G. Scorrano, *Acc. Chem. Res.* **2000**, *33*, 609–616.

[8] J. Cuny, K. Sykina, B. Fontaine, L. L. Pollés, C. Pickard, R. Gautier, *Phys. Chem. Chem. Phys.* **2011**, *13*, 19471–19479.

[9] N. Vankova, T. Heine, U. Kortz, *Eur. J. Inorg. Chem.* **2009**, 5102–5108.

[10] L. P. Kazansky, T. Yamase, *J. Phys. Chem.* **2004**, *108*, 6437–6448.

[11] M. Pascual-Borrás, X. López, A. Rodríguez-Fortea, E. R. Errington, J. P. Poblet, *Chem. Sci.* **2014**, *5*, 2031–2042.

[12] M. Pascual-Borrás, X. López, J. P. Poblet, *Phys. Chem. Chem. Phys.* **2015**, *17*, 8723–8731.

[13] R. Sharma, J. Zhang, C. A. Ohlin, *Phys. Chem. Chem. Phys.* **2016**, *18*, 8235–8241.

[14] A. Klamt, *J. Chem. Phys.* **1995**, *99*, 2224–2235.

[15] A. Klamt, V. Jonas, *J. Chem. Phys.* **1996**, *105*, 9972–9981.

[16] L. L. G. Justino, M. L. Ramos, M. L. Kaupp, H. D. Burrows, C. Fiolhais, V. M. S. Gil, *Dalton Trans.* **2009**, 9735–9745.

[17] *Amsterdam Density Functional package*, `http://www.scm.com`.

[18] F. Wang, T. Ziegler, E. V. Lenthe, S. V. Gisbergen, E. J. Baerends, *J. Chem. Phys.* **2005**, *122*, 204103.

[19] P. R. T. Schipper, O. V. Gritsenko, S. J. A. van Gisbergen, E. J. Baerends, *J. Chem. Phys.* **2000**, *112*, 1344–1352.

[20] L. Vilá-Nadal, J. P. Sarasa, A. Rodríguez-Fortea, J. Igual, L. Kazansky, J. P. Poblet, *Chem. Asian. J.* **2010**, *5*, 97–104.

[21] T. T. Nguyen, J. Jung, X. Trivelli, J. Treébosc, S. Cordier, Y. Molard, C. J. Pollés, Pickard, J. Cuny, R. Gautier, *Inorg. Chem.* **2015**, *54*, 7673–7683.

[22] M. Buhl, M. Kaupp, *Computational Inorganic and Bio-inorganic Chemistry, ed.* **2009**, *2009*, 91–108.

[23] M. J. Frisch, G. W. Trucks, H. B. Schlegel, *Gaussian 09 Revision D.01* **2009**, 7384–7402.

[24] J. Tomasi, B. Mennucci, R. Cammi, *Chem. Rev.* **2005**, *105*, 2999–3093.

[25] C. Adamo, V. Barone, *J. Chem. Phys.* **1999**, *110*, 6158–6159.

[26] F. Weigend, R. Ahlrichs, *Phys. Chem. Chem. Phys.* **2005**, *7*, 3297–3305.

[27] F. Weigend, M. Haser, H. Patzelt, R. Ahlrichs, *Chem. Phys. Lett.* **1998**, *294*, 143–152.

[28] J. H. V. Lenthe, J. N. J. V. Lingen, *International Journal of Quantum Chemistry* **2005**, *106*, 2525–2528.

[29] E. V. Lenthe, E. J. Baerends, J. G. Snijders, *J. Chem. Phys.* **1993**, *99*, 4597–4610.

[30] A. D. Becke, *Phys. Rev. A* **1988**, *38*, 3098–3100.

[31] J. P. Perdew, *Phys. Rev. B* **1986**, *33*, 8822–8824.

[32] J. P. Perdew, K. Burke, M. Ernzerhof, *Phys. Rev. Lett.* **1996**, *77*, 3865–3868.

[33] J. P. Perdew, K. Burke, M. Ernzerhof, *Phys. Rev. Lett.* **1996**, *78*, 1396.

[34] N. C. Handy, A. J. Cohen, *Mol. Phys.* **2001**, *99*, 403–412.

[35] W.-M. Hoe, A. Cohen, N. C. Handy, *Chem. Phys. Lett.* **2001**, *341*, 319–328.

[36] J. P. Perdew, J. A. Chevary, S. H. Vosko, K. A. Jackson, M. R. Pederson, D. J. Singh, C. Fiolhais, *Phys. Rev. B* **1992**, *48*, 4978.

[37] J. P. Perdew, J. A. Chevary, S. H. Vosko, K. A. Jackson, M. R. Pederson, D. J. Singh, C. Fiolhais, *Phys. Rev. B* **1993**, *46*, 6671–6687.

[38] A. D. Becke, *J. Chem. Phys.* **1993**, *98*, 5648–5652.

[39] O. W. Howarth, M. Jarrold, *J. C. S. Dalton* **1978**, 503–506.

[40] O. W. Howarth, *J. Chem. Soc. Dalton Trans.* **1989**, 1915–1923.

[41] R. I. Maksimovskaya, N. N. Chumachenko, *Polyhedron* **1987**, *6*, 1813–1821.

[42] R. I. Maksimovskaya, V. M. Bondareva, G. Alesgima, *Eur. J. Inorg. Chem.* **2008**, 4906–4914.

[43] P. J. Domaille, *J. Am. Chem. Soc.* **1984**, *106*, 7677–7687.

[44] M. A. Fedotov, R. I. Maksimovskaya, *J. Struc. Chem.* **2006**, *47*, 952–978.

[45] W. G. Klemperer, W. Shum, *J. Am. Chem. Soc.* **1978**, 4891–4893.

[46] R. I. Maksimovskaya, K. G. Burtseva, *Polyhedron* **1985**, *4*, 1559–1562.

[47] E. R. Errington, S. S. Petkar, P. S. Middleton, W. McFarlane, W. Clegg, R. A. Coxall, R. W. Harrington, *Dalton Trans.* **2007**, 5211–5222.

[48] B. Kandasamy, C. Wills, W. McFarlane, W. Clegg, R. W. Harrington, J. M. Rodríguez-Fortea, Poblet, P. G. Bruce, R. J. Errington, *Chem. Eur. J.* **2012**, *18*, 59–62.

[49] D. C. Duncan, C. L. Hill, *Inorg. Chem.* **1996**, *35*, 5828–5835.

[50] E. Radkov, Y. Lu, R. H. Beer, *Inorg. Chem.* **1996**, *35*, 551–552.

Conclusion and Future work

Macroscopic studies do not suffice the complete understanding of important chemical processess like mineral dissolution and precipitation. The reaction dynamics of these metal oxides are completely understood by studying the chemical reactivity of the nanometer-sized soluble clusters such as polyoxometalates which broadly describe the behaviour of minerals at solid-solvent ineterface. NMR is a powerful tool to detail the site-specific reactivities at each site. The thesis also shows that theoretical predictions are also important to complement experimental measurements.

The work re-interprets the pKa values of various sandwich polyoxometalates and compares the pH-dependent reaction dynamics of a Wells-Dawsons sandwich manganese (II)-polyoxometalate and the corresponding manganese hexa-aqua ion. The study of rates of exchange of bound waters show that the rates are independent of pH for the manganese (II) hexa-aqua ion, while for the manganese(II) polyoxometalate, the rates increased by seven-fold on at low pH. Protonation of the complex substantially affects the lability of the bound aqua ligands even though the protonation site is not directly associated with the aqua ligands. These results correlate to dynamics at a mineral surface where reactivity at one site in extended metal oxides may not be entirely independent, and is likely to be affected by the events occuring on another site such as a neighbouring kink site.

The work also shows that the reactivities of structural oxygen atoms in polyoxometalates are affected by events involving a single atom such as protonation and substitution. The two isostructural and isovalent complexes differing only by a single atom can have vast difference in their pH stabilities, pKas and reactivities at each oxygen site. However, within each complex, all the oxygens respond to the changes in the pH enviornment unanimously. The rates of exchange between different oxygen atoms may differ by 10^2-10^4, but each site acts cooperatively to give the complex its overall effect. Similarly, the dynamics at a mineral surface is also an interactive interplay of all the individual sites which require microscopic

level investigation.

To be able to use NMR for site-specific information, it is imperative that the signals are correctly assigned to the corresponding atoms. For fulfilling this aim, the work involves theoretical prediction of NMR chemical shifts of different nuclei in polyoxometalates. Density functional theory proved to be highly beneficial in prediction of NMR chemical shifts. The work shows that by fine tuning of computational parameters like exchange-correlation functional and basis sets, DFT can predict the correct order of NMR signals and the distance between them. Predicting the correct absolute shifts may be possible with the help of linear regression. Using Gaussian 09 and PBE0/def2-tzvp//PBE)/cc-pvtz (H-Ar), lanl2dz (K-), the ^{17}O NMR chemical shifts were predicted with good accuracy. In ADF package, SAOP/TZP and PBE0/TZP methods correctly predict ^{51}V and ^{183}W NMR chemical shifts, respectively. Overall, a general trend in the chemical shifts can be accurately predicted which can complement the experimental observations and help a wider community of scientists in assigning the signals.

Future work

In the future, it is envisaged that more polyoxometalate compounds will be studied for their reaction dynamics to further the understanding of mineral surfaces. There is a scope of investigating the rates of exchange of substituted decaniobate complexes like $[NiNb_9O_{28}]^{6-}$ and $[FeNb_9O_{28}]^{6-}$, and comparing the oxygen-exchange process with the parent complex. They are particularly challenging, yet interesting because of the presence of paramagnetic ions in the complex. Experimental and theoretical investigation on the exact loci of protonation in polyoxometalates is another area which has lot of scope and will further enhance the knowledge of these complexes.

Furthermore, thermodynamic and speciation data for niobium and tantalum oxides is still missing from literature. The two isoleptic polyoxoniobates, the Lindqvist hexaniobate, $[Nb_6O_{19}]^{8-}$ and the decaniobate ion, $[Nb_{10}O_{28}]^{6-}$, exist in equilibrium. The thermodynamic properties of this equilibrium has not been studied to date and therefore, it opens up the scope for unfolding the complexity of their behaviour.

Appendix

Listing 1: Gnuplot script used to fit the DOSY data and generate DSOY plot
set term postscript eps enhanced color
set output 'dosy.eps'

set border 3
set xtics nomirror
set ytics nomirror

I0=1
gamma=10829.1
D=1.12005$\cdot 10^9$
LD=0.005
BD=0.1
kB=1.3806485279$\cdot 10^{-23}$
n=8.9E-4
r=5.68154884541974$\cdot 10^{-10}$
pi=3.14159265358979
T=298

I(g)=I0*exp(-D*(gamma**2)*(g**2)*(LD**2)*(BD-(LD/3))*10**4)
Ir(g)=I0*exp(-(T*kB/(6*pi*n*r))*10**4*(gamma**2)*(g**2)*(LD**2)*(BD-(LD/3)))

fit I(x) 'data.txt' u 2:3 via D, I0

fit Ir(x) 'data.txt' u 2:3 via r

set xlabel 'Gradient (G/cm)'
set ylabel' Intensity'
plot 'data.txt' u 2:3 w points pt 7 notitle, I(x) w lines lt 3 title 'D = 2.67$\cdot 10^{-10}$ m^2/s, r = 9.183$\cdot 10^{-10}$m'

Listing L2: Gnuplot script to generate a z-plot fitted using speciation model.

```
set term postscript eps enhanced colour
set output 'zplot.eps'

set border 3
set size 0.5,0.5
set xtics nomirror
set ytics nomirror

set xrange [5:10]
set yrange [-2:2]

set xlabel 'pH'
set ylabel 'Z'

intercept=404.4
slope=-56.8
pH(emf)=(emf-intercept)/slope

s(ph)=10**(-pk)/(10**(-ph)+10**(-pk))
pk=-log10(10**(-9))
A = -1.5
HA = 0

s2(ph)=10**(-pk2)/(10**(-ph)+10**(-pk2))
pk2=-log10(10**(-6))
A2 = 0
HA2 = 1.3

k(ph)= (1-s(ph))*HA + s(ph)*A
k2(ph)= (1-s2(ph))*HA2 + s2(ph)*A2

s3(ph)=s(ph)+s2(ph)
k3(ph)=k(ph)+k2(ph)

vinit=0.005
cm=0.004
ca=0.099
cb=0.103
kw=10**(-13.997)
emfinit=-52.1

z(va,vb,emf)= -( ( 10**(-pH(emf)) + (cb*vb/(vinit+va+vb)) - (ca*va)/(vinit+va+vb) -
kw/(10**(-pH(emf))) )/( cm*vinit/(vinit+va+vb) ))
```

fit [5:10] k3(x)'alldata.dat' u (pH(3)) : ((z(1/1000,2/1000,3)-z(0,0,emfinit))) via pk,pk2

plot 'acid.dat' u (pH(3)) : ((z(1/1000,2/1000,3)-z(0,0,emfinit))) w points pt 6 lc 1 title 'Acid addition','base.dat' u (pH(3)) : ((z(1/1000,2/1000,3)-z(0,0,emfinit))) w points pt 4 lc 1 title 'Base addition', k3(x) w lines lt 1 lc 3 ti ''

Listing L3: Gnuplot script for fitting NMR signals to yield the area under the peak.

```
set term postscript eps enhanced colour
set output "FILEmu2.eps

set border 3
set xtics nomirror
set ytics nomirror

    pi=3.141592653589793
set samples 5000
set fit errorvariables

    lor1(x)=height1*((1/pi)*(0.5*width1)/((x-center1)**2+(0.5*width1)**2))
lor2(x)=height2*((1/pi)*(0.5*width2)/((x-center2)**2+(0.5*width2)**2))

    set xlabel 'Shift (ppm)'
set xrange [550:400]
set ylabel 'Intensity'
set yrange [-0.1E8:3E7]

    center1=475.6
width1=1
height1=3.5E7

    center2=470.5
width2=3
height2=3.5E7

    fit lor1(x) "FILE" u 4:2 via center1, width1, height1
fit lor2(x) "FILE" u 4:2 via center2, width2, height2

    fitinfo1 = sprintf("fit height1: fitinfo2 = sprintf("fitheight2 :
    plot "FILE" u 4:2 w lines lt -1 ti 'obs',
lor1(x) w lines lt 1 t fitinfo1,
lor2(x) w lines lt 1 t fitinfo2,
" u 4:((lor1($4)+(lor2($4))-$2) w lines lt 1 ti 'residual'
```

Table 1: XYZ coordinates of $[PV_2Nb_{12}O_{42}]^{9-}$ using PBE0/cc-pvtz (H-Ar), lanl2dz (K-)

O	-3.77864	-2.62534	-2.86518
O	-5.50321	-0.00661	-0.00048
O	-3.78378	2.67306	-2.81486
O	-0.20226	0.05380	-5.50877
O	-3.16227	0.01387	-1.65069
O	-3.47598	-1.83864	-0.01902
O	-1.53905	-3.60580	-1.40035
O	-1.23283	-1.32935	-3.16971
O	-1.23810	1.39139	-3.14673
O	-3.77876	-2.68251	2.81365
O	-3.48428	1.83293	0.01862
O	0.20932	-5.50819	-0.05559
O	-1.54203	-3.63659	1.32722
O	1.54818	-1.32567	-3.63397
O	-3.16246	-0.02016	1.65027
O	-0.89300	-1.30517	-0.01316
O	1.24155	-3.14414	-1.39209
O	-1.55016	3.63273	-1.32691
O	1.54166	1.40173	-3.60305
O	-0.90761	1.29386	0.01234
O	-3.78441	2.61581	2.86543
O	0.90032	0.01764	-1.29981
O	3.78562	-2.81015	-2.67801
O	-1.23603	-1.39248	3.14370
O	1.23884	-3.17032	1.32864
O	-1.54738	3.60164	1.39983
O	1.22983	3.17326	-1.32805
O	-1.23584	1.32775	3.17254
O	3.47998	0.02269	-1.83501
O	0.89996	-0.00787	1.29980
O	3.16457	-1.64779	-0.01671
O	0.19597	5.51126	0.05551
O	3.77773	2.86957	-2.61974
O	1.23242	3.14741	1.39143
O	1.54466	-1.39884	3.60321
O	3.16084	1.65400	0.01729
O	-0.20295	-0.05722	5.50887
O	3.78536	-2.86133	2.62145
O	3.47970	-0.01494	1.83560
O	1.54422	1.32857	3.63432
O	5.50335	0.00518	0.00045
O	3.77698	2.81873	2.67737
V	-3.90915	-0.00038	-0.00026
V	3.90928	0.00383	0.00031
Nb	-2.46213	-2.00948	-1.88055
Nb	-2.46565	2.04177	-1.84233
Nb	0.07199	0.03719	-3.77863
Nb	-2.46296	-2.04826	1.83990
Nb	-0.06704	-3.77839	-0.03802
Nb	-2.46540	2.00290	1.88238
Nb	2.46755	-1.83885	-2.04489
Nb	-0.07649	3.78101	0.03785
Nb	2.46081	1.88457	-2.00509
Nb	0.07150	-0.03868	3.77877
Nb	2.46670	-1.87928	2.00640
Nb	2.46104	1.84423	2.04432
P	-0.00001	-0.00062	-0.00019

Table 2: XYZ coordinates of $[V_3Nb_{12}O_{42}]^{9-}$ using PBE0/cc-pvtz (H-Ar), lanl2dz (K-)

O	-3.77597	2.82640	2.67640
O	-5.50828	0.00004	-0.00001
O	-3.77561	-2.44021	3.03033
O	-0.23182	0.36678	5.48427
O	-3.14211	0.10961	1.63033
O	-3.50825	1.84638	-0.12426
O	-1.56512	3.73711	1.12374
O	-1.20742	1.56350	3.01436
O	-1.20215	-1.14841	3.19245
O	-3.77557	2.44026	-3.03031
O	-3.50834	-1.84636	0.12426
O	0.23186	5.48427	-0.36675
O	-1.56738	3.55343	-1.61016
O	1.56741	1.61015	3.55340
O	-3.14211	-0.10959	-1.63034
O	-0.95566	1.39007	-0.09363
O	1.20219	3.19244	1.14840
O	-1.56742	-3.55341	1.61017
O	1.56514	-1.12375	3.73712
O	-0.95575	-1.39004	0.09365
O	-3.77599	-2.82635	-2.67643
O	0.95571	0.09361	1.39005
O	3.77563	3.03028	2.44022
O	-1.20213	1.14839	-3.19239
O	1.20742	3.01436	-1.56353
O	-1.56520	-3.73710	-1.12372
O	1.20740	-3.01439	1.56352
O	-1.20740	-1.56355	-3.01439
O	3.50829	0.12422	1.84637
O	0.95570	-0.09367	-1.39006
O	3.14210	1.63028	-0.10960
O	0.23180	-5.48427	0.36673
O	3.77596	-2.67643	2.82640
O	1.20208	-3.19239	-1.14840
O	1.56517	1.12371	-3.73710
O	3.14212	-1.63039	0.10960
O	-0.23184	-0.36670	-5.48427
O	3.77600	2.67639	-2.82636
O	3.50829	-0.12429	-1.84637
O	1.56739	-1.61018	-3.55344
O	5.50828	-0.00010	-0.00000
O	3.77554	-3.03037	-2.44024
V	-3.91440	-0.00005	-0.00000
V	3.91440	-0.00008	-0.00000
Nb	-2.46606	2.16284	1.71299
Nb	-2.46536	-1.91308	1.98632
Nb	0.08699	0.25326	3.76484
Nb	-2.46535	1.91313	-1.98627
Nb	-0.08696	3.76484	-0.25323
Nb	-2.46605	-2.16281	-1.71303
Nb	2.46538	1.98628	1.91308
Nb	-0.08702	-3.76483	0.25325
Nb	2.46604	-1.71302	2.16284
Nb	0.08699	-0.25322	-3.76484
Nb	2.46607	1.71299	-2.16281
Nb	2.46532	-1.98631	-1.91313
V	0.00000	-0.00001	-0.00000